MEASURING SMALL VALUES OF INTERNAL OPTICAL MODE LOSS IN LASER DIODES

Author:

ROBERT PASCOE
Cardiff University
School of Physics and Astronomy

A thesis submitted in accordance with the
requirements for
the degree of Doctor of Philosophy in Physics

Year: 2016
Supervisors: PETER SMOWTON and PETER BLOOD

Contents

4

List of Figures

List of Tables

8

Abstract

Improvements in fabrication processes have yielded a steady reduction in the Internal Optical Mode Loss, α_i, of semiconductor laser devices in recent decades. Hence, uncertainty in the determination of α_i (roughly ± 1.0 cm^{-1}) has become insufficient. The aim of this work is to reduce the uncertainty within this method to ± 0.1 cm^{-1}.

The modulated multisection method — in which the absorbing length within a device is alternated rapidly compared with the timescales of systemic drift — was introduced to combat errors associated with such drifts in the standard method. Experimental data demonstrated that systemic drift correlates with substantial systematic errors and that these errors are made negligible by application of this modulated method.

A systematic error — due to divergence within the waveguide of broad area devices — of 3.2 cm^{-1} was identified and a method for its correction was developed. Error associated with injection efficiency of the multisection contact geometry was identified. This error is sufficiently small for drive currents greater than 22 mA at device temperatures of 300 Kelvin and greater.

By characterising measurement precision, experimental conditions were established in which drift-associated error *and* imprecision were small with respect to the project uncertainty aim. In optimised conditions, repeated measurements of optical loss below the absorption edge had an associated average deviation of ± 0.017 cm^{-1}.

This low uncertainty was applied to a systematic investigation of optical loss spectra in an InP Quantum Dot device as a function of device temperature. The temperature dependence of α_i was characterised with an uncertainty (approximately ± 0.05 cm^{-1}) that would be impossible using conventional methods. A feature with a peak magnitude of 0.2 cm^{-1} was identified and associated with the occurrence of very large quantum dots. The improved uncertainty demonstrated in this project presents an opportunity for more detailed study of α_i.

Acknowledgements

"...inside my mind, I see the eyes of loss..."

— Goodtime Boys, Daylight

11

Background Material

1.1 Introduction

Quantum heterostructure lasers have undergone steady development in recent decades. As fabrication techniques have progressed, the electronic and optical characteristics of commercial lasers have seen great improvements. However, as the quality of devices improve, so must the experimental techniques through which they are characterised. A quantity known as the *Internal Optical Mode Loss* (denoted α_i) describes the fractional loss of light intensity from a device waveguide per unit length of propagation due to scattering of light out of the optical mode at lattice imperfections and optical absorption due to various intraband mechanisms. In a measured optical loss spectrum, contributions from interband transitions, denoted by A, are also present. Hence optical loss is commonly expressed in the form $(A + \alpha_i)$. Internal loss can be measured in spectral regions in which interband optical loss is negligible. An understanding of internal loss processes is crucial to the development of devices with high operating efficiency and is of particular interest in the fabrication of high power laser diodes. The aim of this project is to measure low values of internal loss using the method for optical loss spectra known as the Multisection Method.

Modern high-power semiconductor laser devices tend to have internal optical mode loss values as low as a few cm^{-1} [1, 2]. In the past, uncertainties of ± 1 cm^{-1} have been typical in Multisection Method measurements of internal optical mode loss in typical Quantum Dot and Quantum Well structures with internal loss values in excess of 5 cm^{-1}. Development of measurement techniques with reduced uncertainty is clearly necessary. In light of this, uncertainty considerations in this document are contrasted with a benchmark value of ± 0.1 cm^{-1}. Optical Loss measurements are made using the multisection (or *segmented-contact*) electrically pumped method which was developed within this research group [3]. A motivation for continued development of this technique is that, unlike in other methods for the determination of optical loss, all measurements are made on a single sample and in the electrically pumped, front-facet emitted arrangement of a standard laser structure (with the concession that longitudinal modes are suppressed).

1.2 Laser Structures and Operation

1.2.1 General Structure of a Semiconductor Laser Device

The main focus of this document is on the loss of light in propagation through quantum dot and quantum well semiconductor laser structures. As such, descriptions of these structures and some related conventions are warranted. Note that only the theory that is necessary in understanding the presented work is given in this document. Exhaustive descriptions of the principles of operation of laser diodes can be found in many sources [4–9] . Figure 1.1 shows schematics of two typical laser structures. Some key differences between these structures are emphasised. Frequent reference will be made to specific orientations and optical polarizations in this document. Orientations are clearly defined by the arrows to the right of the structure diagrams with respect to which light propagation and polarisations are defined . The concepts of Broad Area (BA) and Ridge Waveguide (RW) structures are also introduced.

To produce such structures, layers of varying composition are deposited accumulatively onto a substrate wafer in the transverse direction by epitaxial growth. Thus layers are formed in the lateral plane. This corresponds to growth in the positive transverse direction as defined in Figure 1.1 . The role of these layers in the structure is discussed in Section 1.2.6. The direction running along the length of the device is defined as the Longitudinal orientation. In one dimensional models of light propagation, this is the direction in which light travels out of the device front facet and towards the detection system.
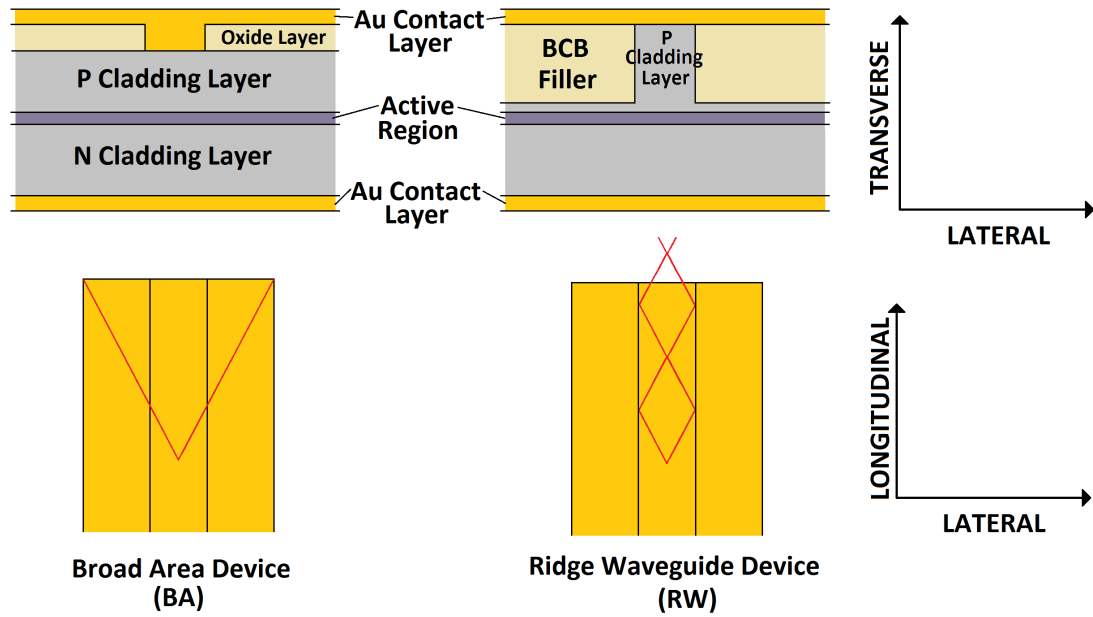
Figure 1.1: The upper figure demonstrates a cross-section through a Broad Area and a Ridge Waveguide device structure. The guiding action of the ridge is illustrated in the lower figures, which depict a plan view of the upper surface of a laser device (from above). The upper edge of this lower pair of figures indicate their front facets (the emitting surface of a device in operation). Key orientations within the structure are given by the arrows to the right of each pair of diagrams.

By etching into the top surface of the structure using a masked pattern before deposition of the gold contact layer, devices with ridges of material centred in the lateral orientation and running parallel to the optical axis of the device can be formed. The etched space is filled by a dielectric and the resultant discontinuity in the effective refractive index introduces transverse optical confinement. The

advantages demonstrated in such 'Ridge Waveguide' (RW) devices are discussed in the following section. The structures on the left of Figure 1.1 are known as 'Broad Area' (BA) devices.

Certain linear polarizations of emitted light are defined as follows. The Transverse Electric (TE) polarization has an electric field vector parallel with the layers of growth of the material, while the Transverse Magnetic (TM) polarization has an electric field vector perpendicular to the layers of growth of the material. Stated another way, the TE electric field vector is parallel with the lateral orientation and TM electric field vector is parallel with the transverse orientation.

For experimental use, the lower gold contact of the device (shown in Figure 1.1) is affixed to a 3 mm long copper block using a silver epoxy which is, in turn, affixed to an 8-pin T0-39 header. Gold contacts on the upper surface of a device can be individually connected to the pins of the header with gold wire and conductive epoxy. This provides a method of applying electrical bias to any required contacts and a standard connection to sample holding apparatus in all of the experimental methods which follow. (The necessity for multiple electrical contacts is described in Section 1.3.4). The copper block acts as a heat sink, conducting heat away from the device and reducing the effect of 'self-heating' during pumping [10].

1.2.2   Electronic States in Semiconductors

The following is a basic outline of carrier behaviour in semiconductors. Full descriptions of the underlying physics may be found in various textbooks [4, 11, 12].

Figure 1.2 shows the $E(\boldsymbol{k})$ dispersion relation for a direct bandgap semiconductor:
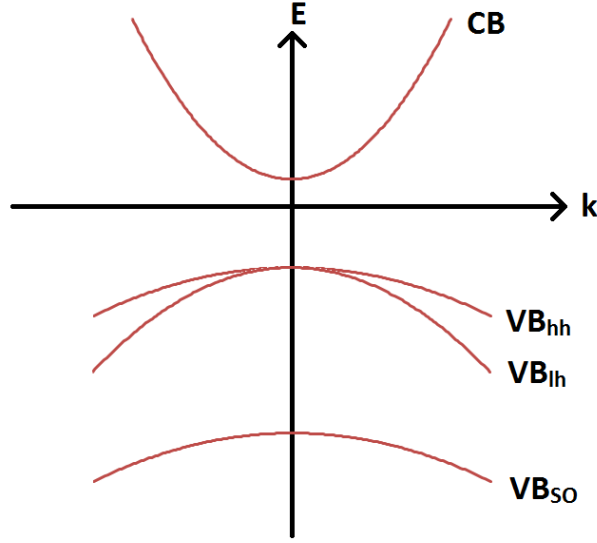
Figure 1.2: The dispersion relation for a semiconductor is given. CB, VB_{hh}, VB_{lh} and VB_{SO} represent the conduction band, heavy-hole valence band, light-hole valence band and split-off band respectively. Effective masses are related to this picture by Equation 1.2. (Bands are not precisely parabolic in this schematic.)

It has been observed that this behaviour is approximately parabolic for small values of $\mathbf{k}$. For example, the energy of a carrier within the conduction band (with respect to the maximum energy of the valence band) can thereby be described by equation 1.1:

$$E(\mathbf{k}) = E_G + \frac{(\hbar^2 \mathbf{k}^2)}{2m^*} \tag{1.1}$$

where m^* is the *effective mass* of a particular band and is related to band curvature by Equation 1.2. $\hbar$ is the reduced Planck's constant and E_G describes the energy gap between the lowest energy state of the conduction band and the highest energy state of the valence band.

$$m^* = \frac{\hbar^2}{\frac{\delta E^2}{\delta \mathbf{k}^2}} \tag{1.2}$$

Effective mass describes the modification of particle motion from its behaviour in free space by the periodic potential of the crystal lattice.

1.2.3 Interband Optical Transitions of a Laser Diode

The band-to-band optical gain and loss properties of a laser device are determined by the choice of material in the active layer. In bulk semiconductors – due to an approximately parabolic dispersion relation – the density of states is proportional to the square root of the transition energy. Due to momentum conservation in optical transitions, the optical absorption spectrum for bulk semiconductors follows the form of the density of states. This relationship between dispersion and optical absorption is examined in Figure 1.3:
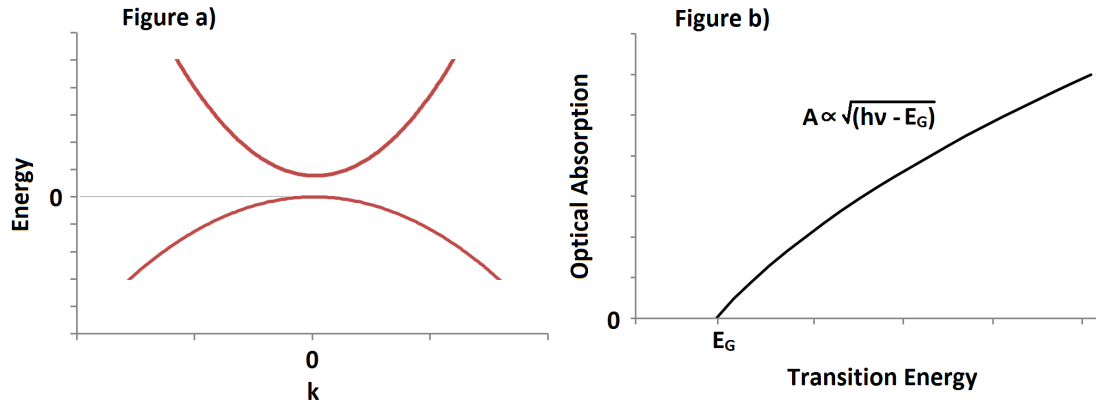
Figure 1.3: A dispersion relation and optical absorption spectrum are given in Figures 1.3.a) and 1.3.b) respectively. The upper and lower curves in Figure 1.3.a) represent the conduction and valence bands respectively.

In order to form a quantum well, relatively narrow bandgap material is grown in a layer which is thin with respect to the de Broglie wavelength of electrons (typically of the order of tens of nanometres). Accordingly, quantum confinement results in discrete carrier energy levels (for **k** aligned with the quantum confined spatial dimension). Interband transitions are restricted by the orthogonality of confined electron and hole wavefunctions and primarily occur between electron and hole states of the same quantum number.

17

Figure 1.4.a) provides a schematic description of quantum well energy bands and confined states are depicted therein. Arrows between conduction band (electron) and valence band (hole) states represent allowed optical transitions (corresponding to the first three energy levels). Figure 1.4.b) demonstrates the optical absorption spectrum corresponding with such a structure. In order to understand the change in energy levels due to confinement in a quantum well, the simple approximation of an infinite potential well is useful. An infinite potential well with an integer quantum number, n, has confinement energies of carriers as given in Equation 1.3 :
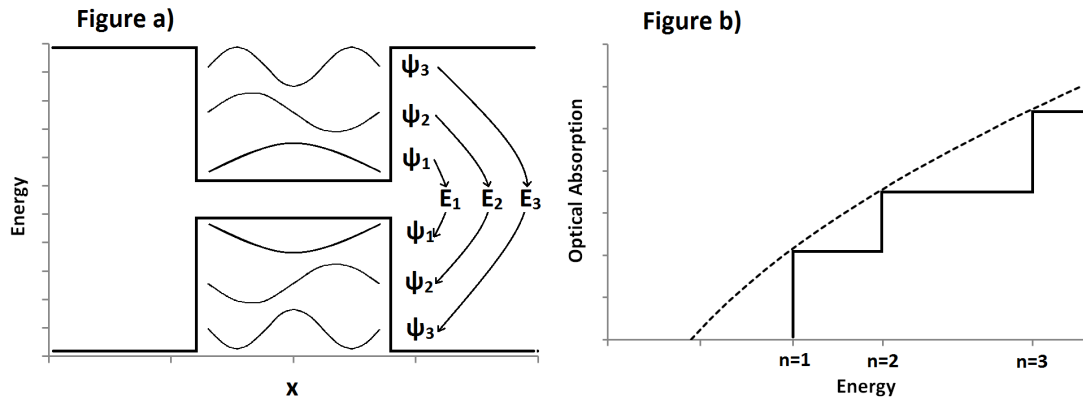
Figure 1.4: Figure 1.4.a) depicts an example of the energy band structure at a quantum well. Quantum confined carrier wavefunctions are depicted at increasing energy levels within the well. These are labelled with their E_n values, as introduced in Equation 1.3. Corresponding energy levels can be seen on the optical absorption spectrum in Figure 1.4.b). These are compared with the bulk material optical absorption (the dashed line) which was introduced in Figure 1.3. Note that this schematic depicts a *finite* square well, for which energy equations cannot be solved analytically.

$$E_n = \frac{h^2 n^2}{8m^* d^2} \qquad (1.3)$$

where h is Planck's constant, m^* is the effective mass of the carrier and d is the width of the well.

The minimum energy of a transition from a conduction to valence band state

in a quantum well is equal to the sum of the band gap of the material, E_G and the *confinement* energies of the electron and the hole, defined for the nth confined state as given in Equation 1.4:

$$\hbar\omega = E_G + \frac{h^2 n^2}{8 m_e^* d^2} + \frac{h^2 n^2}{8 m_h^* d^2} \tag{1.4}$$

where m_e^* and m_h^* are effective masses for the electron and hole respectively and $\hbar\omega$ represents the photon energy associated with the transition. Kinetic energy of the carriers within the plane of the quantum well acts to increase the energy of the transition. This results in the 'step-like' characteristics shown in Figure 1.4.b). Unlike the case of the bulk material described in Figure 1.3.b), an increase in photon energy does not correspond to an increase in absorption coefficient until the energy reaches the next E_n and a new quantum well transition becomes available.

Quantum dots occur in the case where the dimensions of a narrow bandgap material are small in comparison with the de Broglie wavelength of an electron in all three spatial orientations. Quantum confinement of carriers will then occur for each spatial dimension and, consequently, quantum numbers exist for each dimension – n_x, n_y and n_z. Unlike in the case of quantum wells, carriers within a quantum dot are confined in all spatial directions and hence kinetic energy cannot increase the transition energy above that defined by the confinement energy. Consequently, absorption peaks associated with the transitions of a quantum dot take the form of delta functions which are broadened homogeneously (in contrast with the step-like behaviour seen in Figure 1.4.b)).

Figure 1.5.a) depicts the band structure and Figure 1.5.b) depicts the optical absorption spectrum of a quantum dot:
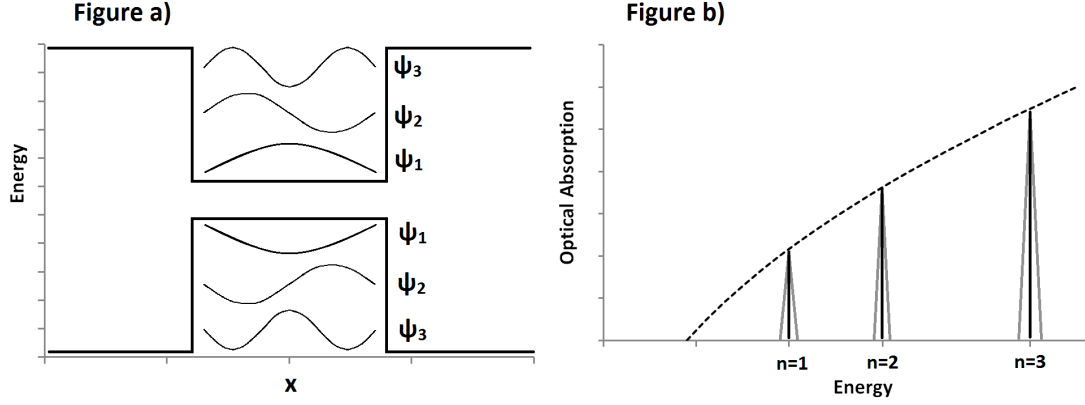
Figure 1.5: Figures 1.5.a) and 1.5.b) show the band structure and optical absorption spectra of a quantum dot structure respectively. In figure 1.5.b), the step-like behaviour of the quantum well is replaced by distinct peaks. Grey triangles in Figure 1.5.b) indicate homogeneous broadening of the absorption peaks.

Using an infinite potential well approximation, the energy corresponding to confined carriers within a quantum dot can be defined as shown in Equation 1.5:

$$E_n = \frac{h^2(n_x^2 + n_y^2 + n_z^2)}{8m^*d^2}$$
(1.5)

and Equation 1.4 can be established, as is shown in Equation 1.6:

$$\hbar\omega = E_G + \frac{h^2(n_x^2 + n_y^2 + n_z^2)}{8m_e^*d^2} + \frac{h^2(n_x^2 + n_y^2 + n_z^2)}{8m_h^*d^2}$$
(1.6)

Equation 1.6 demonstrates that a square well model results in quantum dot states of differing separations. Equally spaced quantum dot state energies have been experimentally observed and hence some, more sophisticated, models use parabolic wells to represent the potential in the plane of the growth layers [13].

1.2.4   Internal Optical Loss Mechanisms

Internal loss processes include scattering of light at irregularities in the crystal structure (especially at interfaces between growth layers), inter-valence band absorption (IVBA) — wherein an electron in the split-off band is promoted to a state in the light or heavy hole valence bands, or from the light hole band to the heavy hole band — and intraband absorption (also known as free-carrier absorption) — wherein an electron is promoted from a low energy state to a higher energy state *within the same band* [13]. In order for momentum to be conserved, interaction with phonons (lattice vibrational states) is necessary.
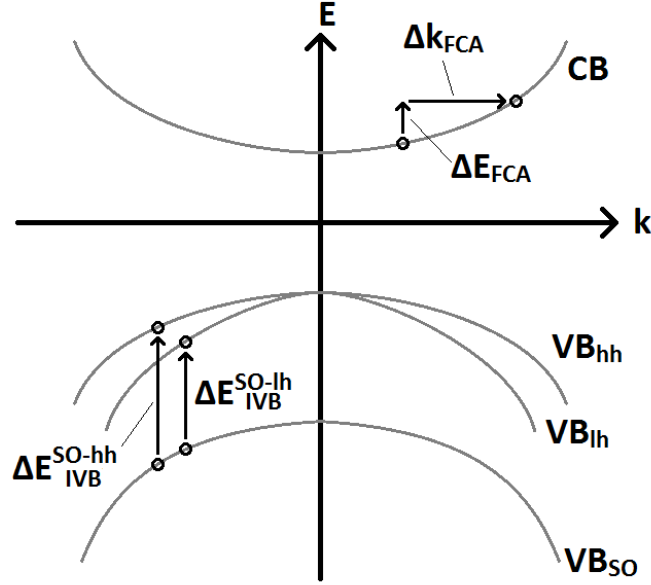
Figure 1.6: The band structure introduced in Figure 1.2 is repeated. A free-carrier absorption transition is demonstrated in the conduction band and two IVBA transitions demonstrated from the split-off band to the light and heavy valence bands. ΔE_{FCA}, ΔE_{IVB}^{SO-hh} and ΔE_{IVB}^{SO-lh} are the respective energies of these transitions and $\Delta \boldsymbol{k}_{FCA}$ is the momentum imparted by the crystal lattice during the free carrier absorption transition.

Assuming $\boldsymbol{k}$ conservation, IVBA occurs at an energy which is dependent upon the separation of the involved bands as a function of $\boldsymbol{k}$. The requirement that the upper state contains a hole tends to limit the total number of states which contribute to IVBA (in which $\boldsymbol{k}$ is conserved) and causes the distribution of carriers

to be crucially important. Due to the requirement of the presence of a phonon for transitions in which $\boldsymbol{k}$ is not conserved, such transitions are less probable and make a smaller contribution. IVBA typically occurs at low photon energies with respect to the bandgap due to the smaller relative separations of the valence bands. IVBA is commonly managed in modern devices by manipulation of valence band offsets and dispersion via the introduction of strain into device structures [14, 15].

Free carrier absorption depends upon carrier density and upon photon energy as described by the Drude Free Carrier equation, given in Equation 1.7 [16]:

$$\alpha_{FCA} = \frac{Ne^2}{m^*\epsilon_0\eta c\tau}\frac{1}{\omega^{n'}} \tag{1.7}$$

In Equation 1.7, ϵ_0, η, e, τ and N represent the vacuum permittivity, the refractive index of the material, the magnitude of the electric charge of an electron, the momentum damping period of the carrier, and the carrier density respectively. ω is the frequency of the absorbed photon.

The exponent of ω depends upon the interaction of electrons with phonons, but is typically taken to be $n' = 2$. (The prime emphasises that n' is not the same quantity as n, the quantum number associated with quantum well states).

1.2.5 The Fermi Function

The temperature-dependent probability of occupation of an electron state as a function of state energy is defined by the Fermi function, $f_e(E)$. The Fermi function has the form demonstrated in Equation 1.8.

$$f_e(E) = \frac{1}{e^{\frac{E-\epsilon_f}{kT}} + 1} \tag{1.8}$$

T is the material temperature and k is Boltzmann's constant. The Fermi function dictates that states with energies beneath a characteristic energy — known as the Fermi level, ϵ_f, — are occupied with electrons at absolute zero and that states

with energies greater than the Fermi level are unoccupied. At higher tempera-
tures, thermal energy excites carriers to energies above the Fermi level, leaving
states unoccupied below the Fermi level. This is demonstrated in Figure 1.7. Hole
occupation probability is defined to be the absence of an electron and is hence
described by Equation 1.9:

$$f_h(E) = \left(1 - \frac{1}{e^{\frac{E-\epsilon_f}{kT}} + 1} \right) \tag{1.9}$$

A single Fermi level is appropriate to describe a population of carriers in thermal
equilibrium. A displacement from equilibrium — either due to optical pumping
or the application of electrical bias — will cause the loss of equilibrium between
conduction band and valence band carriers. In this instance, a separate Fermi level
may be used for each band. In this case, these quantities are described as *quasi*
Fermi levels.
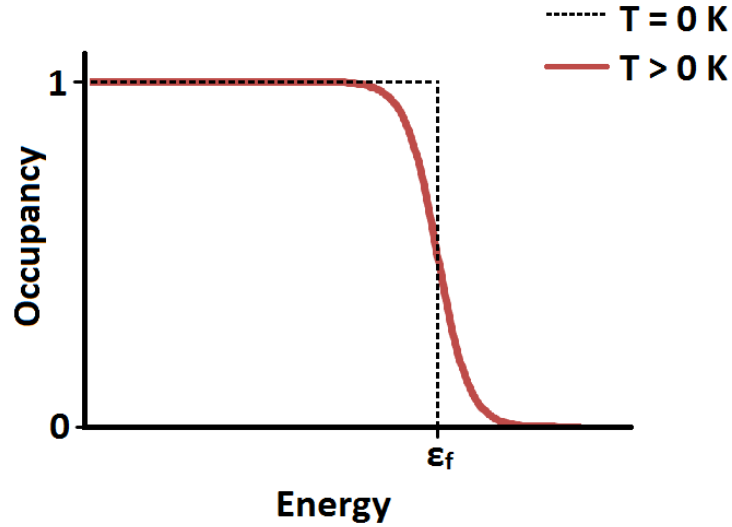
Figure 1.7: The behaviour of the Fermi function at and above absolute zero are demon-
strated by the dashed black and solid red lines respectively.

1.2.6 Significance of Internal Loss in High Power Laser Diodes

The significance of internal loss on the performance of high power laser devices is best understood through study of a Light-Current curve such as the diagram shown in Figure 1.8 :

Internal loss influences the Light-Current performance of high power laser diodes in two ways. Firstly, the threshold optical gain of a device is related to internal loss by Equation 1.10.
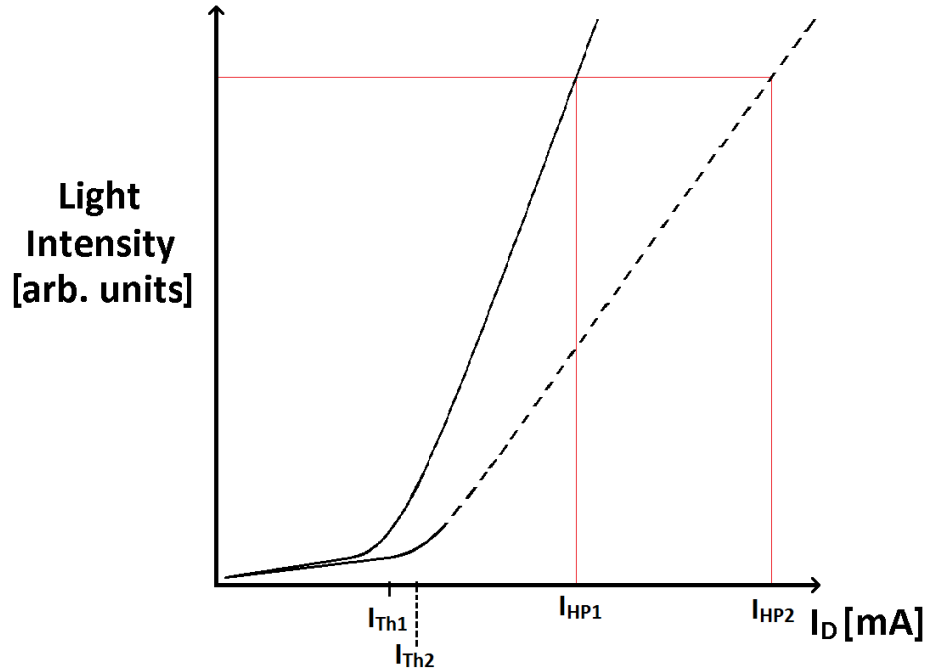
Figure 1.8: A figure representing the L-I characteristic of a laser device. Device light output is plotted against I_D, the device drive current. The threshold currents for both curves, I_{Th1} and I_{Th2} are labelled on the x-axis. The dashed curve depicts a change in extraction coefficient caused by an increase in internal optical loss.

$$G_{threshold} = \alpha_i + \alpha_m = \alpha_i + \frac{1}{2L}\ln\left(\frac{1}{R_1 R_2}\right) \qquad (1.10)$$

24

in which, $G_{threshold}$ is the threshold modal gain, α_m is the distributed mirror loss, L is the longitudinal length of a device and R_1 and R_2 are the respective reflectivities of the front and rear facets. I_D is the device drive current. Clearly, a higher value of internal loss will increase the value of $G_{threshold}$ and, in turn, threshold current. Secondly, internal loss affects the gradient above threshold of the L-I curve shown in Figure 1.8 . This quantity is proportional to the extraction efficiency of the device F_{ex}. F_{ex} is defined to be the fraction of light which exists within an optical mode in the laser cavity which is emitted through the facets (rather than being lost to scattering processes). F_{ex} is critical to the production of high power devices. Due to the high currents at which such lasers are often operated and the low values of I_{Th} obtainable in modern devices, small changes in this gradient can drastically affect device output. Equation 1.11 below describes the relation between α_i and F_{ex} :

$$F_{ex} = \left(\frac{\alpha_m}{\alpha_m + \alpha_i} \right) \tag{1.11}$$

The form of Equation 1.11 dictates that small contributions from α_i can significantly reduce light output from the device *at very high pumping currents*, even for modern devices in which the value of α_m may significantly exceed that of α_i [17]. The effect of two different values of F_{ex} are shown in the two curves in Figure 1.8 . The solid curve represents relatively high output due to a low α_i (and hence large F_{ex}). The dashed curve represents a lower light output due to a higher α_i .

The red lines denote the current values (I_{HP1} and I_{HP2}) required to achieve a particular value of light intensity for the cases of the two F_{ex} values. It can be seen that an increase in internal loss will increase the pump current required to reach a particular desired light output.

Decreasing F_{ex} will both decrease device efficiency and increase the waste heat produced by a device in operation, causing maximum operating temperature to be reached at lower values of light output power. This is especially significant due to the high operating currents in high power devices, typically around 10 times their threshold current. A small change in F_{ex} can drastically change the light output

which a device can obtain. For this reason, this effect dominates over the internal loss dependence of I_{Th}.

1.2.7 Optical Confinement

Emitted light is confined — in the plane of the growth layers — to some region near to the active layer of a device by means of a slab waveguide [18]. This is achieved by use of low refractive index *cladding* layers surrounding a relatively high refractive index *core* layer. Light emitted with an emission angle below the critical angle of total internal reflection for the core-cladding interface is confined in the core and certain modes in which light may propagate are formed. These modes may be examined by solution of Maxwell's equations. Guiding by means of a slab waveguide is illustrated schematically in Figure 1.9:
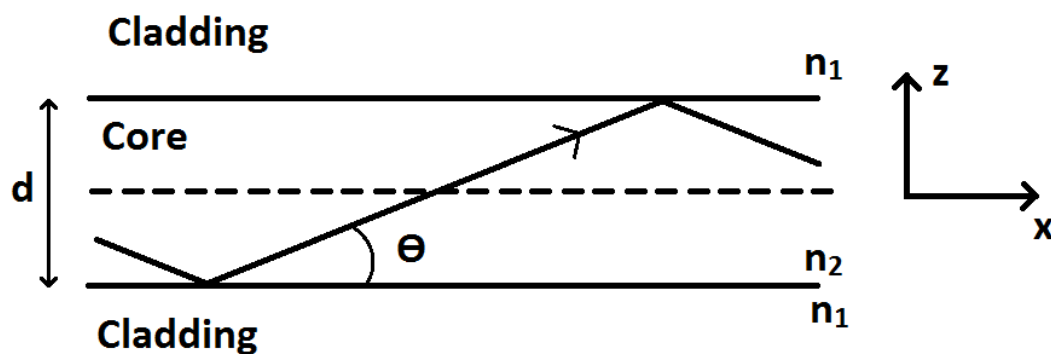
Figure 1.9: Guiding by refraction at the interface between layers of different refractive indices within a slab waveguide structure is shown. The refractive indices of the core and cladding are denoted here as n_2 and n_1 respectively. For guiding to occur, n_2 must exceed n_1. Θ denotes the angle of refraction associated with a particular optical mode.

Hence the properties of various optical modes in both TE and TM polarisations may be examined via a set of transendental equations which depend on d, n_1 and n_2. A common application of this analysis in laser device design is the improvement of device performance by the suppression of higher order optical modes [1].

26

1.2.8 The Double Heterostructure Laser

The concepts of *optical and carrier confinement* are central to understanding the generic structure of the Double-Heterostructure Laser (DHL). Optical confinement is achieved as described in Section 1.2.7 and the use of core layers with a lower band-gap than the cladding material improves the confinement of carriers in the core [7]. The application of these effects in a real device structure can be seen in Figure 1.10. The general structure of device type #1 (introduced in Figure 2.1) is used for this explanation. The use of a relatively low band-gap active material results in the emission of light with a photon energy lower than the band-gap energy of the cladding. Hence, band-to-band absorption of light propagating in the cladding material is small, further enhancing device performance.
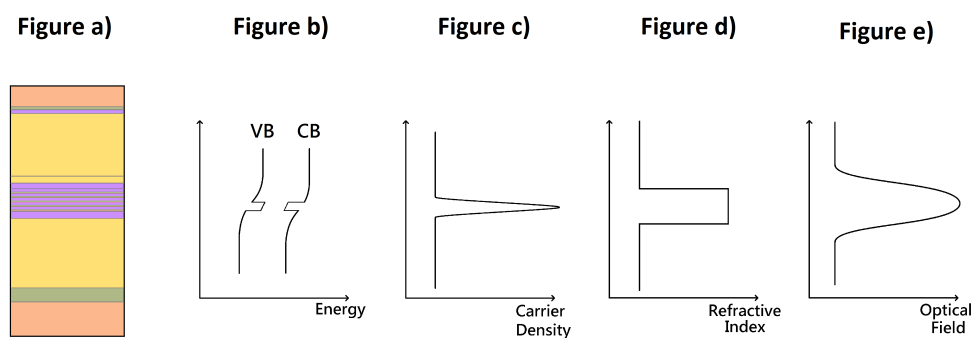
Figure 1.10: The layer structure given in Figure 2.1 is demonstrated alongside quantities relevant to carrier and optical confinement. The unlabeled, vertical axis in each case is a spatial axis representing the spatial distribution of each quantity through the layer structure of the wafer. Figure 1.10.b) demonstrates the effect of a narrow band-gap active region; additional structure within the active region (and the effect of confinement) is omitted in favour of simplicity.

In this example structure, thick layers of AlInP *cladding* on either side of the core layers have a low refractive index compared with the core layers between them. This refractive index step provides optical guiding by total-internal reflection. This is shown in Figure 1.10.d).

27

Comparison of the axes of Figure 1.10 demonstrate the advantages of the DHL. Figure 1.10.b) shows the electronic band structure of the wafer. The labels 'VB' and 'CB' denote the valence band and conduction bands respectively. The characteristic curved bands of a P-N diode can be seen, with an additional potential well due to the presence of low band-gap material in the centre of the structure. This band structure will tend to lead to high concentrations of electrons in the conduction band potential well and holes in the valence band potential well, upon the application of forward bias. This carrier distribution is shown in Figure 1.10.c). Figure 1.10.d) shows the refractive index step at the interface between the waveguide cladding and core layers. Figure 1.10.e) depicts the distribution of the optical field brought about by total internal reflection at these interfaces. This overlap of optical and carrier confinement results in low threshold currents in processed devices.

Figure 1.10 is not to scale and doesn't account for the repeated layers of the active region. It simply provides a basic introduction to the underlying concepts.

1.2.9 Optical Loss and Temperature dependence

Various temperature dependences of internal optical loss have been observed in laser structures [19–21]. Certain key concepts must be covered in order to understand temperature dependence in optical loss spectra.

Optical loss spectra typically become relatively flat at photon energies below the band edge (for example, Figure 1.14). Unlike with interband transitions, the lack of clearly defined features can act to complicate the identification of the dominant source of internal optical loss .

The Varshni Equation is a semi-empirical description of the temperature dependence of the bandgap in a semiconductor and is defined by Equation 1.12 [22]:

$$E_g(T) = E_g(T = 0) - \frac{\alpha T^2}{T + \beta} \qquad (1.12)$$

$E_g(T)$ is the bandgap of the material at absolute zero and α and β are material dependent parameters. For example, in InP the given reference quotes the following values for these parameters $E_g(T = 0) = 1.4206$ eV, $\alpha = 4.906 \text{x} 10^{-4}$ K eV^{-1} and $\beta = 327$ K [22]. (The Varshni fitting parameter, α is distinguished from internal optical loss by the lack of a subscript i in this document.)

$E_g(T)$ from Equation 1.12 has been calculated for illustrative purposes for InP (using the stated values) in Figure 1.11. The temperature dependence described by Equation 1.12 acts to rigidly red-shift transition energies in measured spectra with increasing device temperature. Optical Loss coefficients which are measured at photon energies near to the absorption edge are particularly susceptible to drastic changes in value with temperature as the photon energy of the absorption edge changes. Hence, awareness of this temperature dependence is crucial for accurate assessment of internal optical mode loss. This is particularly true in the instance of systematic investigations with device temperature, such as that described in Chapter 11. It is noted that the localisation of carriers caused by any spatial minima in bandgap can cause a departure from the Varshni equation at low temperatures [23]. In the temperature range examined in this thesis, no such departure is observed.

Transitions associated with a quantum dot sample are broadened inhomogeneously — by the distribution of dot sizes within a particular sample — and dots of each size are broadened homogeneously — due to the finite duration of interaction between dots and light [24]. This broadening is shown in the schematic in Figure 1.12. There is evidence of temperature dependence of homogeneous broadening in quantum dot laser structures [25]. This effect must be considered both in measuring the values of absorption peaks and of measuring values of optical loss at photon energies in sufficiently close proximity to absorption peaks.
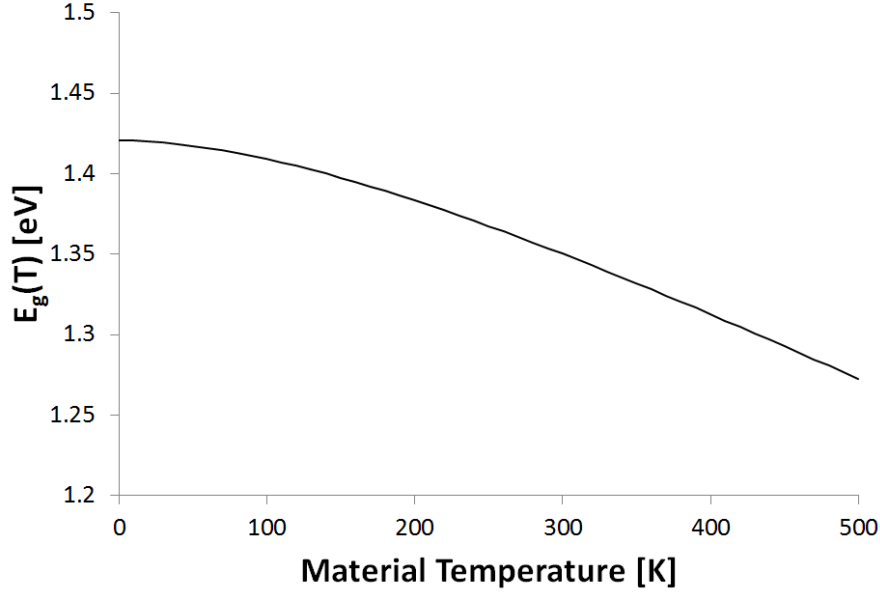
Figure 1.11: The temperature dependence of the bandgap according to the Varshni equation is plotted for InP.

Transitions associated with a quantum dot sample are broadened inhomogeneously — by the distribution of dot sizes within a particular sample — and dots of each size are broadened homogeneously — due to the finite duration of interaction between dots and light [24]. This broadening is shown in the schematic in Figure 1.12. There is evidence of temperature dependence of homogeneous broadening in quantum dot laser structures [25]. This effect must be considered both in measuring the values of absorption peaks and of measuring values of optical loss at photon energies in sufficiently close proximity to absorption peaks.

Other temperature dependent effects upon the optical loss in semiconductors include the temperature dependent occupancy of states throughout the band structure due to the temperature dependence of the Fermi function. Carrier density is calculated via the integral of the product of the density of states with the Fermi function (for a particular carrier) as a function of energy. The resultant absorbing processes depend heavily upon temperature and photon energy [26].
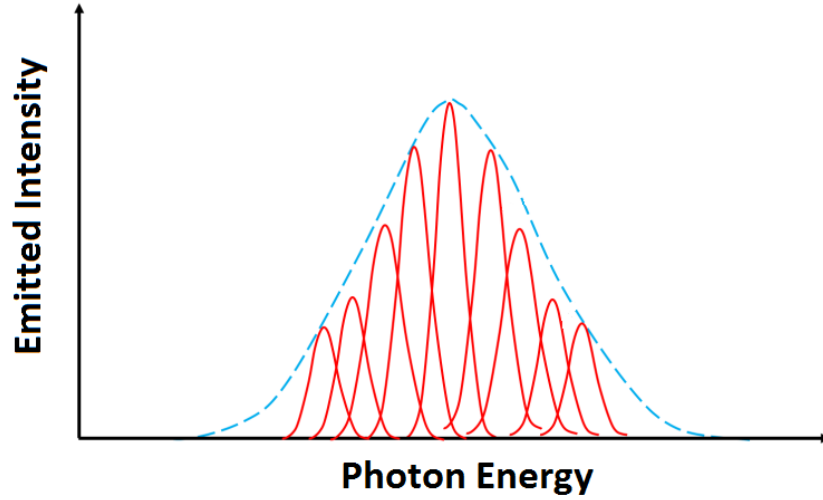
Figure 1.12: Broadening mechanisms are shown for Quantum Dot samples. The red lines represent homogeneous broadening of dots with varying associated photon energies. The blue dashed line is an envelope function representing the inhomogeneous distribution of emitted photon energies. This figure is adapted from the reference [27].

1.3 The Multisection Method for Optical Loss Spectra

1.3.1 Introduction

The Multi-section Method for Optical Loss Spectra was developed by Cardiff University's Optoelectronics group in 1999 [28] and the method and its applications were more fully described in a 2003 paper [3]. In the latter paper the method is described as 'the Segmented Contact Method', but this document prefers the naming convention of the original reference. Both papers present a methodology for the direct observation of gain and loss behaviour in pumped and passive regions of an electrically pumped device respectively. As this project is primarily concerned with Optical Loss, a description of the method for loss will be examined in Section 1.3.2. Gain measurement is not the focus of this document, but a brief description of the method is given in Section 2.6. It ought to be noted that internal

loss can also be determined in an optical gain experiment. Similar electrically-pumped segmented contact experiments have been conducted in the past for gain by Oster et al. and Prince et al. and for gain and loss by McDougall et al. [29–31].

Alternative approaches to internal loss measurement include the Hakki–Paoli technique for optical gain [32]. This method compares amplitude variation in longitudinal modes of below-threshold emission of laser devices to determine gain spectra. Measurement of this spectrum at a photon energy lower than the bandgap of the gain medium provides an internal loss measurement. Past work has highlighted insufficient accuracy of Hakki–Paoli internal loss measurements [33]. As the value of loss measured by the Hakki–Paoli method includes mirror loss, uncertainty in the estimation of mirror loss limits the method's accuracy in the determination of internal loss. Accurate measurement of internal loss using the Hakki–Paoli method additionally requires a high spectral resolution in emitted intensity measurements and has inherent limitations on the Q-factor of the test device cavity [34]

Another common method for the determination of internal loss is the "external differential efficiency versus cavity length" method, in which, a value of internal loss can be extrapolated from external differential efficiency data measured in devices of different lengths [35]. This method assumes Fermi level pinning throughout the device, which results in inaccuracy [36]. Additionally, internal loss and internal differential efficiency are assumed to be independent of cavity length. Experimental work has shown that this is not the case, with corresponding systematic errors in measured values of internal loss of up to 10% [37].

There exist optically-pumped equivalents of the multi-section experiment such as those of Shaklee et al. and Bakker et al. [38, 39]. The primary motivation in use of an electrically-pumped multi-section optical loss measurement is to make the conditions of the measurement match the conditions in which real commercial devices tend to be operated. These methods don't require an electrical connection to the device. As such, they are well suited for rapidly testing wafers in fabrication facilities. However, recent work by Rob Thomas in this research group has demonstrated that systematic error due to charge accumulation in unpumped sec-

32

tions will exceed the ± 0.1 cm^{-1} uncertainty aim of this work, in the absence of an earthing connection to these sections [40]. Furthermore, optically pumping requires an additional optical alignment, potentially further decreasing the accuracy of the measurement.

Refinements of the multi-section method have been developed by Xin et al. and Shahid et al., providing novel methods for compensation for the collection of partially amplified light and performance of the method at low carrier densities/light levels respectively [41–43].

1.3.2 Fundamentals of the Multi-section Method

An Optical Loss Coefficient is defined as the fractional loss in light intensity per unit distance of propagation through a medium. In a waveguide, it is often expressed in the form $(A + \alpha_i)$. The optical loss coefficient is separated into the absorption of light due to excitation of carriers across the (conduction-valence) band gap, A, and internal optical mode loss, α_i.

It is common to attribute internal loss to the scattering of light from the optical mode due to interaction with irregularities within the cavity. However, internal loss has contributions from various sources (see Section 1.2.4). Indeed, internal loss is — by the definition given here —- associated with any optical loss process other than conduction-valence interband absorption.

Internal loss tends to have little spectral dependence within the bandgap of a device. It is therefore common to associate internal loss with a single value for a particular device.

Starting from an expression of the Beer-Lambert Law, consider a one dimensional model in which light travels parallel with a z axis (corresponding to the longitudinal axis described in Figure 1.1 in a real device) [16]. For a beam which is incident on uniform, thin slices of absorbing material of length dz, which are

perpendicular with the direction of the beam, and based on the premise that the fraction of the total light intensity lost is proportional to dz, Equation 1.13 is derived:

$$dI(z) = -(A + \alpha_i)I dz \qquad (1.13)$$

where $dI(z)$ is the small change in light intensity in passing through the thin slice of structure of length dz and I is the light intensity.

In a real measurement of an optical loss spectrum, interband absorption, intraband absorption, free carrier- and exciton-related loss processes all contribute to measured coefficients [13, 16]. Additionally, transition properties are often modified by quantum confinement in modern devices. This leads to complex spectral distributions of loss processes. As both A and α_i have spectral dependences, Optical Loss spectra are constructed using a spectrograph system (as discussed in Section 2.2). Such spectra are commonly expressed as a function of wavelength or photon energy. The latter will be favoured in this document.

It is worth noting that measurements of Optical Loss Spectra in the wider literature do not necessarily discriminate between loss and absorption processes. Consequently, what is commonly referred to as an 'Absorption spectrum' may have some contribution from non-absorptive loss processes (such as scattering).

The action of a loss mechanism in a waveguide is dependent upon the overlap between the optical mode in which the light is propagating and the spatial distribution of sources of loss. As such it is common to discuss Modal Optical Loss (see Section 1.2.7 for discussion of optical modes). Similarly, depending on the device structure, polarization dependence can be expected [4]. In the experiments outlined in this document, for consistency in results, the TE polarization is selected using a polarizer in the optical path. (Unless a statement is made to the contrary).

1.3.3 Mathematical Foundation of the Multisection Method

Equation 1.13 must be integrated in order to be practically applied. This results in Equation 1.14, the inverse exponential power law which is commonly associated with the Beer–Lambert Law:

$$I(z) = I_o e^{(-(A + \alpha_i)z)} \tag{1.14}$$

Rearranging for the Optical Loss coefficient, we obtain Equation 1.15:

$$(A + \alpha_i) = \frac{-1}{z} \ln \left(\frac{I(z)}{I_o} \right) \tag{1.15}$$

This is a general expression for fractional change in light intensity through some length of a lossy medium. It is worth noting that I, dI and $(A + \alpha_i)$ all have spectral dependences. These have been omitted from the equation for clarity of the derivation. In the following section, the specific device geometry of the Multisection Method is applied to this equation. Since α_i is only weakly dependent on photon energy, it can be measured through the application of Equation 1.15 at photon energies sufficiently below the absorption edge that A becomes negligible.

1.3.4 The Multisection Method in Practice

This section will establish the device geometry of the Multisection Method and apply it to the exponential model of loss of optical intensity. Section 2.7 will address further complexities in the acquisition of successful Multisection Method Optical Loss spectra. Assuming two device sections (such as those shown in Figure 1.13) are optically and electrically equivalent, the light intensity upon independently pumping each section will be identical given identical pumping current. As such, by changing the pumped section we are effectively changing the position of a light source of fixed output power longitudinally within the device. Under a *paraxial approximation* (i.e. one in which all of the light rays measured from a device front facet are parallel with the longitudinal axis), this shift in position results in a change in absorbing length of material in the optical path equal to the section

length, L_s.

Using terms introduced in Equation 1.15 , this light source has an intensity of I_0 at the edge of the pumped section nearest to the front facet (i.e. when z=0). By measuring the front-facet emitted light intensities from sections 1 and 2, I_1 and I_2, one can determine how much of I_1 is lost in traveling through L_s microns of passive (unpumped) path length by which the two sections differ. The following equation substitutes the practical geometry of the experiment into Equation 1.15:

$$(A + \alpha_i) = \frac{1}{L_s} \ln \left(\frac{I_1}{I_2} \right) \tag{1.16}$$

Figure 1.13 demonstrates the use of etching of the metallic contact layer on the top of a device to achieve the pumping geometry described in Equation 1.16.
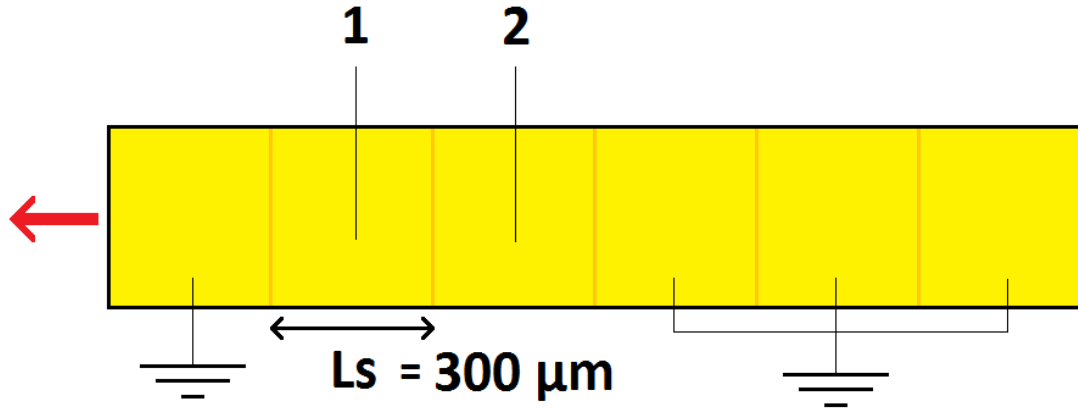
Figure 1.13: Typical pumping geometry of a Multisection Method device viewed from above. Bright yellow regions indicate intact contact layer whereas orange strips indicate etched 6 μm contact breaks. The red arrow represents the emission of light from the front facet of the device. Connections 1 and 2 allow electrical pumping of two of the 300 μm sections.

Figure 1.13 depicts the typical device geometry of the Multisection Method. Due to their positions relative to the front facet, section 1 will be referred to as the 'front' section and section 2 as the 'rear' section during further discussion. The device section nearest to the front facet is not pumped so that there may always

be earthed material on either side of a pumped section. Hence, it is ensured that the pumping arrangement is symmetrical for each device section. (This is further discussed in Section 2.7.) Edge emitted light is collected by a spectrometer from the front facet of a laser structure as is described in Figure 2.4 . It is assumed that emission from the facet and passage through the detection optics has an identical fractional effect on light of a particular photon energy regardless of its section of origin [3].

The metallic top contact layer and the underlying (highly conductive) p-doped layer are etched away using a masked etching process to leave electrically isolated sections. These 'contact breaks' are typically 6 μm in length. In the experiments in this document, 300 μm long sections were used and a typical device consisted of 6 sections. All sections are grounded while not being pumped. This, combined with the presence of connected sections on either side of the two pumped sections, ensures that the two pumped sections are in equivalent electrical environments. This will be discussed further in the current spreading discussion in Section 2.7 .

Figure 1.14 demonstrates the combination of I_1 and I_2 spectra into a measured Optical Loss spectrum using Equation 1.16. A polariser was used in this measurement to select only TE polarised light.

The optical loss spectrum in the above figure can be seen to have the characteristic 'step-like' structure of a Quantum-Well device. The absorption edge corresponding to the bandgap of the active region material can be seen at roughly 1.34 eV. At some given photon energy, there will generally be a contribution to optical loss from interband absorption as well as internal loss processes. However, the flat region at the low photon energy end of the spectrum has a lower optical loss coefficient as this region corresponds to photon energies within the bandgap of the material. As such, no interband absorption is occurring here and the A component of $(A + \alpha_i)$ tends to zero as the observed photon energy decreases. It follows that a measured optical loss coefficient in the low photon energy region of the spectrum corresponds to Internal Optical Mode Loss. The optical loss coefficient averaged in this region is taken as the internal optical loss for the device.

The α_i value taken for the data in Figure 1.14 is stated next to the dashed line.
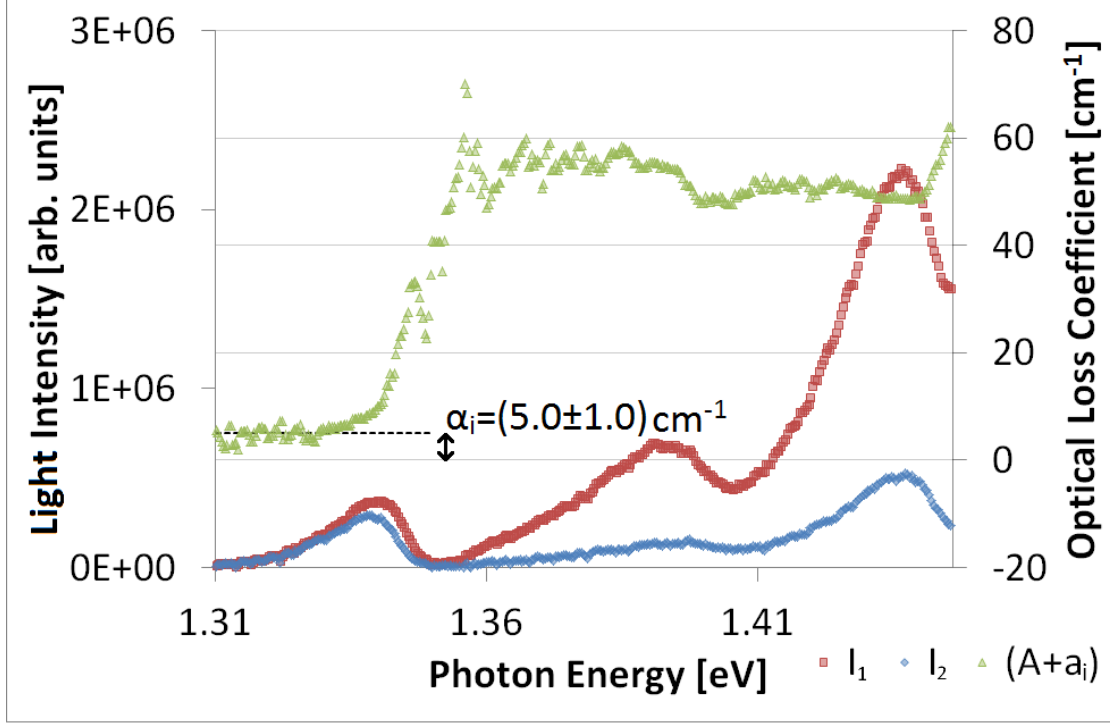
Figure 1.14: The I_1 and I_2 spectra which are substituted into Equation 1.16 to derive a measured Optical Loss spectrum are shown as red and blue markers respectively. The resultant Optical Loss spectrum is indicated by green dots. This measurement was carried out on a device of type $\#2_{RW}$ (in the terms introduced in Section 2.1).

It is noteworthy that any light is collected at all for photon energies corresponding to the device bandgap. Measured light is generated in a pumped region of material. This region has a substantially higher carrier density than the passive, unpumped region in which the measured optical loss occurs. The presence of charge carriers has a screening effect on the electric potential of the crystal lattice, resulting in an effect known as Bandgap Narrowing. Hence high carrier densities in the pumped sections shift the I_1 and I_2 spectra to lower energies relative to the band structure in the absence of injected carriers [44]. The number of free carriers is significantly lower in the unpumped absorbing region, and loss processes occurring in the unpumped regions of the device are assumed to correspond to unshifted transition energies.

38

A number of further conditions exist in ensuring high confidence in the uncertainty of a measurement of multisection optical loss. A full understanding of this topic requires an understanding of the experimental apparatus used in order to make the measurement. As such, these conditions will be described in Section 2.7, following the description of the apparatus in Section 2.2 .

Precision in an internal optical loss measurement requires precise measurement of I_1 and I_2 signals. Internal loss is measured at low photon energies, at which the spectral intensity tends to be small. Experimental scatter in these intensity measurements is fractionally high. The precise measurement of internal loss is discussed in detail in Chapter 9.

1.3.5 Gain and Spontaneous Emission

While neither gain nor spontaneous emission is directly used in the analysis described in this thesis, both quantities are useful in understanding the origin of the I_1 and I_2 light intensities. This is addressed in Section 2.6.

As described in the 2003 paper on the segmented (multisection) method [3], making a paraxial approximation and examining emission in the plane of the active layer, the light which reaches the device front facet from an emitting element at a distance x from the front facet and with a thickness of Δx, is given in Equation 1.17:

$$I(x) = \left(\beta I_{spon}\right) \left[\mathrm{e}^{(G-\alpha_i)x}\right] \Delta x \qquad (1.17)$$

in which, β represents the fraction of spontaneous emission coupled into the waveguide, I_{spon} describes the rate of spontaneous emission in all directions in the plane of the active layer (per photon energy interval per unit area) in a particular polarization.

The light generated by a section composed of sources such as that described in Equation 1.17 of length, ℓ, is derived in Equation 1.18 by the integration of

Equation 1.17 with respect to section length:

$$I(\ell) = \left(\beta I_{spon}\right) \left[\frac{\mathrm{e}^{(G-\alpha_i)\ell} - 1}{(G - \alpha_i)} \right] \tag{1.18}$$

Assuming that the pumped section is adjacent to the device front facet (and hence that the intensity defined in Equation 1.18 is not reduced by optical loss before emission from the device), the light collected by a detection system is reduced by mirror loss (reflection at the facet) and some prefactor which depends on the collection efficiency of the optics. As these contributions remove an equal fraction of measured light intensity regardless of its section of origin, they will not be explicitly described in this treatment.

Following the derivation given in the original paper [3], an equation for multi-section optical gain over a pumped section of some length, L, may be defined as follows:

$$\left(G - \alpha_i\right) = \frac{1}{L}\ln\left(\frac{I(\ell = 2L)}{I(\ell = L)} - 1\right) \tag{1.19}$$

in which, I_{2L} and I_L are defined to be the intensity described in Equation 1.18 in which $\ell = 2L$ and $\ell = L$ respectively. Experimentally, I_{2L} corresponds with pumping two adjacent device sections to the same current density.

Additionally, an expression for the measured spontaneous emission, I_{spon}^{meas}, can be defined as:

$$I_{spon}^{meas} = \frac{I_L^2}{I_{2L} - 2I_L}\frac{1}{L}\ln\left[\frac{I_{2L}}{I_L} - 1\right] \tag{1.20}$$

This defines the amount of the spontaneously emitted light that is coupled into the optical mode and propagates towards the front device facet.

Experimental Techniques

2.1   Device Fabrication

The devices used for the experimental work found in this thesis are from two different sources. The first series of devices derive from a 710 nm emitting Quantum Dot (QD) laser structure wafer, produced by Dr Andrey Krysa at the University of Sheffield for research by my colleagues in Cardiff University into the effect of strain in confinement layers on the performance of such devices [45] . This series is labeled #1 in this work. The other series of devices were processed from a batch of $850\,nm$ emitting Quantum Well (QW) wafers supplied by the CASE award sponsor for this project, Oclaro Inc. Devices of this wafer will be labeled #2 in this work. As the technologies of the Oclaro wafer are commercially sensitive information, few specifics were given regarding its structure. Accordingly, my description of device fabrication will be based on the #1 wafer. BA devices of the Oclaro Wafer were not used in these experiments. Table 2.1 summarises the above discussion and assigns sample number designations to the devices used in this project.

As the main focus of this body of work is on the development of the understanding and application of experimental techniques, the following discussion of device layer structure is a shallow overview of the technologies involved. A wealth of resources is available for the development of further understanding of the pre-

Table 2.1: Sample Designation

Wafer Source	Broad Area	Ridge Waveguide
Sheffield Oclaro	$\#1_{BA}$ - -	$\#1_{RW}$ $\#2_{RW}$

cise role of each layer and the processes and technologies involved. The following references give some generic examples [4, 5, 7, 8].
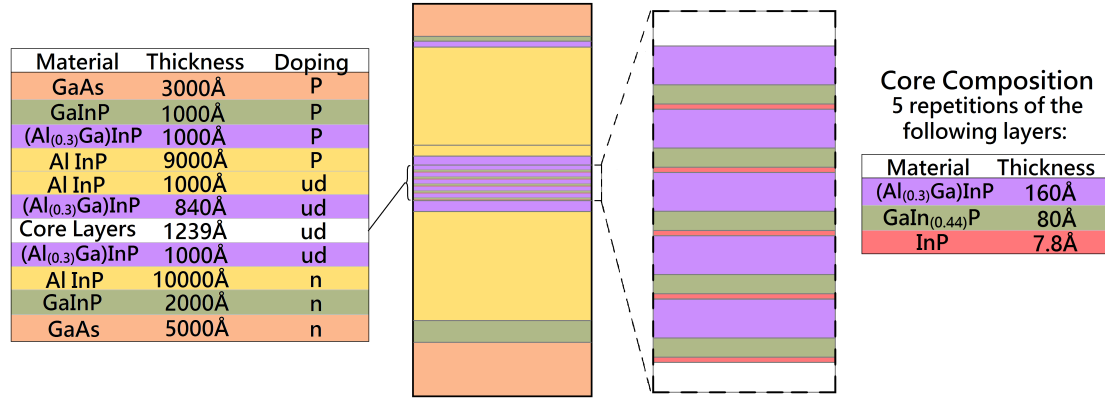
Figure 2.1: The #1 wafer is given as an example of layer structure in a laser device.

In Figure 2.1 above, the left-hand table and diagram depict the layer compositions and thicknesses for the structure of this specific device, while the right-hand table and figure give this information on the repeating structure of the wafer's active region. The left-hand table additionally gives information on doping in the structure (where 'p', 'ud' and 'n' represent p-type, undoped and n-type semiconductor material respectively). The layers were grown on a GaAs substrate using MOVPE (Metalorganic Vapour Phase Epitaxy). InP Quantum Dots are grown in the active region upon an AlGaInP layer and are covered by a layer of GaInP. The core layers and neighbouring AlGaInP layers were all grown at 730°C.

Electron confinement is achieved as described surrounding Figure 1.10; core layers with a lower band-gap than the surrounding material improves the confinement of carriers in the active region [7]. The thick layers of AlInP *cladding* on either side of the core layers have a low refractive index compared with the core

layers between them, causing optical guiding by total-internal reflection, as described in Figure 1.10.d) . Devices used in this body of work have been designed such that only one transverse optical mode exists.

2.1.1 Broad-Area and Ridge-Waveguide Devices

Processing of devices into either Broad-Area (BA) or Ridge-Waveguide (RW) devices took place in the on-site clean room by skilled technical staff.
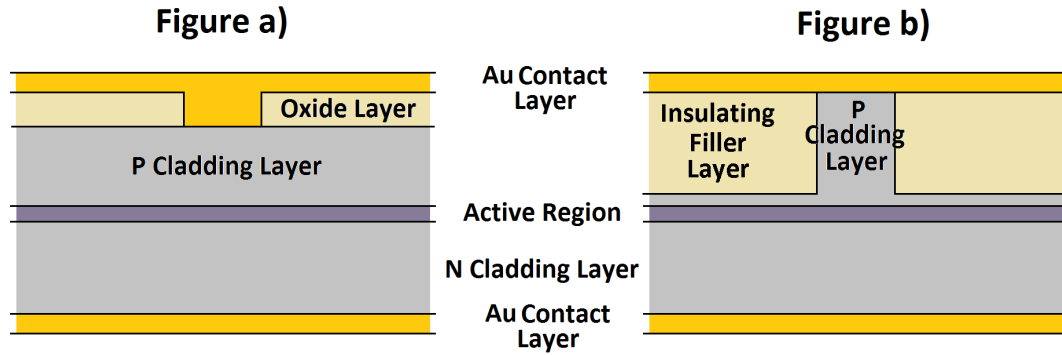
Figure 2.2: Cross-sectional structure of a BA and RW device is given in Figures 2.2.a) and 2.2.b) respectively. (Not to scale) .

A BA device is produced through growth of an oxide layer on the top surface of the wafer, removing a 50 μm stripe by photolithography and finally depositing a metal contact layer to the top surface. This method of selectively pumping within the surface area of a top contact is known as an *oxide-isolated stripe*. An example of a BA structure is shown in Figure 2.2.a) . This structure limits the lateral spread of a beam by gain-guiding. Gain-guiding is the process in which beam divergence is reduced by spatially limiting its amplification by the gain medium. In this case, gain is limited to regions of the wafer below the stripe such that only light propagating toward a device facet is fully amplified). BA devices are uncommon in commercial devices, as they have been superseded by more sophisticated technologies for lateral optical confinement. They are, however, commonly used as test structures in characterization of the material properties of wafers.

A RW device, such as the schematic shown in Figure 2.2.b) features improved lateral optical guiding by introduction of a step in refractive index. By etching to leave a mesa of material and then filling with an insulating filler substance, we retrieve a flat top surface onto which a metal contact is deposited. The filling substance is chosen to have a lower refractive index than the material it has replaced. As such, a waveguide is formed, acting to confine light in the lateral orientation (as introduced in Figure 1.1). This index-guiding effect is stronger than the gain-guiding of the BA device, however it is expected that non-uniformity at the ridge interface will add to optical loss in the cavity. As indicated in the figure, the etch doesn't reach the active region of the device. This achieves index-guiding of generated light while minimising compromise of device performance due to etch-related defects in active material. The RW devices used in this body of work have 50 μ m wide ridges.

Finally, the metal contact on the top surface is etched into the segmented structure described in Figure 1.13 .

For use in the experiments described in this document, devices are mounted onto copper block (heat sink) upon a TO-39 header. The header is then soldered into place within a cryostat during measurement to control and stabilise the device temperature. Unless otherwise stated, all experiments noted in this body of work were carried out with a set device temperature of 300 K.

2.2   Spectrograph System

Acquisition of light emitted from a laser device is carried out using an Andor Spectrograph/ICCD (Intensified Charge Coupled Device) system, allowing for simultaneous collection of data across the spectral region of interest. A boxcar integration experiment is carried out, in which the output intensity from a device is only measured within drive current *pulses*. This is achieved using the gating

function of the intensifier [46].
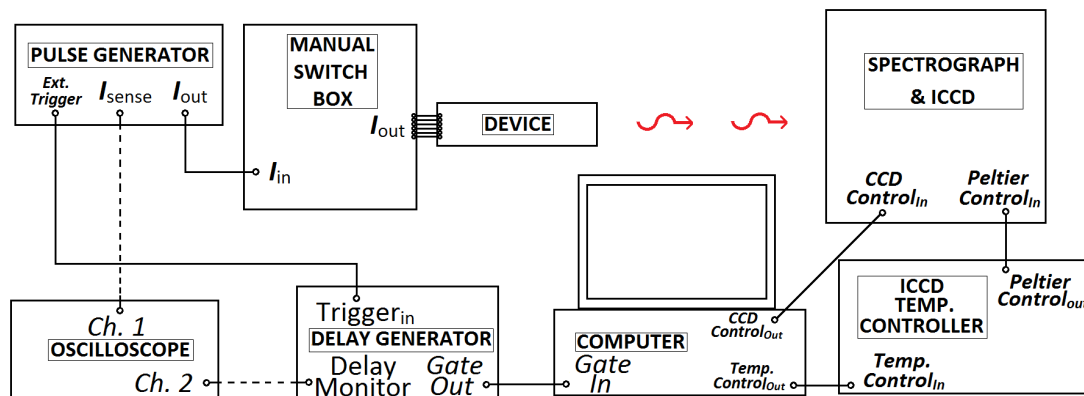
Figure 2.3: A schematic for the experimental apparatus used in the Multi-section Method for Optical Loss spectra. This apparatus is used for measurement of spectral and spatial distributions of emitted light. The function of each component is described in the following text.

The ICCD system is triggered externally by the pulse generator which supplies current to the device. A typical pulse frequency and current is 5 kHz and 80 mA respectively. A standard pulse width of 1.5 μ s is used in these experiments. The use of a delay generator allows a gate pulse to be generated within each current pulse. By synchronising with this gate pulse, the ICCD only collects signal whilst the device is emitting light. A full description of the nature of the triggering system and detailed data acquisition process will later be described in reference to Figure 2.5.

Light from the device is coupled into the detection system using the optics described below in Figure 2.4. The detection system itself consists of a commercial Czerny-Turner type spectrograph, which acts to spatially separate input light of different wavelengths in the horizontal orientation and focus this image onto an array of CCD pixels. The ICCD system is calibrated such that each column of CCD pixels collects light of a known wavelength. By reading out charge from these columns sequentially, spectral data is obtained. Spectra are converted to be

45

a function of photon energy during the data analysis process. A spectral resolution of around 1 nm is achieved using a 150 l/mm grating. A maximum measured intensity of $8,000$ counts is collected on the CCD in any single exposure in this body of work, based upon the limitations of the detector. This limit is crucially important in Chapter 9.

The intensifier acts to amplify the collected light signal, allowing for detection of relatively low light intensities. When no voltage is applied across the vacuum tube of the intensifier, the transmission of light can be considered negligible. (The apparatus documentation suggests a transmission of roughly 0.1%. This small systematic error in measured intensities is canceled out in the calculation of optical loss coefficients by the quotient in Equation 1.16.). As such, gating of the measurement is achieved allowing boxcar integration. A more complete description of the operation of the ICCD may be found in the manufacturer's manual and accompanying documentation [47, 48] .

A delay generator is used to select a period of time within the current pulse for light to be acquired by the CCD. Output from both the pulse generator and delay generator are monitored on an oscilloscope to set the widths and phases of all pulses and the magnitude of the current pulse to appropriate values. Further detail is given on the timing of pulses in the discussion following Figure 2.5 . Synchronisation of the delay generator and ICCD is carried out with a computer, on which software controls various parameters of the ICCD and spectrograph operation. This software also sets the temperature of a Peltier cooler at the photocathode of the CCD (which reduces dark signal and associated shot noise). The CCD is typically operated with a set photocathode temperature of –18 °C up to Chapter 9 and –30 °C henceforth upon acquisition of a water cooler.

Between the pulse generator and the laser device itself, a switching box is introduced to allow current pulses to be directed to different device sections (a concept introduced in Section 1.3). Sections that are not pumped are earthed during a measurement. A background signal is subtracted from the measured signal in each acquisition. This is taken by physically blocking the light from the test device and

acquiring the signal from the ICCD in the same conditions as the light intensity signals are to be acquired.

By setting the spectrograph to collect light from the the 0th order of the grating one may measure specular reflection from the grating on the ICCD. As such spatial, rather than spectral, information regarding device light emission is accessed. This method is used to obtain the spatial distributions of emitted light that I will go on to describe in Section 2.4 .
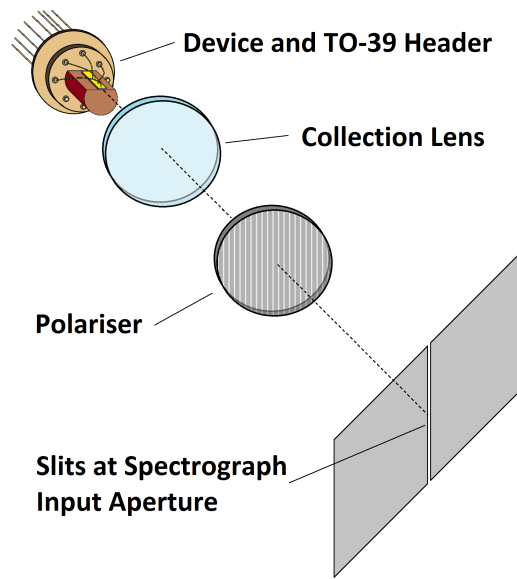
Figure 2.4: An overview of the optical components used in the collection of emitted light into the spectrograph system. Front-emitted light is focused on the input plane of the spectrometer. A polariser in the optical path allows selection of TE or TM polarised light.

Light emitted from the front facet of the laser device is collected by a 4x magnification lens and imaged onto the input plane of the spectrograph. An input slit in this plane selects the central portion of the incoming light (in the horizontal plane), improving the resolution of the spectrograph. This causes spatial filtering of the light which is collected from the device. The significance of this point is discussed in Chapter 3. Spatial filtering, achieved using a lens with a low collection angle (5°), ensures that the paraxial approximation of the Multisection Method

47

is appropriate [49]. The polariser in the optical path allows TE or TM light polarisations to be selected. This selection of polarisations is significant as internal loss may depend upon polarisation. Additionally, interband transitions involving different valance sub-bands are associated with different transition strengths in different polarisations due to the symmetry of the Bloch functions of their associated carriers [4]. This is significant in the identification of the cause of optical loss processes, especially when attempting to characterise internal loss through identifying spectral regions in which inter-band loss is negligigble.

Figure 2.5 demonstrates the timings and scale of the processes involved in the acquisition of data using the spectrograph/ICCD system. The I_{pump} axis depicts a 5 kHz pulse generator output into the laser device. The gate axis shows the output from the delay generator on the same time scale. This gate signal is sent to the ICCD via a computer interface and determines when voltage is applied to the Intensifier, and hence when signal will be accumulated. A measurement is gated within each current pulse (during an exposure of the CCD). The exposures are typically 0.1 second long and are separated by some readout time, the duration of which depends upon the acquisition settings. The CCD has a readout delay of 0.007 s. Longer exposure times are possible, but limited by the charge capacity of the CCD. The exposure chosen in a particular experiment depends on the light output of the tested device. To achieve acceptable Signal-to-Noise Ratio, many exposures are accumulated in a particular measurement. There are of the order of 500 current pulses (and hence gated measurements) within each 0.1 second exposure and 100 such exposures are taken in a typical accumulated light measurement. Accounting for readout time for each exposure, such an accumulation will take roughly 12.5 seconds. This is shown on the Acc. (Accumulated) Signal axis. The light signal is physically blocked and a 100 exposure background signal is acquired. At the marker 'A', the beam is unblocked, only device section 1 is pumped and a 100 exposure accumulation of light signal is collected. This signal is I_1. At marker 'B', only device section 2 is pumped and a 100 exposure accumulation of light signal is collected. This signal is I_2. The background signal is automatically subtracted from the light signal by the software.
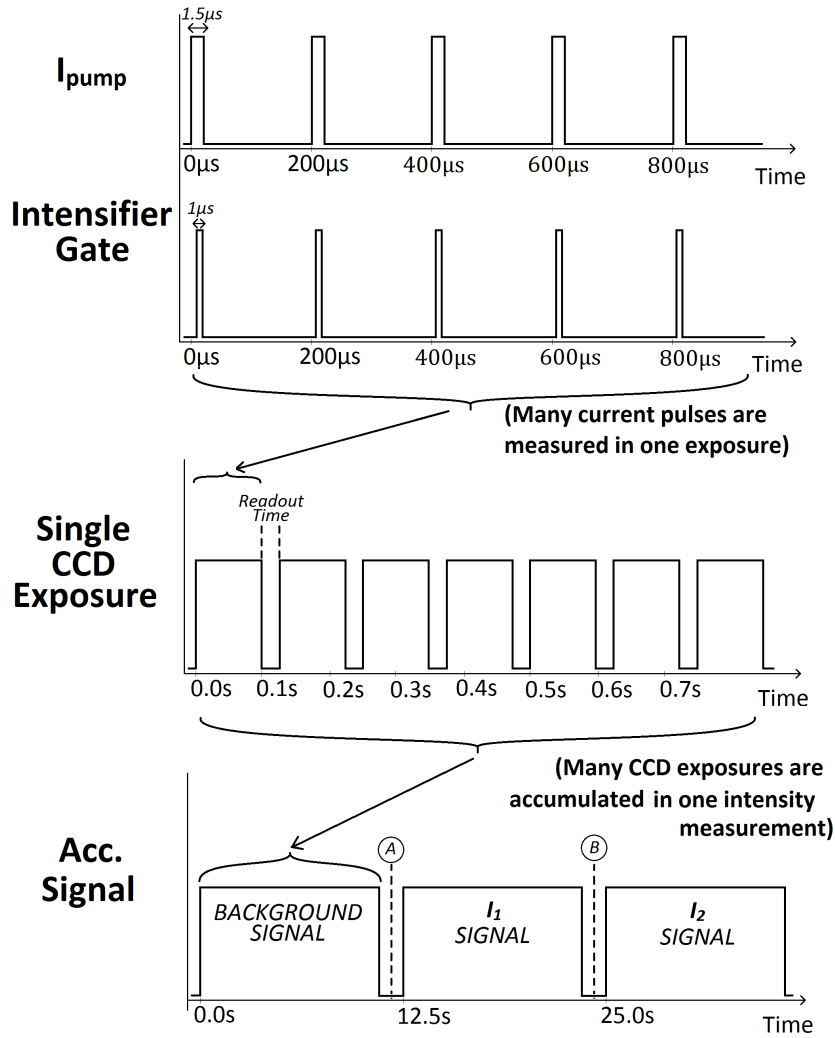
Figure 2.5: A plot of the timings involved in a measurement of light signals using the ICCD and spectrometer system. Note the different scales on the time axes. The relative pulse widths are not shown to scale on the first and last time axes for clarity. The relation between these pulses and the apparatus described in Figure 2.3 is described in the following text.

2.3 Emitted Light Spectra

Figure 2.6 shows a light intensity spectrum as measured by the spectrograph/ICCD system:

49
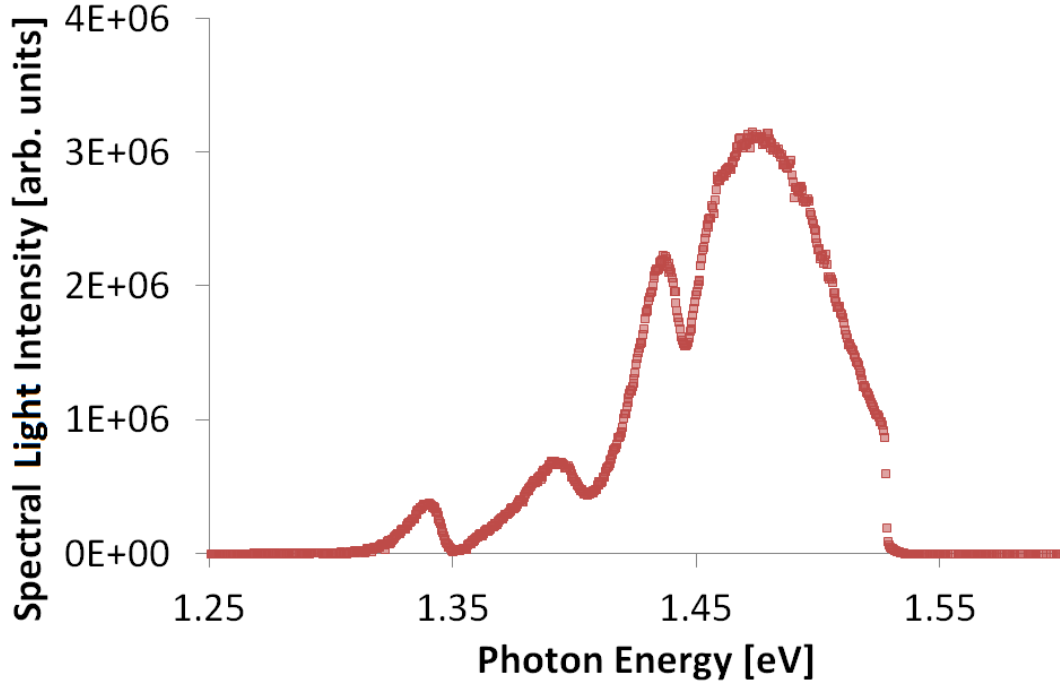
Figure 2.6: A measured light intensity spectrum as a function of photon energy. Sample is of wafer $\#2_{RW}$ and section 1 was pumped for this measurement.

Such spectra of edge-emitted light, measured whilst pumping different device sections provide us with I_1 and I_2 spectra. These can be combined to acquire Optical Loss spectra, as described in Section 1.3. By calibrating the detector to several spectral regions, broad spectra such as this can be assembled from multiple measurements. However, for investigation of internal loss, calibration in a narrow, low photon energy spectral region is sufficient. The discontinuity at the high photon energy end of the spectrum marks the edge of the intensifier. A similar discontinuity exists at a low photon energy but is not discernible at this scale. The units of the Intensity axis represent counts in the CCD readout, and can be converted to standard units of Intensity by considering the spectral response of the detector. However, the technique outlined in Figure 1.3.4 makes use of fractions of intensities and fractional changes; arbitrary units are sufficient.

2.4 Lateral Spatial Distribution of Emitted Light

The following figure shows the spatial distribution of edge-emitted light collected by the spectrograph/ICCD system:
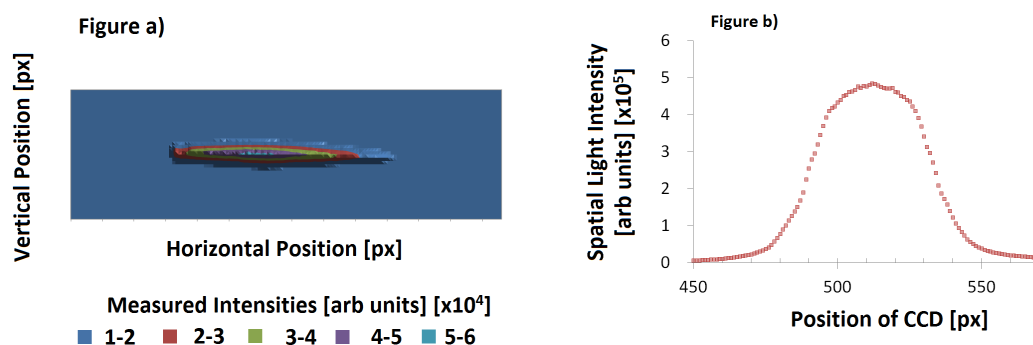
Figure 2.7: A spatial distribution measurement of the emitted light. This device is of wafer $\#1_{BA}$ and section 1 was pumped.

By selecting the 0th order reflection from the diffraction grating of the spectrograph, the spatial distribution of the emitted light can be measured. The measurement is made by a lens focusing at the beam waist of the emitted light. This quantity will be described as the '*lateral spatial light distribution*'. As in measurements of the *spectral* distributions, a reading of the background light is taken and automatically subtracted from measurements of spatial light distribution. With the input aperture slits fully open, this results in imaging device emission from across the facet to be focused onto the ICCD. Figure 2.7.a) shows the amount of light collected by each CCD pixel in such a measurement.

The section under examination was pumped at 20 mA with current pulses of 2 kHz and a width of 1.0 μs. It is often more convenient to focus on the lateral behaviour of this profile. The lateral spatial distribution of device emission may be obtained by summing the intensity within each column of CCD pixels. The result of this analysis is shown in the lateral profile in Figure 2.7.b).

Lateral spatial light distribution measurements are used for three purposes.

Firstly, to check optical alignment of a device prior to making an spectral measurement. Secondly, to check that the light emitted by each device section is appropriately similar with no evidence of filamentation (Further details will be given on this point in Section 1.3.4). Thirdly, (as will be shown in Chapter 3) to quantify and correct for the effect of divergence of generated light as it propagates through a device on measured Optical Loss coefficients.

2.5 I-V measurement

A measurement of the I-V characteristics of each device is carried out through boxcar integration measurements of a pulsed current as a function of voltage using the apparatus described in Figure 2.8.
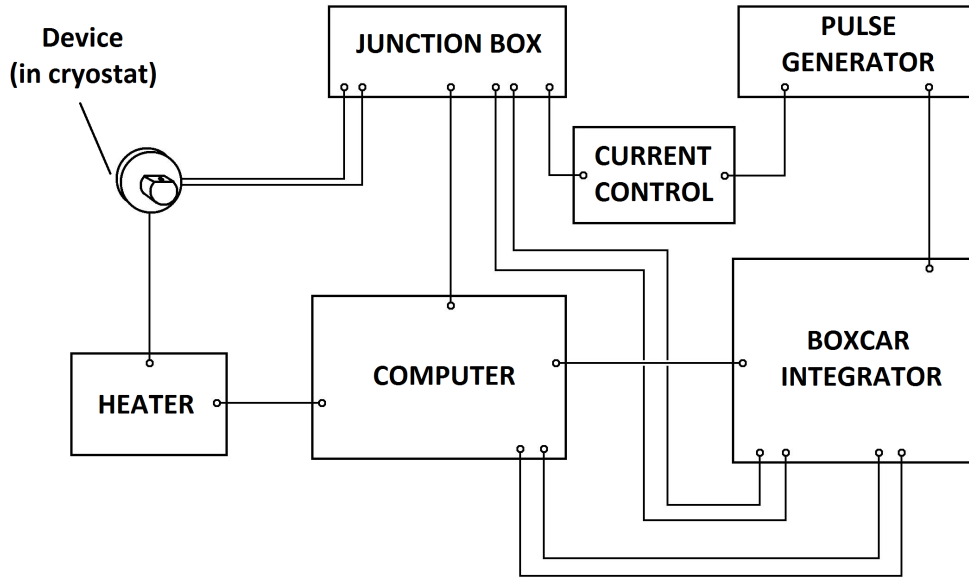
Figure 2.8: Apparatus for boxcar measurement of device I-V characteristics is described.

The pulse generator produces 1 μs current pulses at a frequency of 1 kHz which

pump a section of the device. The current controller allows a computer to increment the current applied to the device section under examination. The boxcar integrator averages the current and voltage during current pulses. A program written specifically for this apparatus [50] allows rapid measurement of I-V characteristics for a range of currents.

Such I-V characteristics are shown for two device sections corresponding with I_1 and I_2 in Figure 2.9. Comparison of I-V measurements between different device sections are used to check that sections possess similar electronic characteristics. Poor connections and short circuits will be immediately apparent from this data. Further details are given on this point in Section 2.7 .
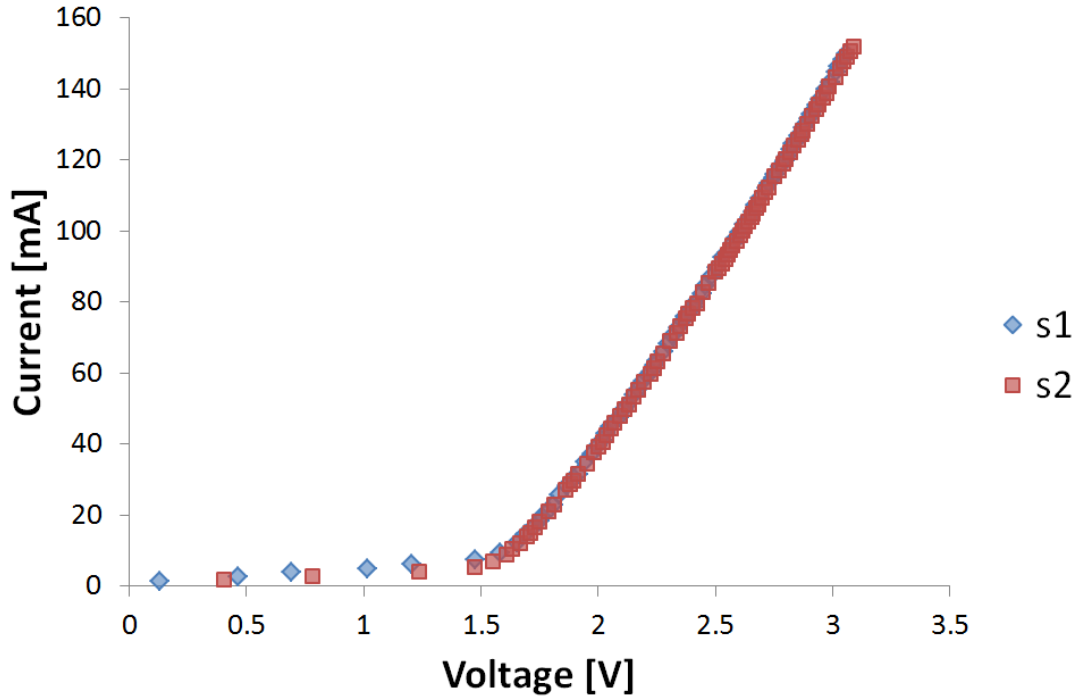
Figure 2.9: Section 1 and 2 I-V characteristics for a device of type #1.

2.6 Edge-Emitted Optical Intensities in the Multi-section Method

The edge-emitted light generated by a multisection device can be understood by considering an optical gain coefficient in pumped regions, and an optical loss coefficient in passive (unpumped) regions and the respective amplification and attenuation that these processes apply to spontaneous emission in a pumped device section. The amplification of spontaneously emitted light by stimulated emission is known as Amplified Spontaneous Emission (ASE).

Having defined optical mode loss in Equation 1.16 and modal gain and spontaneous emission in Section 1.3.5, these quantities are examined in a real device. I_{spon}^{meas}, $(G - \alpha_i)$ as well as $(A + \alpha_i)$ all have respective spectral dependences. These have been omitted in their respective derivation for brevity, but are apparent in experimental data. Figure 2.10 demonstrates spectral data for each quantity in a sample of type $\#1_{BA}$:
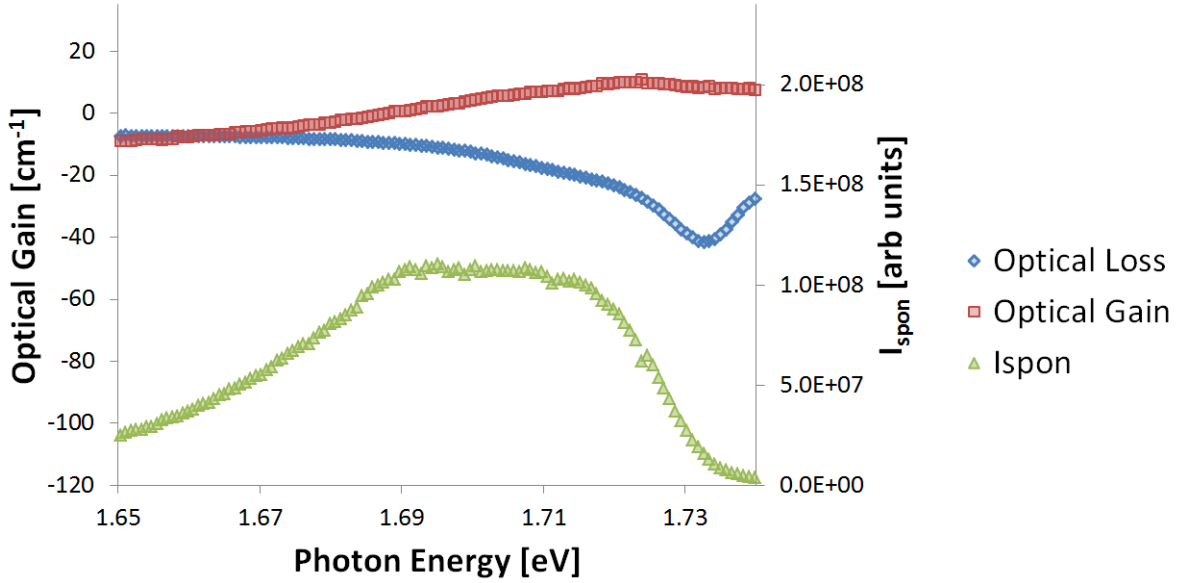
Figure 2.10: Measurements of $(G - \alpha_i)$, $(A + \alpha_i)$ and I_{spon}^{meas} are given for a sample of type $\#1_{BA}$. The convention has been used in which optical loss in passive regions of the device is depicted as negative optical gain.

54

The blue series in Figure 2.10 is the negative optical mode loss spectrum, $(-A - \alpha_i)(h\nu)$. At low photon energies in this spectrum, such as around 1.65 eV, interband absorption is negligible and optical loss is approximately constant. This is where the value of α_i is typically measured. At higher photon energies, interband absorption increases and a peak is observed at 1.73 eV due to the transition between conduction and valence band QD ground states. The red series is the modal gain spectrum, $(G - \alpha_i)$, and is measured in a pumped section of the device. A state of a particular energy can only contribute to gain if the applied drive current is sufficiently high to populate it with carriers. In this instance, pumping is insufficient to resolve the 1st gain peak. Additionally, the presence of carriers in the pumped material results in *bandgap narrowing* [13]. This shifts features of the gain spectrum to lower energies than those observed in the optical loss spectrum. The green series represents spontaneous emission. It plotted in arbitrary units here, although methods *do* exist for its calibration [3]. While gain and spontaneous emission are not directly analysed in this thesis, an appreciation of the interaction between these three processes is crucial to understanding how ASE is generated in experiments described herein.

The raw data which these spectra are based on tend to zero at the edges of the ICCD (as seen in Figure 2.11). This occurs due to *both* limitations of the ICCD itself and, at relatively high photon energies, absorption of light within the device (recall that there is absorbing unpumped material between the front facet and the front-most pumped section). Depending upon the chosen wavelength calibration of the spectrometer and on the dynamic range of the detection system, this results in poor data quality at the extremes of the spectrum.The real spontaneous emission within the device does not truly tend to zero nor does the gain become flat above 1.73 eV (as the measurement in Figure 2.10 suggests). This is simply where the ASE signals start to become negligible and data quality is lost. Note that this is a shortcoming of the sample geometry and detection system settings and not of the multisection method itself. Beyond this point in this thesis, data is only included from parts of the spectrum which are *meaningful*. Confidence in data was ensured by checking that optical loss is not dependent upon the centre-wavelength of the spectrometer nor upon detection parameters (such as ICCD exposure length).

Having defined the processes which result in measured intensities having particular spectral behaviour, their relationship with measured light intensities in the multisection method for optical loss may be examined.

Regardless of the section which is pumped, —in an ideal device — the light produced by spontaneous emission in the optical mode is represented by I_{spon}^{meas} and the total light generated over a pumped section of length, L, is equal to $I(L)$ (as defined in Equation 1.18). This is equivalent to I_0 (as introduced in section 1.3.3) and represents the ASE generated by pumping a single device section, at the edge of that section which is nearest to the front facet. I_0 is shown in Figure 2.11. This was calculated, in this instance, by multiplying I_1 by $e^{(A+\alpha_i)L}$. I_0 cannot be measured directly for reasons discussed in Section 2.7.1.
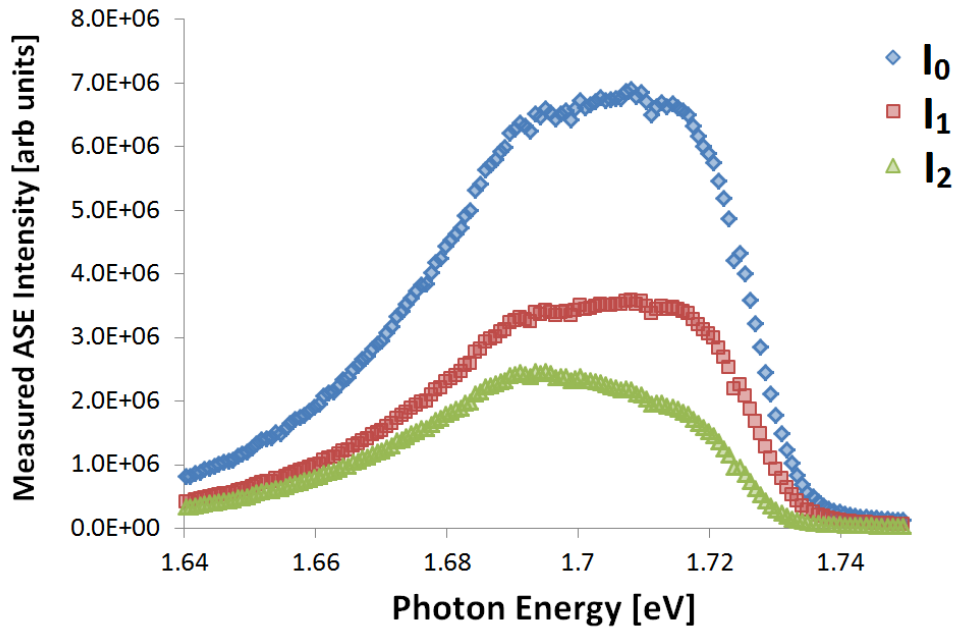
Figure 2.11: Data series denoted I_0, I_1 and I_2 are the measured intensity spectra generated by a pumped section, having undergone different degrees of optical loss in propagation to the device front facet. Light intensities I_1 and I_2 are collected having passed through a length of L and $2L$ of passive absorbing material respectively. I_0 is then constructed using I_1 and the optical loss spectrum deduced from I_1 and I_2.

The pumped sections are not adjacent to the device facet in the experiments described in this thesis and hence the optical loss of the unpumped material will affect the characteristics of all light intensities measured in this document. Intensity spectra, I_1 and I_2, measured from a real device are given in Figure 2.11. In passing through each additional unpumped section of the device, an additional factor of $e^{-(A+\alpha_i)L}$ is lost.

2.7   Further Conditions

There are further conditions which must be met to ensure that the approximations described in Section 1.3.4 are valid. For clarity, these will be expressed in subsections, under the titles held in the following bulletpoints:

- Symmetry of device sections

- Optical Mode Considerations

- Round Trip Propagation of Light

Additionally, the effect of collection geometry is discussed. However, as this discussion is somewhat more involved, it is examined separately in Chapter 3.

2.7.1   Symmetry of device sections

Before being considered acceptable for use in experiments I rigorously tested the optical and electrical properties of devices, both upon collection from being processed and after mounting to a TO header. As stated in Section 1.3.4 , the function of the Multisection Method depends strongly on the assumption that I_0 can be considered to be equal for both device sections. One cannot directly measure the light intensity as the light leaves sections 1 and 2, but tests of the I-V and inter-contact resistance throughout the structure can give confidence that the behaviour of these two pumped sections is the same. (Recall that what has been defined to be sections 1 and 2 in this document are the 2nd and 3rd sections from the front facet respectively). The effect of I-V mismatches are discussed in more detail in

Chapter 10.

The pumping current and pulse characteristics, the gating pulse characteristics and the intensifier gain are identical during the pumping of each device section to ensure that I_0 is reproduced identically at each section. Furthermore, the position of all components in the external optical path is unchanged between the two section measurements.

It is expected that some degree of '*current spreading*' will occur, as current injected at a contact will dissipate in the lateral plane as it passes through the transverse structure of the device [51]. Indeed, models exist for the correction for such effects in gain measurements [52]. However, provided that a device demonstrates comparable electronic behaviour between its sections (i.e. they have comparable I-V curves) current spreading is assumed to affect the distribution of carriers and subsequently the light emission in a comparable way for each section. While current spreading may change the effective boundaries of the device sections (with regards to where light is generated), recall that it is the *change* in absorbing length, L_s, which determines the measured optical loss coefficients. Given electronic equivalence of the device sections, the distance by which changing between pumping section 1 and pumping section 2 moves the effective light source longitudinally will be equal to L_s regardless of current spreading. Hence the measured optical loss coefficients will be preserved.

Figure 2.12 clarifies these concepts. Figures 2.12.a)-c) represent the pumping of the 3 sections nearest to the front facet. (The front facet being the left-most edge of each schematic). Layers of the material system are labeled to the right of the top diagram. Dashed angled lines demonstrate the spreading of current as it flows down from the top contact. Yellow and red regions represent pumped regions of cladding and active material respectively.
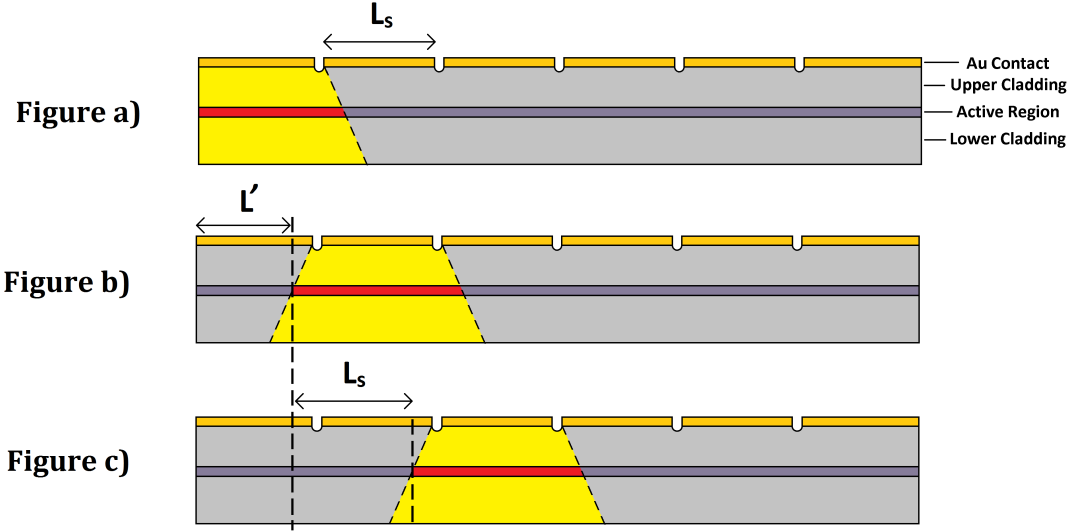
Figure 2.12: The lateral spreading of injected current is shown through a cross-section of device along the longitudinal axis. An exaggerated current spread of the order of 100 μm is shown here to emphasise the effect. (Current spreading of a few microns is typical in real devices). Additionally, for the sake of clarity, the active layer is depicted as being (proportionally) much further from the upper contact than is typical in modern device design.

Dashed vertical lines are used to demonstrate the mechanism by which current spreading does not influence measured optical loss coefficients. The label L_s denotes the length of a section in Figure 2.12.a). In Figure 2.12.b), L' is defined to be the mean distance between the device front facet and the nearest point of the active region to which current has spread. In Figure 2.12.c) it is demonstrated that – given identical current spreading conditions in each section – pumping the third section of the device effectively shifts the light source in the middle diagram an additional distance of L_s away from the front facet. The difference in optical path length between two sections is preserved (provided that neither is adjacent to the device front facet).

The presence of current spreading is one reason that the section nearest to the device facet is not used in this experiment (as made clear by the section definitions described in Figure 1.13). The underlying problem is made apparent in Figure 2.12. Light from the section nearest the front facet is not used experimentally as

59

altered current spreading behaviour would alter the current density (and hence the light generation) and mean optical path length relative to the other sections. (If pumping the section nearest to the front facet was required in a particular experiment, the fractional effect of current spreading upon a measurement could be minimised by increasing the device section length). Furthermore, the beam generated in a pumped section will be partially reflected by the front facet of the device [53]. This can cause systematic error in an optical loss measurement, as the degree to which light intensity increases due to this reflected wave is different for the two pumped sections. This is reduced by the introduction of angled facets and an unpumped front section. All devices used in this body of work follow this convention.

It is essential that the front facet is properly cleaved and undamaged, and that no dust or dirt is allowed to settle on the facet since its fabrication, otherwise scattering at such an irregularity may treat emitted light differently for the two pumped sections and therefore constitute a systematic error in the measurement. Inspection of the facets under a microscope with a 50x magnification objective lens is routinely carried out. Measurement of the spatial distribution of light intensity across the device front facet allows a further check for uniform light emission. This procedure corresponds with the experimental method described in Section 2.3 and is integral to the new method introduced in Chapter 3. This technique allows one to rule out the presence of 'filamentation' effects, a term used to describe a family of phenomena related to effects such as nonuniform light emission due to localised defects in the crystal lattice in the optical path, non-uniformities in the contact layer and various non-linear effects [54, 55]. The presence of such effects imply that loss processes do not occur uniformly along the optical path and that the exponential model of optical loss is inappropriate. The presence of filamentation also implies that the Optical Loss Coefficient is no longer uniform in the lateral plane, the significance of which will be stressed under the Optical Mode Considerations section, later in this chapter.

It is also necessary that the propagation of light is independent of its section of origin. Measurements of the lateral spatial distribution of light intensity across the device front facet for each connected section are taken. This data provides evidence

that light is emitted and subsequently propagates in a comparable fashion in each case. This topic is discussed in more detail and examples of such spatial distribution measurements are given in the discussion of divergence effects in Chapter 3.

2.7.2 Optical Mode Considerations

The following mode description will rely heavily on orientations defined in Section 1.2.1. Standard calculations of optical loss coefficients are carried out individually for each optical mode and polarisation in a device, and demonstrate optical mode dependence. As such, it is conventional to consider optical loss coefficients for a particular mode and polarisation. While a single polarisation can be selected using a polariser in the optical path, optical modes cannot be filtered in this way. If more than one mode exists the measurement no longer represents the loss of light from any particular mode. Rather, some manner of 'effective *multimodal* loss' is measured. Some factors which influence this effect include spatial distributions of the modes in relation to the position of sources of optical loss, the acceptance cone of the detection system, the distribution of light between optical modes and the magnitudes of the modal optical loss coefficients themselves. In particular, it is established that defects at ridge interfaces result in high optical losses for modes with a high spatial overlap with these interfaces [4]. The following is a consideration of the existence of modes in three spatial dimensions of a typical device.

Longitudinal modes occur along the long axis of the device and are determined by the distance between the front and rear facets. However, generated light only passes through the device once in the Multisection method. Longitudinal modes are not expected to influence the propagation of light. As such, the effect of these modes are neglected.

In both the BA devices and the relatively wide-ridged (50 μm) RW devices which are used in the following investigations, a lateral single-mode model is not appropriate. However, uniform lateral distribution of loss processes is expected due to symmetry of lateral device structure. As such, identical loss is expected

between different modes and so no further consideration is required. This assumes that the device is perfectly symmetrical in the lateral plane. As suggested in the previous section, irregularities within a device and facet damage can break this symmetry and cause systematic error in an optical loss measurement.

Conversely, the optical loss is expected to vary as we pass between layers of the device structure in the transverse plane. This spatial distribution of optical loss coefficients implies that different modes may be attenuated differently in propagation. It is likely that Oclaro Inc. laser structures (wafer #2), which are nominally for use in high power devices, have been designed to have a single transverse mode. The QD wafer designated wafer #1 is known to have been designed to have a single transverse mode.

2.7.3   Round Trip Propagation of Light

As spontaneous emission occurs in all directions in the active region, the generated light will be equally guided towards the rear facet as to the front facet. The multisection method for optical loss is nominally a single pass technique; light is generated within a device and some fraction of the light which propagates towards the front facet is collected by the detection system. However, light which completes a 'round trip' back to the front facet after reflection from the rear facet will constitute a systematic error in the measured optical loss coefficients as the absorbing path length will differ for the two pumped sections. This is particularly significant to work on measuring small values of α_i as small loss coefficients imply that a relatively small fraction of emitted light is lost in propagation to the detection system. Long, passive rear sections are used to reduce the impact of round-trip light on optical loss measurements [3].

The difference in optical path lengths for reflected beams originating from two device sections is indicated in Figure 2.13. A difference in paths lengths is shown for light propagating towards the front facet (arrows pointing left), compared with light travelling towards the rear facet and being reflected back (initially pointing right). The curved right-hand arrow simply represents reflection from the rear

facet. This is drawn in this way to avoid arrows overlying and does *not* imply that light travels further in this section than in others. In each diagram, the upper rows of arrows represent light that has yet to reach a device facet since its emission. The lower rows of arrows represent light which has been reflected from the rear facet and is propagating back towards the front of the device. Taking a paraxial model of exponential loss in which light travels through the device along a central longitudinal axis, a calculation has been made of how much single *and* round trip light intensity reaches the front facet for each pumped device section. Zero reflectivity of the front facet is assumed in this basic model and a reflectivity of $R = 0.3$ is used for the rear facet.
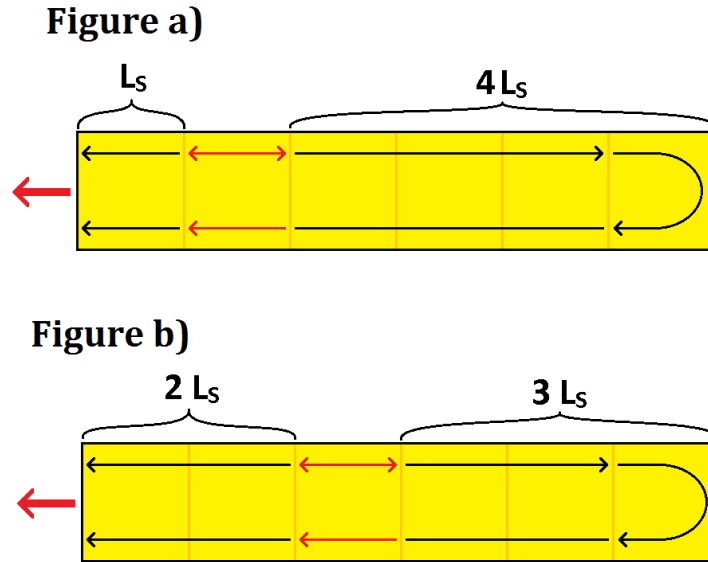
Figure a)

Figure b)

Figure 2.13: Figures 2.13.a) and 2.13.b) represent a device viewed from above in which sections 1 and 2 are being pumped respectively. Large red arrows outside of the left side of the devices represent emitted light being collected from the device front facet. Red lines indicate light travelling through electrically pumped material and undergoing optical gain. Black lines indicate light passing through unpumped material and undergoing optical loss.

The increase in measured light intensity due to the 'round trip' light for I_1 and I_2 are calculated, by summing contributions from front travelling and reflected rear

travelling light which reach the front facet. Considering the optical path length of each contribution, and applying Equation 1.13 to the resultant *total* intensities, it can be shown that, for a device which is N_s sections long, the error associated with round trip light is given by ϵ_{RT} in Equation 2.1:

$$\epsilon_{RT} = \frac{1}{L_s} \ln \left(\frac{1 + R \ e^{-(2N_s - 4)(A + \alpha_i)L_s} \ e^{(G - \alpha_i)L_s}}{1 + R \ e^{-(2N_s - 6)(A + \alpha_i)L_s} \ e^{(G - \alpha_i)L_s}} \right) \tag{2.1}$$

The characteristics of this error can be examined by calculating ϵ_{RT} as a function of the true value of optical loss. This is carried out for a device of standard length ($N_s = 6$ sections of $L_s = 300 \ \mu m$) as well as longer lengths to determine whether increasing device length is a practical approach to reducing error due to round-trip light.

Figure 2.14 demonstrates the absolute value of calculated systematic error in an optical loss measurement as a function of optical loss coefficient for a range of device lengths.

The exponential terms that differ between the numerator and demoninator of the natural log in Equation 2.1 are critical to interpreting this result. Generally, the latter is seen to be greater than the former, resulting in a systematic error which becomes more negative with increasing optical loss coefficient. (Note that the *absolute value* of this error is plotted in Figure 2.14). However, these curves each have a maximum value of ϵ_{RT} as the aforementioned exponentials both tend to one for very small optical loss coefficients and to zero for very large optical loss coefficients.
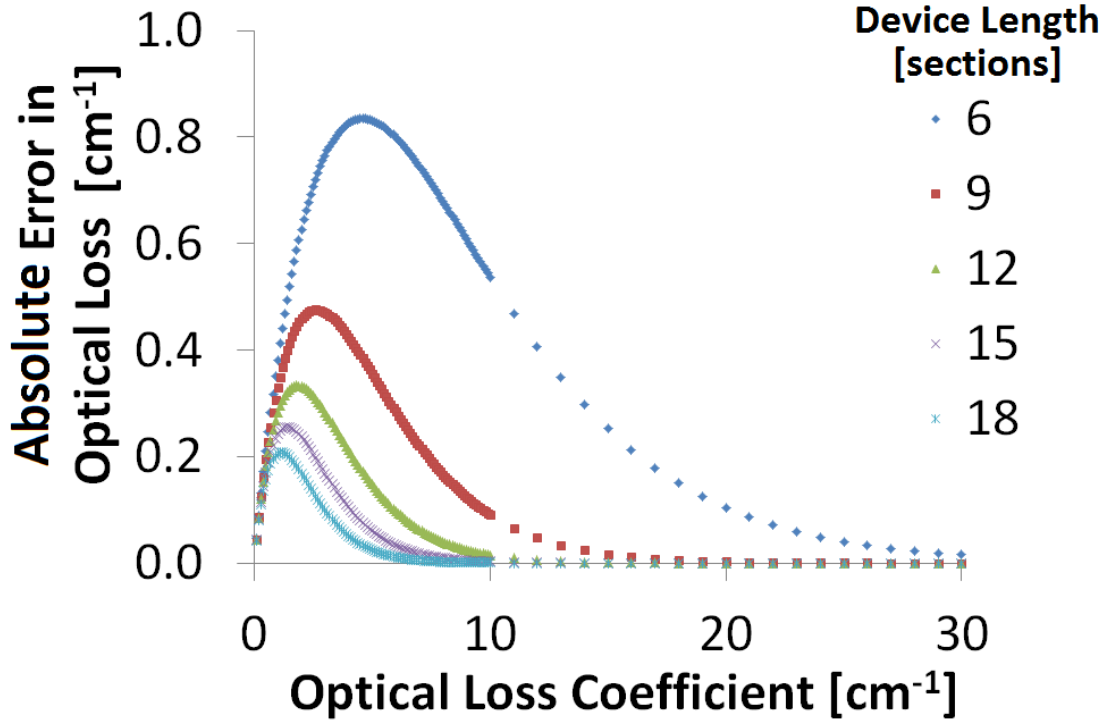
Figure 2.14: A calculation of the error in measured optical loss coefficients as a function of the optical loss itself for various device lengths. The device length in 300 μm sections for each series is given in the legend. The optical loss is calculated for pumping sections 1 and 2 in each case (as depicted in Figure 1.13). This is the absolute value of the error described by Equation 2.1.

While notable improvements to the magnitude of the sytematic error are observed by increasing the length of a device, this length must exceed 3 mm in order to reduce this error in a measured optical loss value of 5 cm^{-1} below the 0.1 cm^{-1} uncertainty threshold (discussed in Section 1.1). This may constitute unnecessary use of material, and would necessitate access to a larger cryostat in which to run experiments. In practice, device facets can be cleaved at an angle from the normal (typically 10°) to scatter round-trip light out of the optical mode. Another method is to damage the back facet of a device after mounting, such that light is arbitrarily scattered rather than specularly reflected. This latter method is employed in the experiments outlined in this document.

As stated, I have neglected the contribution from light which is reflected from

65

the front facet towards the rear facet upon reaching the front of the device. Some of this light will make an additional complete round trip and reach the front facet again. However, this light will pass through an equal distance of pumped and unpumped material regardless of which section is currently being pumped and should have no additional contribution to the measured optical loss coefficients.

2.8   Chapter Summary

Having described the multisection method for optical loss in Chapter 1, this chapter has established the device structures, apparatus and experimental techniques required in this body of work. Measurements of front facet emission — such as that described in Section 2.3 — from different device sections are combined with the multisection optical loss equation (Equation 1.16) to produce a characteristic optical loss spectrum for a particular device. The further conditions for an accurate optical loss measurement (described in Section 2.7) require that the optical and electronic behaviour of the two sections that are to be pumped are appropriately similar, that an unpumped section lies between the front facet and the front-most pumped section (such that current spreading occurs identically between different device sections) and that steps are taken to suppress the round trip amplification of light.

CHAPTER 3

The effect of Divergence upon Multisection measurement of Optical Loss

In preparation for the assessment of Multisection Optical Loss measurements with an uncertainty better than ± 0.1 cm^{-1}, the effect of collection geometry must be examined. In the PhD thesis of Dr. Julie Lutti [49] it was established that collection geometry can make a substantial contribution to inaccuracy in multisection measurements of gain spectra. In her thesis, conditions for the reduction of systematic error associated with collection geometry were determined; the use of a narrow input aperture *and* of a small lens collection angle are both critical.

Measurements of the lateral spatial distribution of emitted light from different device sections in a multisection *optical loss* experiment suggest that the divergence of light in propagation through the device cavity results in section-dependent light collection. Differing efficiency of light collection for two device sections corresponds with a systematic error in measured values of optical loss from the multisection method. This effect must be examined and the magnitude of the resultant loss considered.

67

3.1 Calculating Effective Divergence Loss in the Multisection method

For fully open spectrometer input slits, the lateral spatial distributions of emitted light were measured upon pumping sections corresponding to I_1 and I_2 respectively in a device of type $\#1_{BA}$. The device sections were respectively pumped with 100 mA current pulses at a frequency of 5 kHz, a pulse width of 1.0 μs and a gate width of 0.5 μs. Each measurement constituted 100 0.1 second CCD exposures. This produced the data shown in Figure 3.1.a). Distributions such as this are described as Lateral Spatial Intensity Distributions (LSIDs) in this chapter. The difference in intensity between the two distributions is mostly caused by optical loss in the additional 300 microns of material through which the light associated with I_2 has propagated. However, upon examining the distributions more closely, it was observed that their *shapes* are not identical. Due to lateral symmetry of the device structure, optical loss affects an LSID uniformly and is therefore assumed to have no effect upon the relative shapes of LSIDs corresponding to light emission from different device sections. By normalising the magnitudes of LSIDs from different sections, the effect of divergence can be separated from optical loss within the device structure and consequently, the effect of divergence upon measured values of $(A + \alpha_i)$ can be determined. By *area-normalising* the LSIDs, the area contained beneath an interval in the position (x) axis is equal to the fraction of the total emitted light intensity within that interval. The LSIDs shown in Figure 3.1.a) were area normalised and plotted in Figure 3.1.b). Measurements of these distributions with the slits closed demonstrate the width and position relative to the measured LSIDs. As these LSID measurements are made using 0th order diffraction from the spectrometer which measures the intensities used in optical loss measurements, the resultant optical alignments are those associated with an optical loss measurement.

Comparing the LSIDs corresponding to I_2 with that corresponding to I_1, it is observed that divergence causes a relative reduction in the area-normalised LSID magnitudes at the centre of the distribution and a relative increase in magnitudes further from the centre of the distribution. As only light which passes through the closed slits is collected in an optical loss measurement, divergence clearly causes a

reduction in the *collected* I_2 light intensity relative to the collected I_1 light intensity. This *section-dependent* contribution to collection efficiency results in a systematic error in measured values of $(A + \alpha_i)$. Comparable broadening is observed in other broad area devices.
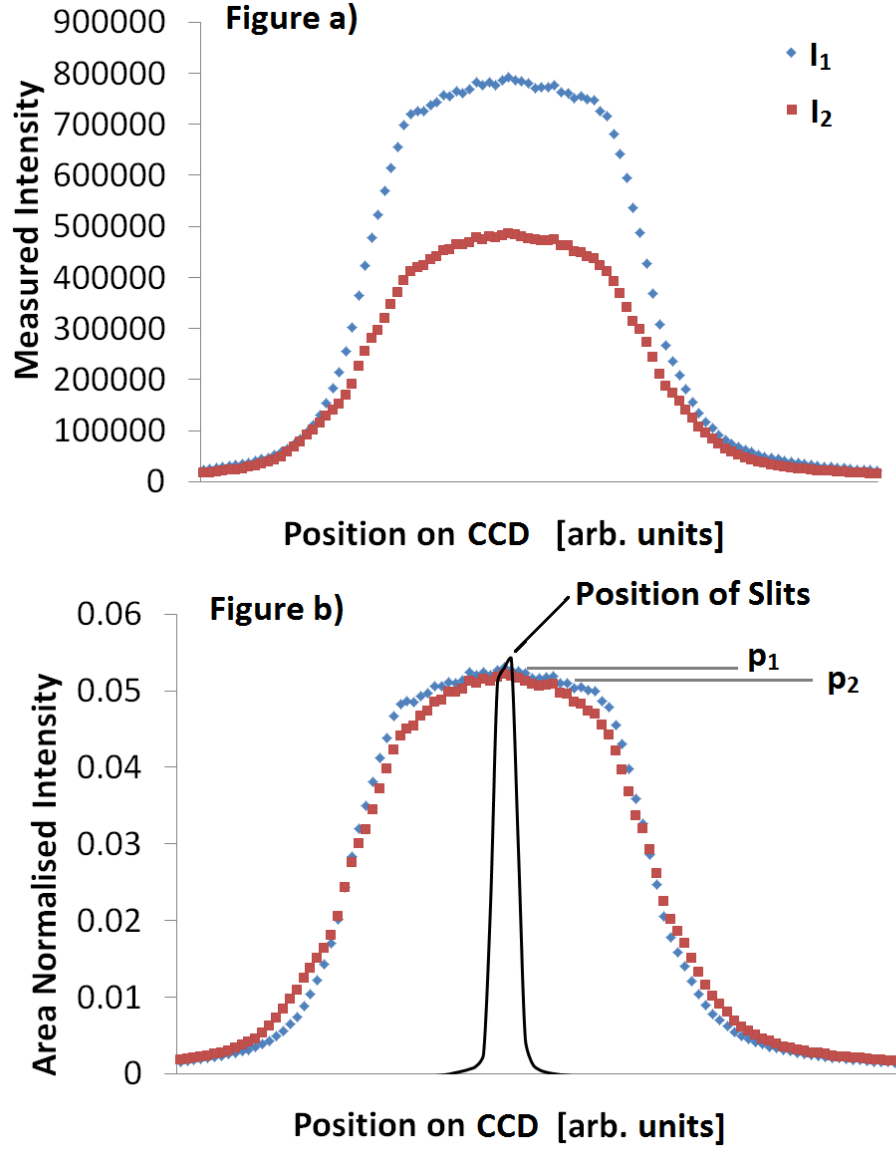
Figure 3.1: Figure 3.1.a) demonstrates LSIDs for device sections corresponding to intensities I_1 and I_2. Figure 3.1.b) depicts the same LSIDs from Figure 3.1.a), but normalised by area. The position of the spectrometer input slits is shown relative to the distributions in Figure 3.1.b).

The fraction of the light within the LSID which is collected for a particular device section is equal to the area beneath the area normalised LSID between the slits in Figure 3.1.b). As the spectrometer input slits are narrow and centred upon the (relatively flat) LSID peaks, this fraction, for a particular device section, is proportional to the peak value of the area-normalised LSID for that section (to within error of $\pm 0.1\text{cm}^{-1}$). Hence, the fraction of emitted light passing through the slits for I_2 and I_1 can be made equal by multiplying I_2 by the ratio of peaks values of the two area normalised LSIDs. Defining p_i to be the peak value of the area normalised LSID for the device section corresponding to I_i —as marked in Figure 3.1.b) —, the measured value of I_2 (denoted here as I_2^{meas}) can be corrected to a value $I_2^{div\ corr}$ such that divergence affects the collected intensity to the same degree as in I_1. This is shown in Equation 3.1:

$$I_2^{div\ corr} = I_2^{meas}\ \frac{p_1}{p_2} \tag{3.1}$$

The *measured* optical loss, $(A + \alpha_i)_{meas}$, can be derived by substituting Equation 3.1 into Equation 1.16, as shown in Figure 3.2:

$$(A + \alpha_i)_{meas} = \frac{1}{L_S} \ln \left(\frac{I_1^{meas}}{I_2^{meas}} \right) = \frac{1}{L_S} \ln \left(\frac{I_1^{meas}}{I_2^{div\ corr}} \frac{p_1}{p_2} \right) \tag{3.2}$$

As $I_2^{div\ corr}$ has been corrected such that divergence has the same effect upon its magnitudes as upon the magnitudes of I_1^{meas}, the true optical loss of the device can now be defined by $(A + \alpha_i)_{true}$ as stated in Equation 3.3:

$$(A + \alpha_i)_{true} = \frac{1}{L_S} \ln \left(\frac{I_1^{meas}}{I_2^{div\ corr}} \right) \tag{3.3}$$

and the error in optical loss associated with divergence is therefore given by the '*Effective Divergence Loss*', denoted by ϵ_{div}, stated in Equation 3.4:

$$\epsilon_{div} = (A + \alpha_i)_{meas} - (A + \alpha_i)_{true} = \frac{1}{L_s} \ln \left(\frac{p_1}{p_2} \right) \tag{3.4}$$

70

3.2 Correcting Effective Divergence Loss in Optical Loss Spectra

The application of this process to experimental data is presented in Figure 3.2. Devices of sample numbers $\#1_{BA}$ and $\#1_{RW}$ were pumped with 100 mA current pulses at 5 kHz, with a gate width of 0.5 μ s within 1.0 μ s current pulses. 100 0.1 second exposures were taken of I_1 and I_2 for each device and optical loss spectra were calculated. The measured optical loss coefficients below the interband absorption edge for a RW device are plotted alongside the divergence corrected and uncorrected data for a BA device. The LSIDs corresponding to I_1 and I_2 for the BA device are those examined in Figure 3.1.a). A correction of 3.2 $\pm$0.04 cm^{-1} is calculated from the area normalised LSIDs. (The stated uncertainty equals three standard errors of ϵ_{div} and is calculated from a measured standard deviation of p_i in data such as that shown in Figure 3.1). Divergence loss correction of the BA optical loss spectrum resulted in optical loss coefficients which are closer to those produced by the RW device. A ϵ_{div} value of 0.004 $\pm$0.01 cm^{-1} was calculated for a $\#1_{RW}$ device. This is *significantly* less than the project aim of 0.1 cm^{-1} .
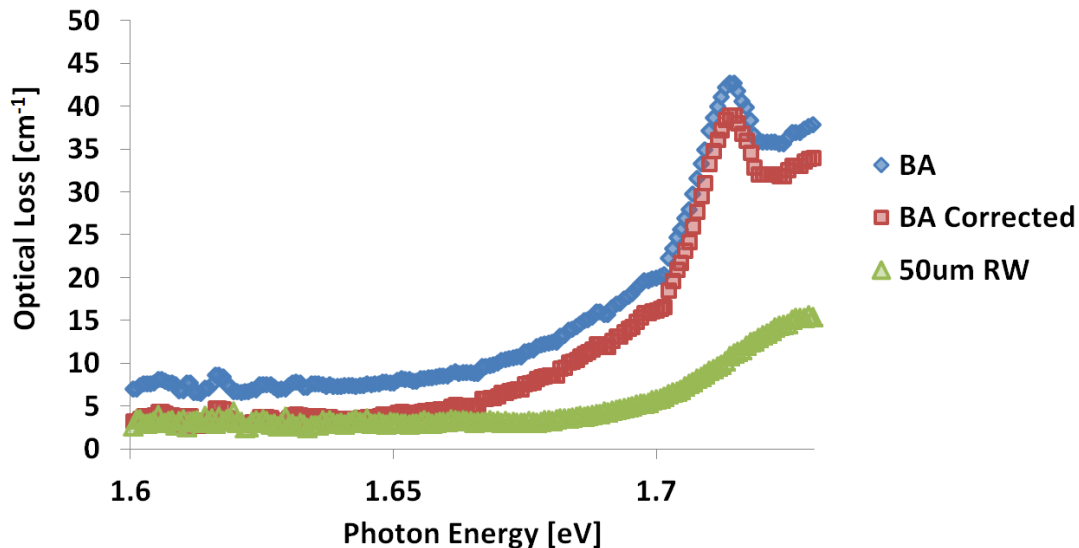
Figure 3.2: Measured Optical Loss spectra below the interband absorption edge for a RW device, a uncorrected BA device and a divergence-corrected BA device (denoted in legend as '50 μm RW', 'BA' and 'BA corrected' respectively).

71

Unlike in later chapters of this thesis, uncertainty in optical loss below the absorption edge in the data shown in Figure 3.2 has not yet been reduced to be below $\pm$ 0.1 cm^{-1}. However, the value of effective divergence loss is sufficiently large that the point may be made that systematic error due to divergence in a multisection measurement of optical loss of a BA device *cannot be neglected.*

While this experimental test of divergence loss correction is encouraging, there are differences between the RW and BA spectra. Further work may address this issue through comparison with wider or narrower ridges, in which the ridge wall defects interact with a proportionally smaller or larger fraction of the total device respectively.

A difference between measured internal loss in BA and RW devices — which has been noted in past research using the multisection method for optical loss — has been wholly ascribed to processes such as additional scattering associated with defects near the ridge wall interface. This work demonstrates that this difference is, in part, due to effective divergence loss. Divergence compensation is necessary to attain low uncertainty measurements of optical loss when characterising a BA device. In later chapters of this thesis, this correction will not be applied to measurements of optical loss spectra in BA devices until such a time as the correction has been examined further. It is acknowledged that an effective divergence error, acting to increase measured optical loss coefficients by 3.2 cm^{-1} is present in the data presented in the later chapters of this thesis.

The Modulated Multi-section Method for Optical Loss

4.1 Introduction and Motivation

A sensible starting point for improving the precision of optical loss measurements using the Multisection Method is to allow the light intensity signal to accumulate for a longer duration. However, attempts to assess the limits of precision in the Multisection Methods in preliminary work uncovered the issue of systemic drift in the detection system. Such drifts are caused by several mechanisms and result in unpredictable systematic error in measured optical loss coefficients, as the conditions of the apparatus vary between the time periods in which I_1 and I_2 signals are accumulated. Changes in measured intensities have been observed due to drifting device alignment and device temperature (temperature dependence of device performance is described in Chapter 11). The effect of these parameters are re-examined following the optimisation of precision in Chapter 9. (Note that, while measures are taken to control device and detector temperatures, some time dependence will remain due to practical limitations in the temperature control systems).

Any time dependence of measured intensities is a serious concern as the more time for which each section is pumped to accumulate signal, the more time the

73

detection sensitivity is given to change between measurements of I_1 and I_2. This potentially results in a larger change in average detection sensitivity for more precise (longer) measurements. In turn, the longer the detection time, the greater the impact systemic drift will have on the uncertainty of a measurement.

Preliminary measurements of the influence of systemic drift on the measured optical loss spectra demonstrate that, even over the time span of a conventional Multisection method experiment (i.e. several minutes), systematic errors *much* larger than ± 0.1 cm^{-1} are possible. The inaccuracy of the measurement exceeds the uncertainty aim of this work and hence the effect of this systematic error must be addressed.

The data in Figure 4.1 demonstrates how the measured value for optical loss can be seen to change over time if the same measurement is repeated many times consecutively. Practically, this was achieved by switching between the two electrically pumped sections using a computer controlled relay, and applying the Multisection method analysis (Equation 1.16) to each pair of intensity measurements (at a particular photon energy). Use of a relay ensured that switching occurred at a regular interval and minimised human disturbance of the apparatus over the course of the experiment. This data was obtained via a series of Multi-section Optical Loss measurements, in which I_1 and I_2 are measured for roughly 12.5 seconds each in each instance. While the influence of the demonstrated drift would differ in a single Multi-section method measurement of this length (i.e. if I_1 and I_2 were each pumped and measured for 2,000 seconds at a time), the purpose of this data is to demonstrate the existence of systemic drift and to be indicative of the magnitude of the systematic error that it is likely to produce.

The measured value of optical loss plotted in Figure 4.1 is taken from a single pixel at a photon energy that is below the absorption edge of the device. (See Section 9.4 for more insight into this topic).

74
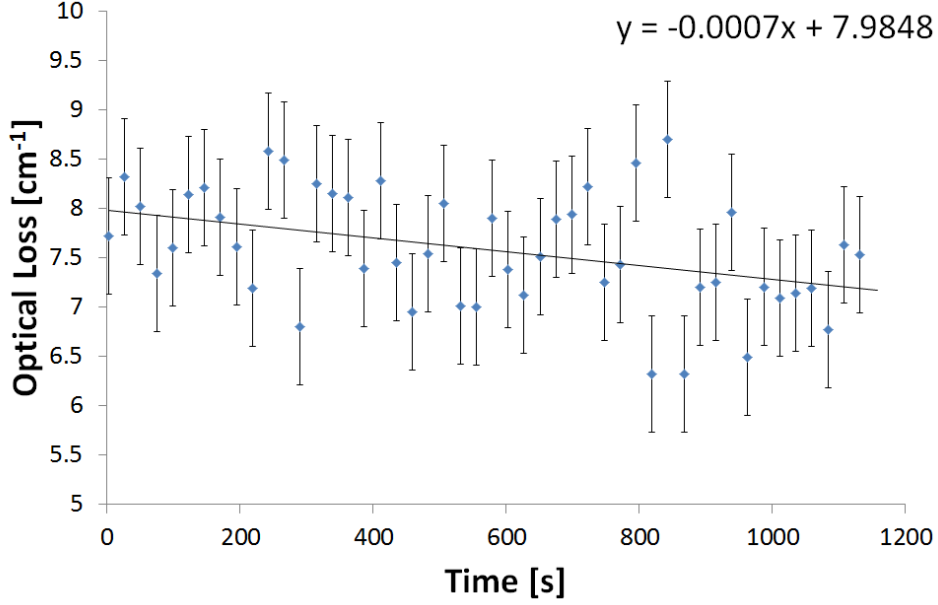
Figure 4.1: Several optical loss measurements are made consecutively to demonstrate the time dependence of the experimental outcome. Absorptive and scattering processes within a device are not expected to change in time in this way. This is considered to be a systematic error in the measurement. A fitting line demonstrates the downward trend of the data. (The equation for which is provided on the plot). A device of wafer $\#1_{BA}$ measured at a photon energy of 1.65 eV was used in this measurement.

The above data suggests that a drift of 0.1 cm^{-1} in an optical loss measurement may occur within a few minutes. This merits further investigation. The standard deviation of the data points (represented by error bars in the figure) is large compared with the gradient of the line of best fit over the measured time range. This raises the question of whether the apparent systemic drift is real, or a coincidence of the statistics in this specific set of sampled data. The slope of the optical loss data plotted in Figure 4.1 is $7.0 \pm 2.3 \times 10^{-4}$ cm$^{-1} s^{-1}$. The eventuality that this gradient is caused by statistical distribution of data rather than by the action of a real systemic drift is improbable, but not beyond reasonable doubt. The standard deviation of each data point in Figure 4.1 is 0.58 cm^{-1}.

Data featured later in this thesis (for example, Figure 6.1) demonstrates that observed systemic drift in measured intensity data is certainly not always a co-incidence of the sample statistics. However, Figure 4.1 demonstrates that — in

order to make strong statements regarding the effect of systemic drift upon optical loss measurements — long experiment durations are required. This achieves both precise measurement of the time dependent behaviour of the system and allows drift processes a longer period over which to occur. Hence, experiment durations which are much longer than those used in typical experiments for optical loss are used in the following chapters (of the order of several hours per measurement).

Physical mechanisms which may cause the kind of systemic drift described in this chapter include variations in detector sensitivity, device wall-plug efficiency, current pulse generator performance and optical alignment of the device as well as the lens and polariser. All of these mechanisms have some temperature dependence and it is known that the temperatureof the apparatus varies by a range of several Kelvin, even within working hours and in spite of the use of an air conditioning unit. The cause of systemic drift in any given set of data is not well known. However, pulse generator output and cryostat temperature have been measured to be sufficiently constant and investigations of the temperature dependence of the CCD photocathode have demonstrated an additive ($B(t)$-type) drift which does not agree with typical background offset behaviour observed in this apparatus (see Appendix A). This suggests that slight changes in device alignment or the variation of a controlling bias voltage in the ICCD are the most likely cause of the observed systemic drift.

4.2 Development of a Modulated Method for Optical Loss Spectra

To counteract the effect of a drift in a measurement system, one must complete a pair of I_1 and I_2 measurements sufficiently rapidly such that the systematic error caused by the drift is small enough to satisfy the uncertainty requirements of the given experiment. Preliminary experiments have shown that over this time period, insufficient signal will have been accumulated to achieve the high level of precision in optical loss measurement necessitated by modern device material and fabrication technique quality. A solution for this problem is to develop a

method by which a great number of rapidly alternating I_1 and I_2 readings can be taken — by synchronising the rapid switching of current between the sections with intensity measurements — and processed into an optical loss spectrum. If time dependent drifts can be negated by rapid section switching, then the duration of an experiment can be freely increased and so precision can be recovered from small signals within each '*modulation cycle*' by allowing more of these cycles to occur. Thus both high precision and high accuracy can be achieved. Such a method describes a modulated variant of the multisection method and hence is refered to as the Modulated Multisection method in this thesis. The modulated method is achieved by varying the absorbing length within a device at a modulation frequency which is rapid in comparison with the systemic drift in the detection system. The length of absorbing material is varied by switching between pumped sections, as in the conventional Multisection Method. A reference signal controlled by a computer engages switching between the two pumped device sections and synchronises the measurements accordingly. The practicalities are described in Chapter 5 .

Implementation of the Modulated Multi-section Method

In this chapter, the modulated variant of the multisection method for optical loss described in Chapter 4 is realised experimentally. The Modulated Multisection method uses the same equation (Equation 1.16) and device pumping geometry (outlined in Figure 1.13) as the conventional multisection method. The section geometry is repeated in Figure 5.1 for convenience and the layout of the experiment is represented schematically in Figure 5.2 . As in the conventional method L_s is known from the structure geometry. The same conditions on optical and electronic characteristics of devices apply as discussed for the conventional Multisection Method in Sections 1.3.4 and 2.7 .

A typical device consists of an unpumped front section, two alternately pumped sections and several unpumped sections at the rear of the device. All sections are earthed while not being pumped. All sections are 300 μm in length.
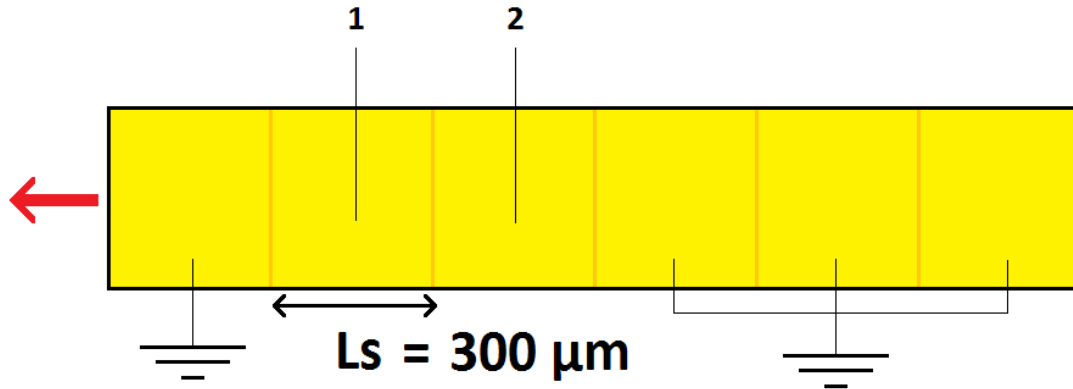
Figure 5.1: A top-down view of the segmented geometry of the (conventional and Modulated) Multisection Method. The red arrow indicates the propagation of light from the front facet.

There are certain key distinctions to make between the apparatus of the modulated multi-section method and that of the conventional multi-section method. These are outlined below in Figure 5.2 . A connection between the switch box and the computer has been introduced. This allows automatic switching of the pumped section by use of a relay. The arrangement to monitor the device input currents on the oscilloscope (marked by dashed lines) is now different. Due to the design of the new circuit in the switching box, not all of the current entering the box goes into pumping the device. As such a current probe is placed at the switching box output to get an accurate current measurement. Switching is controlled through use of a program integrated with the Andor system software (which controls the ICCD and spectrograph [56]). This program is written in a variant of the Basic programming language.

In investigating systemic drifts, the separation of drifts in the sensitivity from drifts in the background signal is fundamental. Consequently, a computer operated shutter has been introduced into the apparatus. A background signal may now be taken on a regular basis over the course of many hours without intervention by the experimentalist. The figure shows this computer-controlled shutter in the optical path. It is controlled by the Andor software.
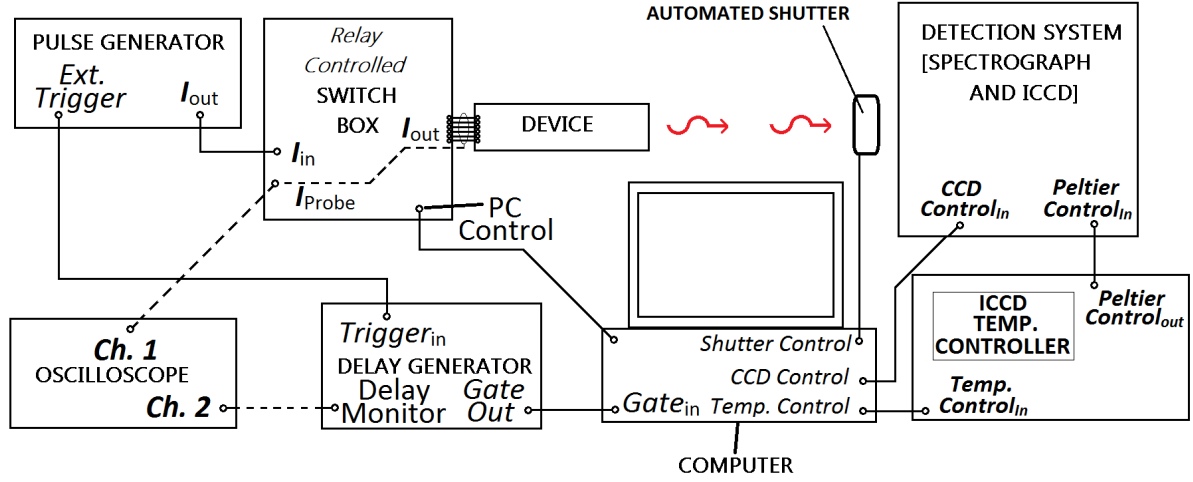
Figure 5.2: The modified apparatus used in the Modulated Multisection method is demonstrated. The corresponding diagram for the conventional method is given in Figure 2.3.

Timings in a modulated multisection measurement of optical loss are explained in Figure 5.3. The current pulses sent to the device and exposure of the CCD are the same as shown in Figure 2.5. Accordingly, the first three sets of axes — in which current pulses, ICCD gate pulses and ICCD exposures are explained — are omitted from Figure 5.3. A large number of measurements of each device section (over 5,000 measurement pairs, even in fully optimised conditions) are required to reach the precision aims of this project. Each measurement must be short such that a pair of I_1 and I_2 measurements occurs more rapidly than any systemic drift processes. In the case that saving and analyzing each pair of measurements is impractical — due to the large number of measurements — the software can be programmed to sum or average the respective I_1 or I_2 values produced by a number of exposures before saving to file. In addition to this, switching between device sections takes a finite amount of time (the modulated method program allows a switching time of 0.01 second); binning several measurements of each section before switching can slightly reduce the total time taken to measure a certain number of exposures. Conversely, it is useful to have a series of I_1 and I_2 measurements,

80

rather than just a single average of each, as this acts to quantify the degree of systemic drift underlying their measurements.

A program has been written to alternate between pumping section 1 and 2, measuring a small number of exposures between each switch (typically 50 exposures) and *accumulating* intensity measurements for each device section. This number of measurements is known as 'm' in later chapters of this thesis. Grey shaded regions within measurements in Figure 5.3 represent multiple measurements of each intensity within each modulation cycle. If m becomes too large, the modulation period becomes long and systematic error associated with systemic drift becomes larger. The optimum operating conditions — with regard to m, the total number of exposures required and the handling of background signals — will be discussed throughout later chapters of this thesis.

Figures 5.3.a) and 5.3.b) depict modulated multisection experiments in which a single background is taken and in which a background signal is measured at regular intervals throughout. The latter case would be necessitated by substantial drifts of the background signal over the course of a typical experiment. This behaviour – for the apparatus described in Section 2.2 – is addressed in Appendix A, in which it is found that repeated background measurement is not typically necessary with this particular apparatus. The possibilty of repeated background measurement is mentioned here in the interest of generality and for the few experiments in which this behaviour is examined.

The time period of a modulation cycle – that is the time taken in pumping one device section and then the other (before pumping the first section again) – is of critical importance in a modulated experiment. In further discussion of this method, this duration is described as the 'modulation period'. A relatively short modulation period of 2.4 seconds is shown in Figure 5.3, corresponding to five 0.2 second exposures of each device section (allowing for section switching and CCD readout time). The shutter has a transfer time of roughly 1 second. This is reflected in the time between groups of exposures in Figure 5.3 (marked by dashed lines).

81
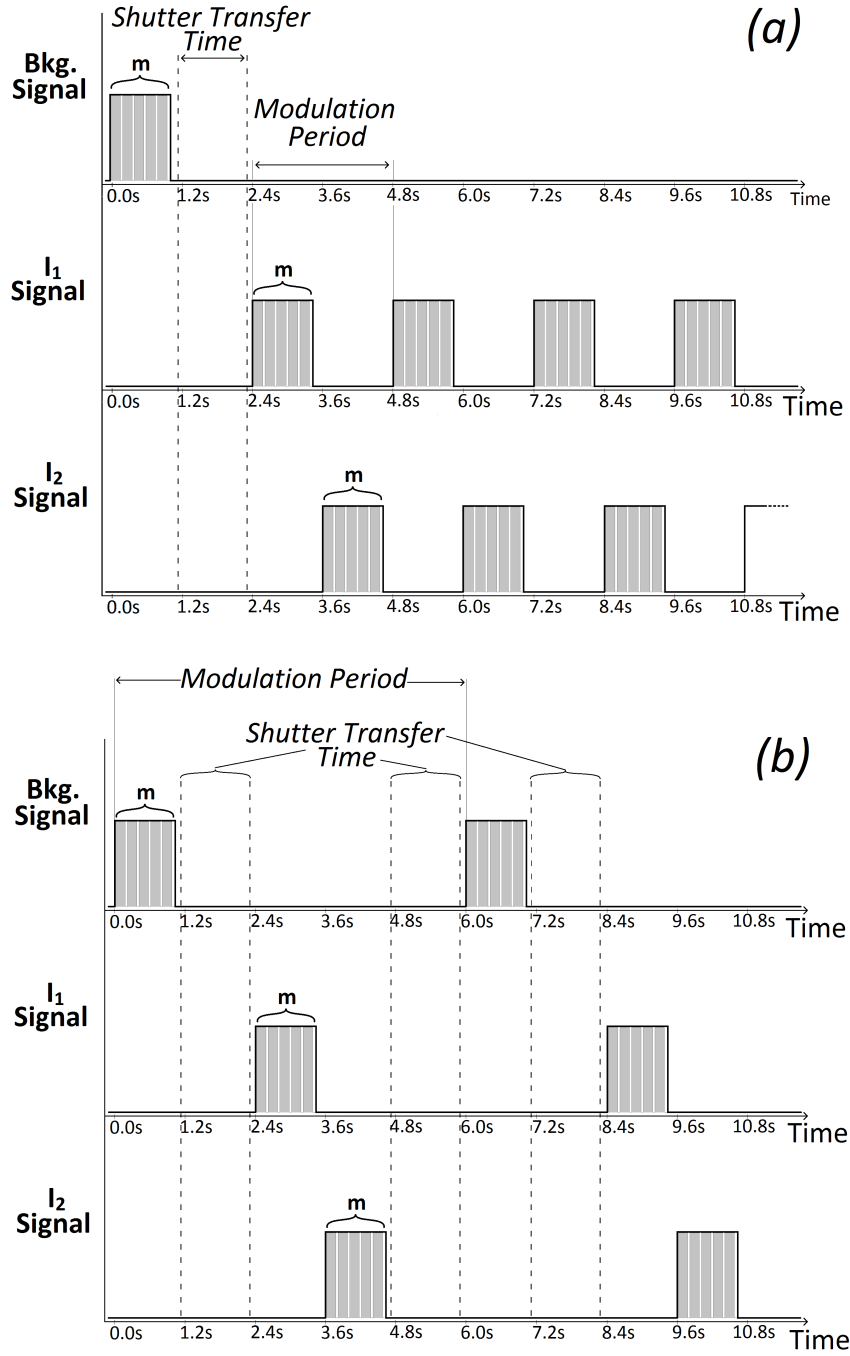
Figure 5.3: The sequence of acquisitions taken in a modulated multi-section experiment. Figure 5.3(a) demonstrates the standard practice of taking a single background reading at the start of each experiment. Figure 5.3(b) demonstrates the practice in which the background signal is regularly monitored through the acquisition. The function of m is clarified by the grey regions within each pulse. ($m = 5$ in this case.)

The Modulated Multisection method: A Proof of Principle

6.1 Comparison of Modulated and Conventional method Optical Loss coefficients

The reduction of error associated with systemic drift in the Modulated Multisection Method with respect to the conventional Multisection Method must be verified in experimental data. A sequence of trials was carried out, alternating between the Modulated and conventional Multi-section methods. Very long experimental durations (of the order of hours) were used in this investigation to allow larger changes in intensity values for typical rates of change of intensity within this apparatus. This ensured that the effect of systemic drift upon optical loss measurements was large with respect to the precision to which it is measured. (A full discussion of precision is given in Chapter 9). The model in Chapter 8 suggests that systematic error due to systemic drift will be reduced by use of the Modulated variant of the method. In order to emphasise the effect, long trial durations were used such that substantial change in the response of the system may occur between I_1 and I_2 measurements.

As established in Chapter 4, the conventional Multi-section Method collects

all I_1 data then all I_2 data whereas the Modulated Multi-section Method takes a short measurement of I_1 and I_2 within a modulation cycle and many modulation cycles constitute an experiment. For the purposes of direct comparison of Conventional and Modulated trials in this experiment, the same *total number of ICCD exposures* are taken for each method upon a sample of type $\#1_{RW}$. For the Modulated Method trials, five three second exposures are taken of light intensity from each device section in a measurement cycle. This cycle was repeated 300 times to acquire accumulated I_1 and I_2 intensities. In the Conventional Method trials, 300 groups of five three second exposures are accumulated of I_1 and then of I_2. For such long switching cycles, the increase in experiment duration due to the delay in switching between device sections is fractionally small enough to be neglected (≈ 30 s of a 2.5 hour trial). A drive current of 80 mA was pulsed at 20 kHz (with a 1 μs gate within a 1.5 μs current pulse). The values of intensity (and hence of optical loss) were derived from 6 pixels of the intensity spectra, from 1.651 to 1.658 eV below the device absorption edge.

The upper four series in Figure 6.1 represent the I_1 and I_2 signals from the Modulated and Conventional methods, as designated by the legend. *MS* and *Mod* designate Conventional and Modulated Multi-section method data respectively. The lower two series represent measured optical loss coefficients determined from the corresponding intensity data. Odd and even trial numbers represent Modulated and Conventional method data respectively. The underlying cause of the time dependence of measured intensity is examined in Chapter 9.

The key difference between the Conventional and Modulated methods is clearly seen in the distribution of intensity measurements within the trials corresponding to each method in Figure 6.1. In the modulated method data, I_1 and I_2 measurements are evenly distributed throughout a particular trial, whereas , in the conventional method data, I_1 measurements and then I_2 measurements occur.
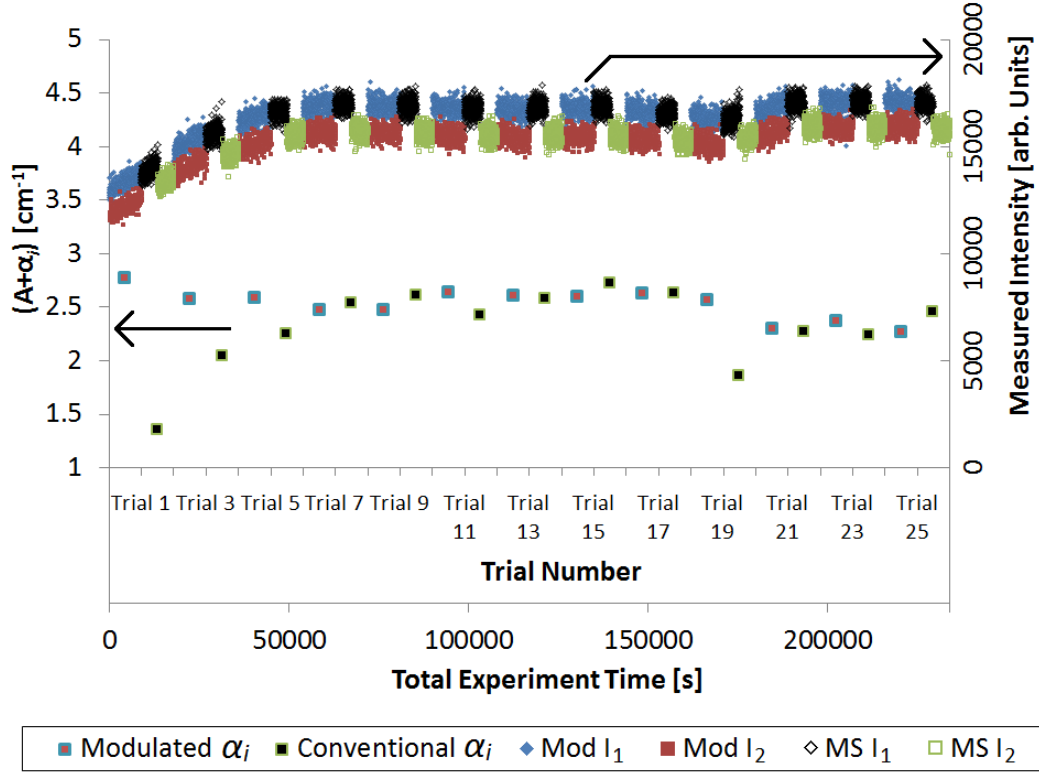
Figure 6.1: Experimental Intensity and optical loss data qualitatively demonstrate correlation between systemic drift in intensity and systematic error in optical loss measurement in Conventional Multi-section method. Such a correlation is not seen in the Modulated Multi-section optical loss data and deviation from mean in modulated method data is appropriately reduced. Black arrows indicate which series corresponds with which y axis.

The key finding from this data is that values of optical loss determined from the Modulated Method deviate from their mean value less than those determined from the Conventional Method. Taking average absolute deviation from the mean as a measure, values of 0.11 cm^{-1} and 0.28 cm^{-1} are found for the Modulated and Conventional methods respectively. Trials in which the measured optical loss value greatly deviates from the mean value correlate with relatively large drifts throughout the intensity time series. The error in optical loss, for Modulated Method trials, in the presence of large intensity drifts can be seen to be small in comparison. Furthermore, optical loss coefficients determined by the Modulated and Conventional methods tend towards agreement in trials for which intensity drift was negligible.

In the Conventional method data, positive drift in intensity can be seen to result in a *reduction* of the measured optical loss. The measured optical loss is reduced in this instance as the I_2 intensity is measured second and hence is relatively large in comparison with the measured I_1 intensity; the data erroneously suggests that less light is lost in the passive section of the device. The relation between systemic drift and the associated measured values of optical loss in this data is discussed in more detail in Chapter 8.

Error bars based upon the standard error in measured optical loss coefficients are plotted in Figure 6.1, but are not large enough to be visible on this scale.

6.2 Examining the origin of systematic error in Conventional method Optical Loss data

Examining the intensity data from various key trials of the Conventional method data allows a clearer view of the drift behaviour. Figure 6.2 examines trial 2, 8 and 20 in more detail. These correspond to Modulated method $(A + \alpha_i)$ measurements featuring varying degrees of deviation from the mean value.

Figure 6.2 demonstrates intensity time series from selected trials of Figure 6.1. As such, the y-axis corresponds to measured intensity, with the scale appropriately altered in each case. The x-axis shows the time elapsed since the start of the trial under scrutiny.

A positive gradient can be seen in the 'Trial 2' data. The 'Trial 8' intensity has a relatively small gradient. An intermediate gradient is visible in the 'Trial 20' data. These trials result in deviation from the average optical loss coefficient (as determined by the Modulated method) of 1.17 cm^{-1}, 0.01 cm^{-1} and 0.67 cm^{-1} respectively. The Modulated method average value of optical loss is used for this comparison under the preposition that it is less influenced by drift error and hence

more accurate than the Conventional method average.
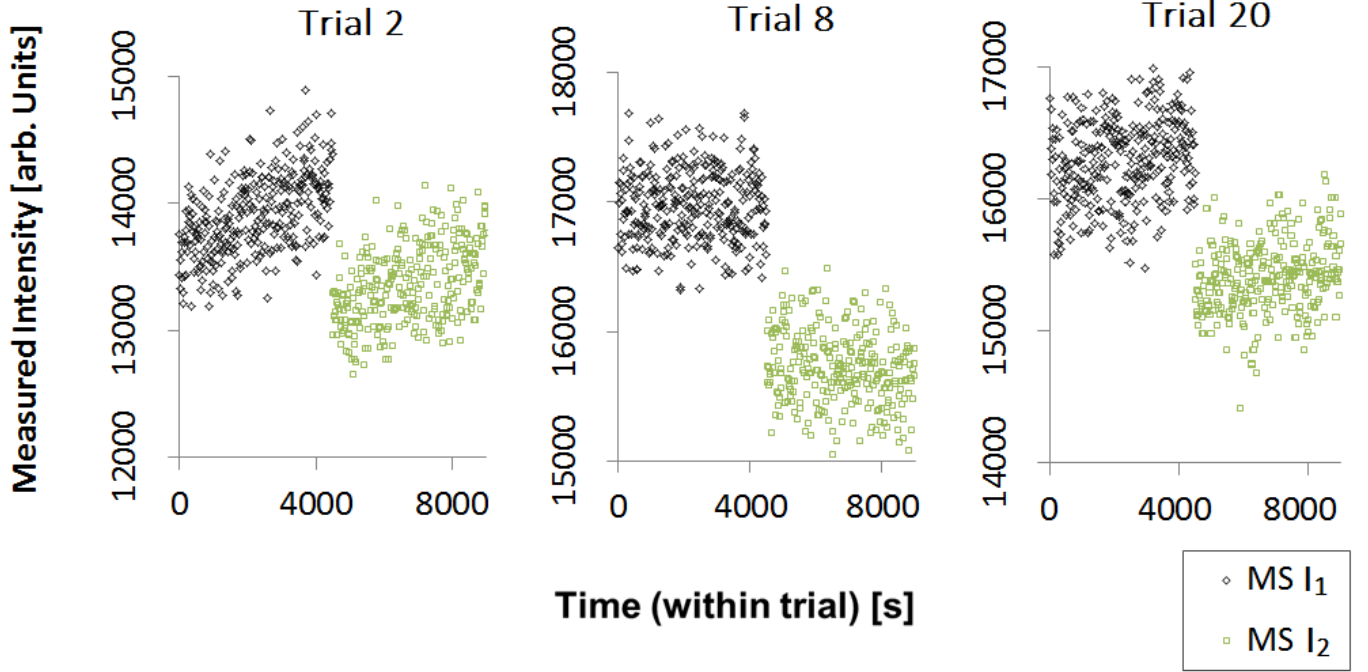
Figure 6.2: Close examination of selected Intensity time series from Figure 6.1. The associated Conventional method trial is indicated above each set of axes.

The gradient of the intensity data for a particular trial is clearly indicative of the behaviour of systemic drifts. However, it would be useful to have a single quantity by which to characterise both I_1 and I_2 data for a given trial. The product of the I_1 and I_2 intensity gradients has been taken as an efficient quantifier. The absolute value of this quantity will be large in the instance of large underlying drift. Furthermore, it will be positive if the net drift acts in the same direction for both sections and negative otherwise.

The 'Intensity Gradient Product' has been determined for both the Modulated and Conventional method intensity data. While the form of this intensity data

differs slightly, the interpretation of the produced value is comparable.

Intensity gradient product is plotted for each trial of Figure 6.1 for Conventional and Modulated methods alongside the deviation from the mean Modulated optical loss coefficient in Figure 6.3 .
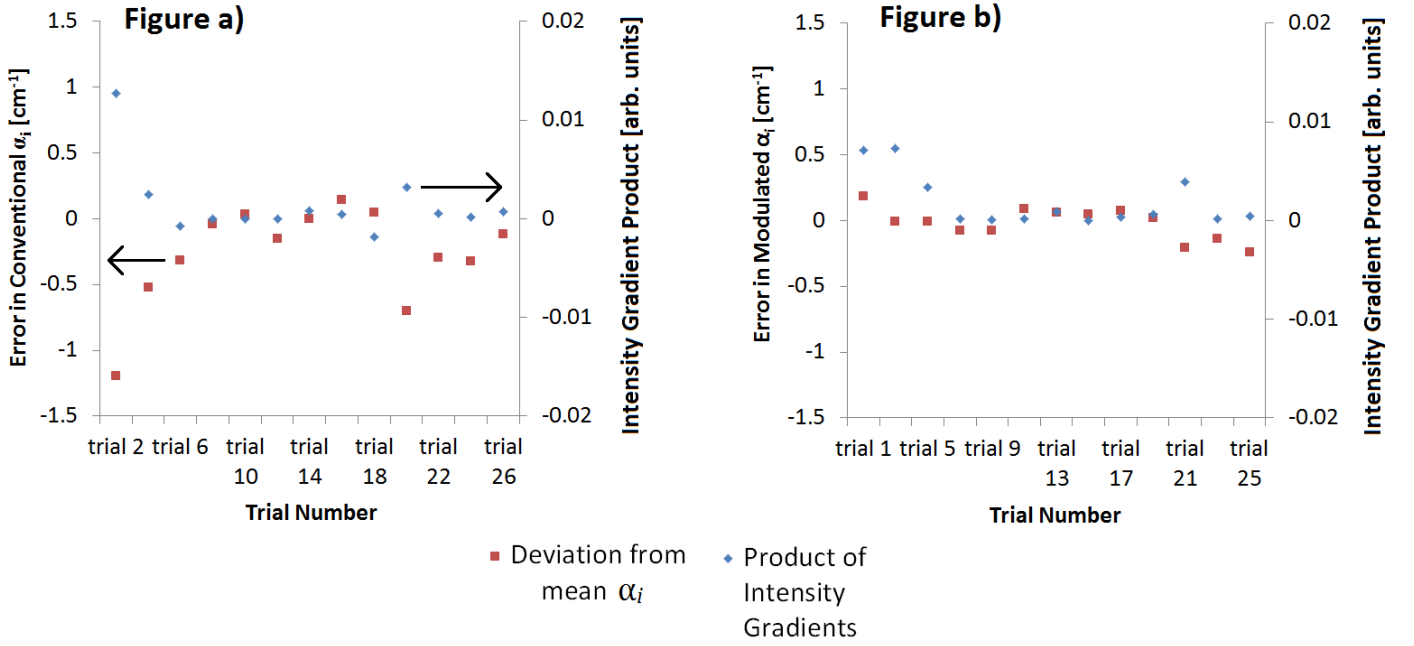
Figure 6.3: Demonstration of correlation between the product of I_1 and I_2 gradients and the deviation from the mean Modulated value of optical loss for each trial. Black arrows on Figure 6.3.a) indicate which series corresponds to which y axis (for both figures).

Figure 6.3.a) and 6.3.b) show data for the Conventional and Modulated methods respectively. The left-hand y axes in Figure 6.3 show deviation from the average Modulated method optical loss value and the right-hand y-axes show the Intensity Gradient Product. For the Conventional method plot, error in measured optical loss correlates with Intensity Gradient Product for each trial. In the Modulated method plot, error in measured optical loss is smaller and such a correlation

is not present. This data demonstrates that error in optical loss due to systemic drift can be reduced by use of a Modulated measurement methodology. This is in agreement with the findings of the model in Chapter 7.

6.3 Considering residual error in Modulated method Optical Loss data

There remains a time-dependence on the Modulated optical loss data. It is informative to determine whether this is due to residual drift error incurred by the finite switching period of the Modulated method in this experiment, or whether this is real time-dependence due to changes in temperature or alignment of the apparatus.

As previously stated, 3σ error bars are present on the optical loss coefficients plotted in Figure 6.1 but are too small to be visible. For the purposes of this chapter, the implication of this is that the deviation from the average optical loss of the conventional and modulated trials in Figure 6.1 is largely due to some systematic error source, rather than due to imprecision. (Precision in optical loss spectra is discussed in depth in Chapter 9).

6.3.1 Residual Systemic Drift

In Chapter 8, it is established that some systemic drift error will remain in optical loss values determined by the Modulated method. While the duration of a modulation cycle is greatly reduced from the Conventional method case — in which it is effectively equal to the experiment duration — the modulation period is still finite. Hence, some error associated with systemic drift is still present. This error is described with the term 'Modulated Drift Error' in this thesis. In the following, this error will be ruled out as the origin of the observed time-dependence remaining in modulated method optical loss coefficients in Figure 6.1.

The magnitude of modulated drift error is quantified in Chapter 8. By quantifying intensity drift using experimentally observed *fractional intensity gradients* (introduced in Section 7.2) and the modulation period used in this investigation, and inserting them into the modulated drift error equation (Equation 8.19), the magnitude of this 'residual' modulated drift error may be determined. For the intensity gradients of 'trial 1', a modulated drift error of 0.004 cm^{-1} is calculated. (Recall that 'trial 1' is associated with a particularly large intensity gradient). This value is much smaller than the 0.11 cm^{-1} difference from the average mean modulated method optical loss value associated with this trial. Additionally, the modulated drift error due to a positive intensity gradient acts to *reduce* a measured optical loss coefficient (to varying degrees in both Conventional and Modulated methods), whereas the measured optical loss coefficient for 'trial 1' has increased with respect to the mean modulated method value. Hence, modulated drift error is not the primary source of inaccuracy in this data. As 'trial 1' features a relatively large intensity gradient, modulated drift error will tend to be smaller than 0.004 cm^{-1} for the other Modulated method trials. Modulated drift error is not a significant source of inaccuracy in any of the modulated method trials detailed in this chapter.

This conclusion implies that the modulated multisection method drastically reduces the systematic error due to systemic drifts. Some drift due to factors such as optical alignment, apparatus temperature, or electrical or optical properties of the device itself remains in modulated optical loss data. These errors will be further discussed in Chapter 9.7.

6.4   Chapter Summary

In this chapter, it has been established that larger systematic errors in optical loss made with the conventional multisection method coincide with larger gradients in the underlying intensity time series. Much smaller errors are observed in the application of the modulated multisection method for optical loss, and these errors do *not* coincide with larger gradients in the underlying intensity time series. The

effect of systemic drifts upon the measurement of optical loss using the multisection method can be suppressed through modulation of the absorbing length.

The general relationship between systemic drifts and the corresponding systematic error in noisy intensity data is examined in Chapter 7. A calculation of the magnitude of systematic error under varying conditions is given in Chapter 8 and hence the conditions in which systematic error associated with systemic drift is sufficiently suppressed are established.

CHAPTER 7

Modelling the Effects of Drift in the Multisection Method

7.1   Introduction

The examination of systemic drift as a source of systematic error in the Conventional and Modulated Multisection experiments encompasses many subtle points and the underlying cause of any particular error in experimental data may be difficult to isolate from other possible causes. The aim of this chapter is to develop a mathematical model of the effect of intensity drift upon the outcome of a multisection optical loss experiment. The investigations described in this chapter are primarily examine the assumptions upon which work in later chapters (particularly the calculations within Chapter 8) are based. Through use of a model, a detailed examination of experimental conditions may occur. The effects which this model will help characterise in later section of this chapter include:

– Systematic error associated with data analysis in the Modulated method.

– Dependence of the magnitude of error in the modulated method upon the magnitude of the $(A + \alpha_i)$ under investigation.

– Misidentification of intensity standard deviations due to systemic drift.

Furthermore, the model outlined in this Chapter is used in Appendix A in order to examine the accuracy of the application of linear error propagation equations to Equation 1.16 .

In principle, one could examine the magnitude of error in optical loss associated with systemic drifts, in both the conventional and modulated methods, using the model described in this chapter. However, a more efficient approach to these tasks is given in Chapter 8.

7.2   Modelling Systemic Drift in Intensities

In order to simulate an Optical Loss measurement, intensities must first be generated. In order to maintain generality, it will not be assumed that systemic drifts are caused by either sensitivity of the detection system or behaviour of the background signal (effects which would have a multiplicative and an additive effect on measured intensities, respectively). Experimental intensity data similar to that shown in Figure 6 has been modelled by means of Equation 7.1:

$$I_{Calc}^{j} = A(t)I_{True}^{j} + B(t) \tag{7.1}$$

in which, I_{Calc}^{j} and I_{True}^{j} represent the measured and true intensity of the jth device section respectively. $A(t)$ and $B(t)$ are defined by Equations 7.2 and 7.3:

$$A(t) = M_A t + C_A \tag{7.2}$$

$$B(t) = M_B t + C_B \tag{7.3}$$

It can be seen clearly in the form of Equation 7.1 that $A(t)$ and $B(t)$ describe multiplicative and additive drift mechanisms respectively. The respective M parameters of $A(t)$ and $B(t)$ determine the gradient of the modelled systemic drift. C_A and C_B allow the incorporation of a constant offset in both of the above quantities. More generally, the intensifier sensitivity will act upon ambient background noise, resulting in an interdependence of $A(t)$ and $B(t)$. This is neglected in this

model, as ambient light only represents a small fraction of the total background signal.

$C_A = 1$ in all models, in this document so that $A(t)$ can be simply interpreted as a fractional change in intensities. As the offset due to background signal is removed in a standard measurement, the initial value of $B(t = 0)$ will be small in real data. Accordingly, $C_B = 0$ in all further modelling, unless otherwise stated.

It is occasionally more convenient to directly describe the time-dependent behaviour of intensity than that of the underlying processes ($A(t)$ and $B(t)$). Consequently, I define the quantity g to be the gradient of the intensity with respect to time. For $B(t)$ type drifts, the derivative of I_{Calc} with respect to time is simply M_B. For the $A(t)$ type drifts, g is defined by Equation 7.4:

$$g = M_A I_{true} \tag{7.4}$$

The distinction between g and M_A is important to understanding this chapter. This document will favour M_A over g, as it is more fundamental to both the mechanism of the systemic drift and the behaviour of the model.

Figure 7.1 demonstrates the generation of $A(t)$ and $B(t)$ which are then combined to produce an example I_{calc}. Figures 7.1.a) and 7.1.b) show $A(t)$ and $B(t)$ functions respectively. Figure 7.1.c) shows I_{calc} as defined in Equation 7.1. In Figure 7.1.a) $M_A = 0.0001$ s^{-1} and C_A=1. In Figure 7.1.b), M_B=1 and C_B=200. These parameters were arbitrarily assigned relatively large values to provide clear I_{Calc} trends in Figure 7.1.c). (These values are not used again beyond this demonstration of the model). Figure 7.1.c) demonstrates the effect of $A(t)$ and $B(t)$ upon a calculated intensity magnitude as a function of time. I_{True} in Figure 7.1.c) is 8,000 counts; as indicated by the dashed line.

I_{true} is assumed to be constant in this model. This aids analysis of $A(t)$ and $B(t)$, but it ought to be noted that factors unrelated to detection sensitivity and background behaviour could result in a time dependent intensity signal. The

concept of the *'true'* values of intensity or optical loss varying with time are not discussed in this chapter.
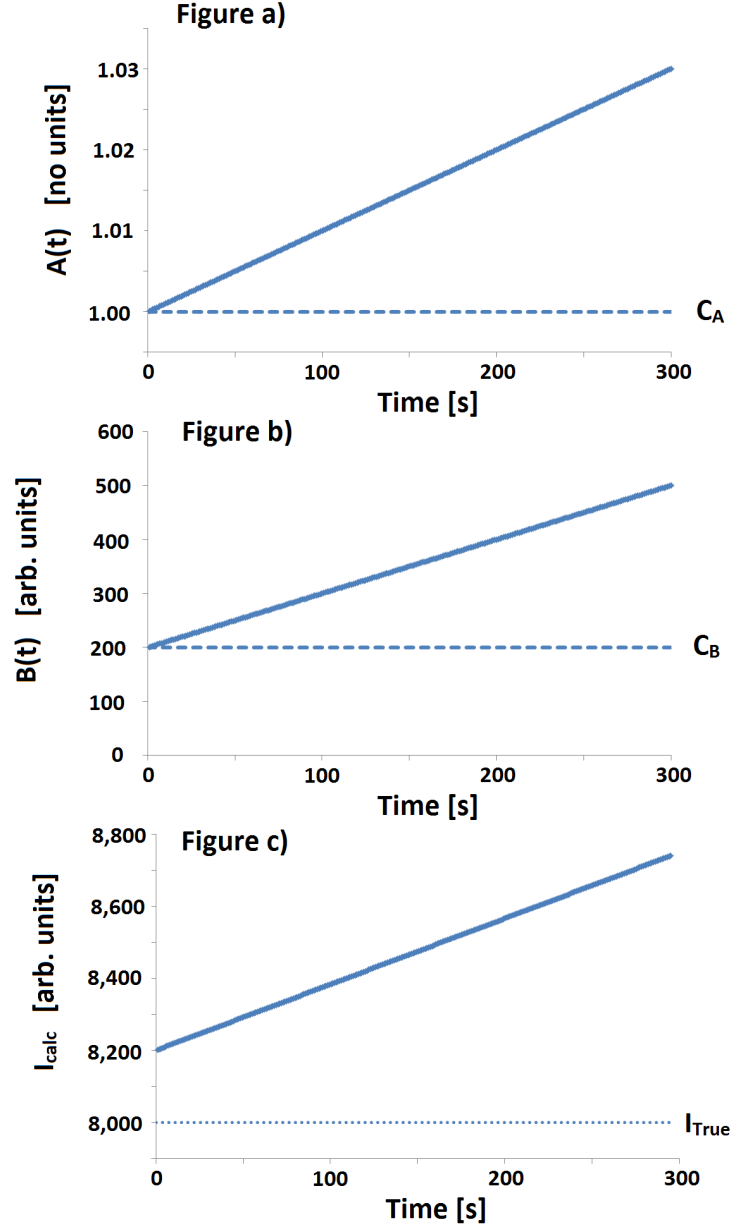
Figure 7.1: Arbitrary A(t) and B(t) functions are combined to obtain an I_{calc} function. Constant offsets are marked by dashed lines on each set of axes. Typically C_B is equal to zero in models in this chapter. It is set to a value of 200 in Figure 7.1.b) purely in order to demonstrate its function.

95

The t-axis can be calibrated such that the user of the model can vary the duration of a modulation cycle (i.e. of an I_1-I_2 measurement pair). In the following discussion, this will typically remain fixed at 1 second per pair of I_{calc}^1 and I_{calc}^2 values. In the subsequent model described in Chapter 8, the t value will be parameterized in order to optimise the experimental conditions.

Having modelled intensity behaviour, optical loss may now be considered.

7.3   Conventional and Modulated Methodologies

To simulate an optical loss experiment, an I_1 and I_2 parameter must both be generated. An experimentally typical value of $8,000$ is set for I_1. I_2 is hence determined from an entered 'true' value of $(A + \alpha_i)$ using Equation 1.16. Variation of this entered $(A + \alpha_i)$ value allows the examination of the effect of drift upon light undergoing varying degrees of optical loss. Typical rates of change in experimentally measured intensities are reproduced in the modelled intensities and effect upon the output values of optical loss is analysed. Having applied $A(t)$ and $B(t)$ drift to both an I_1 and an I_2 function, Conventional and Modulated Multisection measurements may be considered by simulating the temporal sampling of each method (according to the distinction made between the methods in Chapter 4). This is explained in Figure 7.2.

A(t) and B(t) functions exist throughout the duration of the simulated experiment and I_{calc}^1 and I_{calc}^2 values are thereby calculated at regular intervals throughout this duration. Figure 7.2.a) depicts a set of 300 simulated I_{calc}^1 and I_{calc}^2 data points for the $A(t)$, $B(t)$ and I_{true}^1 described in Figure 7.1. An $(A + \alpha_i)$ value of 2.6 cm^{-1} is used.

The two data sets within Figure 7.2.a) are then sampled in the fashion of the Conventional and Modulated methods to construct Figures 7.2.b) and 7.2.c) respectively. In Figure 7.2.b) the (single pair of) I_1 and I_2 measurement periods of the Conventional Multisection method are simulated.
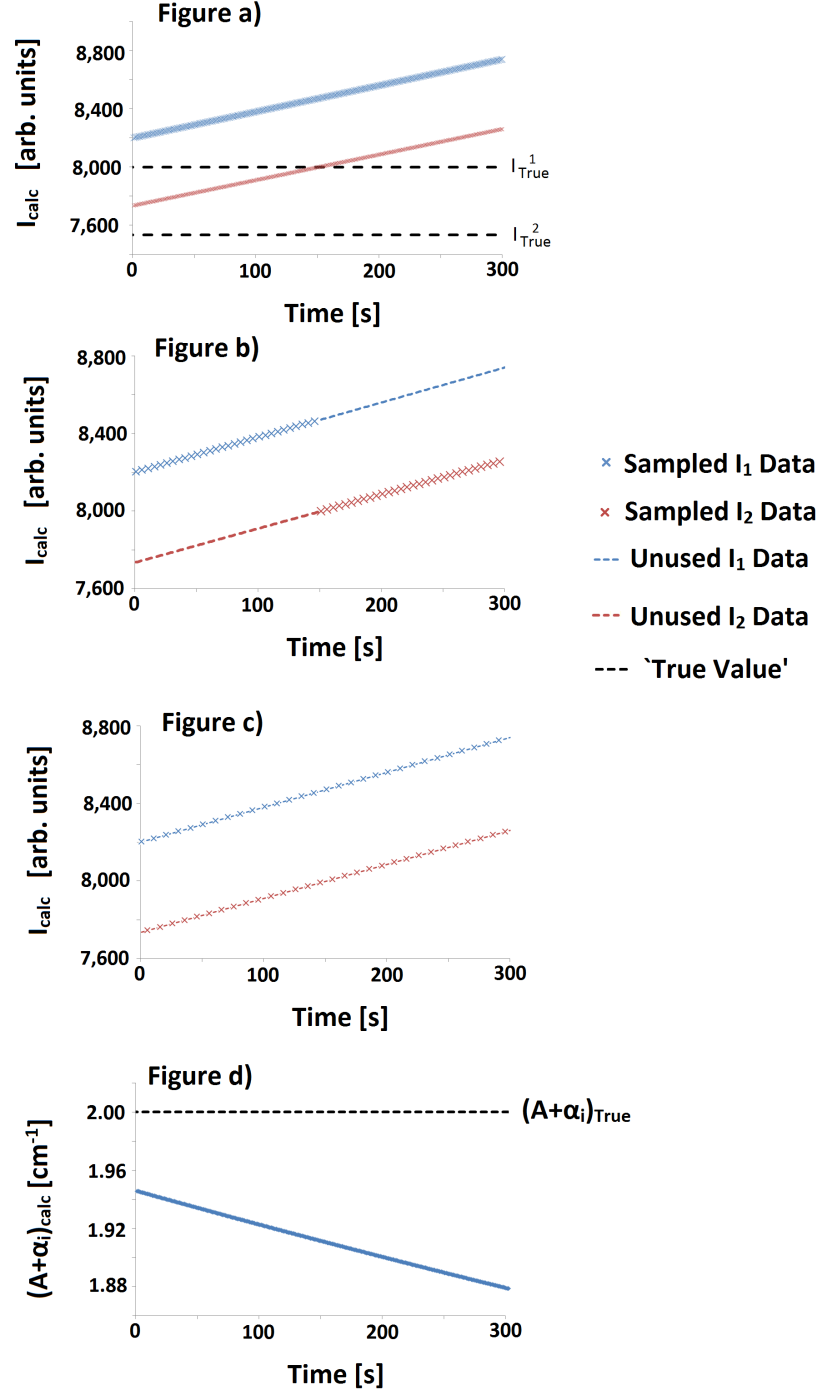
Figure 7.2: Calculated I_1 and I_2 intensity time series are shown in Figure 7.2.a). From which, data points may be sampled to simulate the Conventional or Modulated Multi-section methods as shown in Figures 7.2.b) and 7.2.c) respectively. The optical loss time series was calculated using adjacent pairs of intensity I_{calc} values from the Modulated method data set and plotted in Figure 7.2.d). Black dashed lines represent the true values of a given quantity. Coloured dashed lines represent the varying *measured* values of a given quantity.

In Figure 7.2.c), the alternating rapid pairs of I_1 and I_2 measurements of the Modulated Multisection method are simulated. The intensity *'measurements'* are distributed over the experiment duration such that the same number of I_{calc}^1 and I_{calc}^2 values are acquired in each method. In Figures 7.2.b) and 7.2.c), crosses represent used data and dashed lines represent the trend of the intensities for regions in which data is not sampled. (In Figures 7.2.b) and 7.2.c) the time between the measurements is exaggerated such that data points are not cluttered.)

Analysis of these data sets analogous to that applied to experimental I_{meas}^1 and I_{meas}^2 values can be carried out to produce a corresponding value of *measured* $(A + \alpha_i)$ for each method. Figure 7.2.d) shows $(A + \alpha_i)$ values corresponding to the pairs of intensities produced within each modulation period of the modulation method, that is, adjacent intensities in Figure 7.2.c). The calculated $(A + \alpha_i)$ time series shown in Figure 7.2.d) features systematic error due to the additive and multiplicative drift behaviour. As time increases, the calculated optical loss changes due to the gradients in both $A(t)$ and $B(t)$. The initial error in $(A + \alpha_i)_{calc}$ from its true value is caused by the initial offset in the additive systemic drift (C_B). (Recall that a measurement of background signal is removed from all intensity measurements described in this thesis. The value of C_B corresponding to real experiments is only limited by precision in the characterisation of background, and any offset is negligibly small.)

7.4   Imprecision and Scatter

In order to further approximate real data, experimental scatter (relating to imprecision of the measurement) can be introduced. (A detailed treatment of experimental uncertainty is given in Chapter 9). A standard deviation from the mean from typical experimental intensity data (with negligible long-term systemic drift), has been taken to be roughly 180 counts (arbitrary units) in a signal of $8,000$ counts. A scatter component with this standard deviation is added to each I_{calc}^1 and I_{calc}^2 data point using a normally-distributed value generator.

An updated form of Equation 7.1 in which this scatter component is included may be expressed as:

$$I_{calc}^{j} = A(t)I_{True}^{j} + B(t) + S_{scatter} \tag{7.5}$$

In Equation 7.5, $S_{scatter}$ represents the scatter component. This scatter is characterised solely by its standard deviation, σ_{SD}^{calc}. A new value of $S_{scatter}$ is generated to be added to each I_{calc}^{1} and I_{calc}^{2}.

The entered value of σ_{SD}^{calc} may then be varied to investigate predicted experimental outcomes with varying degrees of scatter (or indeed, no scatter at all). As such, the propagation of imprecision in intensity data through to $(A + \alpha_i)_{calc}$ values can be studied.

By setting the M_A and M_B values to zero, the case of constant $A(t)$ and $B(t)$ functions can be investigated. This approach is employed in the simulated data shown in Figure 7.3 to demonstrate modelled scatter in the absence of systemic drift. For the data shown in Figure 7.3, 300 I_{calc}^{1} and I_{calc}^{2} data points were alternately generated, wherein $C_A = 1$, $C_B = 0$ counts and $\sigma_{SD}^{calc} = 180$ counts.

Figure 7.3.a) shows a series of I_{calc}^{1} and I_{calc}^{2} values with zero drift behaviour and scatter with a σ_{SD}^{calc} value of 180 arb. units. The frequency distribution of both of the time series in Figure 7.3.a) are shown in Figure 7.3.b).

Each pair of adjacent I_{calc}^{1} and I_{calc}^{2} values from Figure 7.3.a) is used to obtain an $(A + \alpha_i)$ value. These are expressed as a separate time series in Figure 7.3.c). The associated frequency distribution of the data shown in Figure 7.3.c) is plotted in Figure 7.3.d).

99
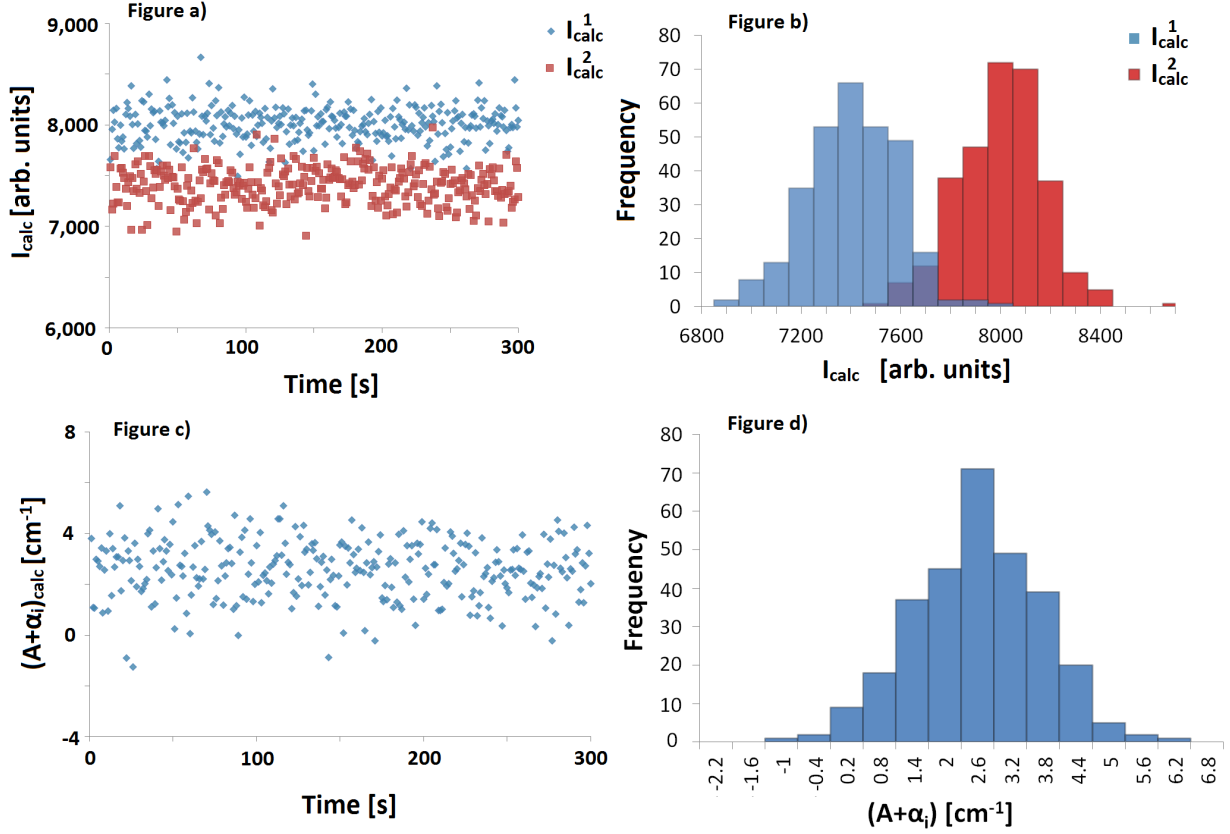
Figure 7.3: The upper pair of figures depict the introduction of scatter into calculated Intensity time series I^1_{calc} and I^2_{calc} and the frequency distributions associated with these respective series. The red and blue histograms in Figure 7.3.b) represent the two intensity signals, as indicated by the legend. The intermediate region represents the overlap between the two histograms. The lower pair of figures depict the scatter in the resultant $(A + \alpha_i)$ time series and its associated frequency distribution.

This scatter function aids interpretation of scatter in real experimental data. Scatter in the model will be used to make broad comments regarding the general propagation of imprecise, sampled intensity signals through the multisection optical loss equation and the distribution of resultant optical loss coefficients. (Rather than to extrapolate upon specific experimental outcomes.) Scatter in experimental data will be considered in detail in Chapter 9.

It is seen in Figures 7.3.c) and 7.3.d) that finite samples of I_1 and I_2 with normally distributed scatter result in approximately normally distributed scatter

in resultant values of optical loss. Note that the input parameters roughly correspond to a 2.5% fractional standard deviation in intensities. By standard error propagation equations, this approximately results in a 4% fractional standard deviation in the quotient of I_1 and I_2 and hence a 1.1 cm^{-1} standard deviation in optical loss (for a device section length of 0.03 cm). In this example, a calculated value of optical loss of 2.6012 cm^{-1} was produced. The entered intensity standard deviation (180 arb. units) resulted in an optical loss standard deviation of 1.1045 cm^{-1} (corresponding to a single I_1-I_2 pair) and consequently an optical loss standard error of 0.0638 cm^{-1}. The difference between the calculated optical loss and the entered value is smaller than the standard error associated with the sampling. Repeatibility of similar magnitudes of absolute error upon randomly generating data such as that given here demonstrates that optical loss values are *accurately* reproduced by the underlying mathematics under the stated conditions. However, it was observed that this is not the case when large intensity standard deviations are examined. This error is studied further in Section 7.5.1 of this chapter.

As scatter is introduced additively to calculated intensities (after $A(t)$ and $B(t)$ functions have been applied), scatter is not affected by variation in $A(t)$ and $B(t)$. The scatter distribution does not scale with the magnitude of intensity in this model. This is not perfectly representative of the physical situation. However, for low values of optical loss, I_1 and I_2 intensity measurements will have a similar mean value and are hence unlikely to have drastically different associated standard deviations. Care must be taken in this model while examining larger values of optical loss.

7.5 Investigation of the Modelled Modulated Multisection method for Optical Loss

Now that the model is established, properties of the experiment can be examined through manipulation of the input parameters. As mentioned in Section 7.1. The following topics will be addressed in the discussion in this section:

– The systematic error in optical loss associated with data analysis in the Modulated method.

– Determining whether error in optical loss derived from the Modulated Multisection method depends upon its magnitude.

– The misidentification of intensity standard deviations due to systemic drift.

7.5.1 Assessment of Analysis Approach in the Multisection Methods

Analysis of Conventional Multisection method intensity data to provide an $(A + \alpha_i)_{calc}$ value is straightforward. Given a time series such as that shown in Figure 7.2.b), I_1 and I_2 data sets are respectively averaged and the corresponding loss determined by Equation 1.16.

Analysis of Modulated Multisection method intensity data provides two options; averaging all intensities before applying Equation 1.16 (somewhat similar to the approach taken in the Conventional method), or applying Equation 1.16 to each adjacent pair of intensities to acquire a series of $(A + \alpha_i)_{calc}$ values (such as those found in Figure 7.3.c)) and averaging each of these values.

The term *'The Average-Process analysis'* will be used to refer to the method in which all intensities are *averaged* before being *processed* into an $(A + \alpha_i)$ value. The term *'The Process-Average analysis'* will be used to describe the method in which each intensity pair is *processed* into an $(A + \alpha_i)$ value before these values are *averaged*.

In the instance of zero scatter and zero $A(t)$ or $B(t)$ type drift (in which σ_{SD}^{calc}, M_A and M_B are set to zero) the conventional method and both modulated methods produce an output $(A + \alpha_i)_{calc}$ equal to the input $(A + \alpha_i)_{true}$. This is also approximately the case for experimentally typical degrees of scatter in intensity in the absence of systemic drift (the precision of an optical loss measurement in examined in detail in Chapter 9). However, any scatter will result in some dis-

crepancy between the two methods of analysis of Modulated data.

The effect that analysis method has upon systematic error in optical loss is examined in the simulated data shown in Figure 7.4. For the result to reflect real experimental outcomes, reasonable values of modulation period and experiment duration must be used, thus limiting the precision of any one simulation. A modulation period of 1 second and an experiment duration of 300 seconds are used in the simulations described in this section. In order to examine the effect that these analysis methods have on an optical loss measurement (for a particular σ_{SD}^{calc}), the outcomes of each analysis method must be compared for a great number of such simulated experiments, such that the statistical nature of the sampling is accounted for. $4,000$ of these 300 second long simulated experiments constitute the data presented in this section.

In Figure 7.4.a) and 7.4.c), a typical intensity time series is given for input intensity standard deviations of $\sigma_{SD}^{calc} = 180$ counts and $\sigma_{SD}^{calc} = 1,500$ counts respectively. Having applied both analysis procedures to produce an optical loss coefficient from such sets of intensity data $4,000$ times for both intensity standard deviations, the frequency distributions displayed in Figures 7.4.b) and 7.4.d) were produced respectively. New $S_{scatter}$ values were generated for each of the $4,000$ data sets for both values of σ_{SD}^{calc}. Sampling a large number of times allows examination of the sampling distribution, and allows precise characterisation of the mean experimental outcome. The standard error of the simulated optical loss is approximately 0.001 cm^{-1} and 0.009 cm^{-1} in Figures 7.4.b) and 7.4.d) respectively. These values were calculated using standard error propagation equations.

For the experimentally typical intensity standard deviation of 180 counts, the two methods provide very similar frequency distributions. The Average-Process analysis produces an average $(A + \alpha_i)_{calc}$ of 2.599 cm^{-1} while the Process-Average analysis produces an average $(A + \alpha_i)_{calc}$ of 2.600 cm^{-1}. Considering the $(A + \alpha_i)_{true}$ value is 2.6 cm^{-1} in this model, this error is acceptable for the purpose of achieving the ± 0.1 cm^{-1} aim of this project. The deviation in the values of optical loss derived from the Average-Process method from the value entered into

the model is comparable with the standard error of the simulated distributions. This demonstrates that the outcome of the modulated multisection method for optical loss is dependent upon which of these analysis techniques is used, but that the difference is negligible for the uncertainty requirements and for the apparatus used in the work outlined in this thesis.
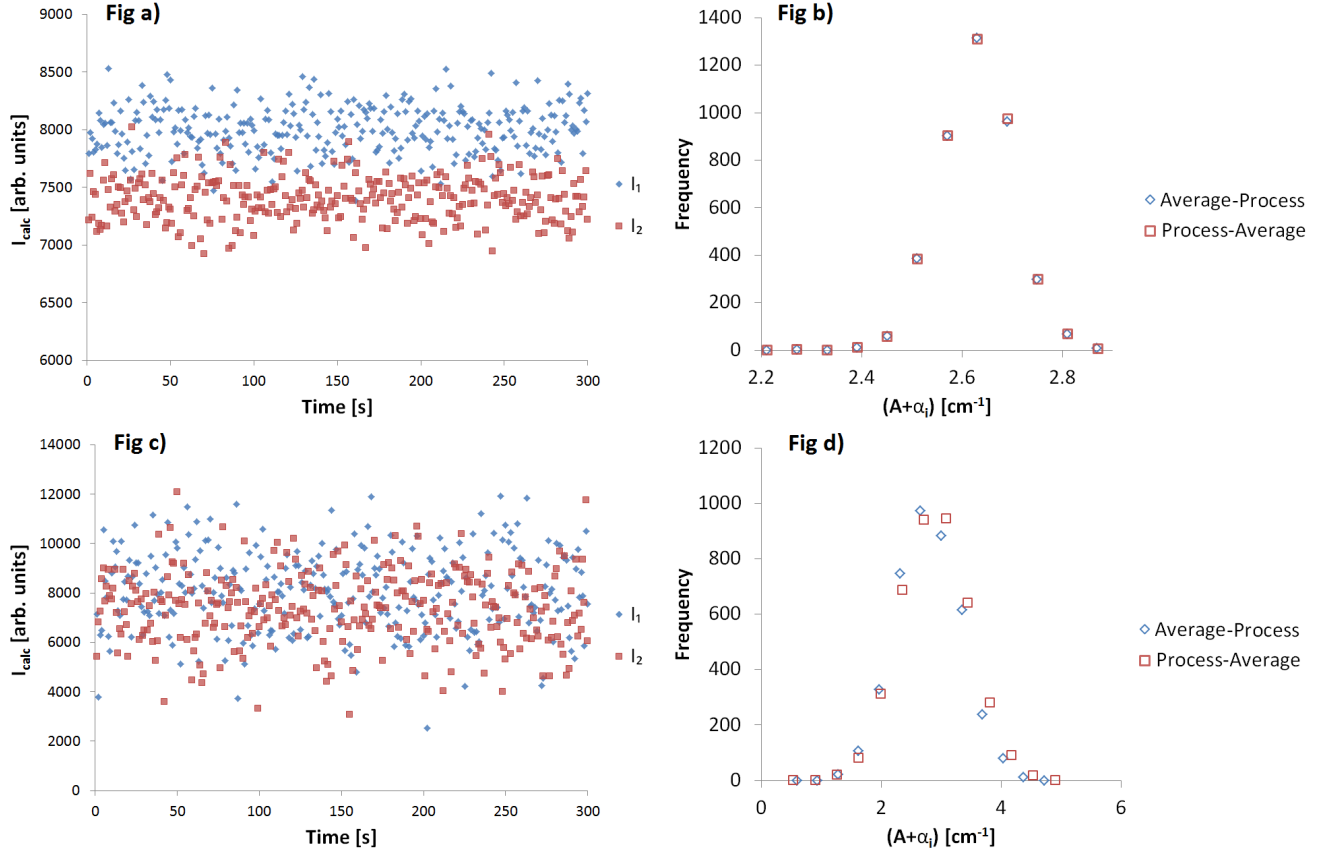
Figure 7.4: Figure 7.4.a) depicts a time series of simulated I_1 and I_2 values in the absence of drift, with an experimentally typical intensity standard deviation (180 counts). Figure 7.4.b) shows the distribution of optical loss values determined using the Average-Process and Process-Average analysis methods, from $4,000$ time series of the type shown in Figure 7.4.a) . Figures 7.4.c) and 7.4.d) fulfil the same respective roles as the previous two figures, but for an exxaggerated intensity standard deviation of $1,500$ counts. There is zero systemic drift in each case.

The instance of relatively large ($\sigma_{SD}^{calc} = 1,500$) scatter was modelled to allow further interpretation of this result. The Average-Process analysis produces an

average $(A + \alpha_i)_{calc}$ of 2.606 cm^{-1} while the Process-Average analysis produces an average $(A + \alpha_i)_{calc}$ of 2.709 cm^{-1}. The standard deviation for this increased intensity standard deviation is 0.009 cm^{-1}. While this value of intensity standard deviation exceeds that expected in experiments, this result is significant as it demonstrates that *some* improvement may be made by simply analysing data in the most appropriate way. Future work may require different experimental conditions or a noisier apparatus, increasing the noise associated with intensity measurements and making the systematic error associated with the Process-Average method significant.

The Process-Average analysis procedure is used to generate optical loss time series in this thesis for illustrative purposes (such as those shown in Figures 7.3 and 9.6.b) as two examples). These times series are useful in examining broad time-dependent behaviour within the measurement. However, due to the systematic error outlined in this section, the Average-Process method is used to determine the single value of optical loss taken from each modulated multisection experiment in this body of work.

Further modelling of instances of greater standard deviation of intensity scatter suggests that this error is due to the normal distributions of the modelled intensity data being distorted upon passing through Equation 1.16. Specifically, the distribution of optical loss corresponding to noisy I_1 and I_2 signals being passed through Equation 1.16 is made asymmetrical by the equations inherent nonlinearity.

It is worth noting that the intensities are not typically made negative by scatter in measurements within this thesis. Negative values of measured intensity cause erroneous values in Process-Average analysis. Assuming that the effect is dominant in the (smaller) I_2 distribution, this results in a truncation of the intensity distribution and hence a reduction of the mean measured optical loss coefficient. Intensities data is relatively precise before being processed into optical loss coefficients in the Average-Process analysis method and so the effect of negative intensities upon measured optical loss is suppressed . This is an additional reason that the Average-Process analysis may have less associated systematic error in op-

tical loss than the Process-Analysis method. This observation is more relevant in apparatus with poorer signal to noise ratios.

The conclusion of this section is that the effect of experimentally typical standard deviations of scatter in intensity data results in a somewhat skewed optical loss distribution. For these values of standard deviation, the resultant systematic error in optical loss is negligible in both the Average-Process and Process-Average analysis techniques. However, the Average-Process technique is more accurate and will be preferred in this thesis.

7.5.2 The dependence of systematic error in $(A + \alpha_i)$ upon the magnitude of $(A + \alpha_i)$

In preparation for further interpretation of the model, knowledge of the dependence of the error in $(A + \alpha_i)$ upon its magnitude would be helpful. In particular, it would be useful to know whether $(A + \alpha_i)$ ought to be parameterised in investigations such as that shown in Chapter 8.

Linear multiplicative $(A(t))$ and additive $(B(t))$ M coefficients were chosen as to reproduce similarly large intensity changes over the simulated time period. typical of relatively large systemic drift. Values of 1.375×10^{-5} s^{-1} and 0.1 arb units s^{-1} were used for M_A and M_B respectively. $C_A = 1$ and $C_B = 0$ arb units in this model. An example for the instance of $M_B = 0.1$ arb units s^{-1} wherein I_1 is set as $8,000$ arb units, $(A + \alpha_i)$ is set to 5.0 cm^{-1} and I_2 is roughly $6,886$ arb units is given in Figure 7.5.a). This simulated experiment has a modulation period of 0.1 seconds and an experimental duration of 180 seconds. This constitutes $1,800$ $I_1 - I_2$ measurement pairs.

The magnitude of $(A + \alpha_i)_{true}$ was then varied for both the $A(t)$ and $B(t)$ drifts and the resultant error examined in each case. The $A(t)$ and $B(t)$ drift components were tested individually by setting the M coefficient of each to zero whilst the other is under investigation. Scatter was omitted from this model. This

was carried out for both the Modulated and Conventional methods and the results were plotted in Figure 7.5.b). Enough data points were calculated to produce line plots for the $(A + \alpha_i)$ region of experimental interest.
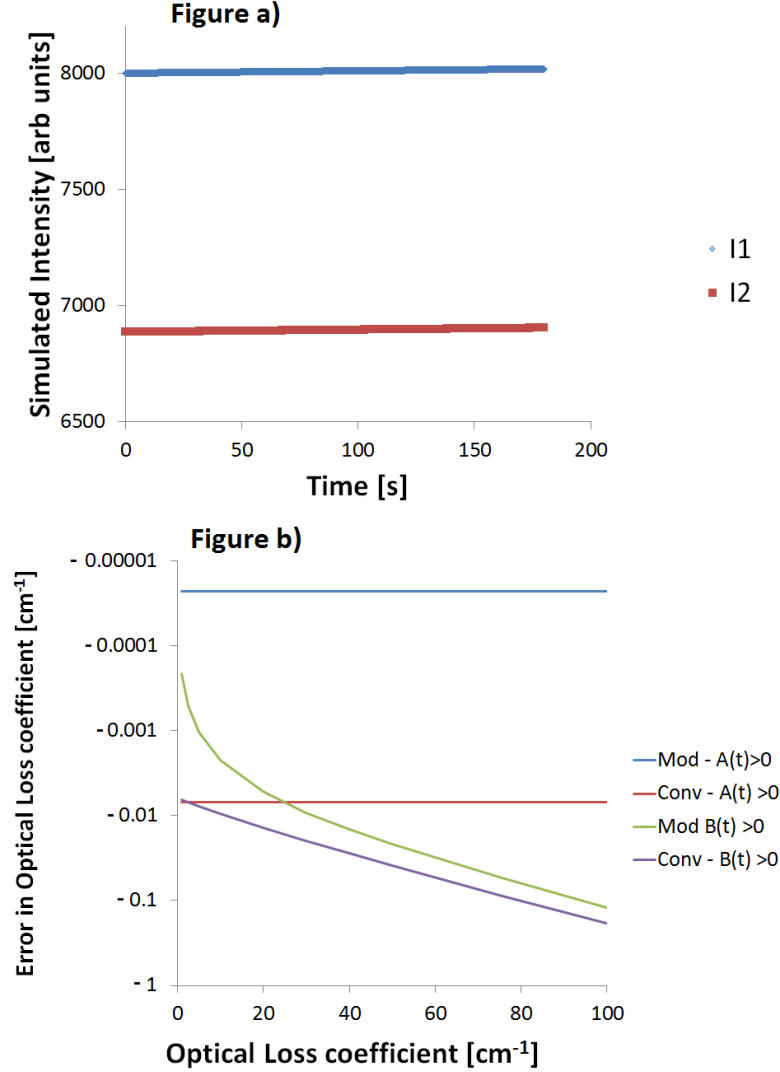
Figure 7.5: Scale of intensity drift is demonstrated in Figure 7.5.a). The error in $(A + \alpha_i)$ due to such a drift is shown as a function of $(A + \alpha_i)$ in Figure 7.5.b)

In the Figure 7.5.b) legend, 'Mod' and 'Conv' denotes values calculated by the Modulated and Conventional methods respectively. $A(t) > 0$ and $B(t) > 0$ denote

that systemic drift in the indicated series is entirely due to $A(t)$ and $B(t)$ type drifts respectively.

In Figure 7.5.b), the error due to $A(t)$ type drifts can be seen to be independent of the magnitude of optical loss under examination. This is due to the fact that a particular $A(t)$ gradient over a particular experiment duration will have the same fractional effect on intensities (and hence $(A + \alpha_i)$) regardless of the magnitude of $(A + \alpha_i)$ (by its very definition). The Conventional method series has a larger associated error (in both $A(t)$ and $B(t)$ type drift data) due to its longer measurement cycle.

$B(t)$ drift causes error which is dependent on the magnitude of $(A + \alpha_i)$. This occurs due to the fact that I^2_{calc} decreases as $(A + \alpha_i)$ increases in this model. Hence, as larger values of $(A + \alpha_i)$ are examined, magnitudes of $B(t)$-type error become relatively large in comparison with I^2_{calc} values to which they are added. $B(t)$ type drift converges to the $A(t)$ drift value for small values of optical loss, as I_2 and I_1 tend towards the same value as optical loss decreases. Hence, the effect of an additive background tends towards a situation where I_1 is equal to I_2, in which the background drift affects the two intensities identically.

The experiment described in Appendix A suggests that $B(t)$ drifts are not the primary cause of systemic drift in experimental intensity data. Due to this observation, the $A(t)$ drift is assumed to be dominant in experimental data. Hence, following the result shown in Figure 7.5.b), further error calculations within this model will not be carried out as a function of $(A + \alpha_i)$.

Examining magnitudes of error in optical loss due to systemic drift is examined in detail in Chapter 8.

7.5.3 The erroneous evaluation of Standard Deviation due to Systemic Drift

In Chapter 9, the standard deviation of optical loss measurements is used to quantify imprecision of experimental data and estimate minimum experiment durations required to reach a particular precision benchmark. In order for the application of standard deviation to be appropriate, error sources must result in a normal distribution of deviation from the mean value. The presence of systemic drift implies that the mean value of a measured intensity distribution is changing in time and the usual definition of standard deviation is invalid. However, standard deviation can still be interpreted in the usual fashion so long as the measurement in which standard deviation is determined occurs rapidly with respect to the systemic drift. In this section, the intensity standard deviations determined from modelled data with varying degrees of systemic drift are considered, and the resultant impact upon standard deviation in optical loss is quantified. These modelled optical loss standard deviations are then compared with the nominal optical loss standard deviation in order to comment upon conditions in which intensity standard deviation is determined with sufficient accuracy for the purposes of this project.

The effect of drift in intensity signals upon the measured intensity standard deviation was calculated in this section by generating intensity time series consisting of $1,000$ measurements, with varying degrees of intensity drift and varying exposure times (and hence measurement durations). This was repeated for I_1 and I_2 intensities. Experimental scatter was simulated in both intensity time series (using the method described in Section 7.4). An I_1^{true} value of $8,000$ counts and an optical loss of $5cm^{-1}$ was used in this model, resulting in an I_2^{true} value of roughly $6,886$ counts. The input standard deviation in the scatter in I_1 and I_2 was 180 counts. Using standard error propagation equations (see Equation 9.8), a standard deviation in optical loss of 1.150 cm^{-1} can be calculated for a standard device section length of 0.03 cm. An example of $1,000$ measurement time series for both I_1 and I_2 intensities are plotted together in Figure 7.6.a). An exposure time of 0.017 seconds and an intensity gradient (M_A) of $0s^{-1}$ were entered into the model to produce this data. Increase in exposure duration is independent of

intensity standard deviation in this model such that the duration of a simulated experiment may be changed without changing the associated precision.
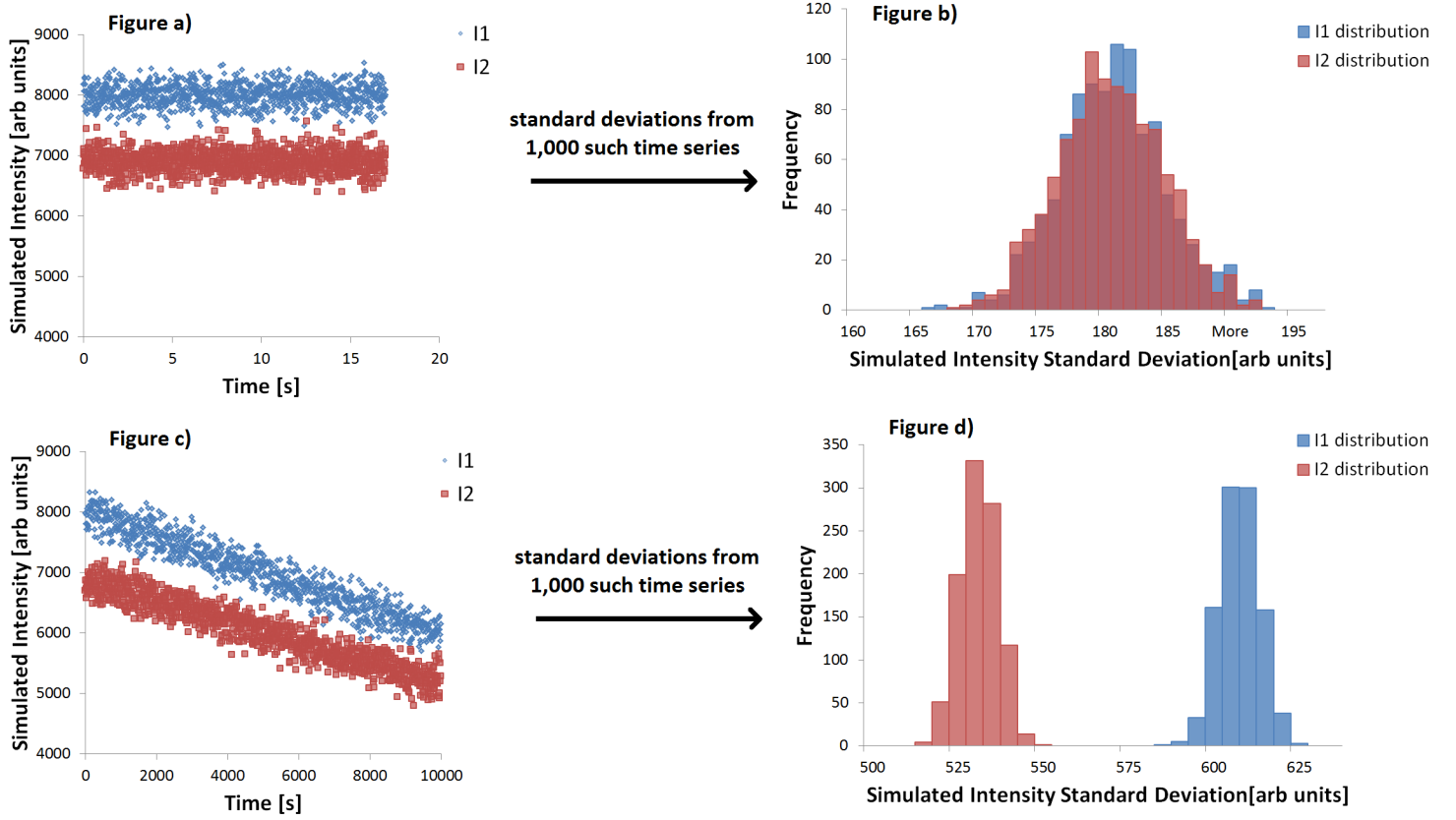
Figure 7.6: Figure 7.6.a) shows 1,000 simulated I_1 and I_2 intensities for $M_A = 0$ s^{-1} and an exposure time of 0.017 seconds. Figure 7.6.c) shows 1,000 simulated I_1 and I_2 intensities for $M_A = -2.50 \times 10^{-5}$ s^{-1} and an exposure time of 10.000 seconds. The simulations shown in Figures 7.6.a) and 7.6.c) were run 1,000 times each and the resultant standard deviations corresponding to both intensities are plotted in Figures 7.6.b) and 7.6.d) respectively.

If systemic drift in an intensity time series is large enough over the course of 1,000 simulated exposures, the standard deviation of the simulated data points will disagree with the nominal intensity standard deviation entered into the model. For the purposes of this investigation, the value of optical loss standard deviation — determined from the values of intensity standard deviation entered into the model

— is compared to that determined from the values of intensity standard deviation which are observed in a pair of simulated I_1 and I_2 time series (such as Figure 7.6.a) and 7.6.c)). This process relates the characterisation of intensity standard deviation to the resultant mischaracterisation of optical loss standard deviation. Comments about the impact of this mischaracterisation upon experimental design are made at the end of this section.

The simulated intensity standard deviations are subject to imprecision due to the finite sample size in each simulation. For this reason, the scatter upon each series of $1,000$ simulated intensity exposures was generated $1,000$ times and the average intensity standard deviation of these $1,000$ time series taken to quantify intensity standard deviation for the corresponding exposure duration and intensity gradient. (This process improves the fractional precision in the identification of each intensity standard deviation from around 2.0% to better than approximately 0.1%.)

Exposure times of 0.017, 1.000 and 10.000 seconds were examined for each intensity gradient. 0.017 seconds corresponds to the smallest exposure duration allowed by the ICCD in its standard operation and hence the most rapid assessment of an *experimental* intensity standard deviation which is possible. The experiment duration corresponding to a $1,000$ measurement time series for these exposure times are roughly 17 seconds, 17 minutes and 167 minutes respectively. Intensities gradients of $M_A = -2.50 \times 10^{-5}$, -1.25×10^{-5}, 0, $+1.25 \times 10^{-5}$ and $+2.50 \times 10^{-5}$ s^{-1} were used. An intensity gradient of $M_A = 2.50 \times 10^{-5}$ s^{1-} corresponds to the largest experimentally measured systemic drift for the apparatus upon which these experiments are carried out (see Figure 9.10).

In Figure 7.6.a), an example of a simulation of 1,000 I_1 and I_2 intensities is given for the case of a 0.017 second exposure time in the absence of systemic drift. The standard deviations of intensity data sets such as those shown in Figure 7.6.a) were taken $1,000$ times and the distribution of the resultant values are given in the histogram shown in Figure 7.6.b). These histograms can be seen to approximately overlie with the *input* standard deviation value of 180 *counts*.

Figure 7.6.c) shows example data for a simulation of 1,000 I_1 and I_2 intensities for the case of a 10.000 second exposure time with a intensity gradient $M_A = -2.50 \times 10^{-5}$ s^{-1}. Figure 7.6.d) shows a histogram of the I_1 and I_2 standard deviations from 1,000 simulations of the type shown in Figure 7.6.c). The systemic drift is clearly visible on the time series of Figure 7.6.c), and has the effect of increasing the standard deviation derived from the simulated intensity data.

In Figure 7.6.d), the histograms corresponding to neither I_1 nor I_2 standard deviation is centered near to the input standard deviation of 180 counts. The two intensities have different intensity standard deviation distributions as it is not the intensity gradient (g), but the prefactor of the multiplicative drift function (i.e. M_A within $A(t)$) which is fixed in this model). Hence, I_1 and I_2 do not have identical gradients in time, resulting in a greater error in measured standard deviation for the larger intensity time series.

This data suggests that, in the instance of large systemic drift and over long measurement durations, the experimentally measured intensity standard deviation can be drastically overestimated (by a factor of roughly three in Figure 7.6.d)). Overestimation of intensity standard deviation could lead to underestimation of the precision of a measurement and to unnecessarily long optical loss experiment durations. It is seen in Chapter 9 that a relatively small overestimation of intensity standard deviation could lead to relatively large overestimation of the experiment duration required to achieve some precision benchmark. Accordingly, the effect of intensity standard deviation being measured incorrectly upon the standard deviation of optical loss is examined further in Figure 7.7.

The erroneous characterisation of intensity standard deviation — such as that demonstrated in Figure 7.6.b) was used to identify the resultant erroneous identification of optical loss standard deviation. This is plotted as a function of M_A in Figure 7.7. The optical loss standard deviation which was calculated from the intensity standard deviations which were entered into the model is represented by a black dashed line. Figure 7.7 demonstrates that the standard deviation of opti-

cal loss is overestimated if systemic drift is present, and that the overestimation is worsened by both longer exposure times (and hence measurement durations) and larger absolute values of drift intensity gradient. For a 10 second exposure duration and the largest observed intensity gradient ($M_A = 2.50 \times 10^{-5}$ s^{-1}), there is an overestimation of optical loss standard deviation of 2.044 cm^{-1}.
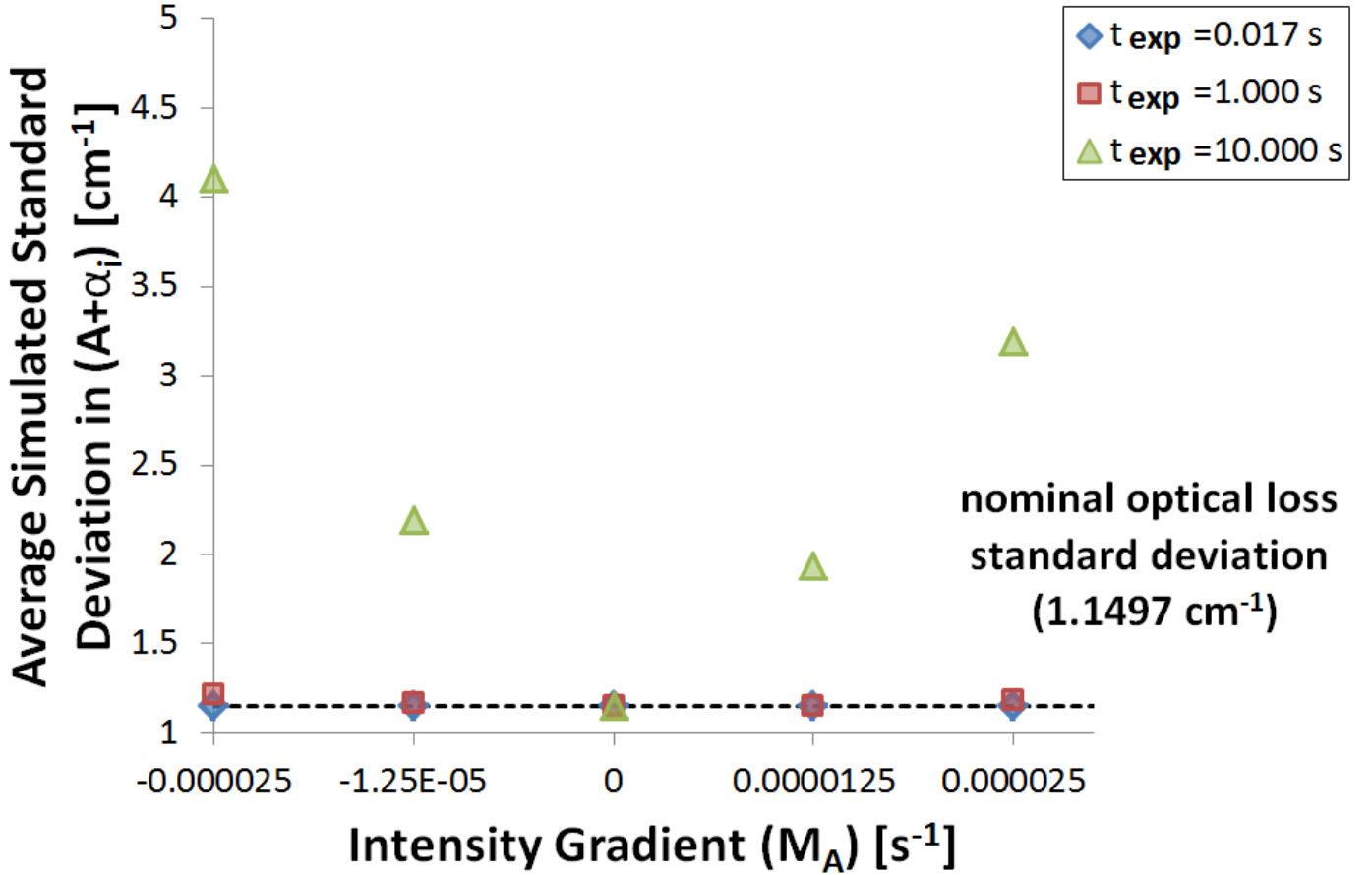
Figure 7.7: Mischaracterisation of the optical loss standard deviation based upon the intensity standard deviations derived from 1,000 simulations of the type depicted in Figure 7.6.a), as a function of intensity gradient and for various exposure durations.

As addressed in Section 9.2, the required experiment duration to reach some precision aim increases with the square of the optical loss standard deviation. This suggests an overestimation of required experiment duration by a factor of roughly

113

eight. Clearly this would be unacceptable for a very precise (and hence long) experiment. The corresponding error in standard deviation of optical loss for the shortest experimentally available exposure duration is –0.0013 cm^{-1}. This has a negligible effect on experiment duration.

It can be seen in Figure 7.7 that the error in simulated standard deviation of optical loss for negative intensity gradients is larger than that for positive intensity gradients. This is associated with the warping of the intensity distributions in being passed through the nonlinear multisection optical loss equation. (This effect is closely related to the concepts discussed in Section 7.5.1).

This analysis does not take into account the fact that longer exposure durations in a real experiment are likely to have smaller fractional standard deviation in intensity. The inclusion of this effect would not change the fact that systemic drifts in intensity will introduce systematic error in measured intensity standard deviation. The key message of this section is simply that short measurements *can* characterise intensity standard deviation more rapidly than typical systemic drifts introduces error into the value (for maximum observed values of M_A).

In summary, this section has demonstrated that large systemic drifts typical to the apparatus used in this body of work cause negligible systematic error in optical loss standard deviation measurements so long as the minimum exposure duration (0.017 seconds) is used. This must be re-assessed in the instance that uncertainty requirements become more stringent or that the method is transfered to a different apparatus. Based upon the *precision* of the assessment of optical loss standard deviation, the addition of several seconds of measurement duration onto the experiment durations that are calculated in Chapter 9 is advised. This will account for any likely error in calculated experiment duration associated with the precision in the identification of the measured optical loss standard deviation. Additionally, care should be taken in using the standard deviation of intensities determined from long (precise) optical loss measurements to quantify the precision of the produced optical loss value.

7.6 Chapter Summary

In this chapter, the modulated and conventional multisection methods for optical loss were modelled. The purpose of this model is to allow the separation of uncertainty in an optical loss measurement due to experimental scatter and both additive and multiplicative systemic drift. Having described this model, several key findings were reported.

It was determined that intensity measurements in the modulated multisection method ought to be averaged before being processed with Equation 1.16. Processing the I_1 and I_2 value determined *within each modulation cycle* to obtain a value of optical loss, and averaging these values for each modulation cycle results in a marginally larger systematic error (due to the effect of the nonlinearity of Equation 1.16 upon the noisy distribution of intensity data). The systematic error is small compared with the $\pm0.1cm^{-1}$ uncertainty aim of this project in either case, given typical intensity standard deviations observed within the apparatus used in this thesis. However, when applying the method to a different apparatus or with a more stringent uncertainty aim in future work, this distinction may be critically important.

Systematic error associated with multiplicative ($A(t)$-type) systemic drift of intensities in an optical loss measurement using the modulated and conventional multisection methods, does *not* depend upon the magnitude of the optical loss coefficient being measured. This demonstrates that the calculation of the systematic error in optical loss associated with systemic drift — carried out in Chapter 8 — needn't be repeated for various magnitudes of optical loss.

It is demonstrated in this chapter that systemic drift can cause systematic error in the evaluation of *standard deviation* of measured optical intensity. The resultant systematic error in optical loss standard deviation is shown to be negligible for the largest observed systemic drifts , provided that the measurement occurs sufficiently rapidly.

Quantifying Systematic Error in Optical Loss due to Systemic Drift

Having developed the Modulated Multisection method, an estimate of the error caused by systemic drift in a Conventional and a Modulated Multisection measurement can now be examined. Analytical expressions for the magnitude of drift error in each method will be determined in Sections 8.1 and 8.2 respectively.

By considering the error in the Modulated method as a function of the modulation period, one may determine how rapidly switching must occur in order to reduce systematic error to an acceptable low level under experimentally typical drift conditions. In particular, the improvement in drift error between the conventional and modulated multisection methods will be examined.

In this section, error values due to linear drift are determined in the form of analytical expressions. The model described in Chapter 7 is not directly used in this process. However, some of the conclusions drawn in that chapter are directly applied in the following. The analytical expressions derived in this chapter include linear functions of intensity with time. Unlike the modelling in Chapter 7, experimental scatter is not applied in this chapter.

A multiplicative systemic drift will be used in these calculations, as defined in Section 7.2. Following the conclusion of Appendix A, it is assumed that additive systemic drift has a negligible effect and will be neglected.

The critical parameter of multiplicative drift is the constant M_A, which describes the gradient of the $A(t)$ function (introduced in Equation 7.2). However, the resultant gradient of an intensity time series is of more immediate experimental relevance. In Section 7.2, this quantity is defined to be g.

In Section 7.5.2, it was demonstrated that the magnitude of systematic error in optical loss caused by multiplicative systemic drift is independent of the magnitude of the optical loss. As multiplicative drifts are considered in this section and additive drifts are neglected, $(A + \alpha_i)$ will not be used as a parameter in the following calculations of drift error.

8.1 Systematic Error due to Systemic Drifts in the Conventional Multisection Method

8.1.1 Derivation

Figure 8.1 depicts a Conventional Multisection method measurement under linear systemic drift.

Square brackets in Figure 8.1 represent the start and end of each intensity measurement. Assuming a negligible contribution from additive drift, the calculated I^1_{calc} and I^2_{calc} signals are defined (in Equation 7.1) to be:

$$
\begin{aligned}
I^1_{calc}(t) &= (M_A t + 1)I^1_{true} \\
I^2_{calc}(t) &= (M_A t + 1)I^2_{true}
\end{aligned}
\tag{8.1}
$$
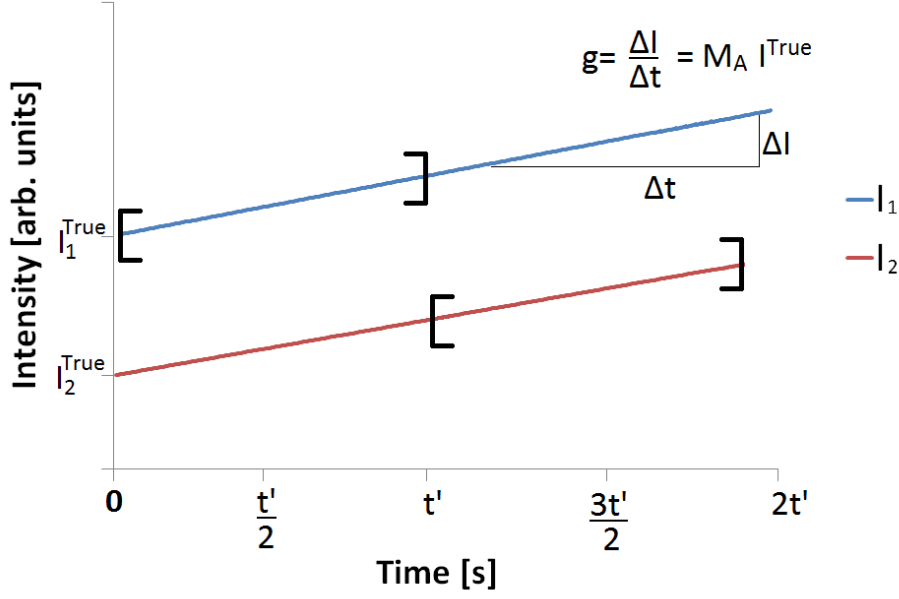
Figure 8.1: For linearly drifting intensities, the periods during which I_1 and I_2 are measured in a conventional multisection optical loss method measurement are represented by square brackets.

Given knowledge of the intensity gradient and the duration of the I_1 and I_2 measurements, one can calculate the discrepancy between the true and the measured $(A + \alpha_i)$ values. This quantity is to be described as *conventional drift error* in this thesis and is expressed with the symbol, $\Delta(A + \alpha_i)_{Conv}^{Drift}$.

M_A does not, itself, provide the gradient of $I(t)$ with respect to time, which is defined to be g (defined in Equation 7.4). Multiplying M_A by some duration, t, produces the resultant fractional change in an initial intensity over that duration. In this chapter, I will use the symbol χ to denote this product:

$$\chi = M_A t \qquad (8.2)$$

Future users of the modulated multisection method may apply plotted numerical results from this chapter to their own apparatus by calculating a χ value for typical systemic drift in their intensity measurements (provided that systemic drift is primarily multiplicative in their apparatus).

118

The 'trial 2' intensity data surrounding Figure 6.1 is representative of a substantial systemic drift over an extended period (within the apparatus in question), giving a g value of 0.11 arb units s^{-1}, an initial intensity of $13,700$ arb units and thus an M_A value of $8.0 \text{x} 10^{-6}$ s^{-1}. These values of g and M_A are typical of large systemic drifts for long experiments in my apparatus for the purposes of the following calculations.

A distinction exists between observed intensity gradients common in short experiments (up to 30 minutes) and longer experiments (greater than an hour). In particular, larger intensity gradients are common in the shorter experiments described in Chapter 9. A *large* intensity gradient in one of the measurements described in Chapter 9 corresponds to an M_A value of $2.5 \text{x} 10^{-5}$ s^{-1}. A separation is made in this chapter; calculations over timescales of several hours and those over time scales of less than an hour will use M_A values of $8.0 \text{x} 10^{-6}$ s^{-1} and $2.5 \text{x} 10^{-5}$ s^{-1} respectively.

In a typical measurement, I_1 is collected before I_2 and a period of t' is given for *each measurement*. Given linear drift, the average intensity is equal to the instantaneous intensity halfway through a measurement. Accordingly, in the case of the Conventional Multisection method, Equations 8.1 can be expressed as:

$$I_{calc}^1 = (\frac{M_A t'}{2} + 1)I_{true}^1$$
$$I_{calc}^2 = (\frac{3 M_A t'}{2} + 1)I_{true}^2$$

(8.3)

By substituting Equations 8.3 into the standard equation for Multisection optical loss (Equation 1.16), Equation 8.4 is obtained:

$$(A + \alpha_i)_{meas} = \frac{1}{L_s} \ ln \left(\frac{(\frac{M_A t'}{2} + 1)I_{true}^1}{(\frac{3 M_A t'}{2} + 1)I_{true}^2} \right)$$

(8.4)

By applying the product law of logarithms, Equation 8.5 is derived:

$$(A + \alpha_i)_{meas} = \frac{1}{L_s} \; ln \left(\frac{\frac{M_A t'}{2} + 1}{\frac{3M_A t'}{2} + 1} \right) + \frac{1}{L} ln \left(\frac{I^1_{true}}{I^2_{true}} \right) \tag{8.5}$$

Studying the form of Equation 1.16, this can be simplified to Equation 8.6:

$$(A + \alpha_i)_{meas} = \frac{1}{L_s} \; ln \left(\frac{\frac{M_A t'}{2} + 1}{\frac{3M_A t'}{2} + 1} \right) + (A + \alpha_i)_{true} \tag{8.6}$$

It is practically useful to define the error in optical loss due to linear drift in a conventional Multisection measurement, $\Delta(A + \alpha_i)^{Drift}_{Conv}$, to be the true value of optical loss subtracted from the measured value of optical loss. This results in the expression for conventional drift error given in Equation 8.7:

$$\Delta(A + \alpha_i)^{Drift}_{Conv} = \frac{1}{L_s} \; ln \left(\frac{\frac{M_A t'}{2} + 1}{\frac{3M_A t'}{2} + 1} \right) \tag{8.7}$$

In Equation 8.7, $\Delta(A + \alpha_i)^{Drift}_{Conv}$ is only a function of L_s, M_A and t'. By setting an appropriate L_s value for a given calculation, $\Delta(A + \alpha_i)^{Drift}_{Conv}$ can be uniquely defined by the product of M_A and t' – the fractional change in an intensity over the period t'.

Finally, from Equation 8.7 and 8.2:

$$\Delta(A + \alpha_i)^{Drift}_{Conv} = \frac{1}{L_s} \; ln \left(\frac{\frac{\chi'}{2} + 1}{\frac{3\chi'}{2} + 1} \right) \tag{8.8}$$

L is 300μm in all models described in this thesis. χ' identifies the fractional change in intensity over the time period for which the intensity emitted by a device section is measured, t'.

8.1.2 Results

The relationship described in Equation 8.8 is plotted in Figure 8.2. Figures 8.2.a) and 8.2.c) show calculated Drift Error in a Conventional Multisection experiment as a function of the parameter χ'. Figures 8.2.b) and 8.2.d) show calculated conventional drift error as a function of M_A and t' separately. The axis scales differ between the left-hand plots and the legend differs between the right-hand plots. Expressing this relationship in terms of χ' is useful as it provides a single expression of the degree of drift over the course of an intensity measurement. Given knowledge of the maximum magnitude of M_A likely to occur in an apparatus, Figures 8.2.a) and 8.2.c) both provide an indication of whether the adoption of the Modulated Multisection method is necessary. Separately studying this relationship through t' and M_A allows a more in-depth examination of trends in the model.

The upper pair of plots show conventional drift error for a wide range of M_A and t' values. Figures 8.2.a) and 8.2.b) describe the drift error in experiments with very high durations. These describe drifts similar to those related to the experiments described in Sections 6.1 and 8.2.4 and are useful for considering drift behaviour for the long duration experiments shown in these sections. (A χ' of ±0.28 is approximately the product of a t' of $36,000$ s and an M_A of $\pm8.0\mathrm{x}10^{-6}$ s^{-1}).

Figures 8.2.c) and 8.2.d) examine drift error in experiments with durations similar to those discussed in Chapter 9. The timescales are useful for consideration of conventional drift error for durations similar to those used in both precise measurements of optical loss (Chapter 9) and for durations similar to those used in the less precise optical loss measurements that precede this body of work (corresponding to timescales of several minutes). (A χ' of ±0.045 is the product of a t' of roughly 30 minutes and an M_A of $\pm2.5\mathrm{x}10^{-5}$ s^{-1}).
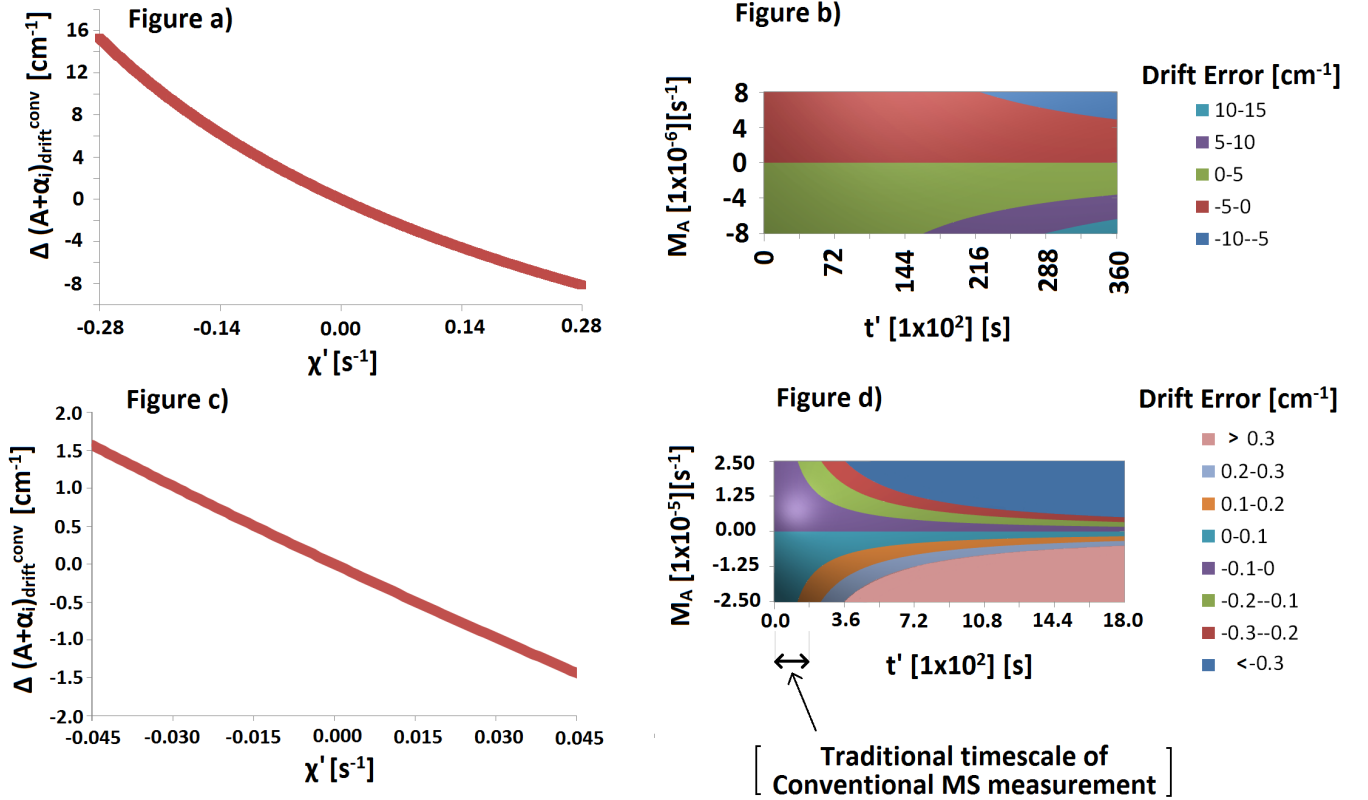
Figure 8.2: Figures 8.2.a) and 8.2.b) quantify drift error for large (but experimentally feasible) drifts. Figures 8.2.c) and 8.2.d) allow closer examination of drift error in a domain near to the 0.1 cm^{-1} uncertainty aim of this project . The left-hand figures present drift error as a function of the χ' product and the right-hand figures present drift error as a function of M_A and t' separately.

Figures 8.2.a) and 8.2.c) show the absolute value of conventional drift error due to systemic drift increasing as the absolute value of χ' increases. This follows intuitively from Equation 8.8. It can be seen from Figure 8.2.a) that the magnitude of drift error is not symmetrical for positive and negative drift gradients. This is due to the logarithm in Equation 8.8. This fact could be of experimental interest if systemic drift is more likely in a particular sign than the other in a particular apparatus.

The most important implication of Figure 8.2.a) is that drift error due to experimentally feasible extrema in χ' result in systematic errors that are far in excess

of 0.1 cm^{-1}. Significantly, these calculations suggests that a drift error of several cm^{-1} is possible over the time scales described by Figure 8.2.b) and a drift error of greater than ±0.1 cm^{-1} is possible for the time scales described by Figure 8.2.d). In a conventional multisection measurement with an uncertainty aim of ±1.0 cm^{-1}, experiment durations of several minutes are required for sufficient precision and experimentally observed values of M_A correspond to negligible drift errors of around ±0.1 cm^{-1}. If the uncertainty aim is changed to ±0.1 cm^{-1}, experiment durations of at least 20 minutes are required for sufficient precision (see Chapter 9) and drift error can exceed the uncertainty aim for experimentally observed values of M_A.

Figure 8.2.b) spans the entire range of likely drift error which an experimentalist is likely to experience. When $t' = 36,000$ s in Figure 8.2.b), the extrema of drift error are +13.74 cm^{-1} and –7.51 cm^{-1} respectively. It is unsurprising that a 10 hour experiment with a significant intensity gradient results in an extremely inaccurate measurement.

The scale of Figures 8.2.c) and 8.2.d) are determined for the purpose of designing a *Conventional* Multisection experiment in which drift error affects uncertainty by less than the ±0.1 cm^{-1} aim of this project. Considering the extrema of plotted M_A values in Figure 8.2.d), the model results in drift errors in excess of 0.1 cm^{-1} for t' values of roughly 122 seconds for either positive or negative drift. A conventional multisection measurement of optical loss cannot exceed roughly 4 minutes without a significant risk of its associated drift error exceeding ±0.1 cm^{-1}. (That is — of course — without use of the Modulated Multisection method.)

8.2 Systematic Error due to Systemic Drifts in the Modulated Multisection Method

8.2.1 Derivation

A similar analytical expression for drift error in a *Modulated* Multisection measurement can be derived. Figure 8.3 aids the understanding of this derivation.
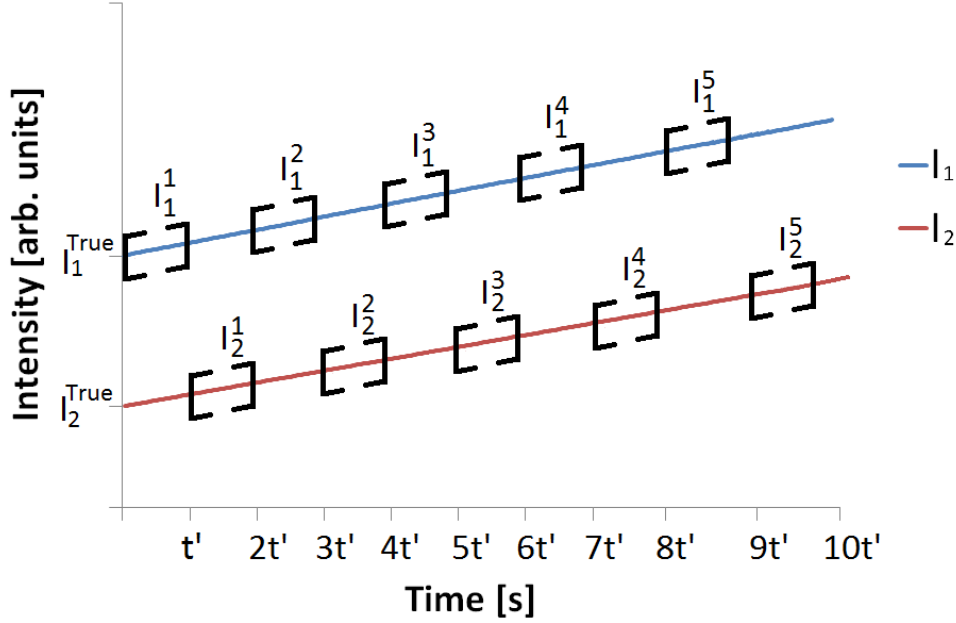
Figure 8.3: The periods during which I_1 and I_2 are measured for many cycles of a Modulated Multisection experiment.

As in Figure 8.1, the square brackets in Figure 8.3 represent the start and end of an intensity measurement. As in Section 8.1.2, the parameter t' represents the time over which a single intensity measurement takes place. However, there are many measurements of I_1 and I_2 in a Modulated Multisection experiment and hence many t' intervals. This figure is representative of the sampling described in Figure 5.3.a).

In order to determine an expression for the experimental outcome of the Modulated Multisection method, an additional parameter must be introduced to define the experiment duration. N will denote the number of pairs of I_1 and I_2 measurements. The systematic error in optical loss due to linear drift in a modulated multisection measurement is described as *modulated drift error* in this thesis, and denoted by the symbol, $\Delta(A + \alpha_i)_{Mod}^{Drift}$.

As the drift is linear, the average value of each measurement is taken to be

124

equal to the value halfway through the measurement. Optical loss is then determined through Equation 1.16 using the average I_1 and I_2 values (following from the discussion in Section 7.5.1). Determining the average value of each intensity measurement requires that the time of the midpoint (and hence resultant average) of I_1 and I_2 measurements must both be defined for all N measurement cycles. In Figure 8.3, it is seen that the midpoints of the nth I_1 and I_2 measurements respectively occur at a time defined by Equation 8.9.

$$
\begin{aligned}
t_1^n &= \frac{(4n-3)t'}{2} \\
t_2^n &= \frac{(4n-1)t'}{2}
\end{aligned}
\tag{8.9}
$$

By substituting these time values into Equations 8.1, a general expression for the average value of the nth I_1 and I_2 measurement can be calculated:

$$
\begin{aligned}
I_1^n &= I_{True}^1 \left(1 + M_A \frac{(4n-3)t'}{2} \right) \\
I_2^n &= I_{True}^2 \left(1 + M_A \frac{(4n-1)t'}{2} \right)
\end{aligned}
\tag{8.10}
$$

For N I_1 and I_2 pairs, the average intensity values can be defined as I_{ave1}^N and I_{ave2}^N respectively:

$$
\begin{aligned}
I_{ave1}^N &= \frac{\displaystyle\sum_{n=1}^{N} I_{True}^1 \left(1 + M_A \frac{(4n-3)t'}{2} \right)}{N} \\
I_{ave2}^N &= \frac{\displaystyle\sum_{n=1}^{N} I_{True}^2 \left(1 + M_A \frac{(4n-1)t'}{2} \right)}{N}
\end{aligned}
\tag{8.11}
$$

By observing that the sums in Equations 8.11 constitute the sums of arithmetic

series we hence arrive at equations 8.14:

$$I_{ave1}^N = \frac{I_{True}^1}{2N} \left(2 + \frac{M_A(4N-2)t'}{2} \right) \tag{8.12}$$

$$I_{ave2}^N = \frac{I_{True}^2}{2N} \left(2 + \frac{M_A(4N+2)t'}{2} \right) \tag{8.13}$$

$$\tag{8.14}$$

By substituting into Equation 1.16 we find Equation 8.15:

$$(A + \alpha_i)_{Meas} = \frac{1}{L_s} \ ln \left(\frac{I_{True}^1}{I_{True}^2} \frac{2 + \frac{M_A(4N-2)t'}{2}}{2 + \frac{M_A(4N+2)t'}{2}} \right) \tag{8.15}$$

and hence Equation 8.16:

$$(A + \alpha_i)_{Meas} = \frac{1}{L_s} \ ln \left(\frac{2 + \frac{M_A(4N-2)t'}{2}}{2 + \frac{M_A(4N+2)t'}{2}} \right) + (A + \alpha_i)_{True} \tag{8.16}$$

Modulated drift error, $\Delta(A + \alpha_i)_{Mod}^{Drift}$, is given by Equation 8.16. This results in Equation 8.17:

$$\Delta(A + \alpha_i)_{Mod}^{Drift} = \frac{1}{L_s} \ ln \left(\frac{2 + \frac{M_A(4N-2)t'}{2}}{2 + \frac{M_A(4N+2)t'}{2}} \right) \tag{8.17}$$

It is sensible to express this equation in terms of the time parameters which are most relevant to real experiments: the total experiment duration, t_{exp}, and the duration of a switching cycle, t_{mod}. These relate to t' and N as described by Equation 8.18:

$$t_{mod} = 2t'$$
$$t_{exp} = 2Nt' \tag{8.18}$$

and hence Equation 8.19 is derived:

$$\Delta(A + \alpha_i)_{Mod}^{Drift} = \frac{1}{L_s} \; ln \left(\frac{4 + M_A(2t_{exp} - t_{mod})}{4 + M_A(2t_{exp} + t_{mod})} \right) \tag{8.19}$$

Equation 8.19 could be used to compare the modulated drift error corresponding with experiments of the same total duration for different modulation periods.

As in Section 8.1.2, one may choose to simplify the argument of the natural logarithm by defining the following parameters:

$$\chi_{mod} = M_A t_{mod}$$
$$\chi_{exp} = M_A t_{exp} \tag{8.20}$$

As these χ quantities represent fractional changes in intensity per unit time multiplied by a time variable, they represent the fractional change which occurs throughout a single modulation period and throughout the entire experimental duration respectively. This is useful as it allows an experimentalist to intuitively relate the findings of the model in this chapter to the parameters from real experiments.

By substituting Equations 8.20 into Equation 8.19, Equation 8.21 is derived:

$$\Delta(A + \alpha_i)_{Mod}^{Drift} = \frac{1}{L_s} \; ln \left(\frac{4 + 2\chi_{exp} - \chi_{mod}}{4 + 2\chi_{exp} + \chi_{mod}} \right) \tag{8.21}$$

In Equation 8.21, $\Delta(A + \alpha_i)_{Mod}^{Drift}$ is a function of L_s, χ_{mod} and χ_{exp}. By setting an appropriate L_s value for a given calculation, $\Delta(A + \alpha_i)_{Conv}^{Drift}$ can be examined as a function of the two χ parameters. L_s is 300 μm in all models shown in this thesis.

Equation 8.21 indicates that modulated drift error is small when χ_{mod} is small in comparison with $(4 + 2\chi_{exp})$. As the same M_A acts upon both χ parameters, modulated drift error tends to zero as t_{mod} decreases (for an experiment of a particular duration and a particular systemic drift). This agrees with the intuition that the effect of systemic drift upon optical loss measurements can be overcome with sufficiently rapid modulation. The conditions in which modulated drift error

is kept sufficiently small is examined in Section 8.2.2.

The L_s dependence of systematic errors described by Equations 8.8 and 8.21 suggests that drift related error may be reduced through the use of longer section lengths. It is shown in Section 8.2.3 that this is not necessary for the measurement of this sample upon this apparatus. If a future experiment had more stringent optical loss uncertainty requirements, required longer experiment durations or had to be carried out upon an apparatus which was more susceptible to systemic drift, drift error could be reduced by the application of longer device section lengths. (Although the effect that the resultant decrease in measured I_2 has on precision and experiment duration would have to be carefully considered. Refer to Chapter 9 for an example of analysis of precision in the measurement of optical loss coefficients).

8.2.2 Results

Equation 8.21 is plotted in Figure 8.4. As explained in Section 8.1.2, different maximum intensity gradients are applied to long experiments (roughly 10 hours) and experiments whose durations are optimised for precise measurement of optical loss (up to 30 minutes). Typical values of χ_{exp} for long experiment durations were taken from the 'Trial 2' data of the experiment described surrounding Figure 6.1. From an M_A value of $8.0\text{x}10^{-6}$ s^{-1} and a maximum experiment duration of 10 hours, a maximum χ_{exp} of 0.28 was calculated. The initial intensity values were taken from Figure 6.1. An M_A value of $2.5\text{x}10^{-5}$ s^{-1} is used to typify large systemic drift intensity over timescales of the order of 30 minutes. Figure 8.4 examines the case of 10 hour experiments in order to establish the general properties of Equation 8.21, before these 'long' and 'short' timescales are examined in detail in Figure 8.5. The 2nd and 4th quadrant data corresponds with the unphysical cases in which χ_{mod} and χ_{exp} are of different signs. Data for values of χ_{mod} exceeding the corresponding value of χ_{exp} in not plotted as the modulation period clearly cannot exceed the experiment duration. These regions have been assigned modulated drift error values of zero.As in the previous results section, an experimentalist may relate

values of χ_{mod} and χ_{exp} which are likely to occur in their own apparatus to values of drift error in their experiments.
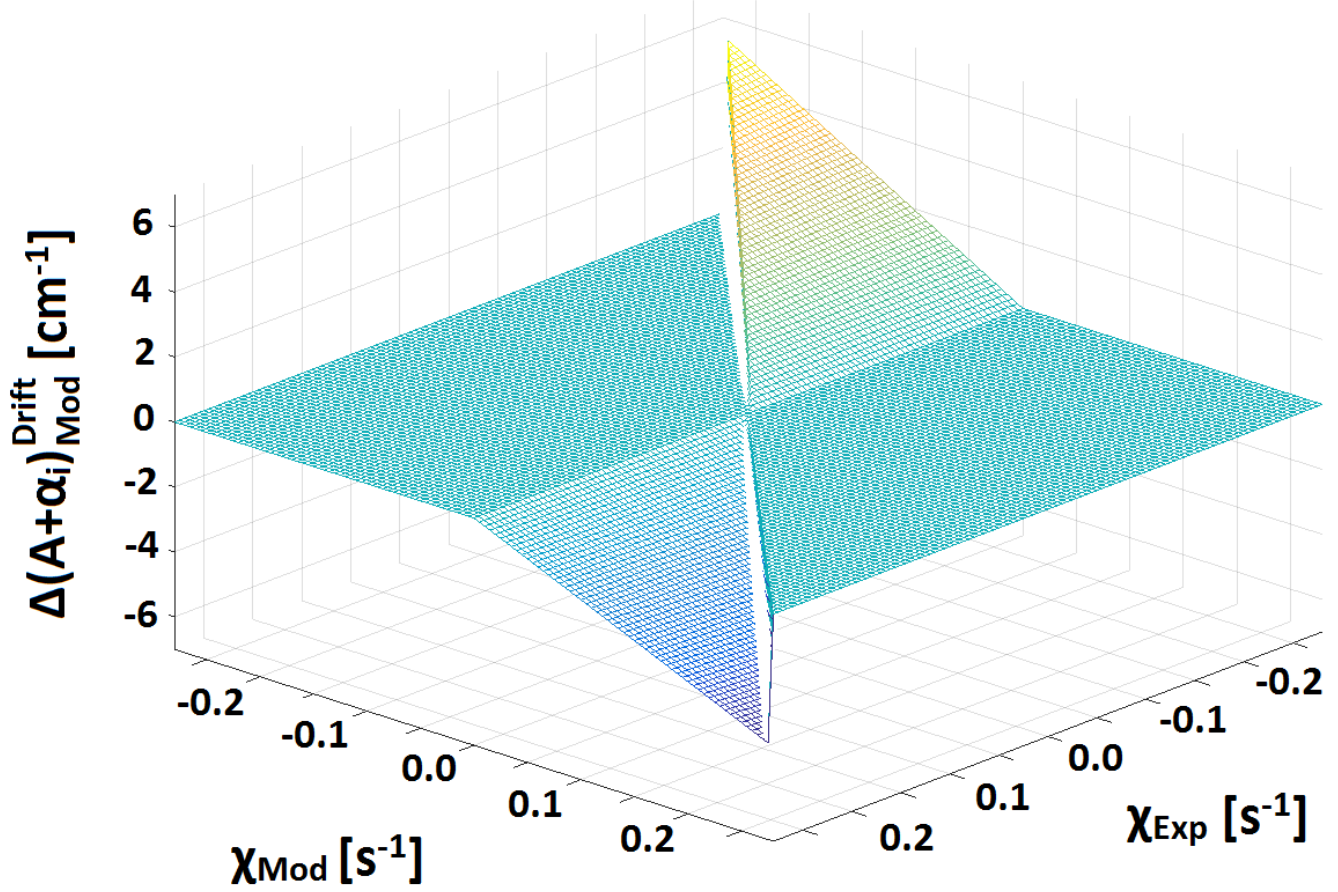
Figure 8.4: Calculated drift error as a function of χ parameters.

A key feature of the data shown in Figure 8.4 is that modulated drift error can be seen to decrease with decreasing absolute value of χ_{mod}. The implication of this is that, for a particular intensity gradient, modulated drift error can be reduced to arbitrarily small values so long as the modulation period is not limited by the apparatus. Modulated drift error does not change as drastically as one varies χ_{exp} for a particular χ_{mod}. This is due to the fact that an approximately equal drift error is generated in consecutive modulation periods of equal length for a fixed intensity gradient. However, for a fixed χ_{mod}, large increases in the absolute value

of χ_{exp} (i.e. in the experiment duration) slightly reduce the drift error for positive intensity gradients, and increase error for negative intensity gradients. The fundamental reason for this is that I_1 and I_2 in a particular modulation cycle are not measured simultaneously (see Equations 8.9). While the intensity gradient is fixed, the fractional difference in I_1 and I_2 measurements separated by half of a modulation cycle is not constant.

The edge of the plotted area defined by the line, $\chi_{mod} = \chi_{exp}$, describes the case of a conventional multisection optical loss measurement. By substituting Equations 8.18 into Equation 8.21 and setting N equal to 1 , the conventional drift error equation (Equation 8.8) is recovered.

Figure 8.4 demonstrates broad trends of the mathematical model. Figure 8.5 demonstrates the dependence of modelled drift error upon the experiment duration (t_{exp}) and modulation period (t_{mod}) for a typical *large* value of intensity drift gradient in the apparatus used in this thesis. This follows the relationship described in Equation 8.19. In Figure 8.5.a), a range of modulation periods was chosen to examine the occurrence of drift errors of the order of the 0.1 cm^{-1} uncertainty aim of this project in an arbitrarily long – 10 hour – experiment. As in the previous section, an M_A magnitude of 8.0×10^{-6} s^{-1} was taken to typify *large systemic drifts* over these timescales. In Figure 8.5.b), experiment durations and modulation periods that are similar to those discussed in Chapter 9 are examined. Accordingly, a larger M_A magnitude of 2.5×10^{-5} s^{-1} is used in this figure. The calculated values shown in the figure correspond with negative values of M_A. The difference in absolute value of drift error due to the choice of sign of M_A is negligible for drift errors below around 1.0 cm^{-1}. The small region of missing values of modulated drift error near to the t_{mod} axis correspond with experiment durations which are smaller than a single modulation period – and hence experimentally impossible.

As in Figure 8.4, these plots show that increasing the modulation period for a particular experiment duration increases the magnitude of drift error. As the M_A is negative in this calculation, increasing the experiment duration for a particular modulation period increases the resultant drift error.
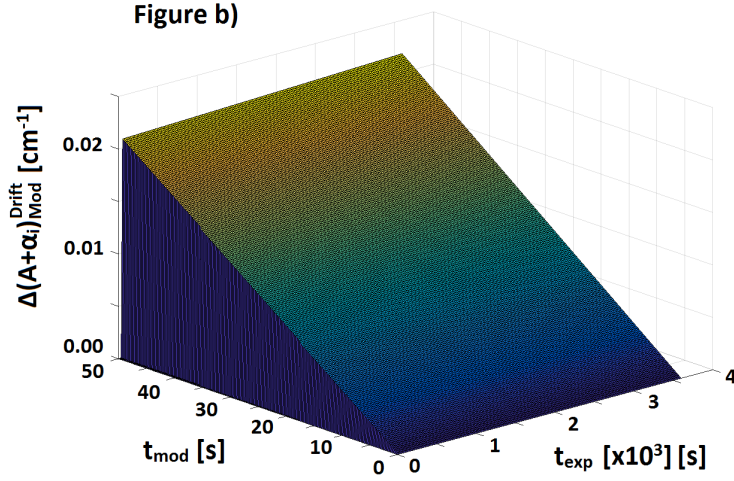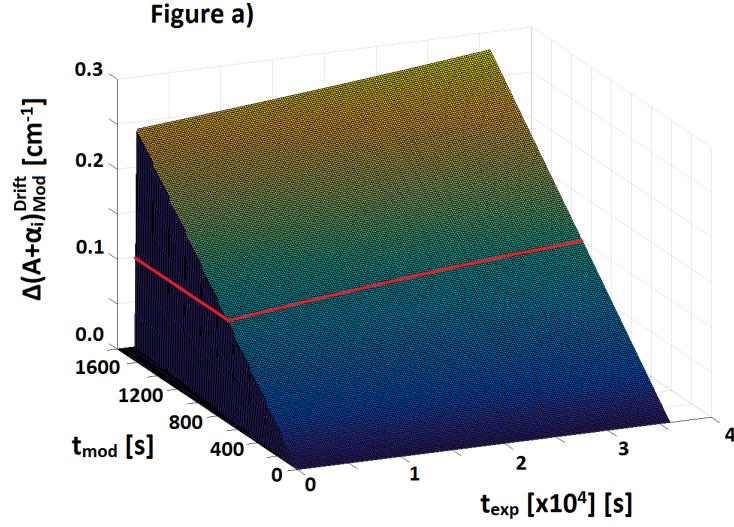
Figure 8.5: Calculated Modulated drift error for a large systemic drift is plotted against the experiment duration and modulation period for two different ranges. Figure 8.5.a) examines time scales which produce drift error of the order of 0.1 cm^{-1} (the uncertainty aim of this project). The red line on the surface demonstrates a modulated drift error of 0.1 cm^{-1}. Figure 8.5.b) examines time scales similar to those discussed in Chapter 9.

Figure 8.5.a) suggests that — for a particular experiment duration — there exists some maximum value of modulation period above which modulated drift error is likely to exceed ± 0.1 cm^{-1} for typical large systemic drifts within the apparatus

described in this thesis. The identification of this maximum modulation period and hence practical guidelines for the application of the modulated multisection method for optical loss are carried out in Section 8.2.3.

8.2.3   Considering a Maximum Modulation Period

In order to determine the maximum modulation period for which the 0.1 cm^{-1} uncertainty aim of the project may be met, the value of t_{mod} at which modulated drift error exceeds ± 0.1 cm^{-1} and ± 0.03 cm^{-1} were examined for many experiment durations. These two threshold values of modulated drift error respectively demonstrate the value of t_{mod} where systematic error is equal to the uncertainty aim of the project and where systematic error becomes *small* compared with the uncertainty aim of this project. Positive and negative instances of the largest observed systemic drift magnitude ($M_A = 2.5 \times 10^{-5}$ s^{-1}) are examined such that the resultant drift error is indicative of the maximum drift error that is likely to be observed. The outcome of these calculations is plotted in Figure 8.6.

It is observed in Figure 8.4 that, for a particular modulation period, modulated drift error increases with increasing experiment duration for negative values of M_A. In Figure 8.6, this results in a reduction — as a function of experiment duration — in the modulation period at which modulated drift error exceeds a threshold value. Hence the ultimate limits to the maximum values of modulation period which can be used in a real experiment are described by the calculations in Figure 8.6 which correspond with *negative M_A* values.

The experiment duration required to reach the precision aim of this project is found to be of the order of 30 minutes in Chapter 9. This significant value of t_{exp} is marked with a dashed grey line. The larger values of experiment duration plotted in Figure 8.6 allow comparison with experimental data such as that shown in Sections 6.1 and 8.2.4.
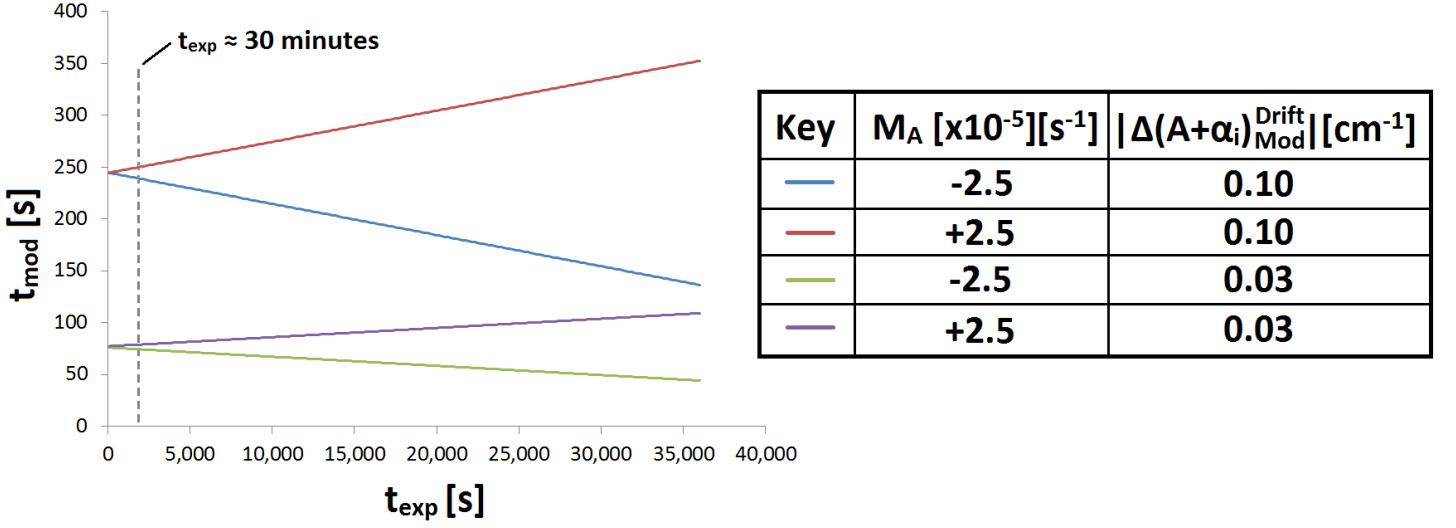
Figure 8.6: The value of modulation period for which modulated drift error exceeds significant threshold values plotted as a function of experiment duration.

The blue and green lines in Figure 8.6 can be seen to govern the maximum value of t_{mod} for which modulated drift error is less than a 0.1 and a 0.03 cm^{-1} threshold respectively. The key finding of this section is that a modulation period of roughly 150 seconds is sufficient such that modulated drift error remains less than ± 0.1 cm^{-1}, for experiment durations up to 10 hours. Similarly, a modulation period of 239 seconds fulfills this requirement for an experiment duration of 30 minutes. For a threshold value of modulated drift error of ± 0.03 cm^{-1}, experiments of 10 hour and a 30 minute durations correspond to maximum modulation periods of 44 and 74 seconds respectively. Following this finding, modulation periods are of the order of seconds in the precise measurements documented in the latter chapters of this thesis.

The minimum experimentally available modulation period is approximately 0.054 seconds. Therefore, the suppression of drift error by the modulated multi-section method for optical loss is experimentally viable for the purpose of reaching a ± 0.1 cm^{-1} uncertainty aim. Figure 8.6 demonstrates that modulation periods much larger than 0.054 seconds can be used with acceptable degrees of resultant drift error. This finding allows flexibility in the optimisation of modulation period

133

with respect to rapidly acquiring *precise* optical loss coefficients (carried out in Chapter 9).

8.2.4 Studying Drift Error in Experimental Data

By selectively sampling measured I_1 and I_2 experimental intensity time series, the effect of varying the modulation period may be simulated within a particular set of experimental data. This approach was taken – rather than repeating similar experiments with differing modulation periods – as the time dependent behaviour of intensity time series cannot be expected to be reproduced in different experiments.

Figure 8.7 demonstrates the binning of measured I_1 and I_2 intensities (of a particular photon energy). In standard data analysis, *each I_1 and I_2 data point is respectively averaged* and then processed using Equation 1.16 to produce an optical loss coefficient. This approach is demonstrated schematically in Figure 8.7.a). Blue and red crosses represent I_1 and I_2 measurements in a modulated multisection method experiment. Blue and red pulses represent that a data point is used in processing. Figures 8.7.b) and 8.7.c) represent cases in which *not all of the measured intensity data* is processed. I describe this processing as the '*binning*' of intensity data.

For a bin size of b, the first b I_1 data points are averaged and the first b I_2 data points are discarded. The second b I_2 data points are then averaged and the second b I_1 data points are discarded. This pattern is alternated throughout the entire data set. For example, Figures 8.7.b) and 8.7.c) represent b values of two and seven respectively.
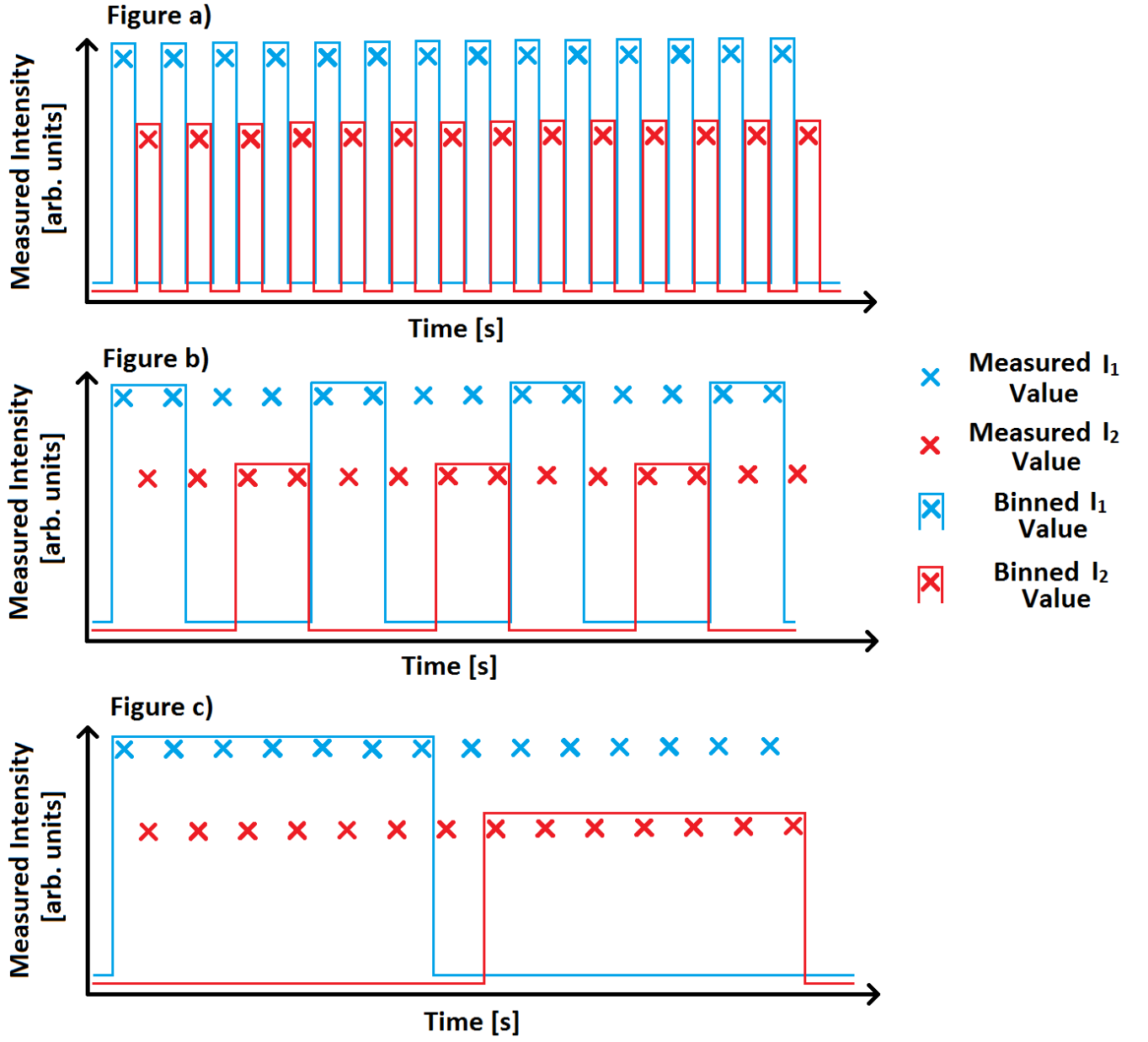
Figure 8.7: The demonstration of effectively changing the modulation period within a measured I_1 and I_2 intensity time series by application of alternating periodic binning is described.

Values of b are chosen such that an integer number of I_1 and I_2 bin pairs span the raw intensity data sets. The periodic acceptance and rejection of intensity data between different bin sizes is comparable to carrying out modulation experiments

with different modulation periods. A modulation period, t_{mod}, is determined for each bin size based on the periodicity of the binning. This period is equal to two times the bin size multiplied by the modulation period of the raw data. It is noted that some precision is lost in this measurement due to the discarded data. However, exactly half of the data is discarded for both I_1 and I_2 so — other than the systemic drift related systematic error which I am investigating — no systematic error is introduced in this process. (For this reason, the analysis implied by Figure 8.7.a) is *not* equivalent to binning with a *b* value of one, as no data is discarded).

It is informative to study extreme values of modulation period. Accordingly, intensity data was acquired with as short a modulation period as the apparatus allows (approximately 0.054 seconds). This allows access to very low values of t_{mod}. Conversely, a long total experiment duration allows access to large values of t_{mod} in this analysis. $720,000$ modulation cycles are acquired such that the total experiment duration was 8 hours. The analytical expression for modulated drift error, derived in this chapter, is then compared with these experimental findings. The intensity measurements for each modulation cycle are shown in Figure 8.8.

In a 0.054 second modulation cycle, there is an exposure time of 0.017 seconds (including CCD readout time) for each device section. The additional 0.02 seconds is made up by two 0.01 second *switching periods* built into the program, such that measurements are not made as the relay is switching. A drive current of 80 mA at 18 kHz was used. A current pulse width of 1.2 μs was used with a gate width of 1.0 μs. This experiment was carried out upon a device of type $\#1_{BA}$.
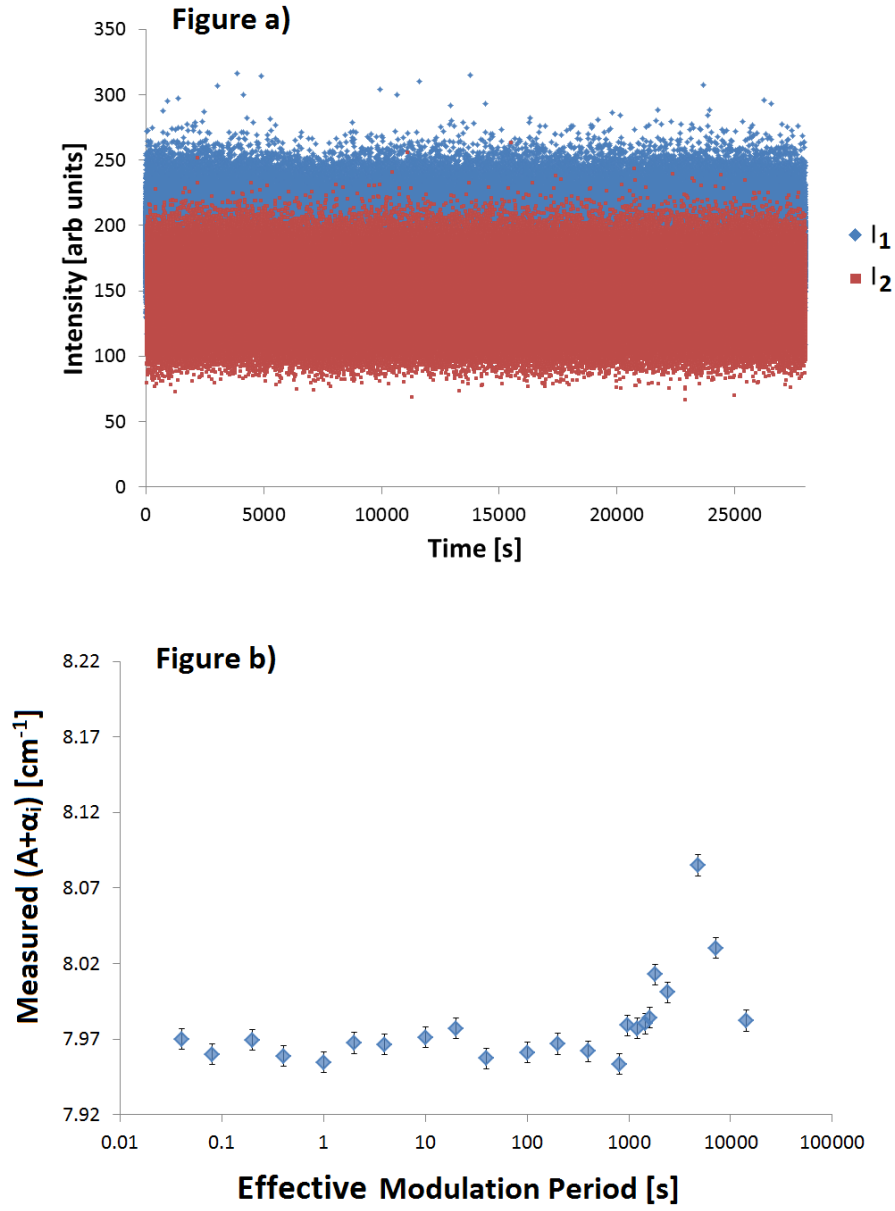
Figure 8.8: Figure 8.8.a) shows experimental intensity times series which rapidly alternates between I_1 and I_2. Figure 8.8.b) shows optical loss calculated from the intensities demonstrated in Figure 8.8.a) using various 'binned' modulation periods (as illustrated in Figure 8.7.

Figure 8.8.b) demonstrates the effect of binning data into various 'effective modulation periods' upon the acquired optical loss coefficients using the experi-

mental intensity time series shown in Figure 8.8.a).

For low values of modulation period, the deviation around the average value of measured optical loss is comparable to the standard error (once half of each intensity time series is discarded in the binning process). This standard error is denoted by error bars in Figure 8.8. For modulation periods greater than around $1,000$ seconds, the measured value of optical loss increases greatly. This occurs as, the less frequently modulation between device sections occurs, the greater the fractional change in intensity that a particular systemic drift will cause within each switch cycle.

Interpretation of this data is complicated by the presence of a slight bowing of the intensity time series. It can be seen that the measured optical loss coefficients corresponding to the two largest values of bin size decrease towards the average value for small bin sizes. The I_1 and I_2 time series have negative fractional intensity gradients (M_A) of -2.25×10^{-6} and -2.21×10^{-6} s^{-1} respectively. Taking a moving average of these intensity time series demonstrates that this is largely due to a substantial decrease in intensity between roughly $6,000$ and $7,000$ seconds on the time axis.

If the intensity time series had varied monotonically, higher switch cycle durations would correspond with higher systematic errors. As real, experimental intensity time series are not perfectly linear, they can affect resultant drift error in complicated ways. However, this effect is related to the regions of the intensity time series from which I_1 and I_2 data is *sampled*, and can be avoided by sampling intensity data as regularly as possible throughout the experiment duration. This can – of course – be achieved through use of rapid modulation.

In Figure 8.9, the experimental data of Figure 8.8 is compared with the drift error model (described in Section 8.2.2). For the appropriate experiment duration, the modulated drift error was calculated for a range of modulation periods based upon the average intensity gradient of the intensity time series in Figure 8.8.a). This corresponds to an M_A value of -2.23×10^{-6} s^{-1}. Modulated drift error as a

function of modulation period was added to the optical loss measurement (averaged over the 6 lowest switch cycle durations, where drift error is not expected to affect the observed value).
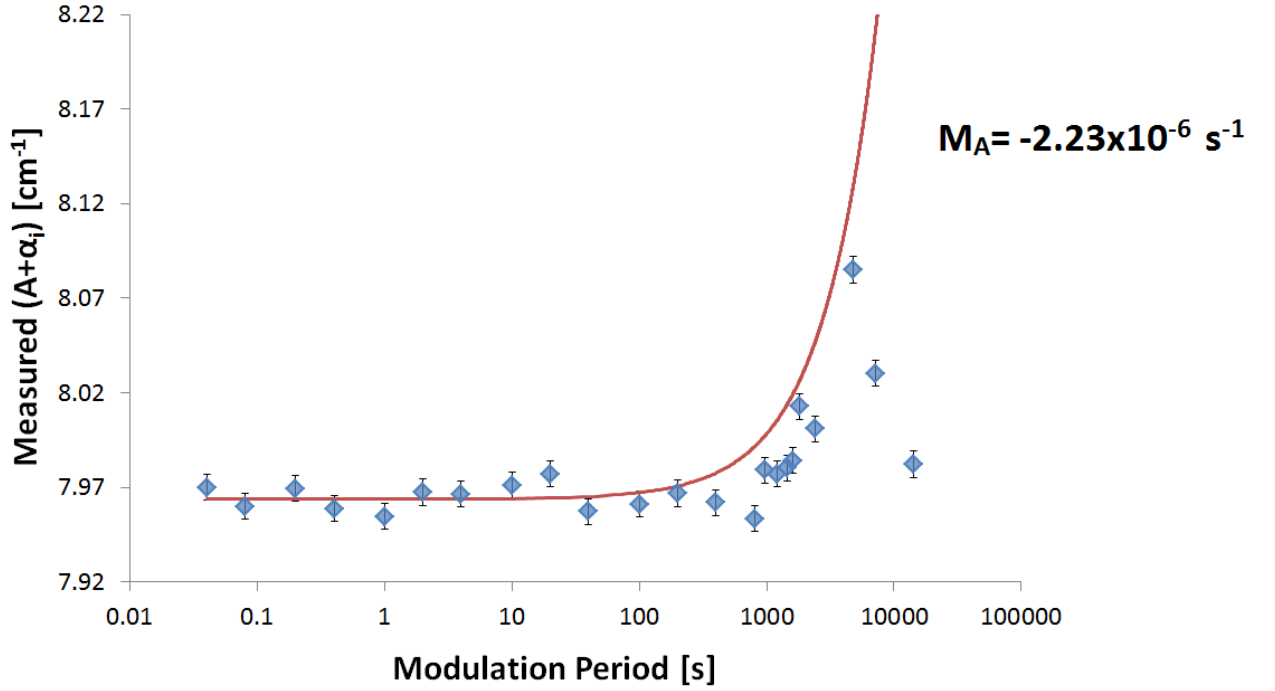
Figure 8.9: The data previously plotted in Figure 8.8 is plotted alongside the modelled dependence of modulated drift error upon modulation period (based upon Equation 8.19) for the average M_A intensity gradient of the I_1 and I_2 time series.

In spite of the non-linear behaviour of the intensity time series and experimental uncertainty, the modelled drift error corresponding with the average measured M_A reproduces the trend in the experimental drift error well (excluding the points for which drift error has been reduced by the bowing of the intensity time series). Increasing the modulation period increased the modulated drift error in this experiment, as suggested by the observations seen in Section 8.2.2.

8.2.5 Chapter Summary

In this chapter, it has been shown that, by taking a sufficiently short modulation period, drift error can be reduced to negligible values for the range of intensity gradients which are common to the apparatus used in this thesis. In particular, the modulation period can be reduced to make modulated drift error small with respect to the corresponding error in a conventional multisection measurement of the same duration.

The dependence of modulated drift error in optical loss upon modulation period has been established. In Figure 8.6, it is shown that a modulated drift error of less than ± 0.03 cm^{-1} — and hence small compared with the ± 0.1 cm^{-1} uncertainty aim of this project — can be achieved in a sufficiently precise ($t_{exp} = 30$ minute) experiment by using a modulation period no greater than 74 seconds. Modulation periods that are three orders of magnitude shorter than this threshold value are possible using the apparatus used in this thesis. It is demonstrated that drift error in the modulated method can be sufficiently suppressed with respect to a ± 0.1 cm^{-1} uncertainty aim.

An additional strength of the modulated multisection method is that, in rapidly switching between device sections, an I_1 and I_2 intensity time series is generated in the natural course of the measurement (provided that the measured intensity in each switch cycle is saved separately). This may be used to quantify the drift error associated with a particular set of experimental data. If intensity gradients — and their associated drift errors — are found to drastically vary within a particular apparatus then it is sensible to use these intensity time series to directly estimate the drift error associated with a given set of data. This would be especially useful in the instance of an experimentalist using the modulated multisection method in a situation where *very* high uncertainty is required, intensity gradients vary much more drastically than those described in this thesis or it is unfeasible to modulate between sections sufficiently rapidly. A modulated drift error could be associated with a measurement of optical loss, based upon the primary intensity data, and this information used to assess the quality of a particular measurement.

If, rather than a drift in detector sensitivity ($A(t)$) or background ($B(t)$), $(A+\alpha_i)$ systematically changes over the course of an experiment due, for instance, to fluctuations in device temperature, then a systematic change in the measured value will occur regardless of modulation period. If the timescale of such behaviour is long compared with the experiment duration, then an accurate measurement of the optical loss at the time of the experiment is made. Otherwise, the measured optical loss is some average of the value over the course of the experiment. This issue of variability of measured optical loss in the modulated multisection method is further discussed in the context of experimental data in which the ± 0.1 cm^{-1} precision aim of the project has been met in Chapter 9.

CHAPTER 9

Precision in the Modulated Multisection method

9.1 Defining Precision in the Modulated Multisection method

The focus of this thesis up to this point has been on the effect of systematic error upon the uncertainy of measured values of optical loss within the multisection method. Naturally, the precision of the measurement also has a crucial contribution. In order to realise the aspiration of an optical loss uncertainty smaller than ± 0.1 cm^{-1}, precision — and its relationship with required experiment duration — must be examined. The purpose of this chapter is to examine the relationship between the minimum experiment duration in which the optical loss can be measured sufficiently precisely and various experimental parameters, such that experiment duration may be minimised. It was observed in Chapter 8 that the drift error in a modulated multisection optical loss measurement is largely governed by the modulation period, and that there is only a small dependence upon the chosen experiment duration. In considering precision, acceptable limits on experiment duration will be introduced. The systematic error described in Chapter 3 is acknowledged in the measurements carried out in this chapter, but will not be corrected herein.

The average value of a series of experimental measurements of some sample size, N_{total}, — in nominally identical conditions — has an associated characteristic sampling distribution. The standard deviation of such sampling distributions will be used to quantify the precision of optical loss measurements in this chapter. This quantity is also described as the standard error of the mean.

The standard deviation from the mean of such an optical loss sampling distribution, $\sigma_{SEM}^{(A+\alpha_i)}$, is defined with respect to the sample size and the standard deviation from the mean of a single measurement, $\sigma_{SD}^{(A+\alpha_i)}$, by Equation 9.1:

$$\sigma_{SEM}^{(A+\alpha_i)} = \frac{\sigma_{SD}^{(A+\alpha_i)}}{\sqrt{N_{total}}} \tag{9.1}$$

By relating experimentally measured values of standard deviation — in different experimental conditions — to the time taken to accumulate N_{total} samples, the precision of an experiment can be related to its total duration t_{total}.

The duration of each modulation period within the modulated multisection method, t_{cycle}, is described in Equation 9.2:

$$t_{cycle} = 2(m(t_{exposure} + t_{read}) + t_{switch}) \tag{9.2}$$

$t_{exposure}$ is defined to be the duration of each exposure of the ICCD array. t_{read} is the readout time of the CCD array. (t_{read} for standard settings of the apparatus described in this thesis is 0.007 seconds). t_{switch} is the time allocated for switching time in each modulation cycle. t_{switch} is set to a value of 0.01 seconds in the program which controls the relay. This may differ for future users of the Modulated Multisection method using a different kind of relay to switch sections. $t_{exposure}$ and t_{read} are considered separately in this chapter, due to their fundamentally different roles with respect to the precision of an experiment. In other chapters of this thesis, read-out time is included in stated values of $t_{exposure}$. m is the number of I_1 and I_2 measurements taken between relay switches (first introduced in Fig-

ure 5.3). This parameter can be important in determining experiment durations as switching time can constitute a relatively large fraction of each total modulation period duration for short exposure times. Taking several measurements of each section between relay switches increases the modulation period and hence the magnitude of modulated drift error, but results in precision being accrued more rapidly. The factor of 2 exists as each device section is measured m times in each modulation period and the state of the relay is switched twice.

The total duration of a series of measurements is equal to the duration of a single measurement cycle multiplied by the number of cycles in the series. As such t_{total} can be expressed as shown in Equation 9.3:

$$t_{total} = N_{cycle} \ t_{cycle} \tag{9.3}$$

The total number of intensity measurement *pairs* (and hence optical loss measurements) in an experiment, N_{total}, is equal to the number of cycles multiplied by the number of measurement pairs within each cycle. This is expressed in Equation 9.4.

$$N_{total} = m \ N_{cycle} \tag{9.4}$$

Substituting the expression for N_{cycle} produced by Equation 9.3 into Equation 9.4 results in Equation 9.5.

$$N_{total} = \frac{m \ t_{total}}{t_{cycle}} \tag{9.5}$$

This expression for the total number of measurements can be substituted into Equation 9.1 to describe precision as a function of time parameters as shown in Equation 9.6.

$$\sigma_{SEM}^{(A+\alpha_i)} = \sigma_{SD}^{(A+\alpha_i)} \sqrt{\frac{t_{cycle}}{m \ t_{total}}} \tag{9.6}$$

This is a useful expression. However, as experiment duration is the primary interest of this investigation, Equation 9.6 is rearranged in terms of total duration of the

series of measurements in Equation 9.7:

$$t_{total} = \left(\frac{\sigma_{SD}^{(A+\alpha_i)}}{\sigma_{SEM}^{(A+\alpha_i)}} \right)^2 \frac{t_{cycle}}{m} \tag{9.7}$$

Equation 9.7 gives an expression for the duration required to achieve a *precision* of $\sigma_{SEM}^{(A+\alpha_i)}$. In this chapter, the behaviour of $\sigma_{SD}^{(A+\alpha_i)}$ is examined as a function of experimental parameters of the apparatus such that the experiment duration, t_{total}, required to reach some degree of precision, $\sigma_{SEM}^{(A+\alpha_i)}$, can be identified.

9.2 Quantification of Precision within a particular apparatus

The steps outlined in this section describe the application of Equation 9.7 to the behaviour of a real experimental apparatus. Similar steps could be taken to apply these arguments to a general measurement system.

The statistical distribution of optical loss measurements is the primary concern of this investigation. However, the behaviour of the intensity measurements which constitute an optical loss measurement allow more direct examination of the behaviour of the system.

In order to relate Equation 9.7 to intensity distributions, it is necessary to relate their standard deviations to the standard deviation of an optical loss measurement $\sigma_{SD}^{(A+\alpha_i)}$. It is important to observe that, within Equation 9.7, both t_{cycle} and $\sigma_{SD}^{(A+\alpha_i)}$ depend upon the duration of a single intensity measurement, $t_{exposure}$.

Through the application of standard error propagation to Equation 1.16, Equation 9.8 is derived:

$$\sigma_{SD}^{(A+\alpha_i)} \approx \frac{1}{L_S} \sqrt{ \left(\frac{\sigma_{SD}^{I_1}}{I_1} \right)^2 + \left(\frac{\sigma_{SD}^{I_2}}{I_2} \right)^2 } \tag{9.8}$$

145

Parameter	Standard Value	Measured Values
Frequency	500Hz	100, 200, 500, 1000, 1500, 2000 Hz
Gate Width	100 ns	50, 100, 200, 300, 400 ns
Exposure Time	0.1 s	0.01, 0.05, 0.1, 0.2, 0.3, 0.4 s
Pulse Current	50 mA	10, 20, 50, 100, 150 mA

Table 9.1: Table of parameters used in characterisation of intensity standard deviation.

$\sigma_{SD}^{I_1}$ and $\sigma_{SD}^{I_2}$ are defined as the standard deviation from the mean of a series of measurements of I_1 and I_2 intensities respectively. Following the form of Equation 9.8, the standard deviation in a measured intensity divided by the intensity itself is an important quantity. This quantity is described by the term '*fractional standard deviation*' within this thesis. The approximation shown in Equation 9.8 is shown to be reasonable in Appendix B.2. Experimentally, the standard deviation of a large sample of intensitiy measurements is taken to approximately be the population standard deviation. Covariance is not included in Equation 9.8, as the dependence of I_2 upon I_1 is handled explicitly in this chapter and the scatter in values corresponding to standard deviation is assumed to not influence this dependence.

Substituting Equation 9.8 into Equation 9.7 results in Equation 9.9:

$$t_{total} \approx \left(\frac{1}{\sigma_{SEM}^{(A+\alpha_i)} L_S} \right)^2 \frac{t_{cycle}(m, t_{exposure})}{m} \left[\left(\frac{\sigma_{SD}^{I_1}}{I_1} \right)^2 + \left(\frac{\sigma_{SD}^{I_2}}{I_2} \right)^2 \right] \quad (9.9)$$

Observation of the standard deviation of intensity measurements within an experimental apparatus is required to understand how Equation 9.9 can be implemented. It can be seen from the form of Equation 9.9 that low fractional standard deviation corresponds with experiments in which high precision is achieved relatively rapidly. In order to gain a practical understanding of Equation 9.8 — and hence Equation 9.9 — the standard deviation and fractional standard deviation in measured intensities were determined for a range of experimental parameters. In this investigation, only I_1 light intensities are directly examined. It is concluded that I_2 intensities can be characterised in the same way in Appendix C. For an intensifier

gain setting of 7, measurements consisting of $1,000$ exposures of I_1 signal were carried out as a function of device drive current, frequency of drive current pulses, gate width within each drive current pulse and the duration of each exposure of the CCD. A fixed current pulse width of 500 ns was used in all measurements. In the investigation of each parameter, the other parameters were held at 'standard' values. The range of values and 'standard' value for each of the parameters in this investigation are shown in Table 9.1. The measured intensity was then set to $8,000$ counts for an intensifier gain of 7 using 'standard' parameters of drive current and pulse frequency by setting the gate width to 400 ns. Without changing these parameters, a series of $1,000$ I_1 exposures was made for each intensifier gain settings (from 0 to 7).

Figures 9.1.a) and 9.1.b) plot the measured standard deviation and fractional standard deviation against measured intensity respectively, for the values of parameters described in Table 9.1 and for each intensifier gain setting. The key finding of Figure 9.1 is that all investigated parameters, other than intensifier gain, reproduce the same standard deviation and fractional standard deviation curves. It can be shown that a similar curve exists — independent of the other stated parameters — for each intensifier gain setting.

For all experimental parameters other than intensifier gain, the fractional standard deviation decreases with intensity as the number of collected intensity counts increases. The implication of the gain data points in Figure 9.1.a) and 9.1.b) is that, reduction in fractional standard deviation may be achieved at a particular measured intensity using lower gain settings. Changes in intensifier gain result in different curves and changes in the other parameters do not. This suggests that the predominant noise mechanisms are independent of the duty cycle of the ICCD, but not independent of the amplification within the intensifier.

147
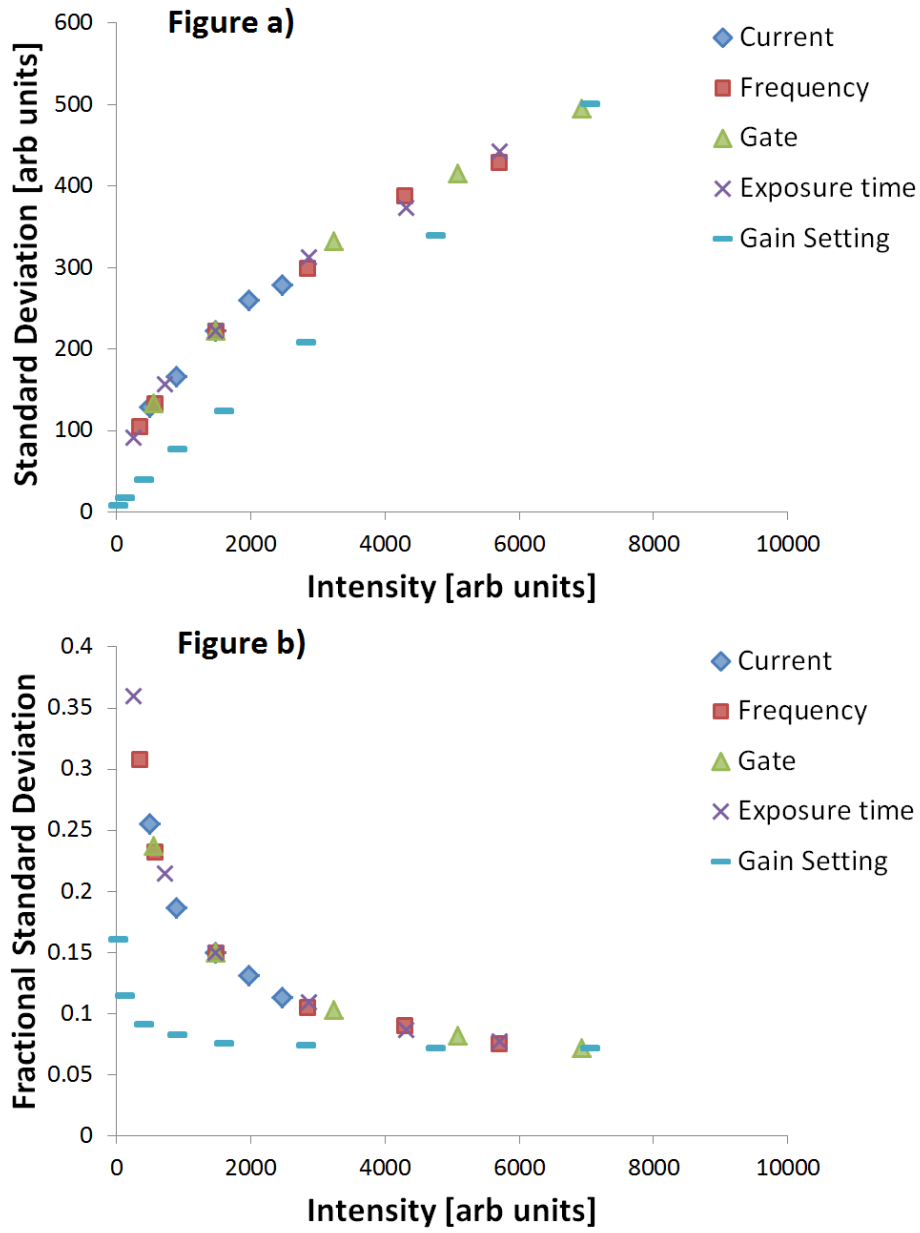
Figure 9.1: Standard deviation (Figure 9.1.a)) and Fraction Standard Deviation (Figure 9.1.b)) of sets of 1,000 intensity measurements are plotted for various values of key experimental parameters. Each data point corresponds to experimental data for one of the parameter values described in Table 9.1 (with intensifier gain values separately described in the surrounding text).

The relationship between standard deviation and intensity was measured for

Gain Setting	Prefactor	Exponent
7	7.4404	-0.529
6	5.007	-0.504
5	42.383	-0.812
4	3.4691	-0.515
3	2.7502	-0.511
2	1.5973	-0.516
1	1.4501	-0.506
0	1.1345	-0.505

Table 9.2: Table of constants describing the power law fits of fractional standard deviation as a function of measured intensity for each intensifier gain setting.

each intensifier gain setting and the results are plotted in Figure 9.2. For gain settings of 3 to 7, pulse frequency was varied to access different intensity values. However, in reducing the gain to 0, 1 or 3, the maximum pulse frequency permitted by the apparatus (20 kHz) could not produce 8,000 counts of measured intensity. Therefore, the duration of each exposure was used to generate the curves for these values of gain.

The fractional standard deviation curve for each gain setting was then fitted with a power law. The resultant expressions for fractional standard deviation as functions of intensity can be used to express Equation 9.9 as a function of measured intensity. For example, the gain 2 curve in Figure 9.2.b) is fitted by Equation 9.10:

$$\frac{\sigma_{SD}^{I_1}}{I_1} \approx 1.5973 I_1^{-0.516} \tag{9.10}$$

A table of constants describing the power law fit for each intensifier gain setting is given in Table 9.2.
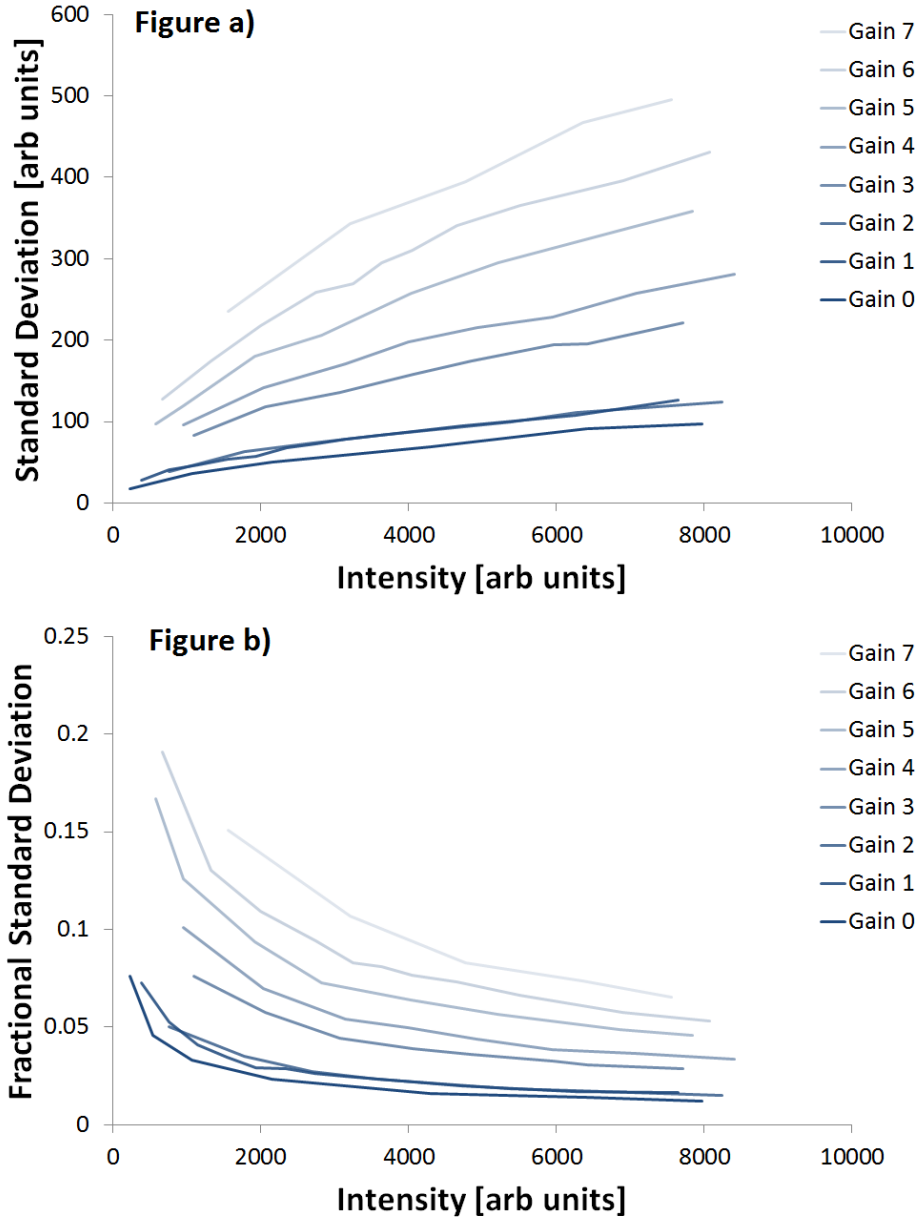
Figure 9.2: Standard deviation (Figure 9.2.a)) and fractional standard deviation (Figure 9.2.b)) of sets of 1,000 intensity measurements are plotted for each value of intensifier gain.

In order for these fractional standard deviation curves to be used to optimise experiment durations (see Section 9.4), it is necessary to relate them to precision in optical loss measurements.

9.3 Relating Fractional Standard Deviation Curves to Precision

Having examined the relationship between fractional standard deviation and measured intensity for each intensifier gain setting in Section 9.2, fractional standard deviation must now be related to the precision of an optical loss measurement. Experimental data in Appendix C suggests that the standard deviation of light intensity from different device sections follow the same curves. Hence, a value for $\sigma_{SD}^{(A+\alpha_i)}$ can be determined from Equation 9.8, either through knowledge of I_1 and I_2, or by knowledge of either of these intensities and an entered value of optical loss.

By substituting Equation 9.10 into Equation 9.9, one may derive Equation 9.11:

$$
t_{total}^{gain=2} \approx \left(\frac{1}{\sigma_{SEM}^{(A+\alpha_i)} L} \right)^2 \frac{t_{cycle}(m, t_{exposure})}{m} \left[(1.5973)^2 \left(I_1^{-1.032} + I_2^{-1.032} \right) \right]
$$

(9.11)

Equation 9.11 is expressed in terms I_1 and I_2. $t_{total}^{gain=2}$ is the minimum experiment duration for these parameters — with an intensifier gain setting of 2 — for which a precision equal to $\sigma_{SEM}^{(A+\alpha_i)}$ can be obtained . (Other gain settings may be examined by substitution of the appropriate values from Table 9.2.)

Given knowledge of approximate values of I_1 and I_2 and the expression for t_{cycle} found in Equation 9.2, the time required to achieve a particular standard error in optical loss can be examined for typical experimental parameters.

By substituting Equation 1.16 into Equation 9.11, total experiment duration may be expressed as a function of I_1 and $(A + \alpha_i)$. This is useful for considering how long an experiment must be for extreme values of optical loss, and is used in the analysis underlying Figure 9.3.b).

In order to study changes in optical loss of the order of 0.1 cm^{-1}, it is necessary to discriminate between experimental scatter on a scale smaller than at

151

roughly $\pm 0.0\dot{3}$ cm^{-1}. Consequently, 3σ experimental precision is achieved by setting $\sigma_{SEM}^{(A+\alpha_i)}$ equal to $\pm 0.0\dot{1}$ cm^{-1}. This is taken to be the benchmark standard error of a '*precise*' measurement in the following.

Equation 9.11 may then be studied as a function of the parameters $t_{exposure}$, I_1, I_2 and m. It is expressed for an intensifier gain setting of 2, a device section length of 0.03 cm, a t_{read} of 0.07 seconds and a t_{switch} of 0.01 seconds in Equation 9.12:

$$t_{total}^{gain=2} \approx \left(\frac{1}{0.000\dot{3}}\right)^2 \frac{2(m(t_{exposure}+0.07s)+0.01s)}{m}\left[(1.59\dot{7}3)^2\left(I_1^{-1.032}+I_2^{-1.032}\right)\right]$$
$$(9.12)$$

The measured light intensities depend upon $t_{exposure}$. The effect of this dependence upon required experiment durations will be examined in Section 9.4, following a broad discussion of the characteristics of Equation 9.12. In Figures 9.3, a range of typical I_1 values is examined as a function of the other experimental parameters. In these calculated values, it can be seen that values of t_{total} vary over many orders of magnitude for the examined parameters. Significicantly, they imply that — in appropriate experimental conditions — sufficiently precise measurement of optical loss can occur within acceptably short experiment durations.

For the calculations carried out in Figures 9.3.a)-9.3.c), an intensifier gain setting of 2 was used with other parameters as described in Equation 9.12. In Figure 9.3.a), m was set to 1 and $(A + \alpha_i)$ was set to 5.0 cm^{-1}. In Figure 9.3.b), m was set to 1 and $t_{exposure}$ was set to 0.1 seconds. In Figure 9.3. c), $t_{exposure}$ was set to 0.01 seconds and $(A + \alpha_i)$ was set to 5.0 cm^{-1}. (A small value of $t_{exposure}$ is taken in the latter case as varying m has a greater effect on calculated values of t_{total} for small exposure durations.)

Figure a)
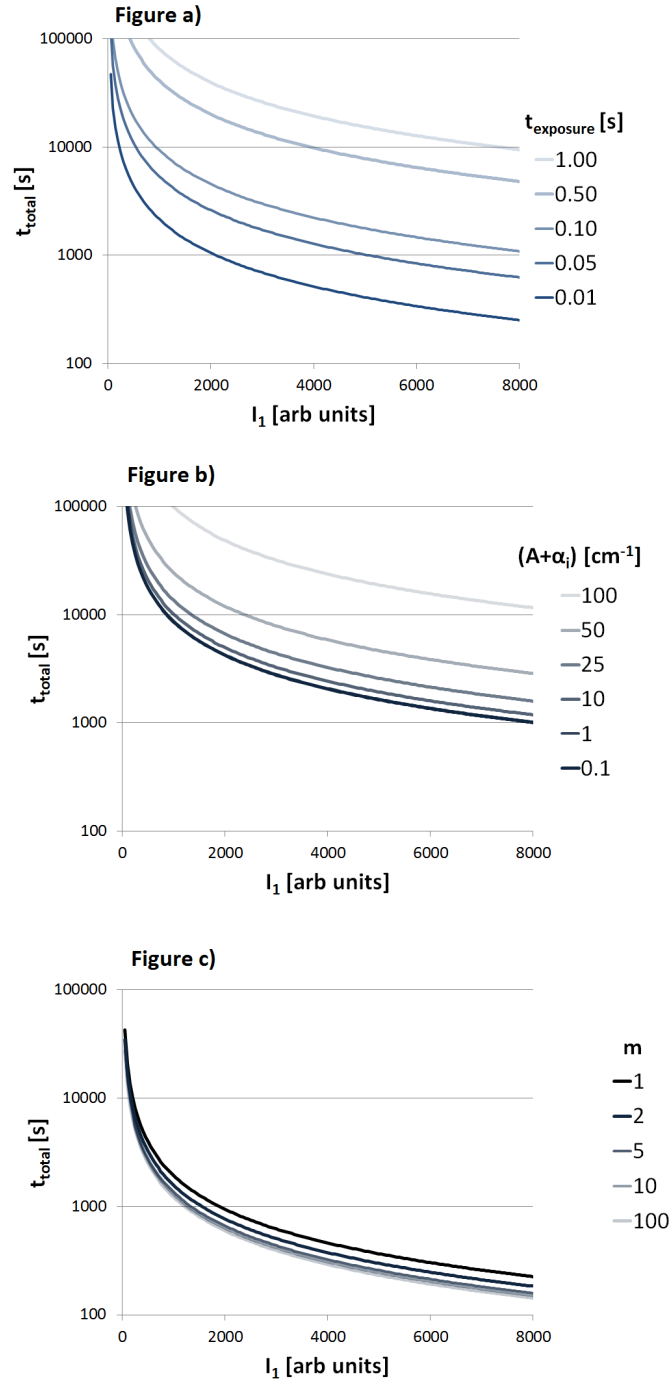
Figure b)

Figure c)

Figure 9.3: Minimum experiment durations required to achieve a standard error in optical loss of $\pm 0.0\dot{1}$ cm^{-1} as a function of measured I_1 intensity in various experimental conditions. Note the logarithmic y-axis.

The calculations plotted in Figure 9.3 generally show that increasing the available light intensity, I_1, decreases the time required to reach the precision benchmark (of $\pm 0.0\dot{1}$ cm^{-1}). This naturally follows the behaviour outlined in Figure 9.2. The implication of this is that parameters which increase measured intensity without increasing noise (such as gain) or increasing modulation period (such as exposure duration) ought to be maximised in any given experiment.

Figure 9.3.a) demonstrates that increasing the duration of each ICCD exposure — for a particular resultant intensity — increases the experiment duration required to acquire sufficient precision. The interpretation of this is simply that experiment duration can be minimised by maximising the acquired I_1 signal in each ICCD exposure. For the stated parameter values and an I_1 value of $8,000$ counts, t_{exp} values of 1.00 and 0.01 seconds correspond with t_{total} values of 9491 and 252 seconds respectively. Figure 9.3.a) allows the comparison of cases in which different intensities are collected within particular exposure durations. However, the different curves shown in Figure 9.3.a) are not representative of the case in which the exposure duration is varied for otherwise fixed parameters, due to the dependence of measured intensity upon exposure duration.

It can be shown that collected intensity is proportional to exposure duration in otherwise fixed conditions. It is, therefore, informative to scale intensity and exposure duration by a particular factor within Figure 9.3.a) and examine the change in t_{total}. For example, $8,000$ counts of I_1 acquired using 0.1 second exposures results in an experiment duration of $1,092$ seconds in Figure 9.3.a). Whereas, 800 counts of I_1 acquired using 0.01 second exposures results in an experiment duration of $2,712$ seconds. This discrepancy is caused by the increased number of modulation cycles, and hence t_{switch} periods, required if less signal is collected within each exposure. The implication of this finding is that — for a particular pump current, pump frequency and gate pulse duration — exposure duration ought to be increased such that peak intensity equals $8,000$ counts (provided that $8,000$ counts are not reached at the minimum possible exposure duration). This will minimise the number of relay switching periods in a given experiment, and hence the experiment duration.

Figure 9.3.b) demonstrates that increasing optical loss results in an increase in the required minimum experiment duration. This plot was achieved by substituting the expression for I_2 in terms of I_1 and optical loss (Equation 1.16) into Equation 9.12 (as opposed to entering specific values of I_2). Greater optical loss for a particular I_1 results in a longer experiment duration (to maintain the same precision) as it reduces the corresponding value of I_2 and hence increases the fractional standard deviation in I_2 (according to Equation 9.10). The resultant increase in experiment duration is a consequence of the form of Equation 9.12.

Practically speaking, measurements of both I_1 and I_2 spectra can be made and this relationship needn't be applied. It is, however, useful in visualising the behaviour of Equation 9.12. For the stated parameters and for an I_1 value of $8,000$ counts, optical loss values of 0.1 and 100 cm^{-1} correspond with experiment durations of $1,009$ and $11,642$ seconds respectively.

Figure 9.3.c) demonstrates that increasing m increases the fraction of each modulation period in which CCD exposures are occurring. The result of this is that the required degree of precision is accrued more rapidly for increasing values of m. This is especially pronounced where t_{switch} is large relative to $t_{exposure}$. Accordingly, this calculation was carried out for the minimum experimentally possible value of $t_{exposure}$, in order to emphasise this effect. If a large value of $t_{exposure}$ is used, increasing m is much less beneficial. Increasing m results in diminishing returns for m greater than approximately 5. However, so long as the modulation period does not become sufficiently large that drift error becomes substantial, the use of a large m parameter can reduce the number of modulation cycles and hence the number of $I_1 - I_2$ data pairs which must be saved and analysed. This may be useful in easing the hardware requirements of long modulated multisection method experiments. For the stated parameters and for an I_1 value of $8,000$ counts, m values of 1 and 100 correspond with experiment durations of 252 and 160 seconds respectively.

9.4 Optimisation of the Intensifier Gain setting

Figure 9.2 demonstrates that the fractional standard deviation in measured light intensity achieved using the various intensifier gain settings of the intensifier decreases with increasing measured intensity. Furthermore, it shows that fractional standard deviation curve associated with a particular intensifier gain setting tends to decrease in magnitude with decreasing gain setting, with diminishing returns for the lowest gain settings. The implication of this is that — if enough light can be emitted from a device that high gain settings are not necessitated — optical loss can be precisely measured in shorter experiment durations at lower intensifier gain settings.

Increasing intensifier gain setting will tend to result in less precise measurement as the intensifier inherently adds amplifier noise to any signal that it collects. For low intensifier gain settings, amplifier noise is smaller compared to other noise sources.

The standard pulse generator used in the experimental work described in this thesis has a maximum attainable current output which is dependent upon its pulse duty cycle. While using the lower intensifier gain settings, the duty cycle and pulse current of the pulse generator which pumps a test device can be maximised at the lowest possible CCD exposure time without attaining $8,000$ counts on the ICCD, and hence, without making full use of the ICCD dynamic range. The implication of Figure 9.3.a) is that the exposure time ought to be increased to minimise experiment duration. It is necessary to understand whether long exposures at low gain settings result in shorter experiment durations than shorter exposures at higher gain settings. Only the 4 lowest intensifier gain settings are examined here, as higher gain settings result in prohibitively long experiment durations due to the higher fractional standard deviation associated with a particular measured intensity.

For a broad area device of type #1, with a high pulse generator duty cycle and pulse current (1.0 μs wide 60 mA pulses at 20 kHz for the pulse generator used in

this experiment with a gate pulse width of 0.5 μs), a peak I_1 signal of $8,000$ counts was achieved for the four lowest intensifier gain settings with $t_{exposure}$ values of 0.642, 0.184, 0.061 and 0.028 seconds respectively.
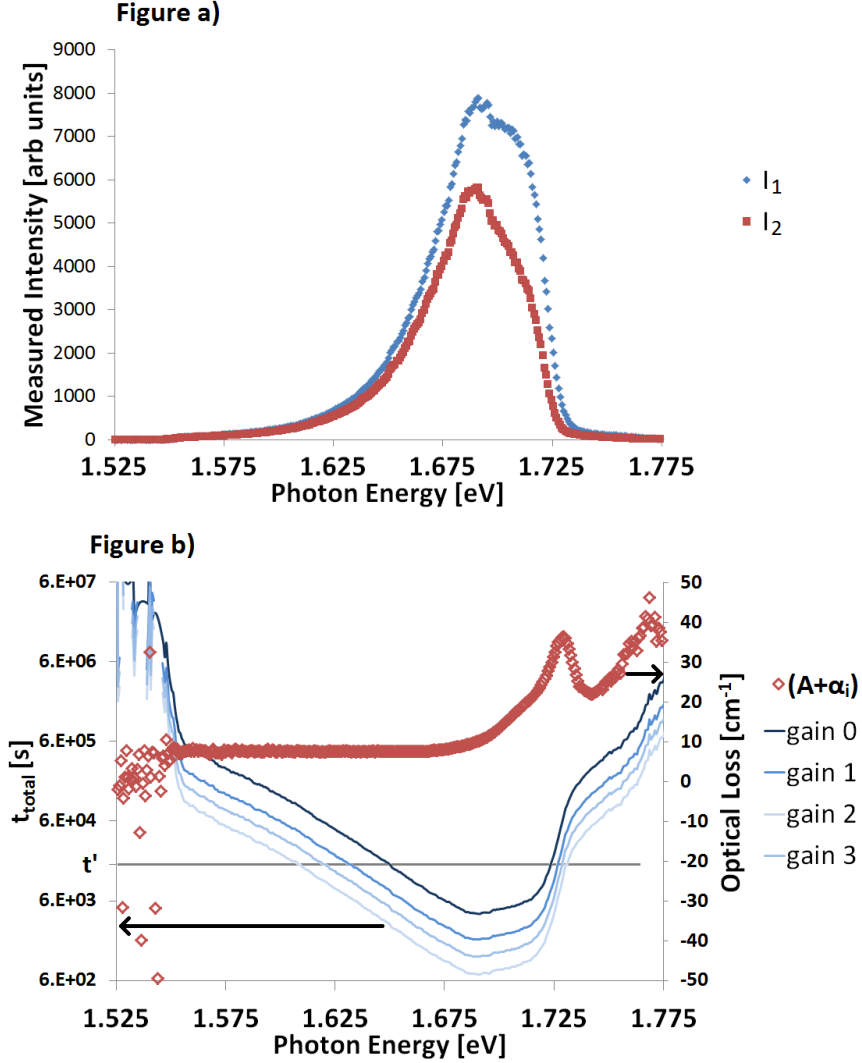
Figure 9.4: Figure 9.4.a) demonstrates typical I_1 and I_2 intensity spectra for a spectrometer centre wavelength of 673 nm. Figure 9.4.b) demonstrates experiment durations calculated from these intensity spectra and the appropriate values of t_{exp} and 'power law' coefficients (found in table 9.2) for the four lowest intensifier gain settings. Black arrows identify which series are associated with which vertical axis.

Figure 9.4 a) shows I_1 and I_2 intensity spectra measured for an intensifier gain setting of 0. Figure 9.4.b) demonstrates how the calculated minimum experiment duration — based on the measured intensities for each intensifier gain setting — depends upon intensifier gain setting. Appropriate values from table 9.2 are used to relate the measured intensity for each intensifier gain setting to its standard deviation. The shortest required experiment durations coincide with the intensity maxima of Figure 9.4.a). This agrees with the discussion surrounding Figure 9.3.

An intensifier gain setting of 2 can be seen to measure optical loss sufficiently precisely in the shortest calculated experimental duration. This is due to an optimal compromise between the (intensifier gain-dependent) fractional standard deviation dependence upon measured intensity and the duration of a modulation period when $t_{exposure}$ is increased to reach $8,000$ counts of measured I_1 intensity.

It is significant that the spectral minimum in experiment duration does not coincide with the photon energy region which is associated with internal loss. Figure 9.4.b) can be used to determine the spectral range for which optical loss is measured to the desired precision by observing the spectral range in which a particular (arbitrary) experiment duration — denoted by t' on the figure — exceeds $t_{total}(h\nu)$.

Internal loss in a multisection device can be characterised by measurement of optical loss in a region of the spectrum in which interband contributions are negligible. Having identified the spectral dependence of t_{total}, it is appropriate to characterise the magnitude of optical loss as a function of photon energy at the absorption edge for this device. For this purpose, a fit of the absorption edge such as that shown in Figure 9.5 is useful. Figure 9.5.a) shows a small spectral region of the optical loss spectrum introduced in Figure 9.4.b). The experimental data is represented by blue diamonds and an exponential fit of the band edge is represented by the thin black line.
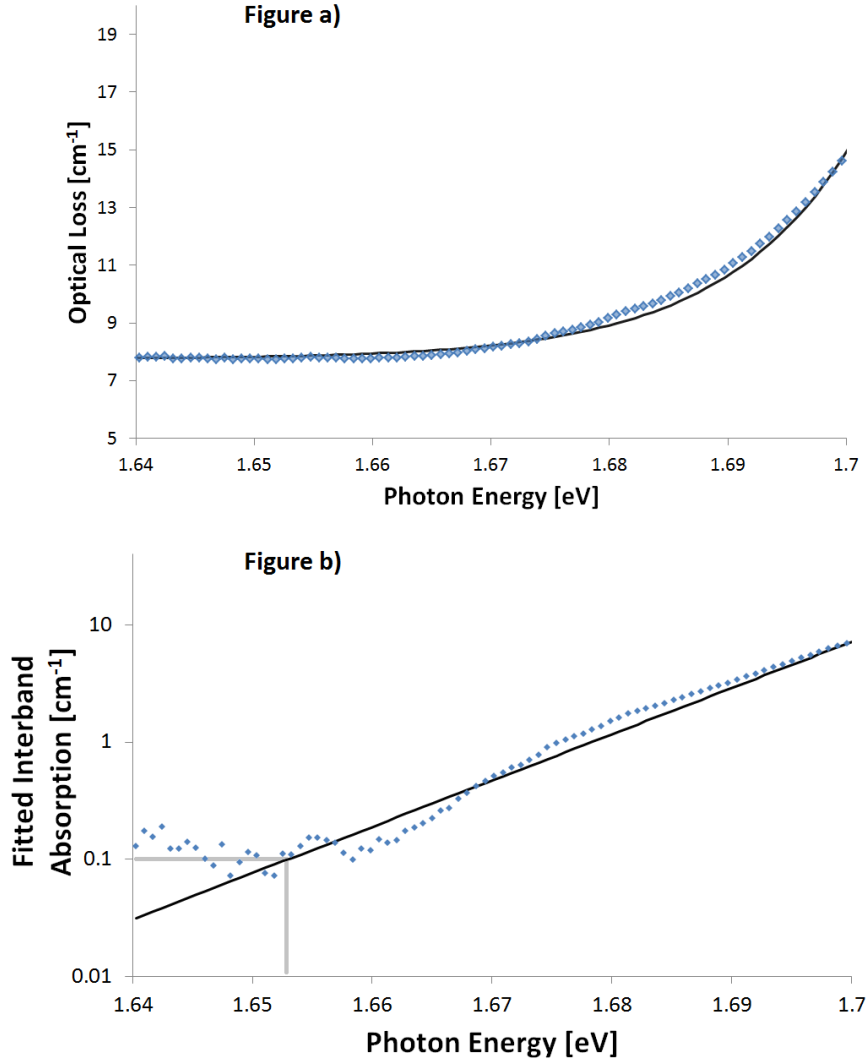
Figure 9.5: Figure 9.5.a) shows an exponential fit of the experimental absorption edge data. Figure 9.5.b) shows this fit on a logarithmic scale with the y-axis offset removed. Blue diamonds and a solid black line are experimental data and the exponential fit respectively.

As the distribution of transitions in question is associated with quantum dots, inhomogeneous broadening dominates. Hence a Gaussian function is appropriate for the fitting of each absorption peak. As an exponential decay approximates the tail of a Gaussian function sufficiently far from its peak, an exponential function is used for the purpose of identifying a photon energy below which interband

contributions to optical loss are negligible. Fit parameters of $E_0 = 1.655$ eV, $\Delta E = 0.011$ eV , $A_E = 0.12$ cm^{-1} for a fit of the form shown in Equation 9.13. An offset value of $\alpha_i = 7.75$ cm^{-1} was taken to be the average value of optical loss in the spectral region $1.640 - 1.645$ eV.

$$(A + \alpha_i)(h\nu) = A_E \, exp^{\frac{(h\nu - E_0)}{\Delta E}} + \alpha_i \qquad (9.13)$$

Figure 9.5.b) depicts the band edge fit with the α_i offset removed on a logarithmic scale. This plot can be used to determine the magnitude of the interband contribution to optical loss as a function of photon energy. The grey lines on Figure 9.5.b) determine the threshold value of photon energy, below which interband transitions have an effect on measured optical loss of less than 0.1 cm^{-1}. For this sample, internal optical loss can be measured to this accuracy from photon energies slightly above 1.65 eV. Thus, in order to directly characterise internal loss up to the high precision standard of this thesis, the optical loss spectrum must be measured with a precision of less than ± 0.01 cm^{-1} *at this photon energy* . This photon energy is refered to as $h\nu'$ in this thesis.

It is established in Figure 9.8 that a feature exists below the apparent absorption edge in this sample, centred at around 1.60 eV. A Gaussian fit of this feature demonstrates that its contribution to measured optical loss at $h\nu'$ is negligible with respect to the $\pm$ 0.1 cm^{-1} uncertainty aim of this project. It would be prudent to carefully consider the contribution from all such small features in future work. The nature of this feature is explored further in Section 9.5 and in Chapter 11.

Consulting the calculation featured in Figure 9.4.b), t_{total} is equal to roughly 55 minutes at 1.65 eV using an intensifier gain of 2. However, for the purposes of this investigation, CCD exposure time is not minimised for this intensifier gain setting. As suggested in Figure 9.3.a), reducing exposure time to a minimum value — for which increasing pulse current and duty cycle can still allow full use of the dynamic range of the detector— reduces t_{total}. For further characterisation of minimisation of experiment durations a pulse generator with higher maximum output at high duty cycles was acquired.

9.5 Precise measurement of Optical Loss in the Modulated Multisection method

The experimental conditions required for a sufficiently precise measurement of optical loss at a photon energy at which interband transitions make a negligible contribution are identified in Section 9.4. An optical loss spectrum can now be measured in these conditions and the statistical distribution of the resultant data can be examined.

Through the acquisition of a pulse generator with a higher maximum current at high duty cycles, the exposure duration in a peak I_1 value of $8,000$ counts is accumulated was reduced to 0.01 seconds. The corresponding experimental parameters were a pump current of 80 mA, a pulse frequency of 20 kHz, a pulse duration of 2.2 μs and a gate width of 2.0 μs. Recalculating t_{total} as demonstrated in Figure 9.4 for these new parameters results in a t_{total} of approximately 20 minutes. Through appropriate choice of an m value of 50 (introduced in Section 9.1), this duration may be somewhat reduced to around 19 minutes. The experiment that this describes produces 481 intensity measurement pairs. This is sufficient to characterise the time-dependent behaviour of intensity, for considerations regarding the effect of modulation upon drift error in a particular experimental trial.

In the discussion in Section 7.5.3, it is suggested that imprecise identification of intensity standard deviation may lead to an underestimation of the required experiment time. I have calculated that the addition of a single modulation cycle is sufficient to account for this. Accordingly, 482 modulation cycles must be taken to measure optical loss to a precision of ± 0.1 cm^{-1} for photon energies as low as 1.65 eV. Following from the optimisation of intensifier gain and determination of minimum experiment duration in Section 9.4, a series of 15 modulated multisection measurements of optical loss were made upon a Broad Area sample of device type #1. Using an m values of 50 and 482 modulation cycles, a series of 15 measurements ('*trials*') of optical loss were carried out, using the device parameters stated above. Using Equation 8.21, modulated drift error calculated for these conditions ($t_{mod} = 2.7$ seconds) allow for absolute values of fractional intensity

gradients (M_A) as large as $\pm 1 \times 10^{-3}$ s^{-1} before systematic error exceeds ± 0.1 cm^{-1} and as large as $\pm 5 \times 10^{-4}$ s^{-1} before systematic error exceeds ± 0.03 cm^{-1} . The latter figure is roughly 20 times the largest value of M_A observed in experimental data using this apparatus. Before comparing the results of the various trials, the data held within the first trial is examined in detail in Figure 9.6.
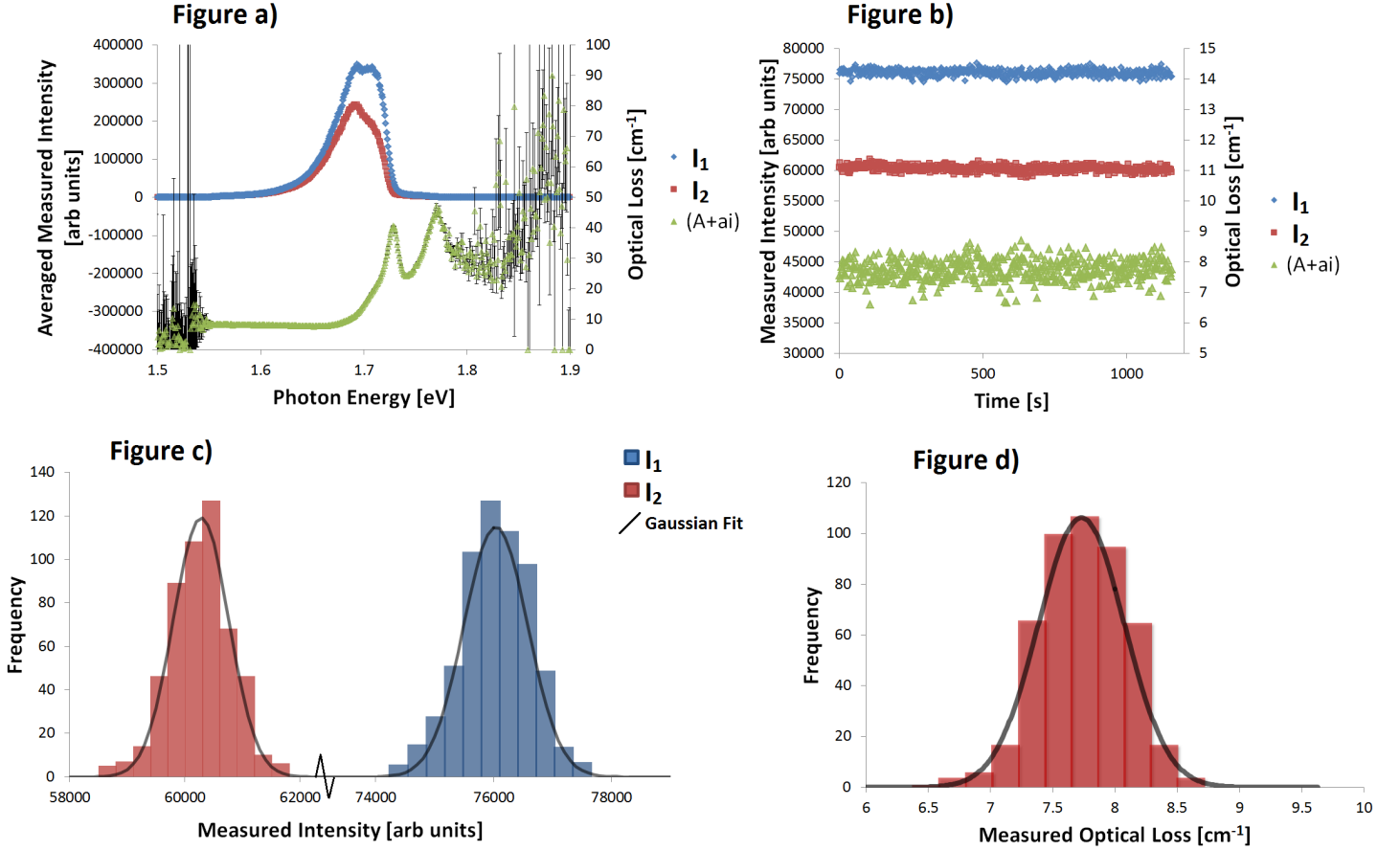
Figure 9.6: Figure 9.6.a) shows the respective sums of the m I_1 and I_2 measurements within each modulation cycle and optical loss calculated from each pair of sums in the instance of a precise measurement of an optical loss spectrum. Figure 9.6.b) examines a time series of the data shown in Figure 9.6.a) corresponding to a photon energy of $h\nu' = 1.65$ eV. Figures 9.6.c) and 9.6.d) demonstrate the distributions of intensity and optical loss from Figure 9.6.b) in the form of histograms. Black lines in Figures 9.6.c) and 9.6.d) represent Gaussian fits of the respective distributions of experimental data. Jagged lines on intensity axis represent a discontinuity between two linear ranges.

Figure 9.6.a) shows summed intensities and the resultant optical loss spectra from within each modulation cycle. $h\nu' = 1.65$ eV is the photon energy at which the interband contribution to optical loss becomes negligible for this particular sample (as discussed in Section 9.4). Figures 9.6.b-d) are data at $h\nu'$ only. Figure 9.6.b) shows the behaviour of $I_1(h\nu')$, $I_2(h\nu')$ and $(A + \alpha_i)(h\nu')$ as a function of time. The stated intensities in Figures 9.6.a) and 9.6.b) are the sum of m measured intensities within each modulation cycle and therefore exceed $8,000$ counts in some spectral regions. (m is equal to 50 in these measurements).

Figures 9.6.c) and 9.6.d) are histograms of the distributions of the data shown in Figure 9.6.b). The Gaussian fits of the distributions shown in Figures 9.6.c) and 9.6.d) use the standard deviation and average of each respective quantity (as suggested by Figure 9.6.b). The approximate agreement between the Gaussian fits and the experimentally measured distributions of each quantity suggests approximately normal distributions of each time series.

The gradient of the I_1 intensity time series (g) shown in Figure 9.6.b) is plotted on the primary y-axis of Figure 9.7.a). The I_2 gradient shows a similar trend, and so is omitted from the figure. By dividing g by the measured I_1 intensity at each spectral point, the M_A coefficient is obtained. M_A is plotted on the secondary y-axis of Figure 9.7.a). The g and M_A values at derived from the I_1 spectrum at a photon energy of $h\nu' = 1.65$ eV are –0.09 arb. units s^{-1} and –1.65766 $\times$ 10^{-6} s^{-1} respectively.

Calculated modulated and conventional drift errors — as described in Chapter 8 — are plotted as a function of photon energy in Figure 9.7.b) and the intensity gradient data upon which they are based is plotted in Figure 9.7.a). The fact that intensity gradient (g) has a significant spectral dependence and fractional intensity gradient (M) is much more flat with photon energy supports the idea that systemic drift is predominantly multiplicative. This supports the discussion found in Chapter 7. The modulated and conventional drift errors at $h\nu'$ are 0.113 cm^{-1} and 0.000235 cm^{-1} respectively. The presence of modulation can be seen to make a substantial difference to the magnitude of drift error; reducing it to a fraction

of the value denoted by the uncertainty aim of this project. Significantly, Figure 9.7.b) demonstrates that modulated drift error calculated based upon noisy experimental intensity gradients, does not itself contain noise which is large in comparison with the optical loss uncertainty aim of this project.
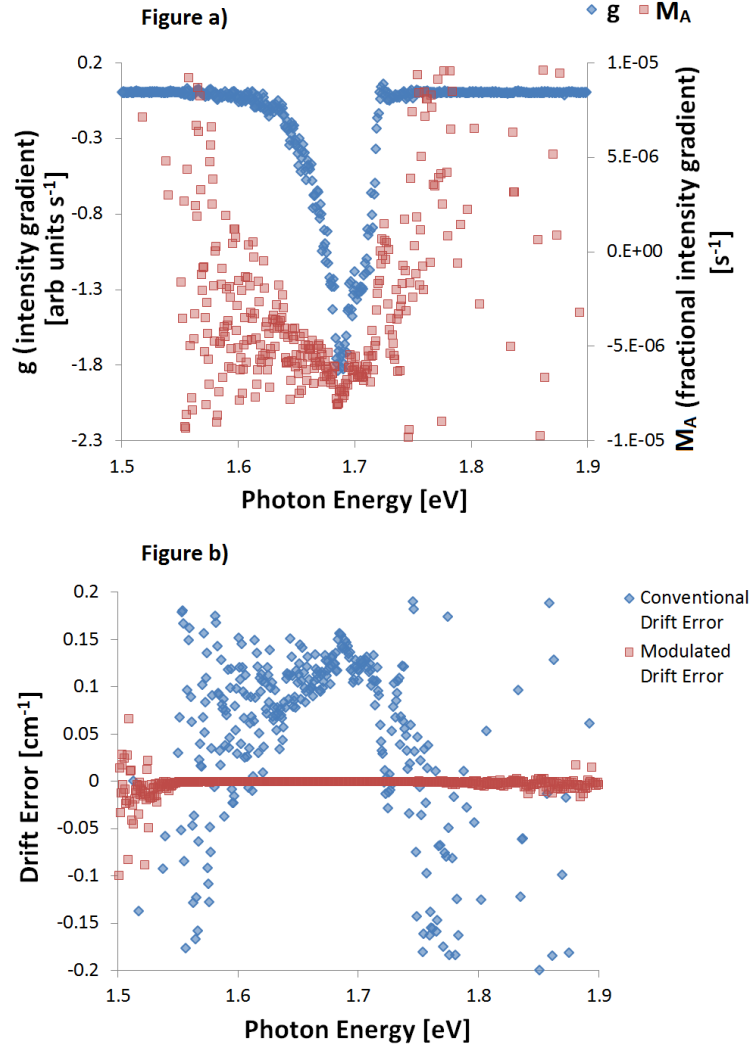
Figure 9.7: Figure 9.7.a) demonstrates the intensity gradients and fractional intensity gradients associated with the intensity spectra shown in Figure 9.6. Figure 9.7.b) shows the conventional and modulated drift errors calculated, as a function of photon energy, using the M_A data presented in Figure 9.7.a).

M_A values are approximately a factor of 10 larger than those described in the longer duration experiments described in previous sections (especially Section 6). This may be due to the fact that variation in temperatures and optical alignment as the apparatus 'settles' at the start of an experiment cause changes in intensity with are large with respect to the systemic drifts later in a measurement series. If the period over which such a 'settling' occurs is short compared to the timescales of the trials described in Chapter 6, then it would have a greater effect upon the observed gradient in the case of *shorter* experiment durations, thus explaining this observation.

Figure 9.8 depicts the same optical loss data as is shown in Figure 9.6.a), but with the photon energy axis rescaled to examine the region in which interband transitions make a negligible contribution. Error bars in Figure 9.8 denote the $3\sigma_{SEM}^{(A+\alpha_i)}$ precision — determined from the standard deviation of the intensity data — for each photon energy. These error bars are roughly ± 0.05 cm^{-1}; slightly larger than the aim of $\pm 0.0\dot{3}$ cm^{-1}.

Examining the underlying intensity data at a photon energy equal to $h\nu'$, the average intensity and standard deviation of a single I_1 exposure are equal to $1,520$ and 76.5 counts respectively. These values for a single I_2 exposure are $1,205$ and 67.9 counts respectively. The average value of $(A + \alpha_i)$ is 7.74 cm^{-1} and its standard deviation is 0.34 cm^{-1}. These values are used in the construction of the Gaussian fits shown in Figures 9.6.c) and 9.6.d). Intensity standard deviations are larger than predicted in previous sections of this chapter due to systematic error sources acting to vary intensity over the course of the 20 minute measurement. (Note that the discussion in Section 7.5.3 confirmed that systemic drift does not drastically affect measured standard deviation for measurement durations of the order of *seconds*. That reasoning does not apply to the standard deviations measured from a 20 minute intensity time series). All optical loss measurements agree to within 0.1 cm^{-1} between 1.64 eV and 1.66 eV. Considering measurements of optical loss within this spectral region to differ by a negligible amount, the small degree of experimental scatter and agreement to within error bars supports the conclusion that the precision aim of the project has been met.

165
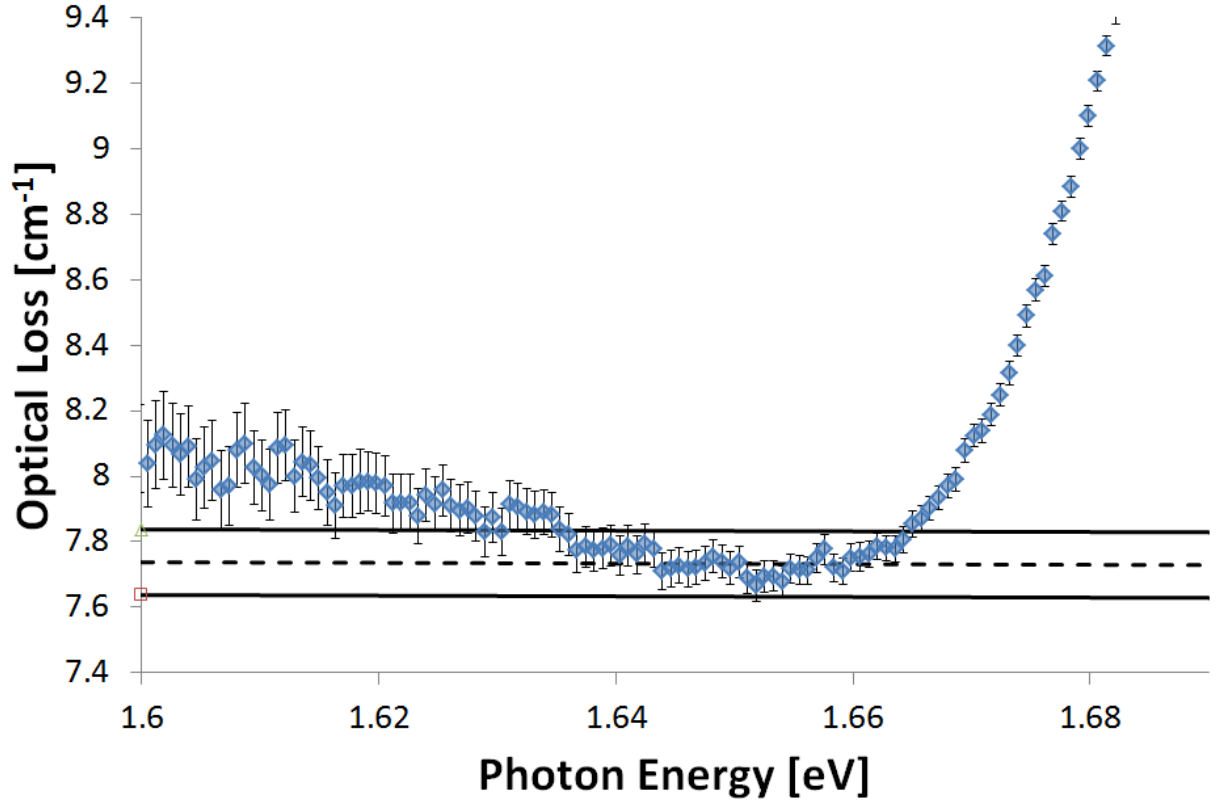
Figure 9.8: In Figure 9.8.a), the spectral region below the bandgap in the data shown in Figure 9.6.a) is examined. The dashed line represents the value of optical loss measured at $h\nu'(=1.65$ eV). Solid black lines represent optical loss values 0.1 cm^{-1} above and below $(A + \alpha_i)(h\nu')$.

The improved uncertainty afforded by the precision optimisation described in this chapter has allowed the discrimination of a feature at low photon energies in Figure 9.8; a broad optical loss peak below the absorption edge of the material. At photon energies as low as 1.61 eV, this feature corresponds to an increase in optical loss above the local minimum value by substantially more than the error bars associated with any particular data point. By manipulating the underlying intensity spectra, it can be shown that a constant systematic error in offset could not cause a feature of this magnitude that does not have a drastically higher gradient in photon energy. Within a particular measurement, this feature was found

to be insensitive to changes in exposure duration and device pumping conditions suggesting that the feature is not dependent upon the magnitude of the intensities or upon the relative magnitudes of the light intensity and background signals. This rules out detector linearity as a cause of this feature. Through use of a 780 nm (1.59 eV) longpass filter, it was demonstrated that the light corresponding to this feature does not originate from stray reflections/diffraction within the spectrometer. The feature is also present in a measurement of a device of the same structure by Edge-Photovoltage Spectroscopy. These observations all suggest that this feature is not caused by systematic error, but by a real loss process within the device. Further discussion of this feature will follow observations made in Chapter 11.

9.6 Precision of repeated measured of Modulated Optical Loss

Having considered the outcome of a single precise Modulated Method measurement of optical loss in Section 9.5, the outcomes of several such experiments will be compared. As described in Section 9.5, 15 trials which are nominally identical to that described by the data in Figure 9.6 were consecutively carried out. The device was not realigned between measurements. Figures 9.9.a) and 9.9.b) respectively depict the values of both intensities and optical loss coefficients measured at $h\nu' = 1.65$ eV for each modulation period (over the course of all 15 trials). Figures 9.9.c) and 9.9.d) respectively depict the same intensities and optical loss given in Figures 9.9.a) and 9.9.b), averaged across each trial. The values of optical loss from each trial agrees within ± 0.1 cm^{-1}. This demonstrates repeatability in the precise measurement of optical loss at a photon energy of $h\nu'$. $3\sigma_{SEM}^{(A+\alpha_i)}$ error bars are plotted (calculated from the distribution of intensity time series for each trial). These error values range from ± 0.047 to ± 0.05 cm^{-1}. Only one of the 15 measurements differs from the average by more than its assigned error. The standard error is slightly larger than the aim of $0.0\dot{3}$ cm^{-1}. As mentioned in the previous section, this is likely to be due to the exaggeration of intensity standard deviations by systemic drift (or other systematic error sources) over the course of a 20 minute measurement . The *average deviation* of the measurements shown

in Figure 9.9.d) is 0.017 cm^{-1}. This is of the order of the precision aim of 0.01 cm^{-1}.
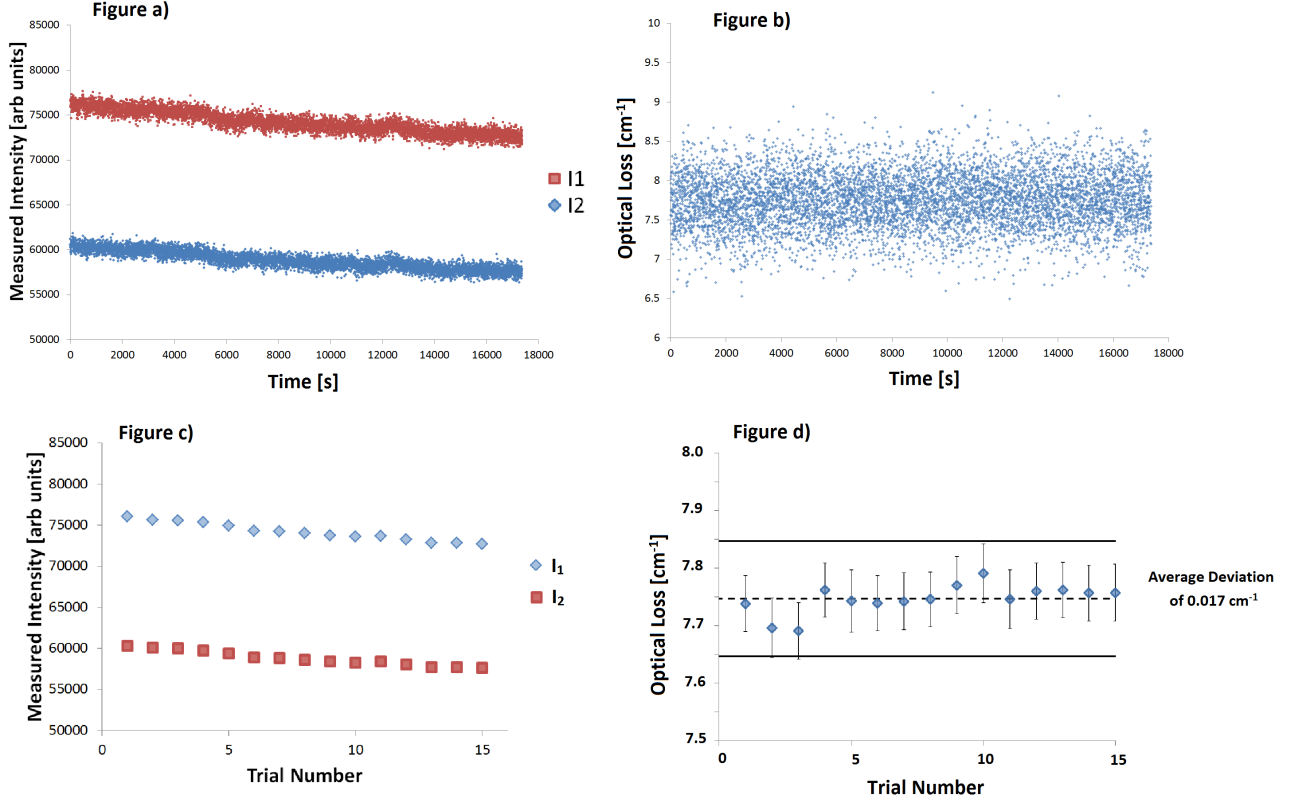
Figure 9.9: Raw and averaged Intensity and Optical Loss data for 15 trials in the same conditions as those described in Figure 9.8. Figures 9.9.a) and 9.9.b) show the measurements from each modulation cycle. Figures 9.9.c) and 9.9.d) show the average of every modulation cycle within each trial. In Figure 9.9.d) the dashed line represents the average optical loss coefficient and the solid lines represent the desired ± 0.1 cm^{-1} uncertainty bounds.

A systemic drift is visible in the intensity data of Figure 9.9.a). It is useful to establish whether the deviation in values shown in Figure 9.9.d) is explained by modulated drift error and — more generally — whether the distribution of optical loss measurements shown in Figure 9.9.d) correlates with the intensity gradient in the intensity time series. In order to examine this, the *difference from the average optical loss* will be examined for each trial, rather than the absolute value of op-

tical loss.

Figure 9.10.a) demonstrates the time dependence of these quantities. For increased clarity, deviation of optical loss from its average value is plotted against the fractional gradient in the intensity for each trial in Figure 9.10.b). Through application of Equation 8.21 to the experimental conditions of this experiment, the modulated drift error is calculated.
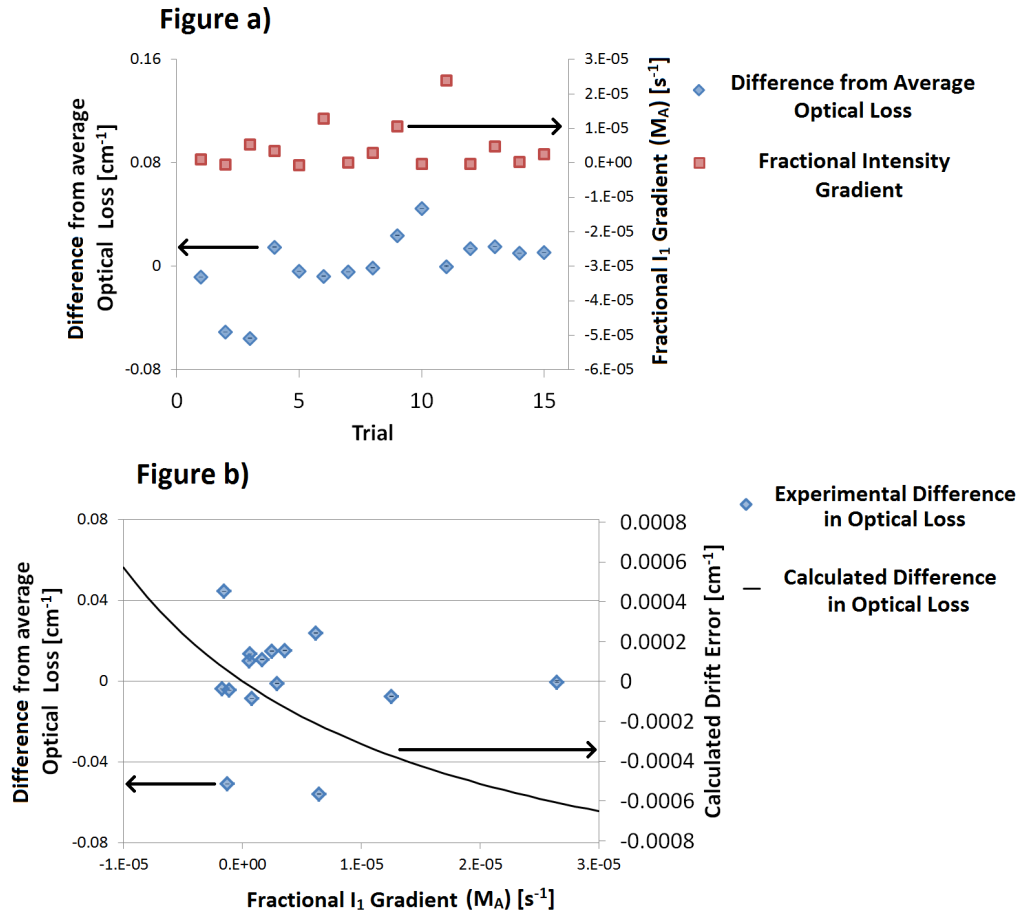
Figure 9.10: Examination of correlation between the difference from the average optical loss and intensity gradient. In Figure 9.10.b), data is plotted as a function of the fractional intensity gradient observed in each trial alongside calculated drift error derived from Equation 8.21. Thick black arrows illustrate which data series corresponds to which axis.

The black line in Figure 9.10.b) represents a calculation of drift error as a function of M_A for these experimental conditions. It can be seen from the secondary y-axis that the predicted error in optical loss corresponding to the largest measured M_A values is a factor of 100 smaller than the measured deviations from average. This supports the conclusion that there is no causal relationship between these parameters.

The difference from the average optical loss for each trial in Figure 9.10.b) is largely scattered around the x-axis origin. In Figures 9.10.a) and 9.10.b), error bars in the difference from the average optical loss are based upon the drift error associated with the intensity gradients of each trial. These error bars are seen to be negligibly small with respect to the y-axis of Figure 9.10.b). The calculated modulated drift error does not account for systematic errors of this magnitude. (Gradients in I_1 and I_2 intensities are comparable the gradient of I_2 could be used with similar results). No strong correlation is observed in Figure 9.10.b), suggesting that any error due to multiplicative drift has been removed and that the remaining variability is due to some other error source.

9.7 Uncertainty associated with Optical Alignment

The data shown in Section 9.6 suggests that the modulated method for optical loss suppresses the action of systemic drift upon measured optical loss coefficients sufficiently to measure with a precision and a modulated drift error of *less* than ± 0.1 cm^{-1}. However, the series of measurements shown in Figure 9.9 relates to a single alignment of a device. In realigning to repeat measurements on different days, systematic error may increase uncertainty from that observed in the data within Figure 9.9.d).

The experiment shown in Figure 9.9 was repeated but with a *realignment of the device between each 'trial'*. In order to give information regarding device alignment and changes in device alignment over the course of each trial, a measurement of the spatial distribution of light collected from the device was taken after realign-

ing — but before starting a new trial — and after each trial. This measurement was taken by setting the diffraction grating to its 0th order, setting the CCD to imaging mode and fully opening the spectrometer input slits.

Figures 9.11.a-d) are new data in the same format as Figures 9.9.a-d), for this new experiment. Figure 9.11.a) shows the I_1 and I_2 values measured within each modulation cycle for all trials. Figure 9.11.b) shows the optical loss corresponding to the $I_1 - I_2$ pair correspding to each modulation cycle across all trials. Figures 9.11.c and 9.11.d) respectively depict the same intensities and optical loss given in Figures 9.11.a) and 9.11.b), averaged across each trial.

It can be seen from Figure 9.11.a) that the act of realigning between trials introduces discontinuities in measured intensity time series. There is no repeated pattern in these intensity time series for measurements made on the same day or on different days.

There is more scatter in the optical loss measurements in Figure 9.11.d) than in those shown in Figure 9.9.d). Standard deviations of the data shown in Figures 9.11.d) and 9.9.d) can be calculated to be 0.085 cm^{-1} and 0.017 cm^{-1} respectively.

Figure 9.11.e) represents the same analysis as was carried out in Figure 9.10.b). Modulated drift error is calculated from the value of M_A corresponding to the I_1 time series for each trial. As in the previous instance, no strong correlation between intensity gradient and the deviation from the average optical loss in each trial is apparent. The black line demonstrates that calculated drift error due to finite modulation period of the experiment is a factor of 100 smaller than the spread in experimentally measured values.
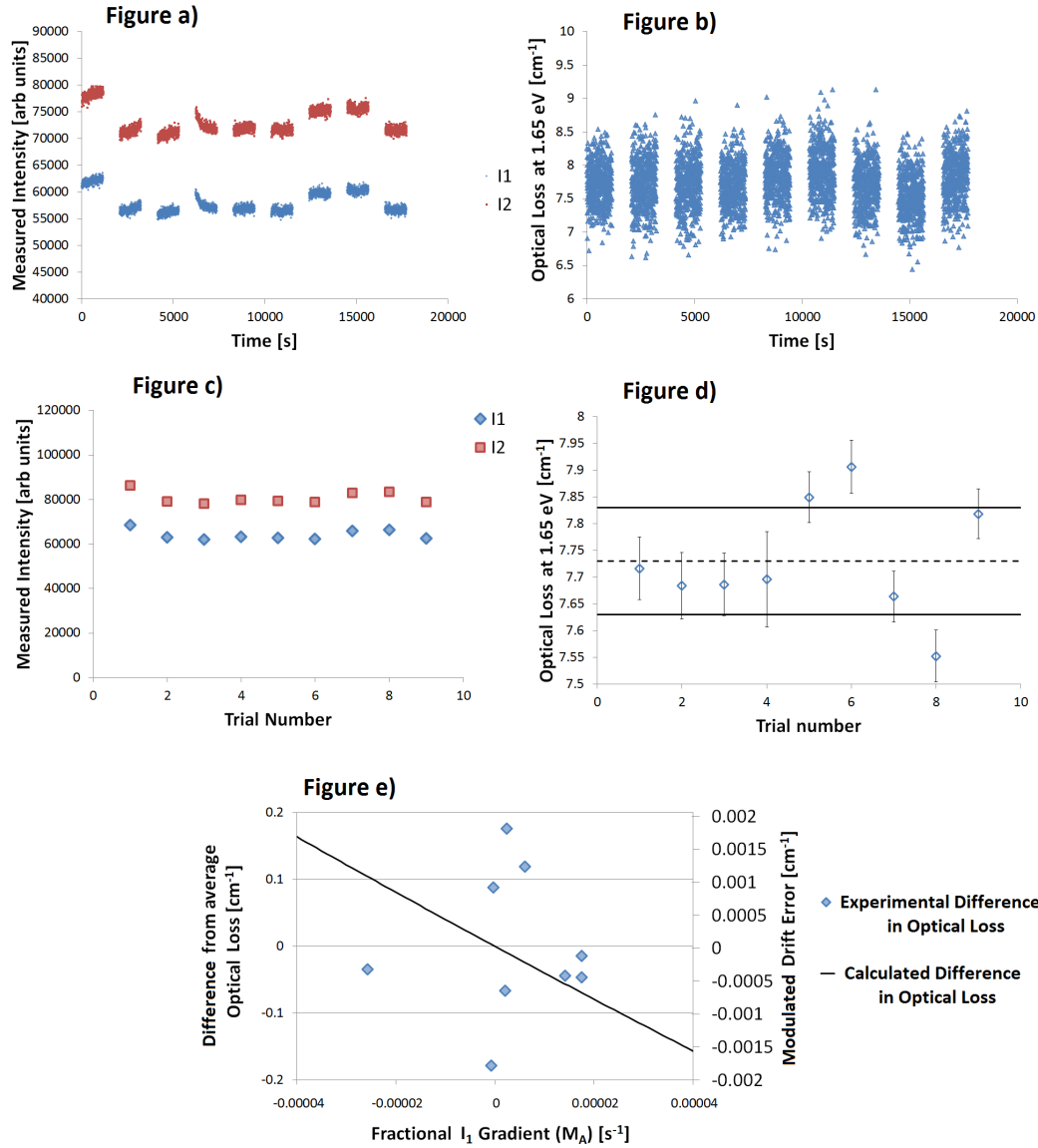
Figure 9.11: Measured intensity and the resultant optical losses are observed for a series of trials, between which the test device is realigned. Figures 9.11 a-d) represent the same analysis as that shown in Figure 9.9 and Figure 9.11.e) represents the same analysis as that shown in Figure 9.10.b), applied to the realigned data.

It must be established whether initial misalignment of the the act of disturbing the apparatus is responsible for the increase in error from the case in which the device was not realigned between trials. No evidence for change in rotational device alignment was found in any of the trials. Accordingly, realignment consisted of

172

horizontal and vertical correction of device position and refocussing of the beam. Following realignment, the apparatus was left to settle for 10 minutes, before the alignment was checked. In each case, alignment had not changed to within the resolution of the CCD array and the next trial was then started. This is the cause of the 'gaps' in the time series shown in Figure 9.11.

Figure 9.12 demonstrates the quantification of alignment and alignment change in a measurement. Figure 9.12.a) shows a contour plot of experimental alignment data. The data shown in Figures 9.12.a) and Figure 9.12.b) are the result of 100 0.01 second exposures of the ICCD in imaging mode.

The measured spatial distribution corresponds to I_1 light intensity for the same experimental conditions as those described in Figure 9.11, but with the pulse frequency reduced to 2 kHz and the intensifier gain reduced to 0. Horizontal and vertical intensity distributions were achieved by summing across each CCD pixel vertically and horizontally respectively. In a well aligned device, the maximum-valued pixel of the horizontal and vertical spatial intensity distributions is co-located with the centre of the distribution in that orientation. This fact was used to quantify the central pixel of the distribution in each orientation before and after each trial.

Only a selected region of the CCD is shown, and hence the axes labels do not represent the absolute position in pixels of the light incident on the CCD. The horizontal origin of the system is defined to be the location of the spectrometer input slit. The vertical origin of the system is defined to be the geometric centre of the CCD array. These are the reference points with which a device is aligned. Therefore, in this frame of reference, the device is aligned within the resolution of the CCD when $x = y = 0$. Translational alignment of a device at a particular time can be characterised by the deviation from zero of the horizontal and vertical position of the collected light. I define the horizontal and vertical alignment at the start of each trial to be h_0 and v_0 respectively, as marked in Figure 9.12.a).
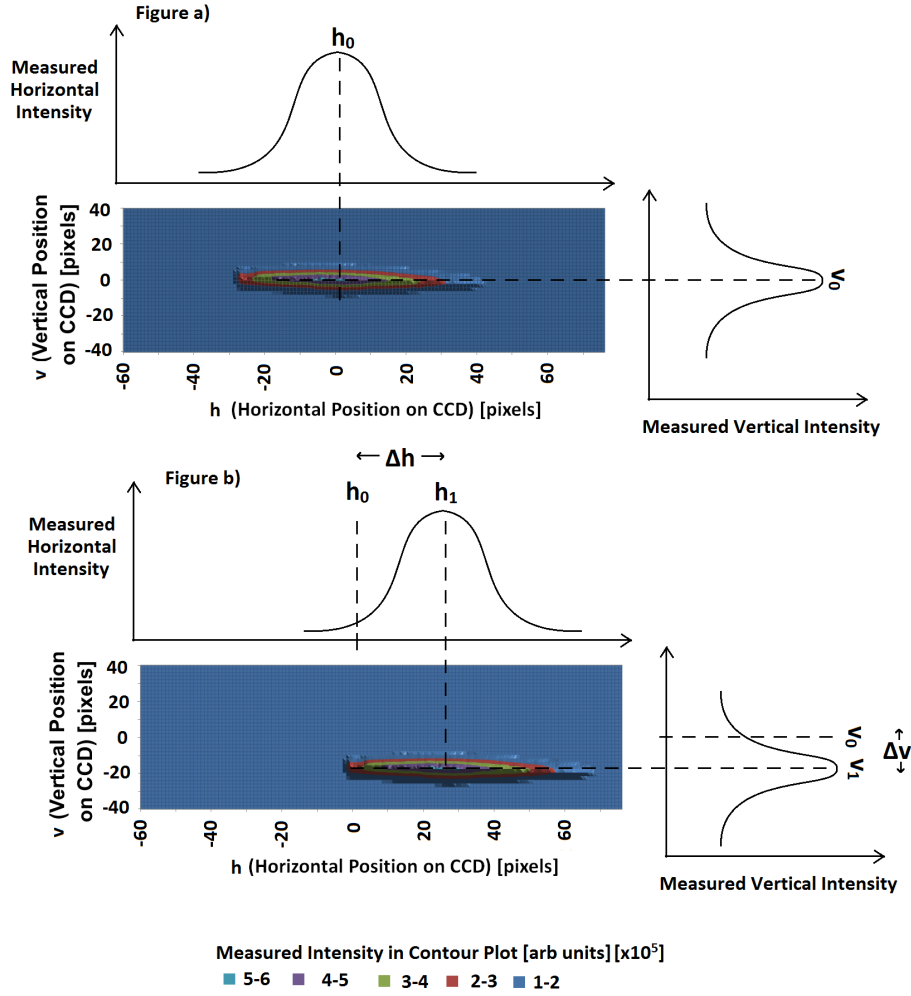
Figure 9.12: Figures 9.12.a) and 9.12.b) represent the characterisation of device alignment before and after a trial of the type examined in Figure 9.11. The misalignment in Figure 9.12.b) is exaggerated for the purpose of a clear demonstration of the characterisation of alignment change within an experiment.

Figure 9.12.b) demonstrates an exaggerated case of a misaligned device. The shift in this figure is exaggerated to highlight the change that is made to the horizontal and vertical distributions. I define the horizontal and vertical alignment after each trial to be h_1 and v_1 respectively, as marked in Figure 9.12.b). An important pair of quantities is the change in alignment parameters over the course of an experiment. These can be defined using the terms introduced in Figure 9.12 as shown in Equations 9.14:

174

$$\Delta h = h_1 - h_0$$
$$\Delta v = v_1 - v_0$$

<div align="right">(9.14)</div>

Additionally, the full width at half maximum of the vertical distribution of collected light can be used to quantify whether changes in focus occur over the course of a trial. This quantity is not prominent in Figure 9.12 as it was only observed to vary beyond the resolution of the CCD array during one of the trials. Only characterisation of device alignment with respect to I_1 intensities is presented here, as alignment data between device sections is identical to the nearest pixel.

The key at the bottom of Figure 9.11 shows measured intensity values of the contour plots. The initial alignment and change in alignment was determined for each trial from alignment measurements of the sort shown in Figure 9.12. Following the assumption that change in alignment is evenly distributed over the course of its corresponding trial (rather than occurring all at once at some point in time), one can relate the measured change in alignment with a change in experimental conditions over the trial. It is informative to plot the difference from average optical loss can be plotted against such a change, as in Figure 9.13. From which, one may learn whether alignment change correlates with systematic error in optical loss measurement.

Initial FWHM was 3 pixels in all trials. Accordingly, initial FWHM is not plotted in Figure 9.13. It can be seen from Figure 9.13.a) that device is horizontally aligned to within one pixel. Figure 9.13.b) shows that there is some distribution in the initial vertical alignment of a device. Fortunately, this initial misalignment is not large enough to be associated with its own optical loss.

Figures 9.13.c) and 9.13.d) show that change in device alignment varies by a few pixels, both vertically and horizontally. Figure 9.13.e) shows that the device focus changed by a measurable amount in only one trial.

All plots in Figure 9.13 show that the difference from average optical loss of a trial does not tend to increase with increasing initial misalignment or with change in alignment over the course of the experiment. This suggests that the systematic error associated with initial misalignment and with change in alignment over the course of a measurement is small with respect to some other error source.

One interpretation of the increased scatter in optical loss between Figure 9.9 and Figure 9.11 could be that inaccuracy in alignment of a device causes an error which is large in comparison with the project uncertainty aim of $\pm$ 0.1 cm^{-1}. However, Figure 9.13 provides evidence to the contrary. It is likely that — in the process of realigning the system — something other than the device alignment itself is disturbed by a user. This may be related to the disturbance of apparatus temperature due to the experimentalist entering and leaving the lab or due to physical interference with the apparatus causing mechanical instability (which is not exhaustively described by the treatment of device alignment described in Figure 9.12). Measured optical loss is expected to become erroneous upon misalignment of the device as the simple paraxial model of light collection can no longer be applied [49]. Additionally, if the device moves during a measurement, the spatial region sampled by the collecting optics will change, causing slight changes to the observed loss coefficient.
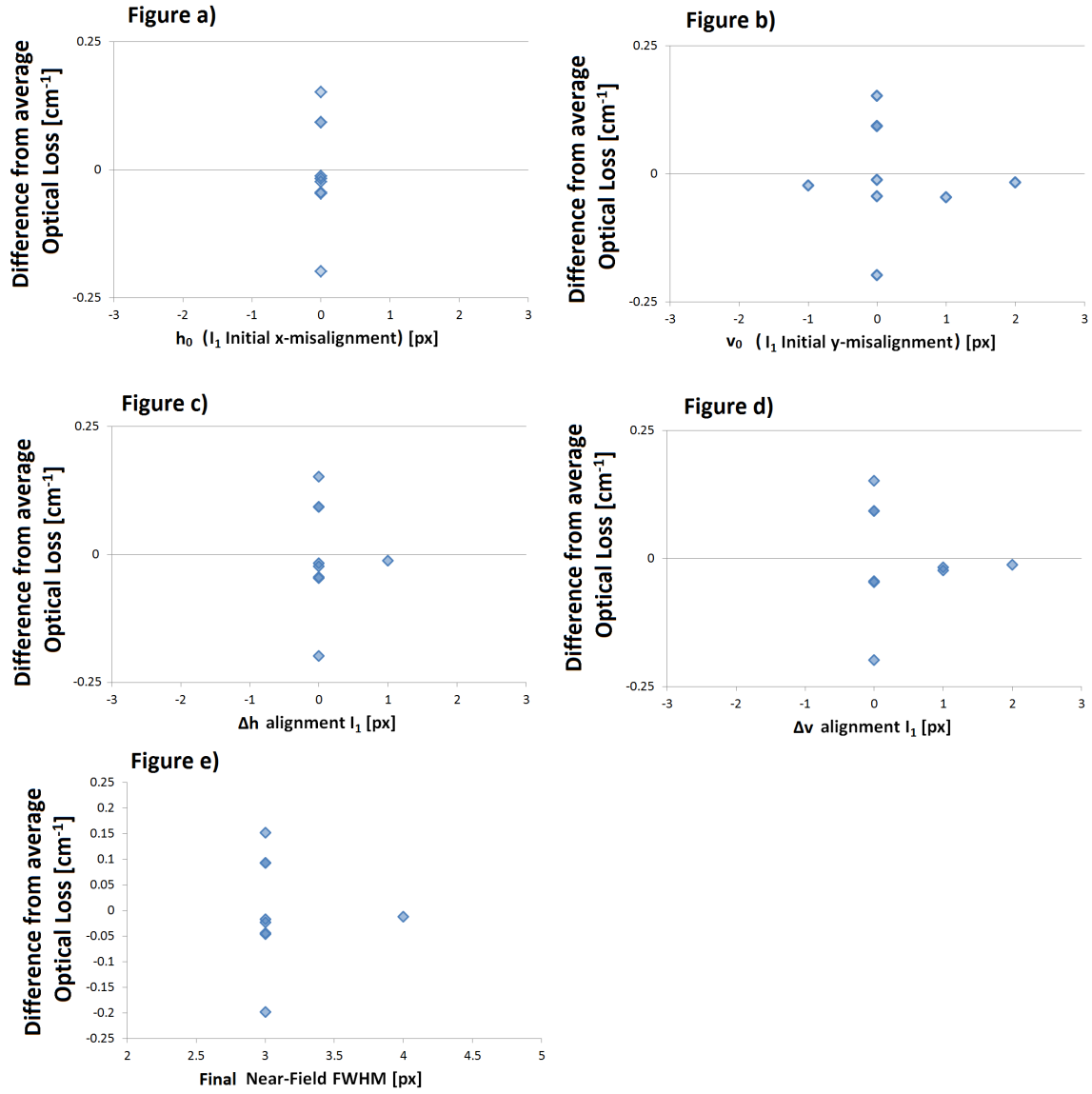
Figure 9.13: Figures 9.13.a) and 9.13.b) plot the difference from average optical loss of each trial against initial device alignments. Figures 9.13.c) and 9.13.d) plot the difference from average optical loss of each trial against change in alignment over each respective trial. Figure 9.13.e) plots the the difference from average optical loss against the FWHM of the vertical distribution of collected light.

9.8 Chapter Summary

In this chapter, the dependence upon experimental conditions of the standard error of an optical loss measurement has been characterised analytically, and the findings applied to experimental data in order to minimise experiment durations. The photon energy at which interband contributions to optical loss become negligible, $h\nu'$, was defined to aid the characterisation of internal optical loss. The minimum experiment duration at which internal loss can be characterised to the precision aim of the project $(3\sigma_{SEM}^{(A+\alpha_i)} = \pm 0.0\dot{3}$ cm$^{-1})$ at $h\nu'$ is defined to be $t_{total}(h\nu')$.

General parameters for the minimisation of t_{total} are described in Figure 9.3. It is established in the discussion surrounding this figure, that t_{total} is maximised for high device light outputs and short exposure durations. It is preferable to use the full dynamic range of the ICCD at the smallest exposure duration allowed by the apparatus. If the test device is pumped with the highest current and duty cycle which is accessible with a particular pulse generator and the detector dynamic range is not fully utilised for measurements with the minimum exposure duration, then t_{total} is minimised when exposure duration is increased such that the ICCD dynamic range is fully utilised. A small reduction of t_{total} is then possible by increasing m.

In Figure 9.4, it is demonstrated that t_{total} values are minimised within this particular apparatus for an intensifier gain setting of 2. Having determined all of the parameters in which the precision of an optical loss measurement is optimised, a spectrum was precisely measured, and the data is presented in Figure 9.6. A t_{total} value of roughly 19 minutes is possible using the minimum exposure duration, upon a device of type $\#1_{BA}$. This corresponds with 482 modulation periods with an m value of 50. Further increasing m provides a negligible reduction in t_{total}.

The outcomes of repeated measurements of optical loss (shown in Figure 9.9) demonstrate that a measurement of optical loss at a photon energy $h\nu'$ to a precision better than ± 0.1 cm^{-1} is possible. The data presented in Figure 9.10 demon-

strates that modulated drift error (introduced in Chapter 8) makes a negligible contribution to the uncertainty of these measurements.

In Section 9.7 it is demonstrated that there is an additional systematic error associated with the realignment of the device. Figure 9.13 suggests that this error is not directly associated with the alignment of the device, but with the disturbance of the apparatus by the experimentalist. Measurements, between which the device is realigned, have an associated standard deviation of the order of 0.085 cm^{-1}. There is an additional day-to-day variability in the measurement which corresponds to systematic errors in optical loss of as large as ± 0.25 cm^{-1}.

The implication of this finding is that optical loss coefficients cannot currently be measured with the desired uncertainty aim of $\pm$ 0.1 cm^{-1} due to a day-to-day variability in experimental results. As experimental results can be reliably reproduced within a particular day of measurements, systematic investigations such as those described in Chapters 10 and 11 are still possible, but any comparison of results taken on different days requires caution.

9.9   Conclusions and Future Work

Figure 9.9 demonstrates that it is quite feasible to measure optical loss at a photon energy corresponding to transitions below the interband absorption edge for a device of sample type $\#1_{BA}$ with a standard error of less than $\pm 0.0\dot{3}$ cm^{-1}. This allows the discrimination of systematic changes in optical loss of the order of ± 0.1 cm^{-1}. However, Figure 9.11 demonstrates that additional error is introduced by the realignment of a device. Figure 9.13 shows that this additional error is not related to initial misalignment, or to change in device alignment over the course of a measurement. The implication of this is that an additional error is introduced by the increased interaction between the experimentalist and the apparatus.

179

Remaining Variability of precise Optical Loss measurements

As correlation is not observed between misalignment and optical loss error, it is assumed that the alignment is sufficiently precise for measurements with precision better than ± 0.1 cm^{-1}; device alignment is not the primary source of error in this measurement. By monitoring the readout of the temperature controller in experiments similar to those described in this section, it was shown that device temperature does not vary by more than ± 0.05 K and measured CCD photocathode temperature does not vary by more than ± 3.00 K over time scales of roughly 12 hours. Taking into account the modulated nature of the experiment, neither temperature varies enough to account for the observed deviation in optical loss coefficients. Furthermore, preliminary experiments demonstrated that measured values of optical loss are independent of the current pulse width and frequency for the duty cycles used in this body of work. This suggests that self-heating does not have an observable effect upon device temperature and hence upon measured optical loss coefficients in the results given in this thesis.

An experiment in which the background signal was measured before each modulation cycle showed that the background signal did not vary enough to account for changes in measured optical loss of the order of those shown in Figure 9.11.d). Neither the background signal, nor the change in background signal over the course of an experiment apparently correlates with deviation from average optical loss in each trial.

The preceding reasoning has ruled out the background signal, initial device misalignment, change in alignment over the course of a measurement, CCD photocathode temperature and device temperature. The pulse generator output has not been monitored through a measurement. However, it is implied in Figure 10.7.a) that very large variations in drive current would be required to produce the observed error in optical loss. (The pump current would need to vary from 60 mA to 20 mA to cause an optical loss error of around 0.1 cm^{-1}. Such a large variation between trials is unlikely to go unnoticed). The temperature of the intensifier is not directly controlled or monitored in this apparatus; it's conceivable that the in-

tensifier temperature *does* correlate with the measured value of optical loss. This could be investigated most directly in future work via an additional temperature probe within the casing of the ICCD.

Further minimisation of t$_{\textbf{total}}$

The centre wavelength to which the spectrometer is calibrated may be varied such that the spectral intensity peaks shown in Figure 9.4.a) are not collected by the ICCD. This means that exposure time may be increased, such that the dynamic range of the detector is — once again — fully utilised. Higher values of $I(h\nu)$ will thereby be collected across the new spectral region, reducing t_{total} for these photon energies.

It can be shown that it is more time-efficient to broaden the spectral region over which sufficient precision is accrued by using this method than it is to increase the duration of a single measurement of a single, broad spectral region. In particular, a precise measurement of optical loss at $h\nu'$ (internal loss) may be made more rapidly by adjusting the spectrometer calibration such that incident light of a photon energy higher than $h\nu'$ is not collected (and the signal increased to make full use of the detector dynamic range). However, this method is not used in the work shown in this document, as I deemed that it was worth slightly extending experiment durations to gather additional data for broad characteristics of optical loss spectra.

Drive Current Dependence of Measured Optical Loss coefficients

---

10.1   Introduction

It is an assumption of the multisection method that the earthing of unpumped sections causes free carriers to be swept away sufficiently rapidly that they will have a negligible effect upon measured optical loss. As optical loss is measured in passive, unpumped material in the multisection method, the measured optical loss is not expected to change as a function of the drive current of the pumped sections. Therefore measuring optical loss as a function of drive current is a useful test of systematic error and also of the appropriate operating regime for a particular sample. Carrier injection is expressed in terms of *current* rather than current densities in the following sections as that convention is most convenient to address the resistive network modelling therein. Current *densities* are discussed in Section 10.5 such that these findings may be applied to other device contact geometries.

The data shown in Figure 10.1 represents repeated modulated multisection measurements of a device of type $\#1_{BA}$ with a current pulse frequency of 15 kHz and a current pulse gate width of 2.0 μs. This measurement is carried out in a

Drive Current [mA]	CCD Exposure [s]
100	0.018
80	0.020
60	0.022
45	0.027
40	0.028
35	0.033
30	0.036
25	0.038
20	0.040
15	0.062
10	0.085
5	0.280

Table 10.1: Table of experimental conditions in drive current experiment

cryostat with the temperature controlled at 300 Kelvin. The drive current was varied in a range from 5 mA to 100 mA and the CCD exposure duration varied such that 8,000 counts were measured at the I_1 peak for each current. This was done such that the resultant precision in optical loss measurement is preserved, at the expense of experiment duration. (An additional experiment confirmed that the same drive current dependence of optical loss is observed if the exposure duration is kept constant at the expense of measurement precision). Optical loss error bars in Figure 10.1 demonstrate that the value of $3\sigma_{SEM}^{(A+\alpha_i)}$ calculated directly from standard deviations of I_1 and I_2 intensity data at each drive current has been made to be comparable by this variation of CCD exposure duration. ($3\sigma_{SEM}^{(A+\alpha_i)}$ is equal to 0.072 ± 0.006 cm^{-1} in each case, slightly smaller than that required to discriminate a change in optical loss of the order of 0.25 cm^{-1}). The CCD exposure duration at each measured drive current is given in Table 10.1:

As in Section 9.4, interband absorption by the material is taken to be negligible at a photon energy of $h\nu' = 1.65$ eV. It was deemed impractical to retain the ± 0.1 cm^{-1} precision discrimination discussed in Chapter 9 in this experiment, as the longer exposures required for precise measurement of lower currents substantially increase their respective experiment durations. A slightly relaxed precision

benchmark of approximately ± 0.25 cm^{-1} was taken, as a compromise. This reduced experimental durations by a factor of roughly 2.5, reducing the t_{total} required for the 100 mA measurement to approximately 3 minutes and the t_{total} required for the 5 mA experiment to 45 minutes. No drive current dependence was observed in the spatial distribution of emission from the device facet.
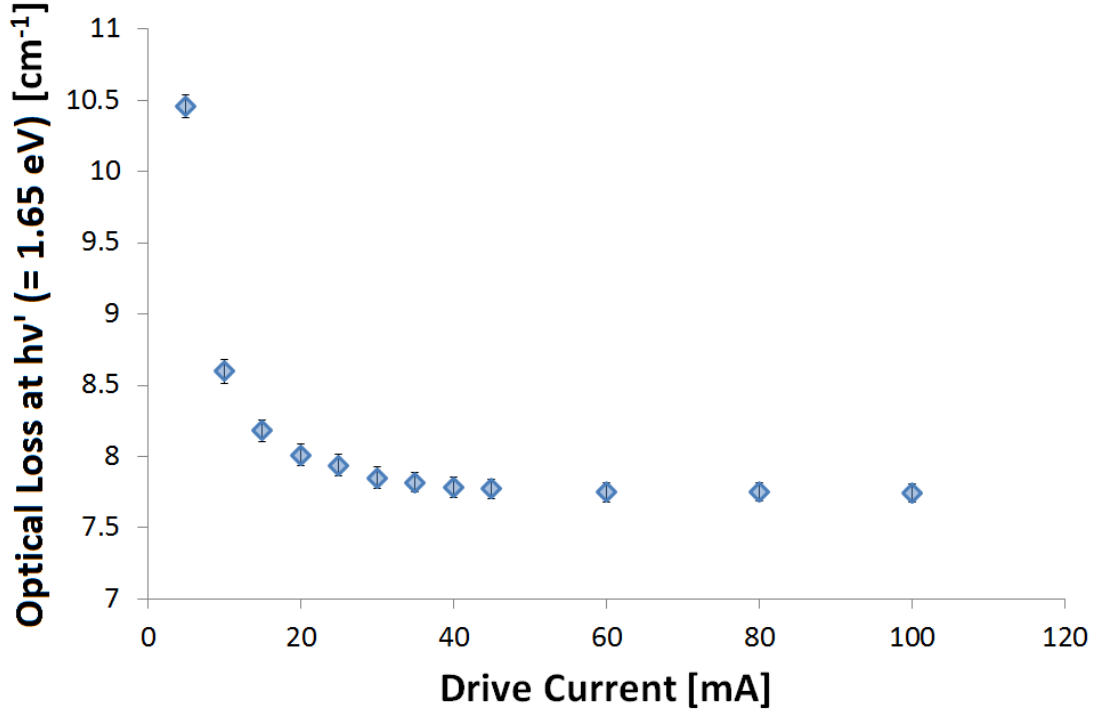
Figure 10.1: The Optical Loss coefficient for $h\nu' = 1.65$ eV for a sample of type $\#1_{BA}$ is plotted as a function of drive current in the pumped region.

An I-V mismatch between the two device sections would cause different fractions of injected carriers wasted to current paths which do not contribute to radiative recombination. (Two such current paths include carrier leakage from the active region and loss of carriers through the resistive intercontact region to the earthed contacts adjacent to the pumped contact). I speculate that the large systematic error at low drive currents is the result of the combination of the small mismatch in I-V characteristics between device sections and the finite resistance between device sections. This source of systematic error is exacerbated in modern

devices due to the prevalence of highly doped cap layers, which reduce resistivity in material between segmented contacts and hence increase the proportion of total injected current lost through this current path. Note that the measured intercontact resistance of the devices used in this thesis is typically of the order of hundreds of Ohms, an order of magnitude lower than what was once considered acceptable in a test device. The analysis within this chapter will allow the management of this systematic error in devices with heavily doped cap layers.

It is useful to consider a intercontact injection efficiency, η_{diode}; the fraction of total current which is not lost to an intercontact current path to earth. In order to do so, the current paths in this model must be examined. The simple circuit diagram shown in Figure 10.2 identifies current paths which do and do not pass through the device active region.
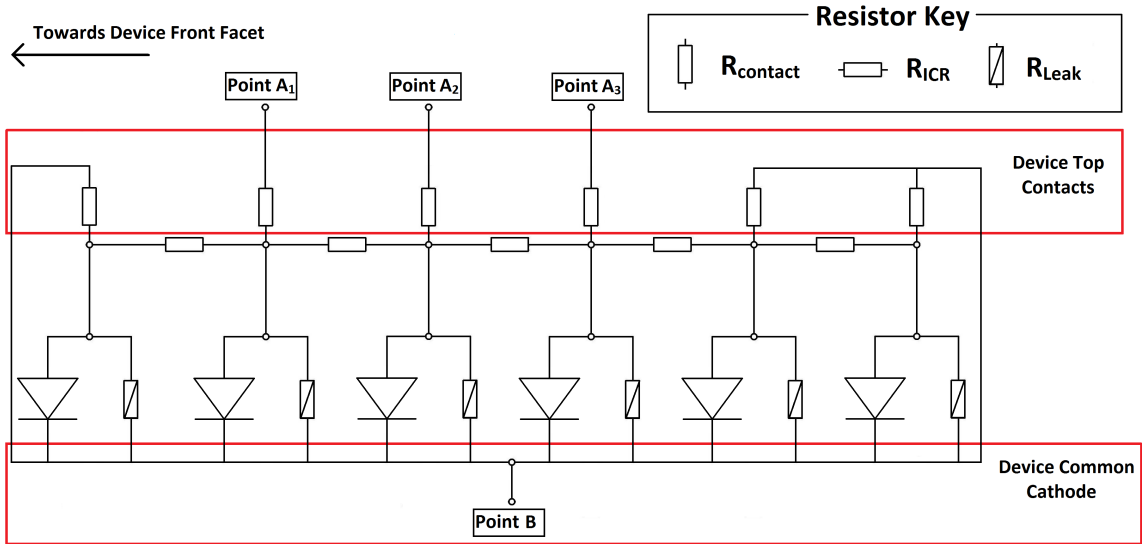
Figure 10.2: An simple circuit diagram for a multisection method device. The row of components at the top of the figure represents the many top metal contacts of a device. Each metal contact has a corresponding diode and leakage resistor representing a current path to the common cathode through the layers of the device. Whilst pumping a particular section, additional current paths exist through the intercontact etch to neighbouring device sections. Three top contacts (labelled as Points A_1, A_2 and A_3) are connected to TO header pins and all other contacts are connected by epoxied wires to the device cathode. The red boxes relate regions of the schematic to the device geometry of the multisection method.

The vertical lines at the top of the circuit diagram shown in Figure 10.2 represent the segmented top contacts of a multisection method device. Each of these contacts is associated with some contact resistance, $R_{contact}$. Three sections of this device, denoted A_1, A_2 and A_3 in Figure 10.2, are connected by epoxied wires to TO header pins and can hence be pumped. These correspond to the sections which produce I_1, I_2 and a third adjacent section, as indicated. The other three sections are connected by epoxied wires to the copper block upon which the device is mounted, and hence the cathode of the device. In a multisection optical loss measurement, while a particular section is pumped, all other top contacts are earthed. The six pairs of parallel components in the lower section of the circuit diagram represent radiative and leakage currents through each of the device contacts. In this treatment, the term 'pumped diode' refers to the current path by which current travels directly through the active layer of the material without passing through any R_{ICR} resistors. Conversely, the term 'unpumped' diode refers to any path by which current passes through the device active region having passed through some intercontact resistance (at least one R_{ICR}). As the cap layer is highly p-doped in the devices examined in this thesis, the metal-semiconductor interface at the device top contact is assumed to be approximately ohmic and $R_{contact}$ is assumed to be small with respect to the intercontact resistance, R_{ICR} (which is determined to be roughly 400 Ω in the analysis given in Section 10.2).

A critical feature of this analysis is that the I-V characteristic of the current path through the active region $(R_{diode}(V))$ is diode-like. No knowledge is assumed of current leakage process. It can be shown that if current leakage increases proportionally with the radiative current passing through the active region then it will not affect the measured optical loss. This proportionality is assumed in this analysis, and hence current leakage is neglected such that the loss of current through 'intercontact' paths can be evaluated in isolation.

10.2   I-V Measurement

I-V measurements were made across the section contacts corresponding to I_1 and I_2 as well as between these top contacts for the device measured in Figure 10.1. These measurements are described in this chapter as the 'Diode' and 'Intercontact' I-V characteristics respectively and are plotted in Figure 10.3.

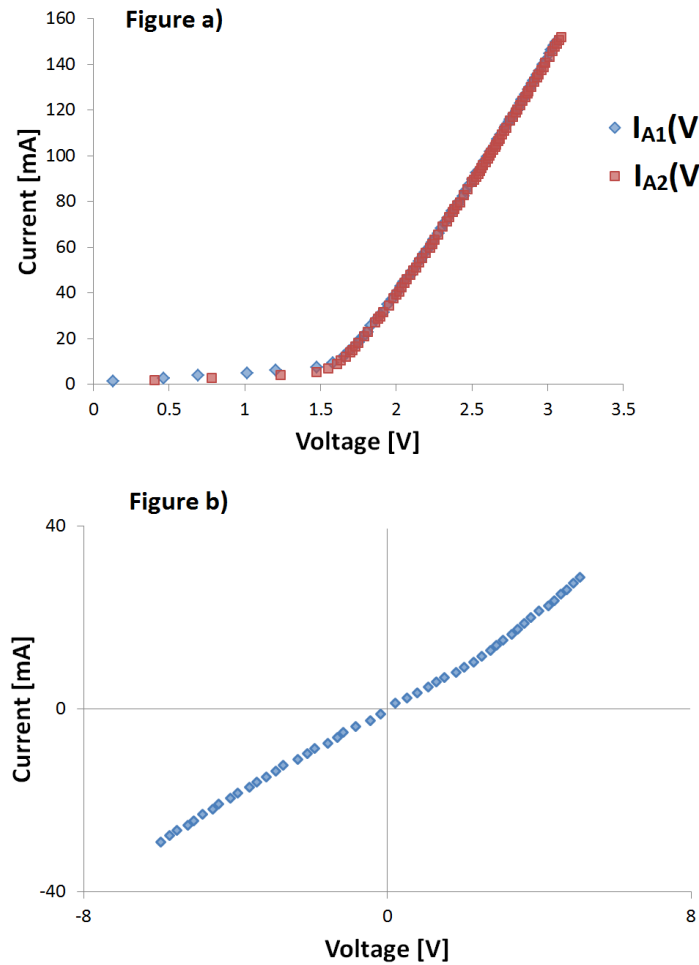Figure 10.3: Figure 10.3.a) demonstrates the I-V characteristics of the diode in forward bias (measured between points A and B in Figure 10.2) . In the key, $I_{A1}(V)$ and $I_{A2}(V)$ refer to the sections associated with light intensities I_1 and I_2 respectively. Figure 10.3.b) demonstrates the (approximately ohmic) intercontact I-V characteristic (measured between points A_1 and A_2 in Figure 10.2).

The I-V characteristic shown in Figure 10.3.a) was measured between points A_i and B (as indicated on Figure10.2) for the device top contacts corresponding to I_i. The top contact associated with point A_3 was not earthed. A_2 was not earthed while A_1 was measured and vice versa. This lack of earthing minimised the current lost to intercontact paths. (However, the contact to the left of A_1 in Figure 10.2 is permanently connected to the common cathode by an epoxied wire.) The I-V characteristic approximates that of the current path across the diode. At typical operating currents (100 mA), the static resistance of this current path is around 20 Ω.

The intercontact I-V characteristic was measured between point A_2 and points A_1 and A_3 in parallel, such that the conditions of an optical loss measurement were approximated and is plotted in Figure 10.3.b). The device common cathode was left floating such that no current is drawn through the diode.

The third quadrant data was acquired by reversing the positions of the I-V terminals. In normal device operation below the turn-on voltage of the PN junction, (and neglecting diode leakage current) the diode current path draws negligible current and the characteristic described in Figure 10.3.b) is hence representative of the I-V of an intercontact current path. The measured slope resistance in Figure 10.3.b) is 200 Ω and approximately ohmic. As there are two earthed neighbouring contacts, neglecting $R_{contact}$, there are two R_{ICR} in parallel in the equivalent circuit in this measurement. Hence, the data shown in Figure 10.3.b) is not directly representative of R_{ICR}, but of two parallel current paths consisting of one R_{ICR} and one $R_{contact}$. It can be calculated that a single intercontact current path corresponds to a resistance of 400 Ω. This view is also appropriate when top contacts further from the pumped section are earthed, rather than floating (such as in an optical loss measurement) as the two adjacent intercontact 'resistors' are taken to contribute to the combined resistance of the intercontact path, as $R_{contact}$ is assumed small enough that its resistance is dominant in parallel with either R_{ICR} or the resistance of an 'unpumped' diode current path. Therefore, only the nearest R_{ICR} in either direction need be practically considered.

It is assumed in further analysis that the majority of the resistance in this path

is due to intercontact resistance (due to the etch through the upper, conductive layers) rather than due to the contact of the metalisation, $R_{contact}$. Based upon the observation that the intercontact resistance, R_{ICR} is 400 Ω and the assumption that $R_{contact}$ is very small, the circuit diagram can be reduced to that shown in Figure 10.4 where R_{ICR}^{Equ} describes the resistance due to R_{ICR} and 'unpumped' diode resistance in two parallel intercontact paths into regions on either side of a pumped device section.

In the context of Figure 10.4.a), the I-V characteristics shown in Figure 10.3.a) describes a current path through the central contact resistance and the central diode. The I-V characteristic shown in Figure 10.3.b) corresponds to a current path through the central contact resistance, through both of the intercontact paths then through top contacts to earth.
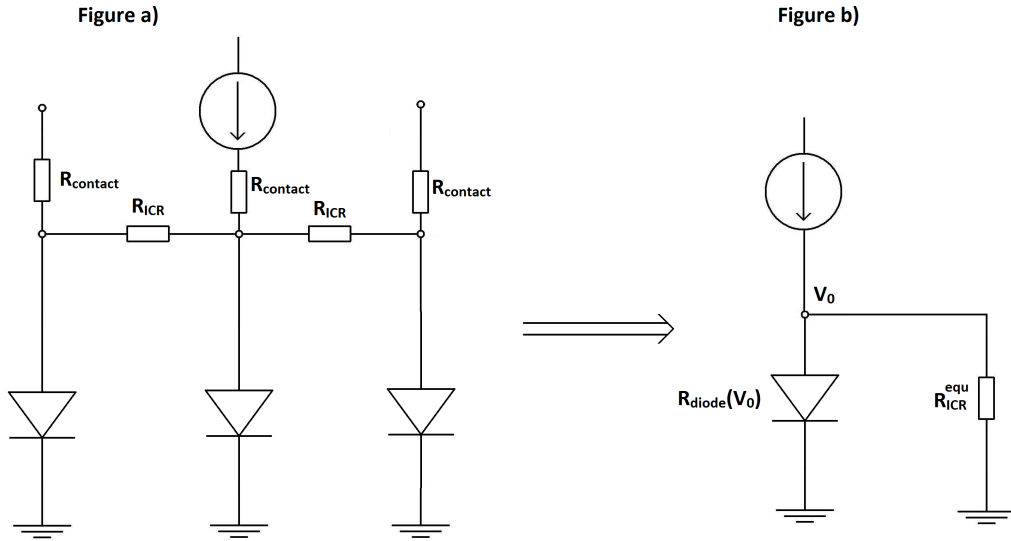

Figure 10.4: Figures 10.4.a) and 10.4.b) represent progressive simplifications of the effective circuit diagram introduced in Figure 10.2.

Assuming a negligible voltage drop over the input contact resistance, the voltage beyond the first contact resistor is approximately equal to the input voltage, V_0. The voltage drop of V_0 in crossing one of the intercontact resistors (to the

left and right diodes of Figure 10.4.a) is determined by the parallel resistance of a contact resistor with an 'unpumped' diode. As some voltage drop occurs over the intercontact resistor, the voltage across the left or right 'unpumped' diode is less than V_0. Therefore the resistance of the 'unpumped' diode is greater than that of the 'pumped' diode and also large in comparison with $R_{contact}$. As previously stated, the parallel resistance of the unpumped diode and $R_{contact}$ is comparable with $R_{contact}$ and small compared with R_{ICR}. The voltage across the 'unpumped' diodes is therefore small compared with V_0 and therefore'unpumped' diodes do not reach their turn-on voltage. Based upon this observation, the behaviour of 'unpumped' diodes can be simplified by defining a piece-wise *low voltage* resistance. $I_{A1}(V))$ and $I_{A2}(V))$ (as introduced in Figure 10.3.a)) are described well by resistances of 286 Ω and 196 Ω respectively in this low voltage regime. The resistance below threshold of the unmeasured 'unpumped diode' current paths are assumed to have a resistance equal to the (low voltage regime) average of sections $I_{A1}(V))$ and $I_{A2}(V))$ in this analysis.

Electronic behaviour of an intercontact path is treated using the single value of resistance taken from the I-V characteristic shown in Figure 10.4.b). (Measurements on other devices with more connected top contacts suggest that if metallisation is of sufficient quality to result in matching diode I-V characteristics between device sections, the intercontact resistances between different adjacent sections also tend to match well).

As calculations of the resistive network shown in Figure 10.2 demonstrate that the low value of $R_{contact}$ causes it to dominate the resistor network beyond the first R_{ICR} in either direction from the pumped section. The combined resistance of any number of device sections (as indicated in Figure 10.2) in either direction from the pumped section is hence approximately equal to the sum of $R_{contact}$ and R_{ICR}. The total resistance of intercontact paths is equivalent to the resistance taken from Figure 10.4.b). This reduces the resistance due to intercontact current paths in this equivalent circuit to be R_{ICR}^{equ} (as shown in Figure 10.4.b)), calculated to be approximately 200 Ω.

10.3   Introducing Intercontact Efficiency

At low values of current, the resistance of the 'pumped' diode is comparable with R_{ICR}^{equ} and a larger fraction of the total injected current is lost to the intercontact current paths. Additionally, the mismatch between I_1 and I_2 I-V characteristics is fractionally larger at lower drive currents. These processes cause a variation in the relative efficiency of injection between device sections that is dependent upon drive current.

By defining an intercontact injection efficiency, η_{diode}^i, to be the fraction of the total drive current which reaches the active region upon pumping the device section corresponding to I_i — rather than being lost to top contact earthing connections through intercontact current paths —, Equation 10.1 can be obtained:

$$\eta_{diode}^i(V_0) = \frac{I_{diode}^i}{I_{total}^i}(V_0) = \frac{V_0}{R_{diode}^i(V_0)}\frac{R_{total}^i(V_0)}{V_0} \tag{10.1}$$

Equation 10.1 can be rearranged to give Equation 10.2:

$$\eta_{diode}(V_0) = \left(\frac{1}{\frac{R_{diode}^i(V_0)}{R_{ICR}^{equ}}+1}\right) = \left(\frac{1}{\frac{R_{diode}^i(V_0)}{200\Omega}+1}\right) \tag{10.2}$$

This quantity can be calculated for each device section from the $R_{diode}(V_0)$ function of that section, which can be achieved from manipulation of the data shown in Figure 10.3.a). $\eta_{diode}(V_0)$ defines the fraction of the nominally injected current which passes through the diode and may contribute to the emission of photons in the active region. At a drive current of greater than around 50 mA, in a typical multisection device, η_{diode} is around 0.8 for both device sections. η_{diode} is more sensitive to differences in device I-V characteristics in the low drive current regime, where the resistance of the diode is comparable to that of the combined resistance of the intercontact current paths. This is explored further in Figure 10.5.a).

Assuming that a fixed fraction of the current passing through the diode con-

tributes to light emission, the light generated upon pumping the device section corresponding to I_i is reduced by a factor of $\eta_{diode}^i(V_0)$. Hence, at their respective edges which are nearest to the front facet, section 1 produces a light intensity equal to $I_0^{ideal}\eta_{diode}^1$ and section 2 produces a light intensity equal to $I_0^{ideal}\eta_{diode}^2$, where I_0^{ideal} is the value of I_0 which would be collected if there were no loss of current to intercontact paths. (I_0 is introduced in Section 1.3.3 and discussed further in Section 1.3.5). This treatment neglects prefactors describing the fraction of total emitted light that is collected by the ICCD, following the convention introduced in Section 1.3.5. This is justified as the quotient of the two intensities constitute an optical loss measurement and any common collection efficiency will factor out.

Accounting for optical loss in propagation through appropriate lengths of unpumped material for each device section, this corresponds with *measured* light intensities of $I_0^{ideal} \, \mathrm{e}^{-(A+\alpha_i)L_s} \, \eta_{diode}^1$ and $I_0^{ideal} \, \mathrm{e}^{-2(A+\alpha_i)L_s} \, \eta_{diode}^2$ for the two device sections respectively. Substituting these values into the Multisection optical loss equation (Equation 1.16) results in the expression given in Equation 10.3. For the purposes of this investigation, it is more convenient to express η_{diode} as a function of total injected current I_{drive}, than of voltage. (To be clear, I_{drive} always refers to a pump current and I with a numerical subscript always refers to an edge-collected light intensity in this thesis).

$$(A + \alpha_i)_{meas} = (A + \alpha_i)^{true} + \frac{1}{L_s} \ln\left(\frac{\eta_{diode}^1(I_{drive})}{\eta_{diode}^2(I_{drive})}\right) \qquad (10.3)$$

Hence, the error in measured optical loss due to mismatch of I-V characteristics between the two device sections is given by Equation 10.4:

$$\Delta(A + \alpha_i)(I_{drive}) = \frac{1}{L_s} \ln\left(\frac{\eta_{diode}^1(I_{drive})}{\eta_{diode}^2(I_{drive})}\right) \qquad (10.4)$$

192

10.4 Application of Intercontact Efficiency to Experimental Data

$\Delta(A + \alpha_i)(I_{drive})$ has been calculated using $\eta_{diode}(I_{drive})$ characteristics measured for a device of type $\#1_{BA}$ as described in Section 10.1. $\eta_{diode}(I_{drive})$ functions derived from the two I-V characteristics shown in Figure 10.3.a) are plotted in Figure 10.5.a). The large difference that the slight I-V mismatch makes to this quantity at low values of drive currents is critical to the derived systematic error in optical loss. As the raw I-V data is measured at different intervals of current and voltage for each device section, piece-wise fitting of diode injection efficiencies was carried out such that these values could be entered into Equation 10.4 to obtain the data shown in Figure 10.5.b).

The optical loss of the same device was measured as a function of I_{drive}. $\Delta(A + \alpha_i)$ was calculated from experimental data by subtracting each value of optical loss from the average value of $(A + \alpha_i)$ measured at high drive currents (for which the observed systematic error becomes negligible). These experimentally observed values of $\Delta(A + \alpha_i)$ are plotted in Figure 10.5.b) alongside modelled values of $\Delta(A + \alpha_i)$ calculated from Equation 10.4 using the experimental values of $\eta_{diode}(I_{drive})$ from Figure 10.5.a). Figure 10.5.b) shows that a simple model of the effect of intercontact resistance and I-V mismatch retains the important trends of experimental measurement of $\Delta(A + \alpha_i)(I_{drive})$. A substantial systematic error exists for small values of drive current. For this device, this systematic error becomes negligible for device currents above around 30 mA. This is below the typical operating conditions in an optical loss measurement. This effect must be noted in any future experimental work which requires low pump currents (or measurement as a function of pump current). Additionally, it is sensible to repeat this process for new devices, in order to increase confidence in measurements made using said device.
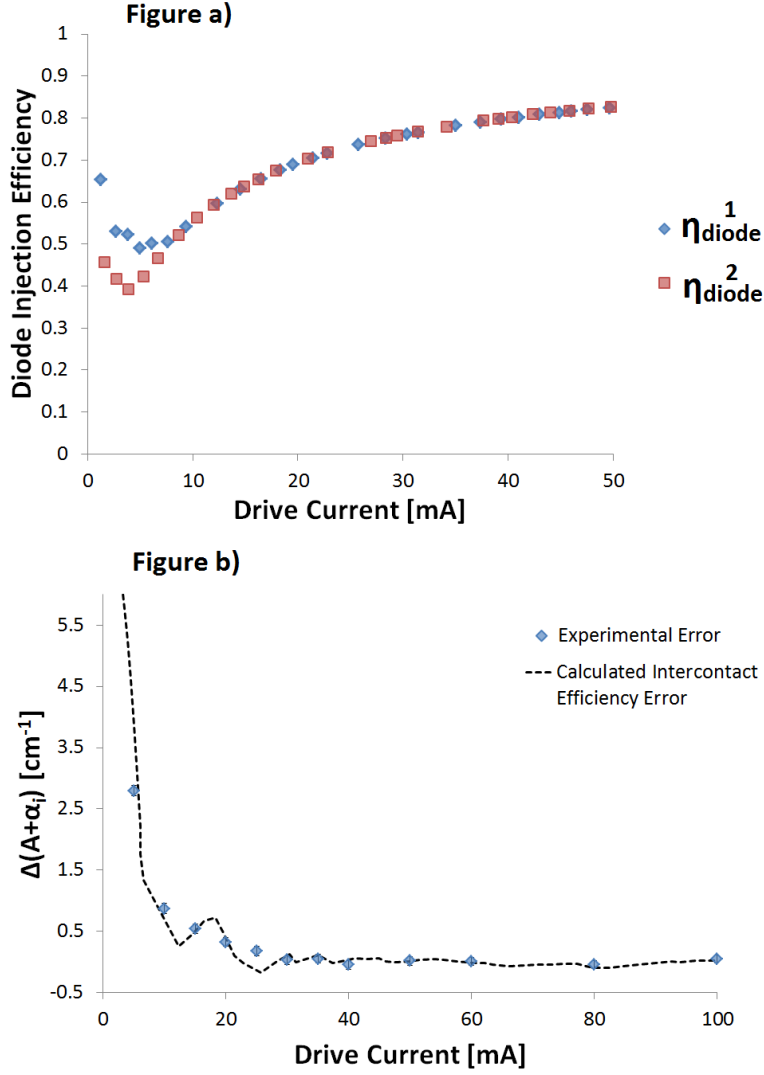
Figure 10.5: Values of $\eta_{diode}(I_{drive})$ are derived for each device section from the I-V measurements shown in Figure 10.3.a). The measured systematic error in an optical loss coefficient as a function of drive current is plotted next to the systematic error calculated from Equation 10.4.

At higher drive currents, there is no evidence of a current dependence of measured optical loss. This indicates that effects which become more pronounced as light intensities within the device cavity increase do not alter the ratio of I_1 to I_2. Further investigation of effects such as the reflection of light from the front facet and photon recycling in the passive region is not necessitated by this finding.

10.5 The effect of Device Temperature upon Drive Current dependence of measured Optical Loss

The temperature dependence of effects outlined in this chapter are of general interest. It is established in Section 10.4 that, for a particular device at a temperature of 300 Kelvin, there is a critical drive current, below which systematic error in an optical loss measurement exceeds 0.1cm^{-1}. The experiments outlined in Chapter 11 measure optical loss for device temperatures *greater than* 300 Kelvin. It is important to establish whether this critical drive current is different for temperatures above 300 Kelvin.

Optical loss spectra were measured for device temperatures of 325, 350 and 375 Kelvin at drive currents of 5, 10, 40 and 100 mA in each instance (using the corresponding exposures times given in Table 10.1). Otherwise experimental conditions were identical to those described in reference to the data shown in Figure 10.1.

Recall that in the 300 Kelvin data, optical loss was examined at a photon energy of $h\nu' = 1.65$ eV. This is taken to be the point at which interband transitions make a negligible contribution to the optical loss coefficient for this device. However, at device temperatures other than 300 Kelvin, the temperature dependence of the bandgap — described by Varshni's equation (Equation 1.12) — causes a relative change in the position of interband transitions within a sample. In order for a direct comparison of behaviour at different temperatures to be meaningful, this spectral shift must be accounted for. This is carried out by determining the spectral separation of $h\nu'$ from a prominent feature of the optical loss spectrum — the 1st optical loss peak, in this case — and examining the value of optical loss at this spectral separation from this feature at each temperature. (This spectral shift is described in more detail in Chapter 11). Observing a photon energy at a fixed energy separation from the 1st optical loss peak is justified for this device, as negligible temperature dependence of broadening is observed in features of the optical loss spectrum for the temperature range observed in this thesis.

At each device temperature, the value of optical loss at a drive current of 100 mA was subtracted from the optical loss at each other drive current to approximate the drive current dependent error. The measurements at the three new temperatures are compared to the 300 Kelvin case (plotted in Figure 10.5) in Figure 10.6.
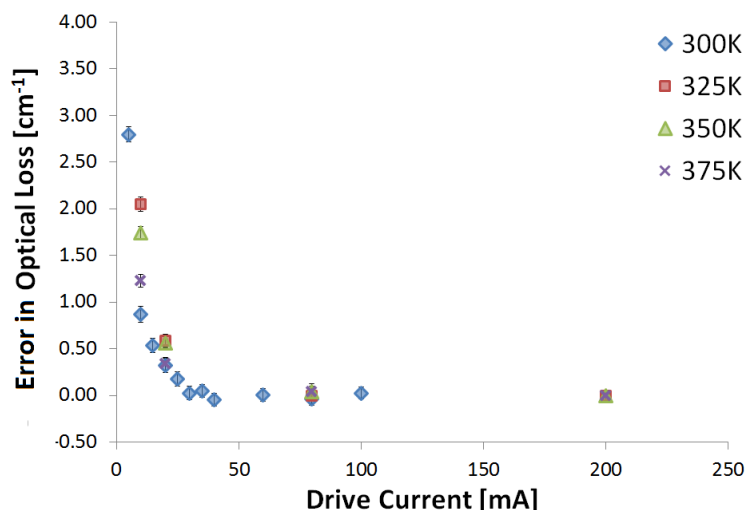
Figure 10.6: Error in optical loss as a function of drive current is compared for various device temperatures. The experimental data taken from Figure 10.5 is plotted against similar measurements for device temperatures of 325, 350 and 375 Kelvin.

It can be seen that a similar general trend of optical loss with current dependence is observed at each temperature, but that — at each drive current — the error in optical loss *decreases with increasing temperature*. This suggests that at temperatures above 300 Kelvin, the drive current at which the observed systematic error in optical loss becomes negligible is smaller than the corresponding current at 300 Kelvin. For this device, critical drive current is no greater for any device temperature (in the range considered in this thesis) than that at 300 Kelvin. The form of Equation 10.2 suggests that the temperature dependence of $\Delta(A + \alpha_i)(I_{drive})$ is due to temperature dependences of the diode or intercontact resistance causing relative changes between η^1_{diode} and η^2_{diode}.

In order to further comment on critical drive current as a function of device temperature, a least squares exponential fit of the drive current dependence of

Device Temperature [K]	Drive Current [mA]	Current Density [mA cm^{-2}] [$\times 10^4$]
300	22.0	14.$\dot{6}$
325	21.5	14.$\dot{3}$
350	21.0	14.0
375	19.0	12.$\dot{6}$

Table 10.2: Table of critical Current and Current Densities for discrimination of $\pm\ 0.0\dot{3}$ cm^{-1} changes in Optical Loss.

optical loss error at each device temperature was carried out. The resultant fitted functions are plotted in Figure 10.7.a). Thin vertical lines with colours that correspond to the plot legend mark the drive currents at which the systematic error in optical loss is equal to 0.1 cm^{-1}.

In the following discussion, the drive current at which the fitted optical loss error exceeds a particular error threshold is described as the '*critical*' drive current associated that particular threshold of systematic error. The critical drive current associated with a systematic error in optical loss of 0.1 cm^{-1}, for each device temperature, is marked by the blue series in Figure 10.7.b). It is also useful to evaluate the drive current at which error in optical loss can be considered *small* with respect to the ± 0.1 cm^{-1} uncertainty aim of this project. An upper bound upon *this* value is taken to be 0.0$\dot{3}$ cm^{-1}. The critical drive currents corresponding to an error in optical loss of 0.0$\dot{3}$ cm^{-1} is also plotted in Figure 10.7.b) and the critical currents and associated current densities are given in Table 10.2. (Current densities are calculated from the area of the top contact of each section, based upon a section length of 300 μm and an oxide stripe width of 50 μm.) The critical drive current associated with 0.1 and 0.0$\dot{3}$ cm^{-1} optical loss error thresholds can both be seen to decrease with increasing device temperature. Figure 10.7.b) suggests that a drive current of 22 mA is sufficiently high to ensure that the systematic error in optical loss described in this chapter does not exceed 0.0$\dot{3}$ cm^{-1}. All precise measurements of optical loss within this thesis use much higher drive currents, of the order of 60 to 100 mA. Hence, error in optical loss due to intercontact current paths is negligible in this thesis with respect to the 0.1 cm^{-1} uncertainty aim.
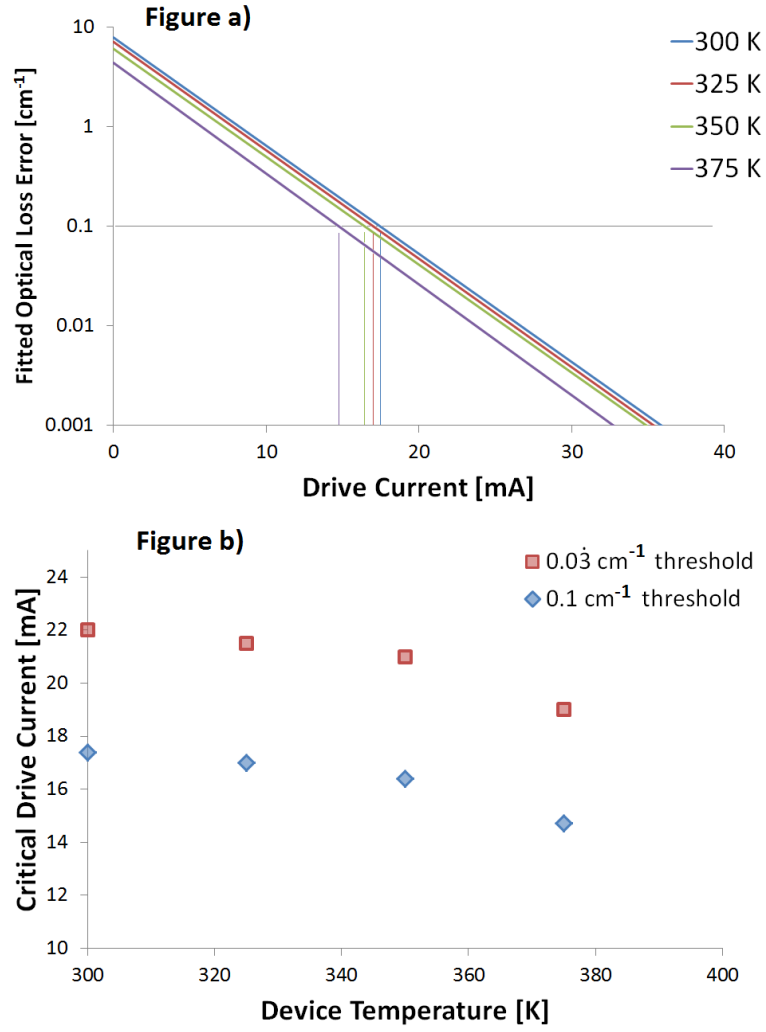
Figure 10.7: Figure 10.7.a) are the exponentials derived from least square fits of the optical loss error as a function of drive current for each measured device temperature. Figure 10.7.b) plots values of 'critical' drive current at which optical loss errors exceed 0.1 cm^{-1} and $0.0\dot{3}$ cm^{-1}.

Temperature dependence of Modulated Multisection Optical Loss in InP Quantum Dots

In this chapter, the high precision developed in Chapter 9 is combined with the suppression of drift error described in Chapter 8, and the resultant low uncertainty is applied to specific study not previously possible by conventional methods. The chosen demonstration is a measurement of temperature dependence of internal mode loss in a quantum dot laser structure. This information is of particular importance in high power lasers which are intended to operate above room temperature.

A device of type $\#1_{BA}$ was pumped with a pump current of 60 mA, a pulse frequency of 20 kHz, a current pulse duration of 2.2 μs and a gate width of 2.0 μs. Following the arguments found in Chapter 9, 482 modulation cycles were measured with an m value of 50.

11.1 Maintenance of constant Optical Loss precision in temperature-dependent intensity measurements

In this chapter, optical loss spectra are examined at device temperature intervals of 5 Kelvin, from 300 to 380 Kelvin. In preliminary measurements, it was observed that measured intensities — I_1 and I_2 — decreased with increasing device temperature as well as shifting with the bandgap of the InP Quantum Dots (see Equation 1.12). This is shown in Figure 11.1.a). In order for the resultant precision of an optical loss measurement to be preserved, either the device light output, the ICCD gate period, the number of measurements within a modulation period (m), or the number of modulation periods must be increased. Varying the number of modulation periods is preferable, as doing so preserves the conditions of each modulation cycle and allows a direct comparison of the intensities averaged over each modulation period at different device temperatures. Standard deviation (and hence precision) decreases more drastically with temperature near the intensity peak of the emission spectrum, where a greater optical loss in the unpumped material results in a greater reduction in I_2 intensities. Accordingly the compensation required to maintain precision is carried out upon the peak value of intensity rather than at $h\nu'$. This will *overcompensate* for the decrease in precision with increasing temperature at $h\nu'$ and maintain precise measurement across a broad spectral region. In optimising the precision of the measurement *at each temperature*, the combined duration of all measurements in minimised.

The number of modulation cycles that must be acquired to maintain a particular precision at an intensity peak which is decreasing in magnitude with temperature can be established by determining the optical loss standard deviation at each temperature (through the application of Equation 9.1 to measured intensity data) and increasing N_{cycle} in Equation 9.1 appropriately. The key details of the process are summarised in Figure 11.1.
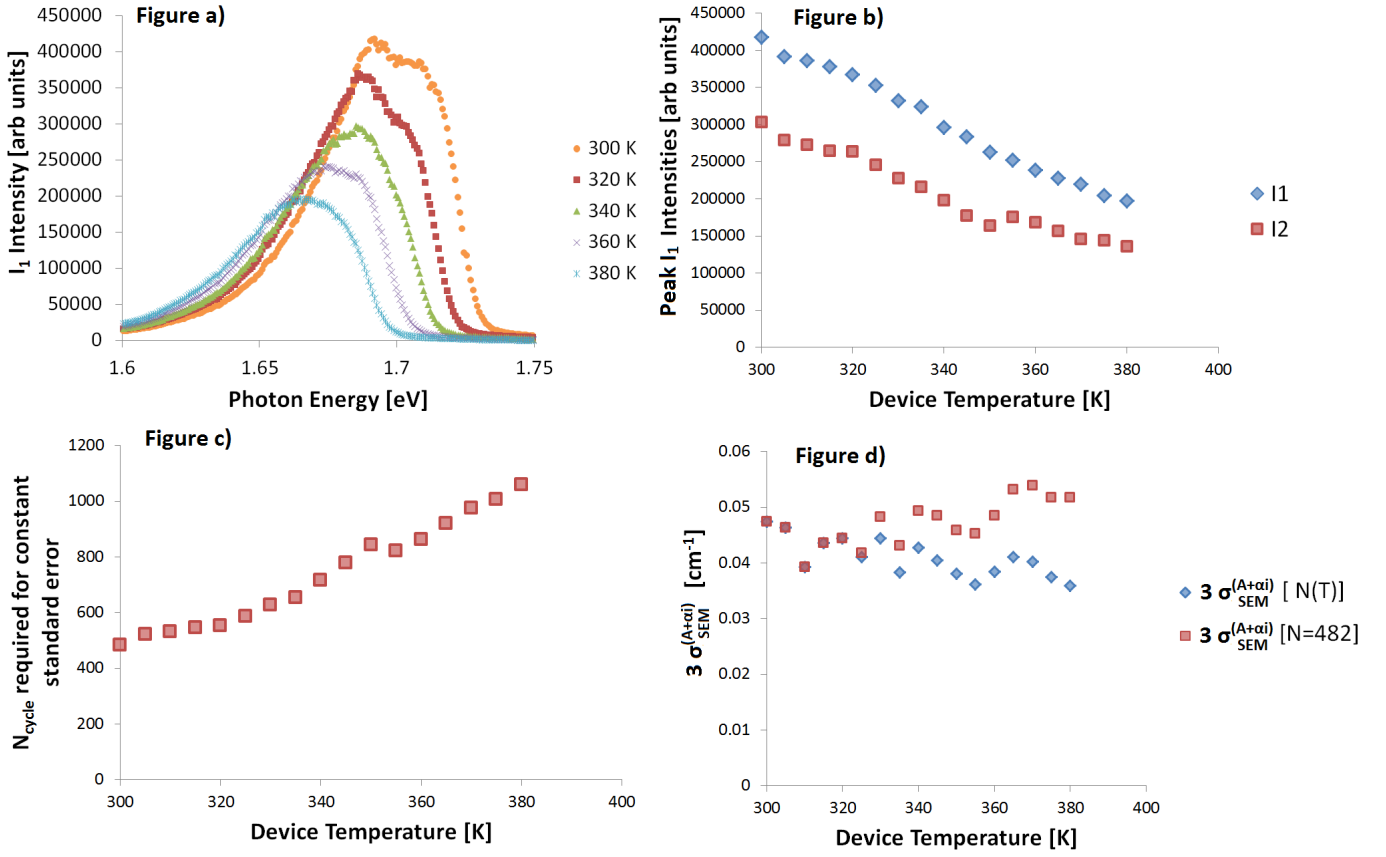
Figure 11.1: Plots summarising the increase in N_{cycle} required to compensate for the temperature dependence of emitted intensities. Figures 11.1.a) and 11.1.b) depict temperature dependence of measured intensities. Figure 11.1.c) depicts the number of modulation cycles required in order to maintain the $3\sigma_{SEM}^{(A+\alpha_i)}$ precision of $\pm 0.0\dot{3}$ cm^{-1} (derived from I_1 and I_2 values corresponding to the I_1 peak at each temperature. Figure 11.1.d) demonstrates that this increase in N_{cycle} has the desired effect upon precision in the experimental data given in Figure 11.2.

The decrease in peak measured I_1 intensity is shown in Figure 11.1.a). Data is plotted every 20 Kelvin, such that the plot is not too cluttered. Measured I_1 and I_2 values corresponding to the I_1 peak photon energy are given at 5 Kelvin intervals in Figure 11.1.b). The resultant number of cycles required to maintain precision is plotted as a function of device temperature in Figure 11.1.c). Figure 11.1.d) demonstrates calculated values of $3\sigma_{SEM}^{(A+\alpha_i)}$ corresponding to values of standard deviation observed in the Optical Loss data shown in Figure 11.2, at the photon energy of the minimum value of optical loss below the bandgap for each

temperature. It is demonstrated that — at this photon energy — $3\sigma_{SEM}^{(A+\alpha_i)}$ (the chosen measure of precision in this document) increases with device temperature if the number of modulation periods, N_{cycle}, is equal to 482 and that $3\sigma_{SEM}^{(A+\alpha_i)}$ decreases if N_{cycle} is increased to the values depicted in Figure 11.1.c). Hence, these N_{cycle} vaues are used in the following investigation.

The origin of the temperature dependence of the peak intensities in Fig 11.1 is not known but is consistent with established mechanisms. The heterobarrier potential wells which facilitate carrier confinement in laser structures have a finite well depth. Above zero Kelvin, the thermal spread of carriers in energy — described by the Fermi function (Section 1.2.5) — results in some fraction of the injected carriers having sufficient energy to escape from the well. This fraction increases with increasing device temperature as the Fermi distribution broadens. As the device was operated at constant drive current, the reduction in radiative efficiency associated with this process ought to decrease emitted intensity with increasing device temperature [4, 27].

Temperature dependent gain saturation has been demonstrated in quantum dots devices [57]. This effect has been associated with a clamping of the Fermi level caused by the relatively high density of states of the wetting layer (compared with that of the quantum dots). This clamping acts to suppress the occupancy of dot states and hence cause a reduction in emission processes in the dots which worsens with increasing device temperature (as the broadening of the Fermi function increases its overlap with the wetting layer states). If required in future work, an investigation of the temperature dependence of gain-current characteristics of this device could confirm this.

11.2 The precise measurement of optical loss as a function of device temperature

As stated, optical loss measurements were made at device temperatures from 300 Kelvin up to 380 Kelvin in steps of 5 Kelvin. As alignment was disturbed by thermal expansion of the apparatus, the device was realigned once the temperature controller readout had stabilised within 0.05 K of the set temperature. The apparatus was then left for a 10 minute settling period before the alignment was checked. Measurements were made initially while increasing the device temperature. Temperature was varied upwards from 300 to 350 Kelvin on one day, then from 355 to 380 Kelvin on a second day. On the third day of the experiment, a measurement was made every 20 Kelvin while decreasing the device temperature back down to 300 Kelvin. The upward and downward data can be compared to determine whether the trend is reproducible and to investigate the effect of temperature lag upon the experiment. Every fourth optical loss spectrum is plotted in Figure 11.2.a). The temperature dependence of the bandgap is visible in the spectral shift of the 1st optical loss peak. These peaks were manually colocated, such that the optical loss peak for spectra at each temperature overlies with the 1st optical loss peak at 300 Kelvin. These colocated peaks are shown in Figure 11.2.b). Having colocated the optical loss peaks — thus compensating for the shift in relative positions of transitions due to the changing device temperature — the data is easier to interpret. The behaviour of these optical loss spectra at photon energies below the absorption edge are examined in more detail in Figure 11.2.c). Figure 11.2.d) shows the temperature dependence of the photon energy of the 1st optical loss peak and of the photon energy of the minimal value of optical loss below the absorption edge. Using an appropriate photon energy offset, the gradient of the temperature dependence described by the Varshni equation is shown to approximately match that of the experimental data (using parameters stated within the figure caption). This suggests accuracy of the device temperature measurement.
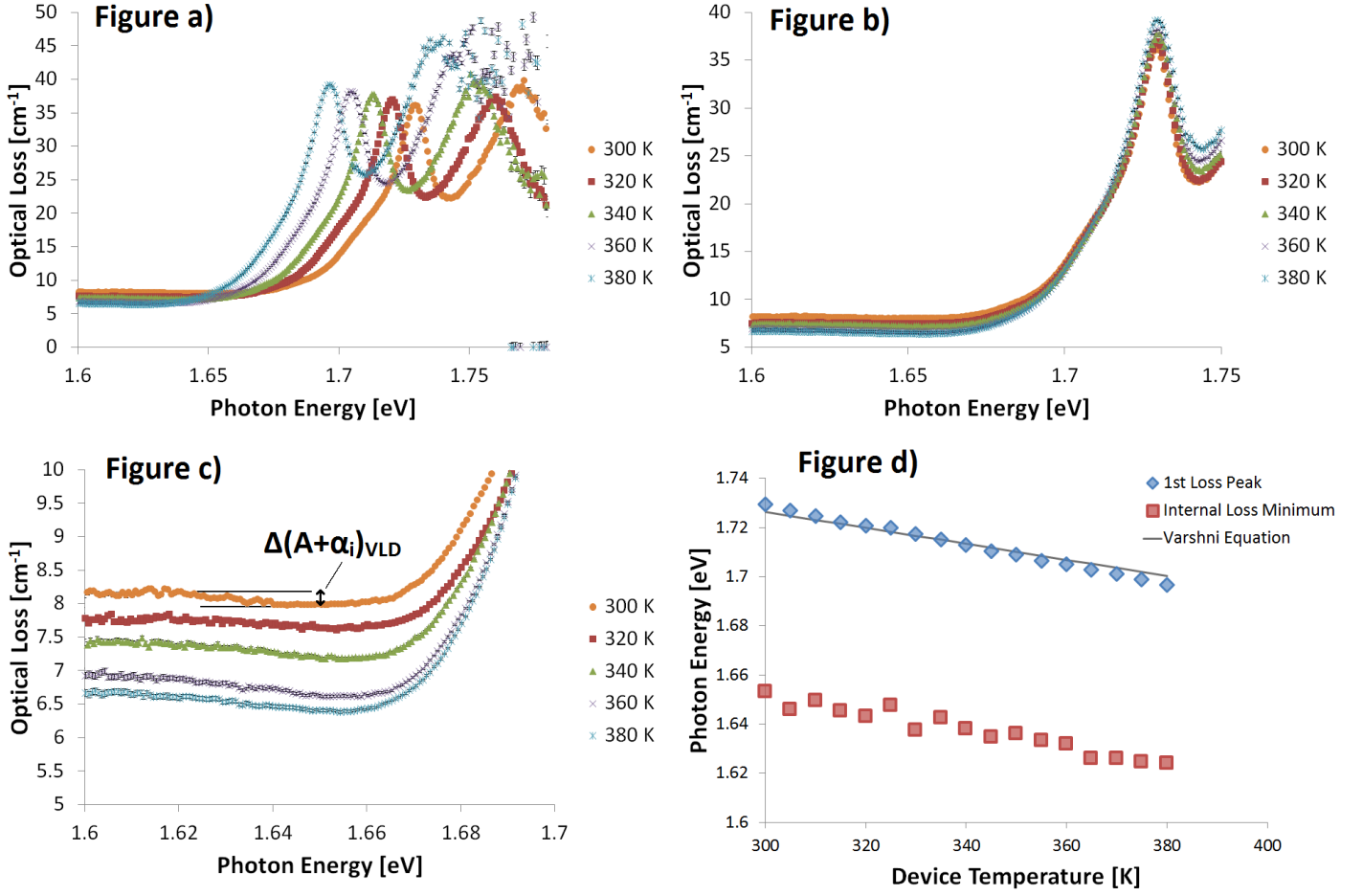
Figure 11.2: Figure 11.2.a) shows the optical loss spectra measured at various device temperatures. Figure 11.2.b) shows the same spectra, but shifted such that the optical loss peaks overlie. Figure 11.2.c) shows the same *shifted* optical loss spectra as in Figure 11.2.b), but with axes scaled to examine photon energies below the device absorption edge. Figure 11.2.d) examines the photon energy of key features of the data as a function of device temperature. Varshni parameters are $\alpha = 3.63 \times 10^{-4}$ eV K^{-1} and $\beta = 162$ K and E_g value of 1.421 eV [58]. (This value is 0.376 eV from the stated bandgap of InP.) $3\sigma_{SEM}^{(A+\alpha_i)}$ error bars are plotted on each optical loss spectrum, but are typically smaller than their associated data marker.

Due to the low uncertainty developed in this thesis, spectral and temperature dependence of the optical loss below the absorption edge can be discriminated in the data shown in Figure 11.2.c). The minimum measured value of optical loss below the absorption edge ranges from 8.13 cm^{-1} at 300 Kelvin to 6.42 cm^{-1} at 380 Kelvin. (This temperature dependence is examined in more detail in Figure

204

11.3.a)). A feature at below the absorption edge (at roughly 1.61 eV) is visible in this data due to the high precision of each measurement.

Any features of the optical loss spectrum which are associated with InP quantum dot interband transitions can be expected to be respectively spectrally colocated in Figure 11.2.b). Contrarily, temperature dependence of the spectral position of a feature in these plots would indicate that it is associated with an interband transition unrelated to the InP quantum dots, or that it is not associated to an interband transition at all. The low photon energy feature in this data (first discussed in Section 9.5) can be seen to be approximately colocated at the temperatures demonstrated in Figure 11.2.c). Thus this feature is associated with states which share the temperature dependence of the spectral shift of the InP bandgap. This suggests that this feature is either caused by quantum dots which are physically larger than those associated with the absorption peak around 1.72 eV (at room temperature) or caused by defect states whose temperature dependence of spectral position is bound to that of the InP bandgap. Previous work by Mohammed Al-Ghamdi on similar structures suggests that the former is the case [59]. These features correspond to the photon energies of a feature which he describes as '*very large dots*' (VLD).

The full characterisation of the VLD peaks is not possible in this data set as only the high energy side of the peak can be discriminated above $300K$. Examination of the ASE intensity spectra demonstrates that this is due to temperature dependence of the bandgap causing a red-shift of the feature past the edge of the intensifier. Full characterisation of this behaviour — in which the spectrometer grating is shifted and re-calibrated, such that the full VLD absorption peak is observed *at each temperature* — is recommended as future work. (For this new data to be useful, precision ought to be re-assessed such that data is sufficiently precise at photon energies lower than $h\nu'$). Low temperature measurements of emission from the VLD states has not yet been carried out.

In order to establish that the dot size of these proposed VLD states is feasible to an order of magnitude, a simple model was used to calculate dot sizes

corresponding to the first absorption peak and the VLD states. A 3-dimensional (cubic) infinite potential well model (as described in Equation 1.6) was used. This method makes the assumption that a separation of variables is appropriate and that an infinite well is an appropriate approximation of the confinement potential. Taking the bandgap of InP to be 1.34 eV at 300 Kelvin, the confinement energies associated with the observed absorption peak at 1.72 eV and the peak associated with the VLD peak are 0.38 and 0.27 eV respectively. m_h and m_e values for InP were taken to be $0.6m_0$ and $0.08m_0$ respectively (where m_0 is 9.11 $\times$ 10^{-31} kg). In this model, the 1.72 eV and VLD peaks correspond with dot lengths of $d = 6.5$ and 7.7 nm respectively. Quantum dot sizes of this order are feasible.

The largest optical loss peak at 1.725 eV as well as the small feature around 1.705 eV in Figure 11.2.b) are both colocated regardless of device temperature. This suggests that all of the features at the higher photon energy end of the optical loss spectra correspond to absorption by states of the InP quantum dots.

Having introduced the broad behaviour of the optical loss spectra (in Figure 11.2) using a subset of the measured device temperatures, the temperature dependence of key features of optical loss spectra at each measured device temperature must be examined. The temperature dependence of the first absorption peak and of the minimum value of optical loss at photon energies below the absorption edge are plotted in Figures 11.3.a) and 11.3.b) respectively. The values corresponding to the experiment in which spectra were acquired every 5 Kelvin as the device temperature was *increased* are depicted by *blue* data points in Figures 11.3.a) and 11.3.b). The values corresponding to the experiment in which spectra were acquired every 20 Kelvin as the device temperature was *decreased* are depicted by *red* data points in Figures 11.3.a) and 11.3.b).

The first observation from Figures 11.3.a) and 11.3.b) is that a systematic decrease in internal loss and increase in peak absorption has been observed, and that experimental scatter is small in comparison with the change in either quantity. Such a measurement would not be feasible with the conventional multisection method.
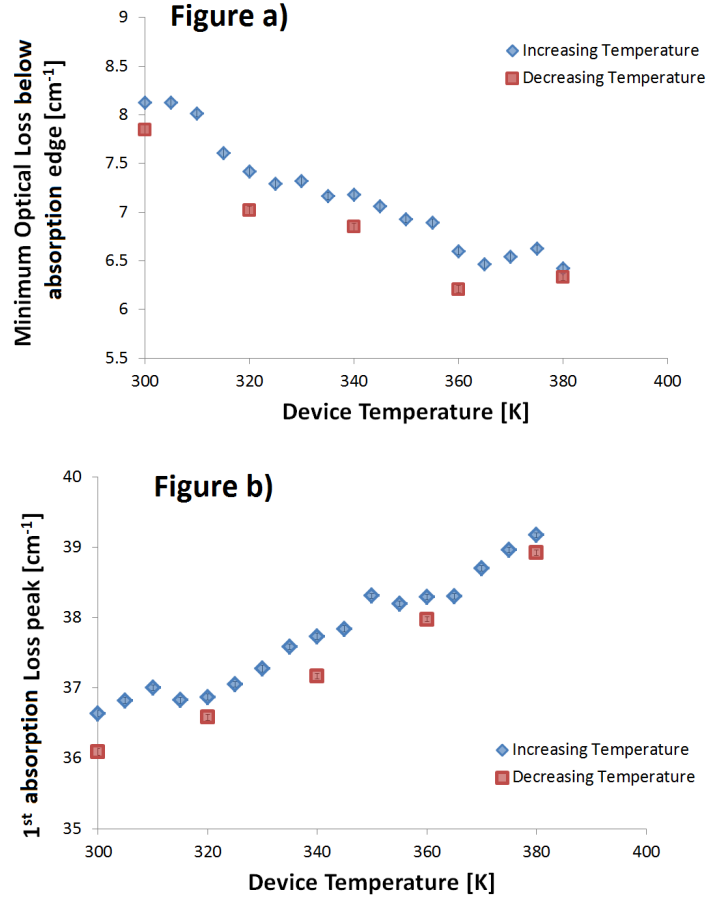
Figure 11.3: The minimum value of optical loss near the absorption edge and at the 1st peak are plotted as a function of device temperature in Figures 11.3.a) and 11.3.b) respectively. The difference in measured values between the cases of increasing and of decreasing device temperature are visible in both plots.

There is a systematic error between the upwards and downwards measurements depicted in both Figure 11.3.a) and in Figure 11.3.b) which is large with respect to the ± 0.1 cm^{-1} uncertainty aim of this project. Repeating this measurement such that spectra were collected every 20 Kelvin upwards on one day and then downwards on the following day produced a systematic error which was smaller and acting in the opposite direction (data omitted). This suggests that the difference between upward and downward observations is related to a day to day variability

in optical loss measurements, rather than lag between the cryostat temperature sensor readout and the actual device temperature. Error due to temperature lag is likely to be reproducible and — while the sign of the systematic error is consistent with temperature lag between the device and temperature monitor for low photon energies — it is not consistent with temperature lag at high photon energies. The origin of this systematic error has not been conclusively identified and is discussed in the Future Work section (Section 12.2). For the purposes of the discussion of temperature dependence of optical loss in this chapter, the systematic error associated with change in measurement direction or with measurement on different days will be neglected and only the blue data in Figure 11.3 will be considered. (It is assumed that systematic error was constant for the measurements with increasing temperature).

11.3   Interpretation of Temperature-dependent Optical Loss

Measured lateral spatial intensity distributions for I_1 and I_2 do not change shape with temperature. This suggests that electronic behaviour of the sample — rather than varying optical confinement — is the cause of the observed temperature dependence of optical loss.

The reduction in the minimum optical loss below the absorption edge with increasing device temperature that is shown in the blue series of Figure 11.3.a) has an associated gradient of -0.02 cm^{-1}K^{-1}.

The small feature below the absorption edge associated with 'very large dot' transitions is not stongly temperature dependent. The quantity $\Delta(A + \alpha_i)_{VLD}$ was introduced in Figure 11.2.c) and is useful in describing the magnitude of the 'very large dot' feature. It is defined as being the maximum value of the feature's peak optical loss with the minimum value below the absorption edge subtracted from it. $\Delta(A + \alpha_i)_{VLD}$ is equal to 0.2 cm^{-1} to a precision of ± 0.07 cm^{-1} at ev-

ery measured temperature. This suggests that the optical loss of the 'very large dot' feature is insensitive to device temperature, and that an additional process is causing the majority of the temperature dependence of optical loss at low photon energies.

Mathematical modelling of possible underlying mechanisms could provide insight into the physical processes occurring within this device. Assuming that an internal optical loss process — rather than one associated with absorption by the VLD states — is responsible for temperature dependence below what appears to be the absorption edge, then the temperature dependence of processes associated with internal loss is a sensible starting point. Cho et al. demonstrated that modelled Inter-Valance Band Absorption may *decrease* with increasing device temperature in InP Quantum Well structures [60]. The work of Krishnamurthy et al. demonstrates the possibility of decreasing free-carrier absorption in bulk InSb with increasing device temperature in both modelling and experimental measurements [61, 62]. The decrease in optical loss below the band edge with increasing temperature may correspond to a reduction of such an absorption process due to the redistribution of carriers in the device bandstructure. Similar modelling in future work would help to clarify this.

CHAPTER 12

Conclusion and Future Work

12.1   Conclusion

A modulated variant of the multisection method for optical loss has been devised, analysed in depth, and shown to effectively reduce systematic error corresponding to systemic drifts in intensity to acceptably small magnitudes. Following a detailed evaluation of precision, measurements of optical loss at a photon energy below the absorption edge and with a nominal uncertainty of better than ± 0.1 cm^{-1} were made. A series of 20 minute long optical loss measurements made within a single day has an average deviation of 0.017 cm^{-1} at a photon energy below the absorption edge. This order of uncertainty is not feasible using the conventional multisection method.

The reduction of systematic error associated with the modulated method was demonstrated in experimental data (Section 6.1) and an analytical quantification of this systematic error was found to be in good agreement with experimental data (Section 8.2.4). For typical large intensity drifts and experiment durations — for the apparatus used in this investigation —- the associated error is made negligible with respect to a ± 0.1 cm^{-1} uncertainty aim for modulation periods of 74 seconds or less.

The improvement in uncertainty afforded by the introduction of modulation and by the optimisation of precion in this project has revealed a day to day variability in measurements of optical loss below the absorption edge of the order of ± 0.25 cm^{-1}.

It is demonstrated in Chapter 3 that there exists a systematic error in optical loss measurements of broad area devices due to the lateral divergence of light in propagation towards the front facet. This error is absent in ridge waveguide devices due to their greater lateral optical guiding. A correction is derived in Section 3.1 and the resultant systematic error is acknowledged. It is demonstrated in Chapter 10 that a systematic error associated with the loss of current through the contact geometry is negligible for pump currents greater than approximately 22 mA for device temperatures of 300 Kelvin or greater.

The low uncertainty developed in this thesis is utilised in a systematic investigation of optical loss with device temperature in Chapter 11 in which spectral and temperature dependence of optical loss coefficients are evaluated in a fashion that would previously have not been possible. A reduction of internal loss with increasing temperature is observed with a gradient of –0.02 cm^{-1}K^{-1}.

Having optimised experimental conditions such that a precision of ± 0.1 cm^{-1} was achieved in a measurement of optical loss below the absorption edge, it was observed that repeated measurements in which a device is realigned each time result in a greater deviation than that predicted by precision. It is demonstrated in Section 9.7 that this error does not correlate with systemic drifts or with any metric of device misalignment. The origin of this error is not yet known.

12.2 Future Work

The low uncertainty method developed in this thesis facilitates the discrimination of finer structure in optical loss spectra and the systematic investigation of less pronounced optical loss processes (and thereby further optimisation of device de-

sign and fabrication processes) than is possible with conventional methods. This simultaneously allows investigation of more subtle device physics and more precise characterisation of systematic error sources in the method itself. This discussion of future work is grouped with respect to these two categories.

Investigations of Device Physics

The temperature dependences of both absorption and internal loss observed in Figure 11.3 are not well understood. To gain understanding of this data, it would be sensible to consider mechanisms which have previously been suggested to explain a negative gradient in internal loss coefficients [60–62].

A general systematic study of the processes which contribute to internal optical loss could be carried out through investigation of device temperature, doping concentration (in various device layers) and optical mode distribution dependence in optical loss spectra.

Further Reduction of Systematic Error

Having eliminated error due to systemic drift and appropriately optimised measurement precision, the uncertainty of the modulated method for the identification of optical loss has been reduced. However, it is now limited by error sources which could not have previously been separated from those associated with systemic drift. Further improvement of uncertainty in optical loss measurement will require the identification of these errors. This includes the day to day variability in measured optical loss coefficients described in Section 9.8.

Further characterisation of the divergence described in Section 3.1 would assure confidence in the correction demonstrated in Section 3.2. In order to gain insight into its wider significance, observation of divergence related error in various material systems is recommended.

In this thesis, it is determined that intercontact current paths due to mismatch-

ing electrical properties of different device sections have a negligible effect upon optical loss measurements provided that the drive current of the pumped section is sufficiently high. If this condition was found to be an obstacle to future investigations, this error could be removed by improved device fabrication or through deeper characterisation of current paths.

Background Measurement in a Sealed Enclosure

Over the course of my studies, a sealed enclosure — for the spectrometer used in the multisection method measurements described in this document — was developed by PhD. candidate, Peter Rees. The intention of this enclosure is to reduce the collection of ambient light by the detection system. All measurements from Chapter 3 onwards make use of this enclosure.

It is shown in this appendix that, following the installation of the enclosure, additive systemic drift (the $B(t)$-type drift introduced in Section 7.2) has a negligible effect upon measurements of optical loss. This finding is significant as it is used to justify the assumption that multiplicative ($A(t)$-type) systemic drifts are dominant and that additive drifts needn't be considered. This is crucial to the work carried out in Chapters 7 and 8 (as well as the application of this work to further chapters). The process of background removal in a normal experiment is described in Chapter 2.

The approach taken was to repeatedly acquire long time series of the background signal, determine what constitutes a '*large*' variation in background and

— in relation to typical I_1 and I_2 values — infer the effect upon an optical loss measurement. This final step was achieved using the model described in Chapter 6.

During a measurement of background signal, the device was pumped and sections were switched with the relay as if a modulated multisection optical loss measurement was under way, such that any electrical effects that these processes have upon a real measurement were present in the resultant data. A device of sample $\#1_{BA}$ was pumped with 20 mA pulses at 5 kHz with a pulse width of 1.2 μs and a gate width of 1.0 μs. The beam was obstructed using a metal block in the optical path. No measurable light intensity from the device reached the detector whilst the obstruction was in place. For each background time series, $1,000$ background spectra were collected. Each spectrum consists of 360 exposures which lasted 0.1 seconds each. The total experiment duration is roughly 10 hours, comparable with the longer experiment durations examined in this thesis. This 10 hour background measurement was carried out on 5 separate occasions, and the resulting time series with the largest gradient was selected to be indicative of relatively large background drift in Figure A.1. For the selected time series, an average background value was calculated for each of the $1,000$ spectra in a spectral region from which internal optical loss may typically be measured, $1.60 - 1.65$ eV. This average background is plotted for each of the 1,000 measurements in the time series in Figure A.1.b). The background (labelled $B(t)$) can be seen to vary approximately linearly from around $30,750$ to around $31,000$ counts.

By recreating this $B(t)$ time series in the drift model described in Chapter 6, the drift error associated with this experimental data was determined for an experiment of this duration. Figure A.1.c) represents the error in a measurement of optical loss. I_1 was set to $8,000$ and I_2 was determined by the various values of optical loss which were examined. C_B is set to zero in this model to simulate the act of subtracting a measurement of the background signal at the start of the experiment. Drift error is determined by subtracting the nominal value of optical loss from the output of the simulation. This is repeated for a range of nominal values to form the data plotted in A.1.c) .
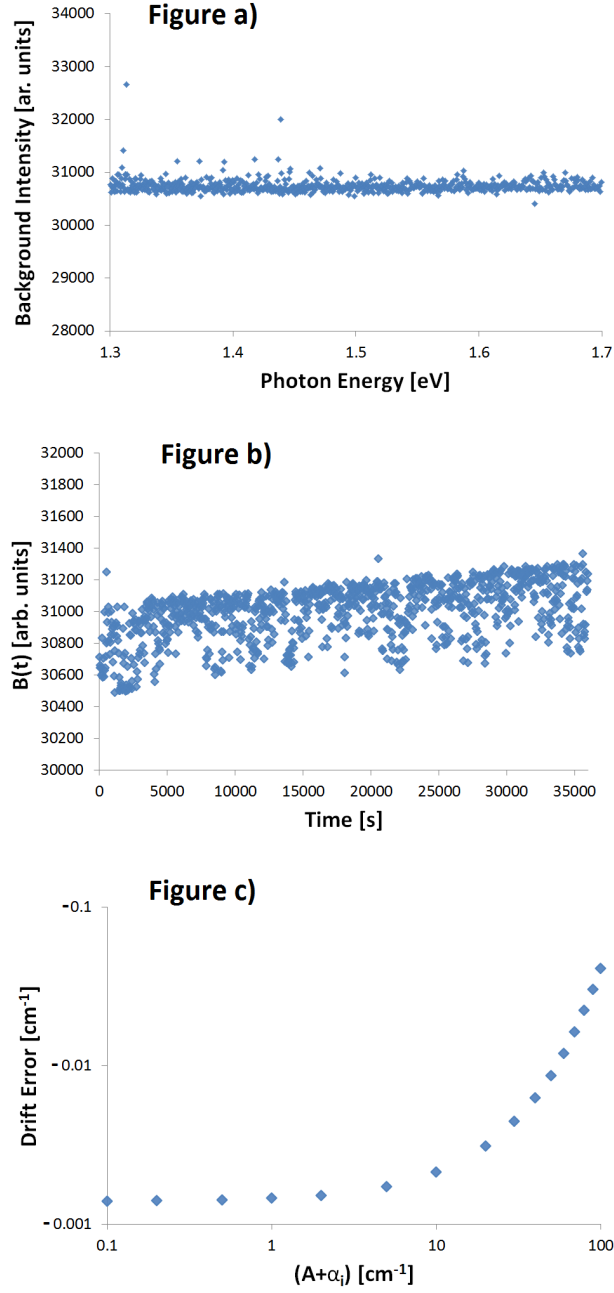
Figure A.1: Figure A.1.a) demonstrates an example background spectrum. Figure A.1.b) shows the behaviour of optical loss below the absorption edge for a succession of 1,000 such spectra. Figure A.1.c) demonstrates the modelled drift error due to this background time series for a range of optical loss values.

$B(t)$ is applied to both intensities as a function of time and the entire set of intensities is sampled to emulate a conventional multisection method experiment. A measured optical loss, and hence drift error, is determined from these sampled intensities. Bearing in mind that the point of this exercise is to evaluate whether drift error associated with additive drift is large enough to merit consideration, the drift error shown in Figure A.1.c) was calculated using a simulation of the *conventional* method. Had the modulated method been simulated, drift error would have been even smaller. Additionally, this model describes the behaviour of a 10 hour measurement. The systematic error in optical loss corresponding to a drifting background offset in an experiment of shorter duration (such as those described in Chapter 9) would be decreased from the values described in Figure A.1.c).

Taking the gradient of the background time series shown in Figure A.1.b) to typify large background gradients for the apparatus in question, the drift error depicted in Figure A.1.c) approximately represents an upper bound on drift error associated with $B(t)$ drifts.

For a relatively large drift in background offset, and over a 10 hour simulated optical loss measurement — using the conventional multisection approach —, the associated drift error does not exceed the 0.1 cm^{-1} uncertainty aim of this project for this range of optical loss coefficients. There is negligible systematic error due to additive ($B(t)$-type) systemic drift in the apparatus described in this thesis.

For an experimentalist using an apparatus in which the background signal *is* drifting sufficiently rapidly that its corresponding drift error is unacceptable in spite of modulation, additional background measurements can be distributed through the experiment duration through use of an automated shutter in the optical path.

Device Section dependence of Precision Characteristics

B.1 Investigating Section Dependence of Fractional Standard Deviation in measurements of Optical Intensity

The precision related calculations found in Section 9.3 depend upon the fact that the same dependence of fractional standard deviation upon measured intensity applies regardless of which device section the light originated from. This appendix demonstrates that this assumption is justified.

The light intensity was varied for I_1 and I_2 light signals by increasing the gate duration of each current pulse in increments of 100 ns. Gate duration was varied for both device sections in a range spanning between 0 counts and $8,000$ counts of intensity, corresponding to a maximum gate duration of 900 ns for the front section and 1300 ns for the rear section.

As in Section 9.2, values of standard deviation were calculated from samples

of 1,000 intensity measurements. A 500 kHz current pulse of 50 mA and a current pulse duration of 1500 ns was used. The CCD exposure time was 0.1 s. Intensifier gain was set to 7.
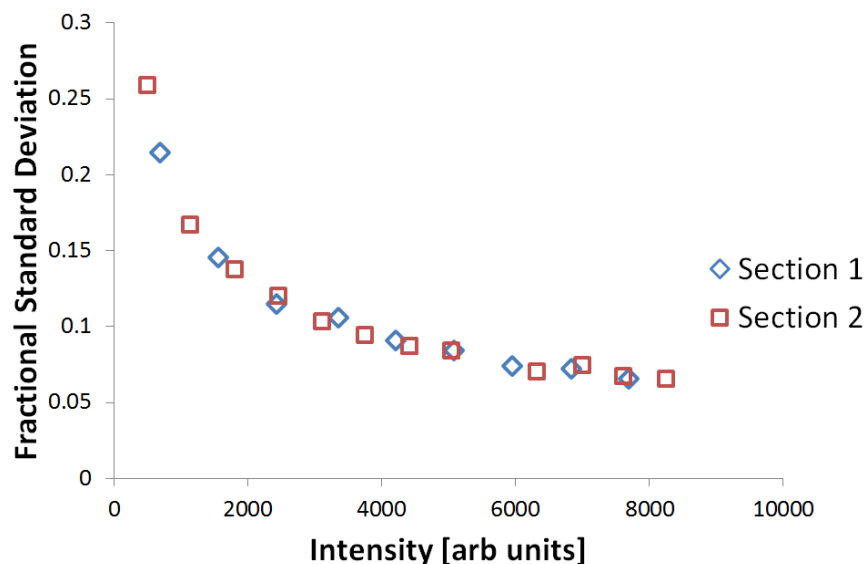

Figure B.1: Dependence of fractional standard deviation of 1,000 rapid measurements upon the measured light intensity for I_1 and I_2 light signals.

The same curve is shown to be reproduced for I_1 and I_2 light signals. It is hence assumed that the fractional standard deviation for a particular gain setting is *not* dependent upon pumped section in Chapter 9.

B.2 Error Propagation in Nonlinear Equations

In Section 9.2, Equation 9.8 is based upon the assumption that standard error propagation equations sufficiently estimate the standard deviation of an optical loss measurement based upon the respective standard deviations and magnitudes of intensities I_1 and I_2.

In order to assess the suitability of this assumption, standard deviation calculated from Equation 9.8 for *modelled* intensity data is plotted as a function of optical loss with no systemic drift (using the model described in Chapter 7). In this calculation, I_1 is set to $8,000$ counts, L is set to 0.03 cm^{-1} and the standard deviation of both intensities are set to 180 arb. units. These parameters are representative of those found in experimental data. This calculation constitutes the blue curve of Figure B.2.
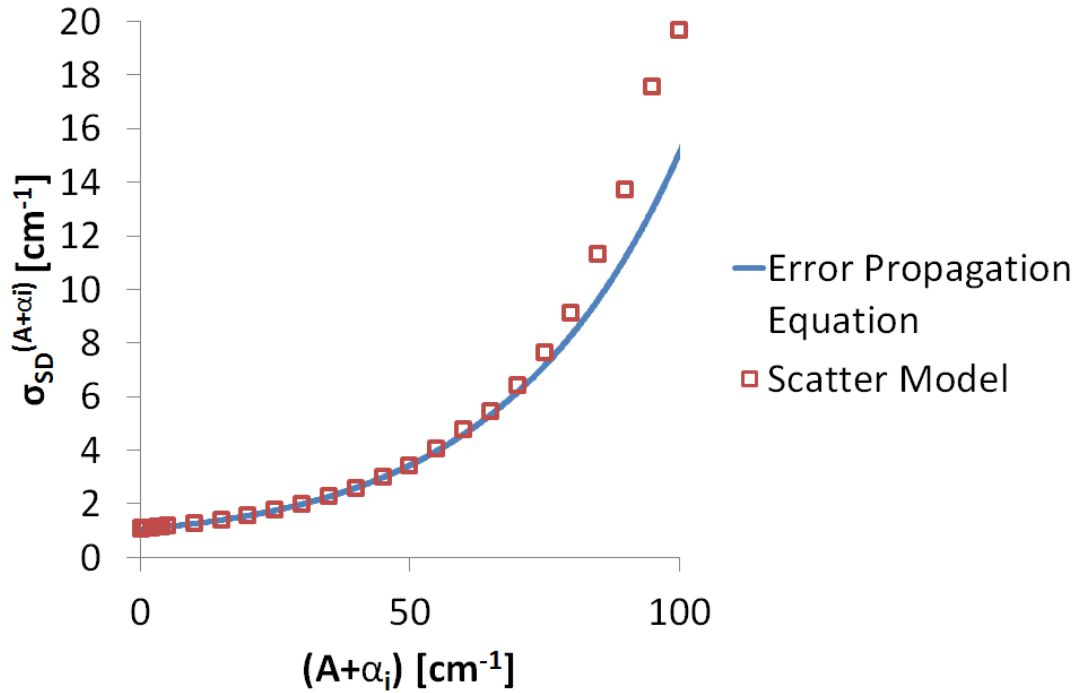
Figure B.2: Study of the approximate uncertainty propagation described in Equation 9.8.

The model described in Chapter 7 is used to simulate 1,000 of optical loss measurements for a range of values of optical loss coefficient. The normally-distributed scatter described in Section 7.4 is present in this model and systemic drift is absent. Intensity, intensity standard deviation and device section length parameters are set to the same values used in the previous (standard error propagation) calculation.

The standard deviation of the sample of 1,000 optical loss simulations is determined for each optical loss coefficient and these points are plotted as the red squares in Figure B.2.

This demonstrates that, for normally distributed samples of I_1 and I_2, the use of Equation 9.8 is appropriate for small values of Optical Loss.

The discrepancy in the calculated values of $\sigma_{SD}^{(A+\alpha_i)}$ for larger values of Optical Loss is due to the assumption (in Section 7.4) that modelled scatter magnitudes are independent of intensity and the nonlinearity of the relationship between Optical Loss and Intensity.

Error in the value determined by the error propagation equation exceeds 1% for optical loss coefficients of 55 cm^{-1} and above. However, in a real experiment, signal intensities tend to be much higher for spectral regions with higher Optical Loss coefficients.

Recall that standard deviation is primarily of practical use in the determination of minimum experiment durations for a particular precision requirement. It can be observed that the experiment duration required to reach a particular precision aim is governed by the intensities colocated spectrally with the lowest optical loss that one wishes to measure (see discussion in Section 9.4). Hence, an overestimation of the standard deviation of large values of optical loss is practically unimportant, as experiment duration optimisation is carried out with respect to (smaller) optical loss coefficients below the absorption edge.

This suggests that Equation 9.8 is appropriate, so long as it is only used in the determination of experiment durations for experiments in which the minimum Optical Loss coefficient in a spectrum is below roughly 50 cm^{-1}. As this work is primarily focused upon identification of low values of optical loss, the effect that this approximation has upon error bars was not assessed in the main body of this thesis.

Demonstration of the General Drift Model

This appendix demonstrates that the model described in Chapter 7 reproduces the general trends of real experimental data. Modelled and experimental intensity data and their respective resultant values of optical loss must be compared.

Trial 1 of the data shown in Figure 6.1 demonstrates the form of the Modulated method in an experiment during which substantial systemic drift exists. The model for systemic drift described in Chapter 7 has been used to reproduce the 'Trial 1' intensity behaviour and hence determine that the model produces results comparable to those found in experimental data.

In normal use of the model, one typically begins with a fixed $I_1(t = 0)$ and produces I_1 and I_2 time series based on multiplicative and additive drift functions and a value of $(A + \alpha_i)$. In this case, modelled data was constructed such that it would reproduce a measured experimental data set in which the true value of $(A + \alpha_i)$ is unknown. As such, gradients and y-axis intercepts determined by line-fitting the 'Trial 1' data were used to reproduce I_1 and I_2 time series. Scatter due to imprecision was then added as described in Section 7.4.

Based on the findings of Appendix A, systemic drift is assumed to be primarily multiplicative (with a negligible $B(t)$ contribution). Accordingly, systemic drift is achieved by varying $A(t)$ parameters with $B(t)$ parameters equal to zero. Applying a linear fit to the 'Trial 1' intensity data produced an optimal value for M_A of 6.8×10^{-6} s^{-1}. C_A is set to a value of 1. $B(t)$ is set to a constant value of zero in this model ($M_B = 0$, $C_B = 0$).

A σ_{SD}^{calc} of 220 arb. units was required to match the approximate distribution in both intensity time series. Figure C.1 compares this 'Trial 1' intensity and $(A + \alpha_i)$ data. The purpose of this test is simply to demonstrate that the model is functional and that it produces sensible values of $(A + \alpha_i)$ when processing familiar intensity data. The model will be used to examine trends in the equations and the method itself rather than to speculate on the underlying physical processes.

The approximate trends of the intensity data in C.1.a) are reproduced in Figure C.1.b). The gradient of 0.08 arb. units s^{-1} in the experimental intensity time series is reproduced in both modelled intensity time series.

The modelled and experimentally measured $(A+\alpha_i)$ time series in Figure C.1.c) can be seen to be comparable. The average $(A + \alpha_i)$ values of the experimental and modelled data are 2.90 cm^{-1} and 2.82 cm^{-1} respectively.

These values were determined using the Average-Process method described in Section 7.5.1.
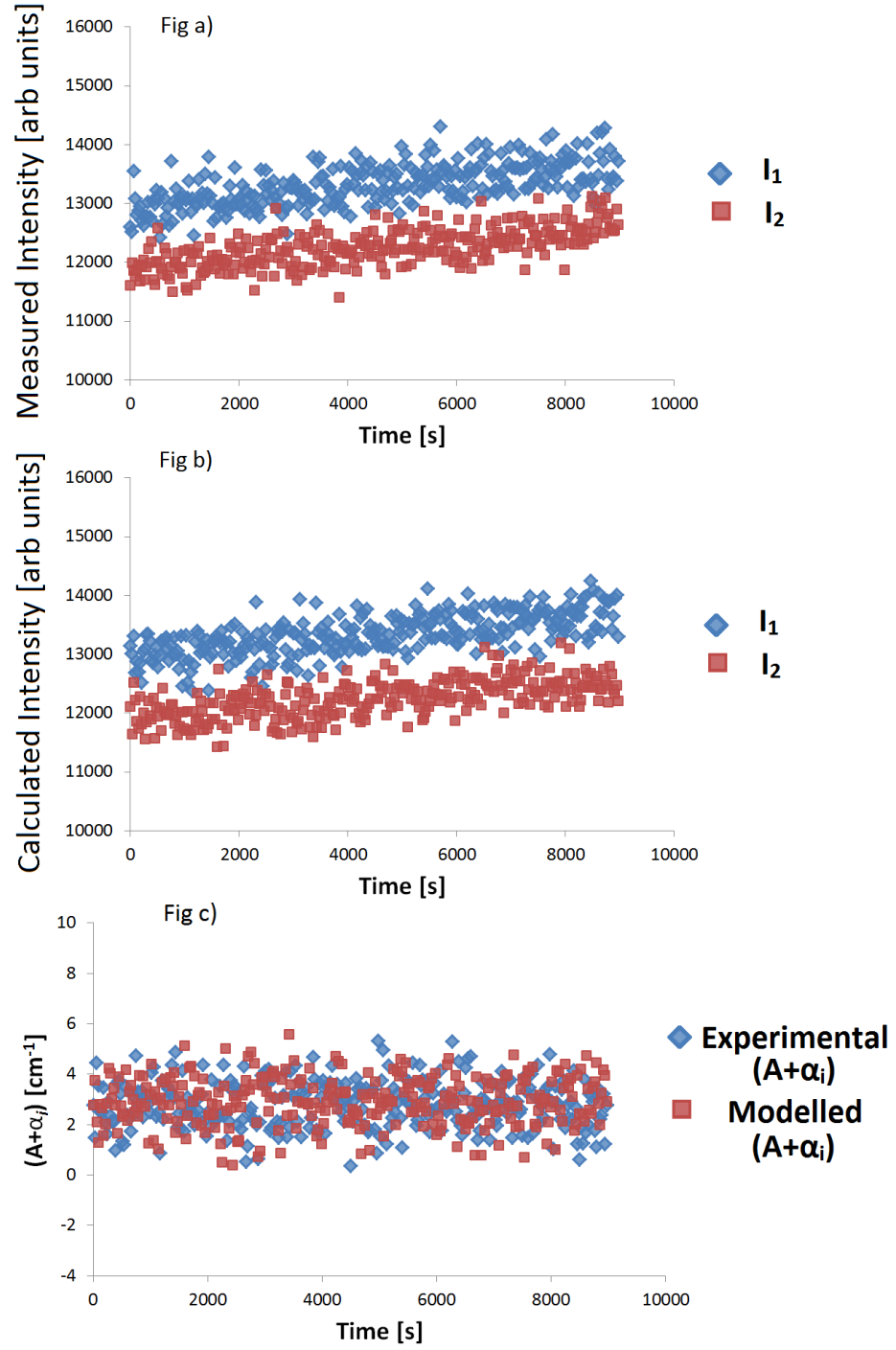
Figure C.1: Figure C.1.a) shows the 'Trial 1' intensity data from Figure 6.1. Figure C.1.b) shows the output of the model. Figure C.1.c) compares the $(A + \alpha_i)$ time series determined from adjacent pairs of I_1 and I_2 data from both the modelled and experimental 'Trial 1' data sets.

224

Conventional Multisection data results can similarly be reproduced using this systemic drift model. As this process is very similar to the above discussion, this demonstration has been omitted. Additionally, the modelled $(A + \alpha_i)$ values are similarly accurate for cases of negative and negligibly small intensity graidents as they are in the case of positive intensity gradients. However, further demonstrations are omitted for brevity.

The modelled data can be shown to reproduce trends and $(A + \alpha_i)$ values from experiment. As such, the use of the model to investigate certain aspects of the experiment is validated. This will allow the study of data analysis techniques and experimental conditions in relation to the uncertainty of the experiment. The model will not be used to infer information regarding particular sets of experimental data.

Bibliography

[1] Victor Ustinov, Alexy Zhukov, Anton Egorov, and Nikolai Maleev. *Quantum Dot Lasers*. Oxford University Press, 2003.

[2] T. Namegaya, N. Matsumoto, N. Yamanaka, N. Iwai, H. Nakayama, and A. Kasukawa. Effects of well number in 1.3- mu;m gainasp/inp grin-sch strained-layer quantum-well lasers. *IEEE Journal of Quantum Electronics*, 30(2):578–584, 1994.

[3] P. Blood, G.M. Lewis, Peter M. Smowton, H. Summers, J. Thomson, and J. Lutti. *Characterization of semiconductor laser gain media by the segmented contact method. Selected Topics in Quantum Electronics, IEEE Journal of*, 9(5):1275–1282, Sept 2003.

[4] Larry A. Coldren, Scott W. Corzine, and Milan L. Masanovic. *Diode Lasers and Photonic Integrated Circuits*. Wiley, New York, 2nd edition, 2012.

[5] Simon M Sze and Kwok K Ng. *Physics of Semiconductor Devices*. Wiley-Interscience, 1969.

[6] Horace Craig Casey and M. B. Panish. *Heterostructure Lasers*. Academic Press Inc., 1978.

[7] O Svelto. *Principles of Lasers*. Plenum Press, 1998. Translated by D C Hanna.

[8] Amnon Yariv and Pochi Yeh. *Photonics: Optical Electronics in Modern Communications*. Oxford University Press, 6th edition, 2007.

[9] Shun Lien Chuang. *Physics of Photonic Devices*. Wiley, 2nd edition, 2009.

[10] Teo Jin Wah Ronnie. *Advances in High-Power Laser Diode Packaging* . `http://cdn.intechopen.com/pdfs-wm/35937.pdf`. 28/09/2014.

[11] J. R. Hook and H. E. Hall. *Solid State Physics*. Wiley, 2nd edition, 1991.

[12] J. S Blakemore. *Solid State Physics*. Cambridge University Press, 2nd edition, 1985.

[13] P. Blood. *Quantum Confined Laser Devices: Optical gain and recombination in semiconductors*. Oxford University Press, 2015.

[14] A. R. Adams. Band-structure Engineering for Low-Threshold High-Efficiency Semiconductor-Lasers. *Electronics Letters*, 22(5):249–250, FEB 27 1986.

[15] P. C. Mogensen. *Strain Limits in $(Al_yGa_{1-y})_xIn_{1-x}P$ Quantum Well Laser Diodes*. PhD thesis, School of Physics and Astronomy, Cardiff University, 1996.

[16] Mark Fox. *Optical Properties of Solids*. Oxford University Press, Oxford, 1st edition, 2001.

[17] TR Chen, L Eng, B Zhao, YH Zhuang, S Sanders, H Morkoc, and A Yariv. *Submilliamp Threshold InGaAs-GaAs Strained Layer Quantum-Well Laser*. *IEEE Journal of Quantum Electronics*, 26(7):1183–1190, JUL 1990.

[18] Amnon Yariv and Pochi Yeh. *Photonics: Optical Electronics in Modern Communications (The Oxford Series in Electrical and Computer Engineering)*. Oxford University Press, Inc., 2006. ISBN 0195179463.

[19] N. A. Pikhtin, S. O. Slipchenko, I. S. Shashkin, M. A. Ladugin, A. A. Marmalyuk, A. A. Podoskin, and I. S. Tarasov. The temperature dependence of internal optical losses in semiconductor lasers (λ = 900–920 nm). *Semiconductors*, 44(10):1365–1369, 2010. URL `http://dx.doi.org/10.1134/S1063782610100210`.

[20] A. Salhi, P. C. Chi, A. Alharbi, G. S. Petrich, A. Al-Muhanna, and L. A. Kolodziejski. Temperature Dependence of Optical Gain and Loss in 2-μ m InP Lasers. *IEEE Photonics Technology Letters*, 23:1523–1525, October 2011. doi: 10.1109/LPT.2011.2163793.

[21] M. Jain and CN. Ironside. Internal optical loss measurements in ingaas-inalgaas quantum-well lasers operating around 1550 nm. 15(5):631–633, 2003.

[22] Y.P. Varshni. Temperature dependence of the energy gap in semiconductors. *Physica*, 34(1):149–154, 1967.

[23] H. S. Kim, R. A. Mair, J. Li, J. Y. Lin, and H. X. Jiang. Time-resolved photoluminescence studies of $al_x ga_{1x} n$ alloys. *Applied Physics Letters*, 76 (10):1252–1254, 2000.

[24] P. Blood. Gain and recombination in quantum dot lasers. *Selected Topics in Quantum Electronics, IEEE Journal of*, 15(3):808–818, 2009.

[25] W. Ouerghui, A. Melliti, M.A. Maaref, and J. Bloch. Dependence on temperature of homogeneous broadening of ingaas/inas/gaas quantum dot fundamental transitions. *Physica E: Low-dimensional Systems and Nanostructures*, 28(4):519 – 524, 2005. ISSN 1386-9477.

[26] S. Krishnamurthy, Z. G. Yu, L. P. Gonzalez, and S. Guha. Temperature- and wavelength-dependent two-photon and free-carrier absorption in gaas, inp, gainas, and inasp. *Journal of Applied Physics*, 109(3), 2011.

[27] Haji Awang Makarimi Haji Awang Kasim. *Threshold Current Temperature Dependence of Indium Phosphide Quantum Dot Lasers* . PhD thesis, School of Physics and Astronomy, Cardiff University, 2014.

[28] JD Thomson, HD Summers, PJ Hulyer, PM Smowton, and P Blood. *Determination of single-pass optical gain and internal loss using a multisection device. Applied Physics Letters*, 75(17):2527–2529, Oct 1999.

[29] A Oster, G Erbert, and H Wenzel. *Gain spectra measurements by a variable stripe length method with current injection. El. Lett.*, 33(10):864–866, 1997.

[30] FC Prince, TJS Mattos, and NB Patel. *Optical Gain Measurements OF 1.3um IN(1-X)GA(X)AS(Y)P(1-Y) As Function of Injected Current-Density. El. Lett.*, 18(24):1054–1055, 1982.

[31] SD McDougall and CN Ironside. *Measurements of reverse and forward bias absorption and gain spectra in semiconductor laser material. Electronic Letters*, 31(25):2179–2181, DEC 7 1995.

[32] B. W. Hakki and T. L. Paoli. *Gain spectra in GaAs doubleâĽŠheterostructure injection lasers. J. Appl. Phys.*, 1975.

[33] Linzhang Wu. *Determination of internal optical mode loss of semiconductor laser diodes. Appl. Phys. Lett.*, 77(12), 2000.

[34] D. Hofstetter and R. L. Thornton. Measurement of optical cavity properties in semiconductor lasers by fourier analysis of the emission spectrum. *IEEE Journal of Quantum Electronics*, 34(10):1914–1923, Oct 1998.

[35] J. R. Biard, W. N. Carr, and B. S. Reed. *Analysis of a GaAs Laser*. In *Trans. Met. SOC. AIME, vol. 230, pp. 286-290, Mar. 1964*.

[36] P M Smowton and P Blood. *Fermi level pinning and differential efficiency in GaInP quantum well laser diodes*. *Appl. Phys. Lett.*, 70(9), 1996.

[37] J. Piprek, P. Abraham, and J. E. Bowers. Cavity length effects on internal loss and quantum efficiency of multiquantum-well lasers. *IEEE Journal of Selected Topics in Quantum Electronics*, 5(3):643–647, May 1999.

[38] K. L. Shaklee and R. F. Leheny. Direct Determination of Optical Gain in Semiconductor Crystals. *Applied Physics Letters*, 18(11):475–&, 1971.

[39] J. Bakker and G. A. Acket. *Single-Pass Gain Measurements on Optically Pumped Al(X)Ga(1-X)As-Al(Y)Ga(1-Y)As Double-Heterojunction Laser Structures at Room-Temperature*. *IEEE J. Qu. El.*, 13(8):567–573, 1977.

[40] *Developing the optically pumped stripe length characterisation method*, 2014. Thomas, R and Smowton, P M, *Unpublished conference proceedings: SIOE 2014*.

[41] Y. C. Xin, Yan Li, Anthony Martinez, Thomas J. Rotter, Hui Su, Lei Zhang, Allen L. Gray, S. Luong, K. Sun, Z. Zou, John Zilko, Petros M. Varangis, and Luke F. Lester. *Optical gain and absorption of quantum dots measured using an alternative segmented contact method*. *IEEE Journal of Quantum Electronics*, 42(7-8):725–732, JUL-AUG 2006.

[42] H. Shahid, D. T. D. Childs, M. A. Majid, K. Kennedy, R. Airey, R. A. Hogg, E. Clarke, P. Spencer, and R. Murray. *Gain spectrum measurement using the segmented contact method with an integrated optical amplifier*. *Journal of Applied Physics*, 115(16), Apr 2014.

[43] M. A. Majid, D. T. D. Childs, K. Kennedy, R. Airey, R. A. Hogg, E. Clarke, P. Spencer, and R. Murray. *Absorption and Single-Pass Gain Measurements in Bilayer Quantum dot Laser Structure*. In BenSaleh, MS and Qasim, SM, editor, *2013 Saudi International Electronics, Communications and Photonics Conference (SIECPC)*, 2013. Saudi International Electronics, Communications and Photonics Conference (SIECPC), Riyadh, SAUDI ARABIA, APR 27-30, 2013.

[44] C. Koughia, Safa Kasap, and Peter Capper. *Springer Handbook of Electronic and Photonic Materials*. Springer-Verlag New York, Inc., 2007.

[45] Stella N. Elliott, Peter M. Smowton, Andrey B. Krysa, and Richard Beanland. *The effect of strained confinement layers in InP self-assembled quantum dot material. Semiconductor Science and Technology*, 27(9, SI), SEP 2012.

[46] T H Wilmshurst. *Signal Recovery from Noise in Electronic Instrumentation*. Adam Hilger Ltd., 1985.

[47] Andor Technology. *A User's Guide to Andor Ixon*. `http://irtfweb.ifa.hawaii.edu/~moris/user/Ixon_User_Guide.pdf`, . 03/04/2014.

[48] Andor Technology. *ICCD Detectors. Course notes.* `http://www.lot-qd.de/files/downloads/andor/en/cc_notesiccd_deen.pdf`, . 03/04/2014.

[49] Julie Lutti. *Optical properties of InP/AlGaInP quantum dotlaser heterostructures*. PhD thesis, School of Physics and Astronomy, Cardiff University, 2005.

[50] Keith Griffiths. *Automated Laser Diode Measurements*. PhD thesis, School of Physics and Astronomy, Cardiff University, 1992. M.Phil Thesis.

[51] G H B Thompson. *Physics of Semiconductor Lasers*. J. Wiley, 1980.

[52] Sergey Suchalkin, David Westerfeld, Gregory Belenky, John D. Bruno, John Pham, Fred Towner, and Richard L. Tober. *Measurement of semiconductor laser gain by the segmented contact method under strong current spreading conditions. IEEE Journal of Quantum Electronics*, 44(5-6):561–566, MAY-JUN 2008.

[53] PS Cross and WG Oldham. *Theory of Optical-Gain Measurements. IEEE Journal of Quantum Electronics*, 11(5):190–197, 1975.

[54] M Mikulla. *Tapered High-Powered, High-Brightness, Lasers: Design and Performance*. In R Diehl, editor, *High-Power Diode Lasers: Fundamentals, Technology, Applications*. Springer, 2000.

[55] J R Marciante and G P Agrawal. *Nonlinear Mechanisms of Filamentation in Broad-Area Semiconductor Lasers. IEEE J. Quantum Electron.*, 32(4): 590–596, Apr 1996.

[56] Andor Technology. *A Programmer's Guide to Andor Basic*. `http://www.lot-qd.de/files/downloads/andor/en/cc_andorbasicmanual_deen01.pdf`, . 03/04/2014.

[57] D. R. Matthews, H. D. Summers, P. M. Smowton, and M. Hopkinson. Experimental investigation of the effect of wetting-layer states on the gain-current characteristic of quantum-dot lasers. *APPLIED PHYSICS LETTERS*, 81 (26):4904–4906, DEC 23 2002.

[58] I. Vurgaftman, J. R. Meyer, and L. R. Ram-Mohan. Band parameters for iii-v compound semiconductors and their alloys. *Journal of Applied Physics*, 89(11):5815–5875, 2001.

[59] M. S. Al-Ghamdi, P. M. Smowton, P. Blood, and A. B. Krysa. Dot density effect by quantity of deposited material in inp/algainp structures. *IEEE Photonics Technology Letters*, 23(16):1169–1171, Aug 2011.

[60] Taehee Cho, Hyungsuk Kim, Youngse Kwon, and Songcheol Hong. Theoretical study on intervalence band absorption in inp based quantum well laser structures. *Applied Physics Letters*, 68(16):2183–2185, 1996.

[61] Srinivasan Krishnamurthy, Zhi Gang Yu, Leonel P. Gonzalez, and Shekhar Guha. Accurate evaluation of nonlinear absorption coefficients in inas, insb, and hgcdte alloys. *Journal of Applied Physics*, 101(11):113104, 2007.

[62] Peter D. Olszak, Claudiu M. Cirloganu, Scott Webster, Lazaro A. Padilha, Shekhar Guha, Leonel P. Gonzalez, Srini Krishnamurthy, David J. Hagan, and Eric W. Van Stryland. Spectral and temperature dependence of two-photon and free-carrier absorption in insb. *Phys. Rev. B*, 82:235207, Dec 2010.

"But who shall dare to measure loss and gain in this wise?
Defeat may be victory in disguise.
The lowest ebb is the turn of the tide."

— Henry Wadsworth Longfellow
In The Harbour: Loss and Gain